

Where'd the Coast Go?
Geoarchaeological exploration of upper Bay of Fundy coastal histories
in Nova Scotia

by

Wesley James Weatherbee

A thesis submitted in partial fulfillment of
the requirements for the Degree of
Master of Arts in Geography

December 2021

Halifax, Nova Scotia, Canada

Copyright Wesley James Weatherbee, 2021

Approved: Dr. Danika van Proosdij
Supervisor

Approved: Dr. Jonathan Fowler
Supervisor

Approved: Dr. Ian Spooner (External)
External Reader

Date: December 16th, 2021

Where'd the Coast Go?
**Geoarchaeological exploration of upper Bay of Fundy coastal histories
in Nova Scotia**

by Wesley James Weatherbee

Abstract

This thesis uses examines coastal histories in the upper Bay of Fundy through a lens of landscape geoarchaeology aided by modern technologies and informed by coastal geomorphology. Three approaches examine multiple scales of analysis providing a set of tools that guide the development of novel approaches to landscape geoarchaeology, supplementing studies of relationships among archaeological sites and geomorphological systems. First, a python-based automated method for measuring surface area of artifacts is presented and applications briefly discussed. Second, a date range is suggested for an archaeological site at Oak Point using microfossils, remote sensing, and geographic information systems to develop an interactive age-depth model for the site. The final chapter models coastal paleotopography using marine limit data from 15.5 to 13.5 thousand years ago. These cases highlight how enriching interactions with technology can provide ductile frameworks to inform human-scale observations and landscape geoarchaeology interpretations in the upper Bay of Fundy.

December 16th, 2021

Preface

“The self-righteousness of judgement is something that no human being has the luxury to pass. Every single one of us survive at the expense of other living things. Although our very existence contradicts our effects our struggle is still relevant in relieving the burdens that we create, but our involvement is based on individual beliefs and ambitions. Hope needs to be nurtured, compassion and understanding will not grow out of scrutiny. Encouragement and tolerance is the only way that activism will evolve from indifference.”

Aus-Rotten, 1998, from ...And Now Back to Our Programming

To provide context for this work, a quote from an anarcho-punk band that first impacted my observations of the world over 15 years ago is provided above. This quote helps frame the tone of my thesis, and perspectives I hold regarding the place of humans in the world. It is provided because I am certain that without the social groups I had during my formative years, I would not have the same appreciation for the world as I currently do. So firstly, I would like to acknowledge all my friends and family who I would not have been able to do this without.

My journey throughout graduate studies has been extraordinary. I am grateful to be coming out of my degree program with an incredibly supportive wife Charlotte, two beautiful and healthy daughters (Nora and Izzy), a home, and more care than I could have ever asked for. Beyond my household, I am exceptionally grateful for all my family, regardless of how much we are in touch at current. Much of what the ongoing COVID-19

pandemic has removed from our daily lives will take years to rebuild, and together as humans we need to nurture hope and encourage tolerance as we begin that restoration.

During my graduate studies, I have been lucky to have been surrounded by people guiding my research and providing much needed insight on a variety of topics. All these people deserve appreciation and words alone cannot communicate how thankful I am for each of the following people to have helped along this project. Some of the smallest insights early on were responsible for dramatically changing the direction and outcome of this project, and for that I am thankful.

My two supervisors, Dr. Danika van Proosdij and Dr. Jonathan Fowler have been on this journey, in some ways, alongside me. Our knowledge exchange during our entire relationship has been more than fair. The leniency provided by my supervisors to orient and re-direct this project has been largely responsible for the success of it. The kind words of Dr. Ian Spooner, who acted as an external examiner for this thesis are also appreciated. I'm excited to investigate and further discuss some of the questions and ideas that arose from your examination of my thesis. The situated knowledge of each of my supervisors has contributed to and enriched my conceptualization of the relationships between archaeology and geomorphology.

I would also like to acknowledge the support of my good friend David Jones who has and continues to be deeply supportive of my research and involved in much research-based fieldwork. Curator of Archaeology at the Nova Scotia Museum, Dr. Katie Cottreau-Robins, has been incredibly supportive of considering and facilitating almost every idea I have considered during this journey. For this I am thankful. I would also like to thank Roger Lewis, Curator of Mi'kmaq Cultural Heritage at the Nova Scotia Museum for his continual

support, critical thoughts, insightful guidance, and friendship throughout this journey. I am excited to pursue future research alongside of each of you.

Also quite importantly are many people who provided more discrete supports to this project. I am grateful to Dr. Michael Deal, and Dr. Ralph Stea for guiding conversations and providing much of the baseline information that I worked from throughout this process. The work of each of you has been fundamental to current archaeological and paleoenvironmental understandings of the Minas Basin.

Thank you as well to Dr. Pierre Jutras, Dr. Myles MacCallum, Tony Bowron, Greg Baker, Emma Poirier, Dr. Aaron Taylor, John Higdon, John Campbell, Chris Ross, and a plethora of others too numerous to list here who I have had conversations about several topics with. Each and every person has a lesson to teach me, and I appreciate those that have taken time to guide me through this journey. If anything, hopefully this thesis can give a little bit back to each of the people who have helped me along the way.

Table of Contents

Chapter 1	Introduction.....	1
1.1	Research Question	2
Chapter 2	Automated Rapid Artefact Surface Area Measurement from Imagery with Computer Vision	6
2.1	Introduction.....	6
2.2	Methods.....	7
2.2.1	Script.....	9
2.3	Results	14
2.4	Applications & Limitations	16
2.5	Conclusions.....	19
Chapter 3	Microfossils, Remote Sensing, and GIS for Proxy-dating Coastal Archaeological Sites and Landscapes: A case from Minas Basin, Bay of Fundy, Canada	21
3.1	Introduction.....	22
3.1.1	Study Area	23
3.1.2	Past Research.....	30
3.1.3	Current Research.....	32
3.2	Materials & Methods.....	32
3.2.1	Preparation of Foraminifera Data	34
3.2.2	Production of Geochronological Boundaries.....	36
3.2.3	Archaeological Survey	36
3.2.4	Geoarchaeological Analysis.....	38
3.3	Results	50
3.4	Discussion.....	60
3.5	Conclusion	66

Chapter 4	Landscape geoarchaeology of ice margins and paleo-coastlines with GIS: A case study from Minas Basin, Nova Scotia, Canada	67
4.1	Introduction.....	68
4.2	Background.....	71
4.2.1	Project background	71
4.2.2	Previous research	73
4.3	Methods.....	76
4.3.1	Re-constructing the Minas Basin paleotopographic elevation model.....	77
4.3.2	Identifying late Pleistocene relict coastal features	80
4.3.3	Considering the landscape geoarchaeology of late Pleistocene Minas Basin...	82
4.4	Results	86
4.4.1	Paleotopographic Surface Model.....	86
4.4.2	Relict Coastal Features.....	88
4.4.3	Landscape Geoarchaeology.....	90
4.5	Discussion.....	96
4.5.1	Constraints on late Pleistocene coastal zone preservation	99
4.5.2	Landscape Geoarchaeology.....	101
4.6	Conclusion	104
Chapter 5	Conclusion.....	106
Chapter 6	Bibliography	109
Supplementary Data.....		126
7.1	Appendix A: Automated Rapid Artefact Surface Area Measurement from Imagery with Computer Vision	126
	Acknowledgements	126
	Data accessibility statement	126
	List of supplementary files.....	127

7.2	Appendix B: Microfossils, Remote Sensing, and GIS for Proxy-dating Coastal Archaeological Sites and Landscapes	128
	Import Packages.....	129
	Correct for Marine Reservoir Effect & Radiocarbon Calibration.....	135
	Calculate Terminus Ante Quem Date of Sea Level Proxy Observations	143
	Visualize Result	149
	Plotting surveyed elevations of sea level proxy observations with calculated dates	
	151	
	References	156
7.3	Appendix C: Landscape geoarchaeology of ice margins and paleo-coastlines with GIS	157

Figures

Figure 1.1: Locational relationship and approximate extent of study areas using Sentinel-2 imagery. SOURCE: USGS, July 7th, 2020.....	5
Figure 2.1: Input image of experimental flakes with circular reference at left.....	8
Figure 2.2: Process of surface area extraction from an image. Top Left - blurred composite greyscale image. Top Right – edge detection after dilation and erosion. Bottom Left – contours identified in the image using computer vision. Bottom Right & Inset – calculated surface area measurement of an artifact from the contour.....	17
Figure 3.1: Location of southwest Minas Basin study area. Inset indicates location within northeastern North America.....	25
Figure 3.2: Estuaries and places referenced in text in southwestern Minas Basin in relation to Oak Point.	26
Figure 3.3: (A) Brush footing of past dyke alignment. (B) Drowned forest exposed through mud overburden at face of salt marsh peat. (C) Sand spit deposit showing strandlines present on both faces. (D) Sand ripples indicating dominant flow direction on scoured surface. Brush footing visible as linear feature of marsh grass crossing centre of photo. Sand spit hook termination visible at right of frame as elevated (lighter, dry) deposit. Drowned forest is located to the left of centre following the erosional face of salt marsh peat toward mudflats. See Figure 3.4 for location and direction of photographs. (E) GPR transect bisecting the sand spit from the limit of recent high tide toward the head of a meander channel from a larger tidal creek.....	29

Figure 3.4: Overview of landscape directly adjacent to Oak Point site. Contours shown at 5 metre intervals in grey with -5m, 0m, and 10m labelled. Location and direction of photos in Fig. 3.3 are shown by labelled blue arrows. Digitized disjoint sand spit hook crest shown as a yellow line. Remnants of the past dyke alignment shown as red line. Approximate area of foram samples shown in labelled green boundary..... 31

Figure 3.5: Location of the surveyed drowned forest at Oak Point shown as green points. Sand spit hook shown as yellow line. Dyke footing shown as red line. Location of GPR transect shown as black line..... 38

Figure 3.6: Movement of beach deposit at Oak Point since 1944. Base image matches year labelled and boldened line feature. 41

Figure 3.7: Trendline and baselines overlaying EPR of the sand deposit at Oak Point.... 43

Figure 3.8: Example of spit hook crest digitization (red line). Square cells measure 1m². 45

Figure 3.9: Distribution of artifacts in relation to lee (red point) and stoss (blue point) side of sand spit hook. White halo indicates non-debitage artifact. Dyke footing shown as red line. GPR transect shown as black line. 46

Figure 3.10: Geochronological boundaries in relation to features at Oak Point. Mean of each boundary shown by labelled contour..... 51

Figure 3.11: EPR calculations for the sand deposit at Oak Point. 53

Figure 3.12: Artifact distribution by side of spit hook. Series one is distance to crest of spit hook, series 2 is distance to nearest artifact. Lee side in blue, stoss in red..... 53

Figure 3.13: Radar surface (centre) and radar facies (left) interpretation of the reflection profile under drier conditions (right). 57

Figure 3.14: Oak Point geomorphology. Sand spit and dyke footing follow prior symbology. Also shown are artifacts (white points), gyre in artifact distribution (black spiral line), current vectors (solid blue lines), drainage (small blue dashed lines), and eddy trajectory (dashed blue line with eddy symbol)..... 59

Figure 3.15: Predicted submergence dates of rooted stumps at Oak Point. Blue polygon shows SLIP uncertainty, red boundary shows age uncertainty..... 63

Figure 4.1: Rudimentary sequence for terrestrial emergence of terrace features at Grand Pré. Source: Fowler & Weatherbee, 2020. 72

Figure 4.2: Probability distribution of calibrated dates for the deposition of the Minas Terrace south of Five Islands. SOURCE: (Amos, 1978; Wightman, 1980) 75

Figure 4.3: Continental-scale boundaries of the Laurentide Ice Sheet over the Maritimes from 15.5 to 14.2 ka CalBP. SOURCE: (Dalton et al., 2020) 76

Figure 4.4: A) Digitized isolines of marine emergence data. B) TIN dataset created from marine emergence data. C) 20m isosurface of marine emergence. D) 1m isosurface of marine emergence. 79

Figure 4.5: Location of finds described in the text in relation to the Laurentide Ice Sheet margin at ~14.9 ka CalBP. 83

Figure 4.6: Artifact found at Medford (left), and section of georeferenced survey map produced by George MacDonald showing location of artifact as "find spot" (right). Images courtesy of Mike Deal, artifact image originally in Bonnicksen et al. (1991)..... 84

Figure 4.7: Location of find at MacKay Head, Minas Basin in relation to modelled marine limit.....	85
Figure 4.8: Overview of the change in elevation on modern and modelled paleotopographic surfaces derived from lidar.	86
Figure 4.9: Selection of 12 areas visualized as shaded paleotopographic relief showing equivalently spaced, cusp-like rhythmic relief appearing on the slopes of regions of raised basin-like topography in Southern Bight. Contours at 3m interval represent elevation above marine limit defined by paleotopographic surface model.....	89
Figure 4.10: Images of the utilized core located in Medford showing flake scars highlighted in red. Arrows indicate location and direction of applied force.....	91
Figure 4.11: Shaded mesh visualization of the utilized core located in Medford showing flake scars. Arrows indicate location and direction of applied force.....	92
Figure 4.12: Dorsal and medial view of the quartz blade collected at MacKay Head.....	93
Figure 4.13: Ventral and lateral view of the quartz blade collected at MacKay Head.	94
Figure 4.14: Conceptual model of landscape development on peri-glacial landscape at Medford. Modified from: Allred et al., 2014.....	98

Tables

Table 2.1: Summary table of Python modules used in the script.....	10
Table 2.2: Output tabular results from experimental data. User entered diameter bolded...16	
Table 3.1: Radiocarbon dates and corresponding depth data from Foram samples at Kingsport as reported in Scott & Greenberg, 1983 & Smith et al., 1984.	33
Table 3.2: Linear relationships calculated describing change in elevation of samples over time.	35
Table 3.3: Relevant data resulting from air photo georectification.	40
Table 3.4: Calibrated (MARINE20) radiocarbon dates and HHW elevations (CGVD2013) for Kingsport marsh.	50

Equations

Equation 1: End Point Rate equation modified to represent beach migration.	43
---	----

Chapter 1 Introduction

The coast frequently provides an intersection of natural and cultural histories, presenting significant material and immaterial records of the past, feeding the development of coastal histories (Land, 2007). Coasts are places of many faces, ends and beginnings, preservation and decay, life and death. For millennia, coasts have provided a landing, home, and point of departure for people all over the globe. During this time, the ostensibly static coastline has migrated in to and out of the landscape, people closely following.

The migration continues to this day, now placing cultural resources throughout the north Atlantic at risk of being lost to coastal erosion or submergence. Examples of archaeological sites vulnerable to the impacts of rising seas through coastal erosion and submergence is a well documented theme in Atlantic Canada (e.g.: Black, 2018; Davis, 1980; Deal, 1991; Erskine, 1960; Simonsen, 1979, 1978; Smith and Wintenburg, 1929; Westley et al., 2011). In Nova Scotia, coastal marshlands of the upper Bay of Fundy possess a deep cultural history sealed by millennia of salt-marsh accretion on pace with sea-level rise. The projected relative-sea-level rise (RSLR) of 0.82-1.21m by 2100 (relative to 1995 baseline, RCP2.6 – 8.51¹) in the upper Bay of Fundy places coastal archaeological and cultural sites at risk of being lost due to inundation and erosion (James et al., 2014). The current impacts of coastal climate change necessitate timely collection of contextual archaeological information before it becomes unrecoverable.

¹ RCP = relative concentration pathway of atmospheric CO₂ (Collins et al. 2013)

The relationship between the changing landscape and people in the upper Bay of Fundy has been largely understudied despite numerous archaeological studies, a select few cited above. Interdisciplinary approaches integrating natural histories of developing coastal marshes aid in locating and contextualizing cultural histories at the coast for protection, awareness, and communication. Protection, location, and contextualization of coastal histories informs tourism and heritage sectors by fostering increased public awareness of and interest in the past. These increased understandings of the diverse heritage within the upper Bay of Fundy benefit social, cultural, and economic development within the Atlantic region, with one example being a more effective and collaborative approach to the planning and execution of coastal climate change adaptation strategies.

1.1 Research Question

The following thesis examines the dynamic location of the coast in the upper Bay of Fundy since the previous process of deglaciation began sometime after 18 thousand calibrated years before present (ka calBP). This thesis presents materials allowing archaeologists to refine conceptual models of where the coastline, and therefore people have been in the past. These conceptual models are applied to landscapes where dynamic site formation processes in the coastal zone have favored preservation.

My research employs a multi-scale approach to landscape geoarchaeology within the upper Bay of Fundy, where relative sea level rise continues to threaten the integrity of archaeological sites. Three short papers are presented as chapters illustrating how multi-scale geoarchaeological approaches to coastal archaeological research in the upper Bay of

Fundy (**Figure 1.1**) can inform our understandings of where archaeological remains will be preserved. Each chapter contributes to answering the following research question at different scales within the upper Bay of Fundy by integrating geoarchaeological approaches marrying natural and cultural histories at the land-water interface in the Southern Bight of Minas Basin:

How effectively can coastal histories in the upper Bay of Fundy be narrated by integrating archaeological and ethnographic information with modern remote sensing and computer-assisted analyses?

Natural histories provide the principal link between physical geography and archaeological prospection through analysis of the changing landscape using studies of sediment dynamics, remote sensing data, and pre-existing data using a GIS. Cultural histories provide links between human geography and archaeology (as the study of past cultures through material remains) employing archival and ethnographic research, archaeological field survey and mapping, and artifact analysis. GIS facilitates the re-integration of past human activities onto the terrain of past landscapes via geovisualization and spatial analysis of archival fieldwork, remote sensing, and archaeological analysis.

The second chapter presents the smallest scale approach, aiming to allow measurements of artifacts to be better understood in coastal geomorphological terms. This is achieved through a method of automatically extracting surface area measurements from artifacts using computer vision, allowing the shape of artifacts in large assemblages

reworked by coastal processes to be rapidly considered in more detail. The paper focuses on the method of extracting surface area, rather than the geoarchaeological application of such method, but touches upon application in the discussion.

The third chapter details a geoarchaeological study of the archaeological site at Oak Point (BgDc-07), Kingsport, Nova Scotia. The study at Oak Point investigates the relationship of the archaeological materials to the environmental conditions and landscape development at the confluence of the Habitant and Cornwallis estuaries.

The fourth chapter is an exercise in landscape geoarchaeology throughout the Minas Basin using GIS to model raised coastlines by considering and correcting for topographical deformation of the landscape during the Late Pleistocene.

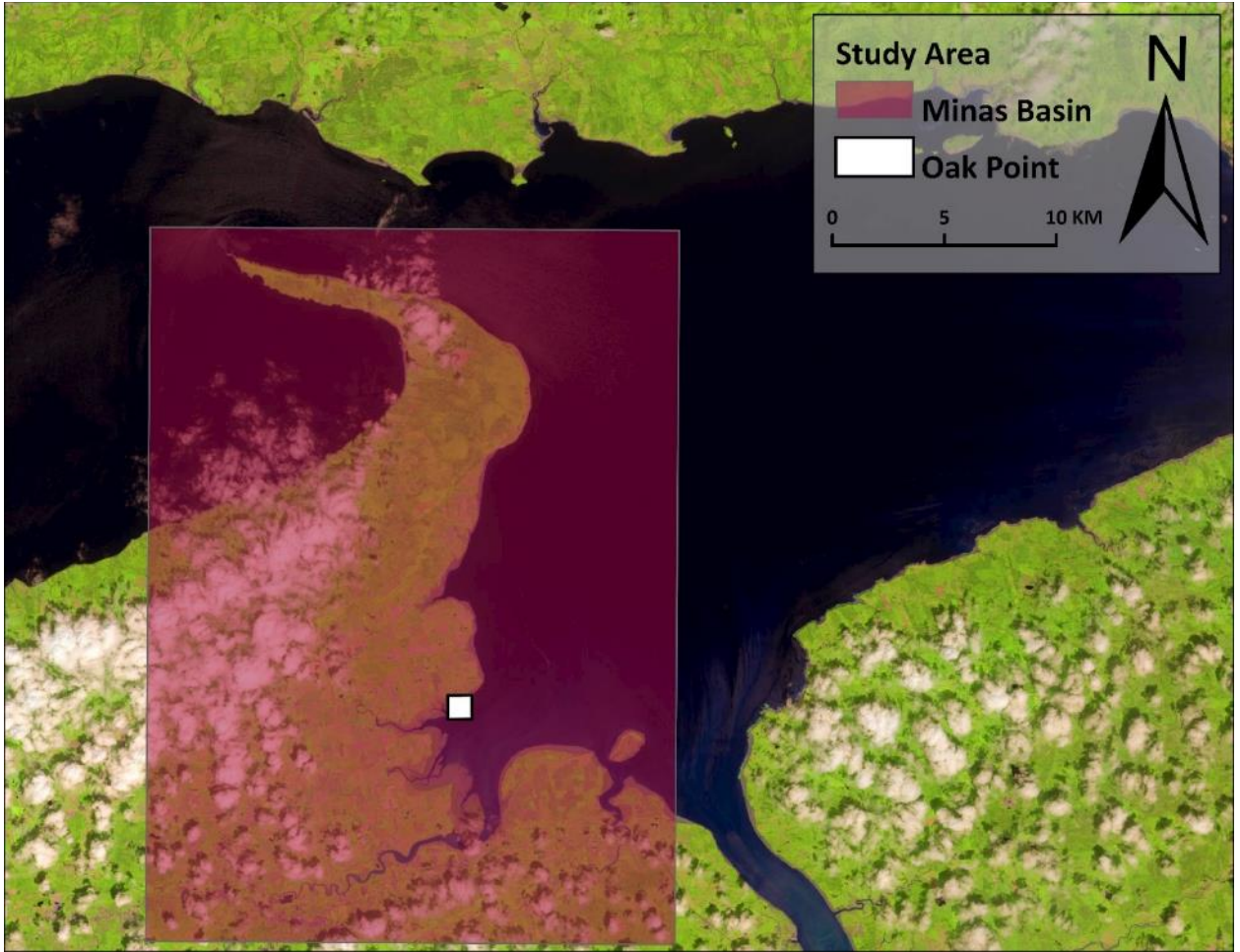


Figure 1.1: Locational relationship and approximate extent of study areas using Sentinel-2 imagery.

SOURCE: USGS, July 7th, 2020.

Chapter 2 Automated Rapid Artefact Surface Area Measurement from Imagery with Computer Vision

Submitted to the Journal of Lithic Studies on May 26, 2021

Accepted with minor revisions August 16, 2021

Abstract:

Automated surface area measurements have been of interest to archaeologists since digital imagery began allowing researchers to remotely collect artefact metrics. The following presents a method of automatically measuring 2D surface area from artefact planform images employing a Python 3 deployment of computer vision. The Python script, provided as a .py file in supplementary data, creates boundaries around regions of relatively homogenous pixels (artefacts) in the image. These bounded regions are called contours. A count of the number of pixels within each contour provides a surface area in pixels. A circular reference object provides a conversion factor for the contours, as well as a point of reference for geometric accuracy of outputs.

Measurements of 2D artefact surface area can be used in combination with measurements of length, width, thickness, and mass, or in some cases, replace such measurements. This technique provides utility to archaeology with applications to new documentation of artefacts, archived artefact images containing a scale, as well as landscape geoarchaeology and sedimentary contexts. Limitations of this type of surface area measurement include the requirement of the image background being of a solid colour heavily contrasting the artefacts being measured. Effectively, the background requirement limits deployment supporting collection of rapid field measurements from in-situ surface scatters without modification to the script or manipulation of the artefacts. Analytical applications utilizing this technique include studies of relative artefact abundance, shape and size class characterizations in artefact scatters, and redistribution of artefacts by geomorphological processes.

Keywords: imagery, automation, digital archaeology, surface area, archaeometry

2.1 Introduction

Automatic extraction of measurements and shape data from artefacts is not a new trend in archaeology. In the early 1990s, the Graphically Oriented Archaeological Database Project produced an environment allowing archaeologists to automatically extract and compare shape information from line drawings of artefacts, primarily pottery vessels (Lewis & Goodson 1990). Within a decade, this approach was employed by archaeologists studying lithic artefacts justifying the process as a means to extract information and metrics that may

be hard to extract using a calliper and other traditional methods (McPherron & Dibble 1999).

Over two decades later, the pace of technological advancement has continued to increase, and digital cameras, laptops, tablets, and mobile phones now commonplace in archaeological fieldwork. While adoption of digital technologies is widespread in archaeology, digital data collection methodologies have not enjoyed the same appreciation. Byrd & Owens identify one factor impeding the adoption of new methods measuring surface area of artefacts, stating that measuring “surface area ... will not likely be adopted by archaeologists unless a relatively simple technique is developed for obtaining such data” (1997, 316).

Here we present a step toward the technique forecasted by Byrd & Owens (1997) by automating the extraction of 2D surface area using computer vision from the OpenCV module in Python 3 (Bradski 2000; Van Rossum & Drake 2009). The method allows archaeologists to extract surface area measurements from an assemblage, collection, or sample of lithic flakes, or other relatively flat artefacts, using images. Images can contain many artefacts, and measurements are automatically output to a CSV file.

2.2 Methods

The script used to derive artefact surface area was modified from a post originally on PyImageSearch using computer vision to measure objects in images (Rosebrock 2016). The resulting method employs computer vision to automatically quantify the 2D surface area of experimentally produced lithic flakes in a planform image. User inputs for the script

are the image directory and diameter of the circular reference object entered during command line execution of the script. Required materials include a circular reference object, camera, background of contrasting colour, artefacts, and a Python 3 installation including the modules in **Table 2.1**.

A circular reference object with a known diameter was placed at the left of the image (**Figure 2.1**). Initial measurements were converted from a count of pixels to user input units from the diameter of the reference object allowing subsequent measurements to use the same units. Our reference object is a Canadian Quarter with a reported diameter of 2.388cm from Royal Canadian Mint technical specifications (“25 Cents Coins,” The Royal Canadian Mint, n.d.).



Figure 2.1: Input image of experimental flakes with circular reference at left.

A selection of differentially shaped, experimental flakes was used to demonstrate the process of extracting surface area measurements using Python. The flakes consist of a light grey Georgetown flint with a white cortex. To contrast the flake material, a matte black background was selected. Flakes were placed to the right of the reference object in the image frame.

2.2.1 Script

Python 3 code is located below, highlighting how the technique works. For a more detailed explanation on this technique, please visit the tutorials on DigitalArchNS (Weatherbee 2020) or PyImageSearch (Rosebrock 2016).

To employ the script, install the required modules (**Table 2.1**), navigate to the directory holding the python script within a command prompt window. Ensure the subdirectories “images” and “csv” exist, the “images” subdirectory contains the image to be measured, and that you have a diameter measurement of the circular reference object, then enter the following:

```
python artifact-area.py --image [directory] --width [diameter]
```

Where [directory] is the directory to the image files relative to the directory of the python script, and [diameter] is the diameter of the reference object in the desired unit of measurement. After entering this information, press the Enter key to begin measuring.

First, the input image is converted to a single channel composite greyscale image. Gaussian blur is executed twice prior to edge detection using an initial kernel of 9x9 followed by a 5x5 kernel iteration promoting smoothed edges while minimizing overall image blur. Edge

detection is then applied to the composite greyscale image using the `auto_canny` method defined at the top of the script (Canny 1986; Rosebrock 2015b). Erode and dilate functions then decrease and increase the thickness of the contour in pixels, respectively. These functions help derive the contours from the input image, therefore providing information fundamental to the process of extracting surface area. Three iterations of the dilate function are followed by two iterations of erode to promote contour connectivity along artefact perimeters in the edge map. Contours are sorted from left to right, then enter a `for` loop measuring X, Y, and surface area.

Table 2.1: Summary table of Python modules used in the script.

Modules

Name	Summary	Reference	Installation	Alias
OpenCV	Open-source computer vision and machine learning library built to simplify and streamline adoption of machine learning and computer vision. <i>Version 4.1.2.30</i>	(Bradski 2000)	pip install opencv-python==4.1.2.30	cv2
SciPy	Open-source mathematical algorithm and convenience function library built on-top of NumPy. <i>Version 1.3.3</i>	(Virtanen <i>et al.</i> 2020)	pip install scipy==1.3.3	distance
imutils	Open-source convenience function and visualization library built on OpenCV, matplotlib, and NumPy. <i>Version 0.5.3</i>	(Rosebrock 2015a)	pip install imutils==0.5.3	perspective; contours
NumPy	Open-source scientific computing library fundamental to many Python workflows. <i>Version 1.17.4</i>	(Harris <i>et al.</i> 2020)	pip install numpy==1.17.4	np
ArgParse	Native Python library simplifying user input to scripts through CMD. <i>Python 3 Version 3.7.5</i>	(Van Rossum 2021)	n/a	argparse
CSV	Native Python library simplifying read and write of CSV files from multiple sources. <i>Python 3 Version 3.7.5</i>			csv
matplotlib	Open-source 2D graphics library for visualization and app development. <i>Version 3.1.2</i>	(Hunter 2007)	pip install matplotlib==3.1.2	n/a
pandas	Open-source data structure and statistical tools library designed to make scientific Python a more attractive and practical statistical computing environment for academic and industry practitioners alike (McKinney 2010, 56). <i>Version 0.25.3</i>	(McKinney 2010)	pip install pandas==0.25.3	pd

```

"""
Title: Automated Rapid Artifact Surface Area Measurement from Imagery using Computer
Vision
Author: Wesley Weatherbee
Date: February 2020
Description: This script is intended to rapidly collect measurements
            from multiple artifacts in a single image using computer
            vision.

Modified from: https://www.pyimagesearch.com/2016/03/28/measuring-size-of-objects-in-an-image-with-opencv/
Original Author: Adrian Rosebrock
Date: March 28, 2016
"""

# USAGE
# open command-line (cmd.exe) and change the directory to the
# directory where the file is loaded using: cd [path to directory here]
# after changing the directory, enter the following code in command-line:
# python artifact-area.py --image images/test_01.jpg --width 2.381

# import the necessary packages
from scipy.spatial import distance as dist
from imutils import perspective
from imutils import contours
import numpy as np
import argparse
import imutils
import cv2
import csv
import pandas as pd

# define the automatic canny edge detection method
def auto_canny(image, sigma=0.33):
    # compute the median of the single channel pixel intensities
    v = np.median(image)

    # apply automatic Canny edge detection using the computed median
    lower = int(max(0, (1.0 - sigma) * v))
    upper = int(min(255, (1.0 + sigma) * v))
    edged = cv2.Canny(image, lower, upper)

```

```

    # return the edged image
    return edged

# define midpoint method
def midpoint(ptA, ptB):
    return ((ptA[0] + ptB[0]) * 0.5, (ptA[1] + ptB[1]) * 0.5)

# construct the argument parser and parse the arguments
ap = argparse.ArgumentParser()
ap.add_argument("-i", "--image", required=True,
                help="path to the input image")
ap.add_argument("-w", "--width", type=float, required=True,
                help="width of the left-most object in the image")
args = vars(ap.parse_args())

# load the image, convert it to grayscale, and blur it slightly, twice
image = cv2.imread(args["image"])
gray = cv2.cvtColor(image, cv2.COLOR_BGR2GRAY)
gray = cv2.GaussianBlur(gray, (9, 9), 0)
gray = cv2.GaussianBlur(gray, (5, 5), 0)

# perform edge detection, then perform a dilation + erosion to
# close gaps in between object edges
edged = auto_canny(gray)
edged = cv2.dilate(edged, None, iterations=3)
edged = cv2.erode(edged, None, iterations=2)

# find contours in the edge map
cnts = cv2.findContours(edged.copy(), cv2.RETR_EXTERNAL,
                        cv2.CHAIN_APPROX_SIMPLE)
cnts = imutils.grab_contours(cnts)

# sort the contours from left-to-right and initialize the
# 'pixels per metric' calibration variable
(cnts, _) = contours.sort_contours(cnts)
pixelsPerMetric = None

# create list object
measure = []

# loop over the contours individually
for c in cnts:
    # if the contour is not sufficiently large, ignore it

```

```

if cv2.contourArea(c) < 10000:
    continue

# compute the rotated bounding box of the contour
orig = image.copy()
box = cv2.minAreaRect(c)
box = cv2.cv.BoxPoints(box) if imutils.is_cv2() else cv2.boxPoints(box)
box = np.array(box, dtype="int")

# order the points in the contour such that they appear
# in top-left, top-right, bottom-right, and bottom-left
# order.
box = perspective.order_points(box)

# unpack the ordered bounding box, then compute the midpoint
# between the top-left and top-right coordinates, followed by
# the midpoint between bottom-left and bottom-right coordinates
(tl, tr, br, bl) = box
(tltrX, tltrY) = midpoint(tl, tr)
(blbrX, blbrY) = midpoint(bl, br)

# compute the midpoint between the top-left and top-right points,
# followed by the midpoint between the top-right and bottom-right
(tlbrX, tlbrY) = midpoint(tl, br)
(trbrX, trbrY) = midpoint(tr, br)

# compute the Euclidean distance between the midpoints
dA = dist.euclidean((tltrX, tltrY), (blbrX, blbrY))
dB = dist.euclidean((tlbrX, tlbrY), (trbrX, trbrY))

# if the pixels per metric has not been initialized, then
# compute it as the ratio of pixels to supplied metric
if pixelsPerMetric is None:
    pixelsPerMetric = dB / args["width"]

# computer centre of the contour
M = cv2.moments(c)
cX = int(M["m10"] / M["m00"])
cY = int(M["m01"] / M["m00"])

# compute the size and surface area of the object
dimA = (dA / pixelsPerMetric)
dimB = (dB / pixelsPerMetric)

```

```

SA = ((cv2.contourArea(c) / pixelsPerMetric) / pixelsPerMetric)

# add measurements to list
measure.append((dimA, dimB, SA))

# draw contours in red
cv2.drawContours(orig, [c.astype("int")], -1, (0, 0, 255), 2)

# draw the object area on the image
cv2.putText(orig, "{:.2f}sqcm".format(SA),
            (int (cX), int (cY)), cv2.FONT_HERSHEY_SIMPLEX,
            0.65, (0, 0, 0), 3)
cv2.putText(orig, "{:.2f}sqcm".format(SA),
            (int (cX), int (cY)), cv2.FONT_HERSHEY_SIMPLEX,
            0.65, (255, 255, 255), 2)

# show the output image
origS = cv2.resize(orig, (1536, 1024))
cv2.imshow("Image", origS)
cv2.waitKey(0)

# take X, Y, and surface area measurements and append them to a CSV
col_titles = ('X', 'Y', 'SA')
data = pd.np.array(measure).reshape((len(measure) // 1, 3))
pd.DataFrame(data, columns=col_titles).to_csv("csv/Measurements.csv", index=False)

```

2.3 Results

Running the script results in contours being created around each artefact in the image, from which surface area measurements are extracted. Our experimental results indicate an error of 2.23% in the geometric measurements of surface area, based on an expected surface area of our circular reference scale (Canadian quarter) being 4.48cm² compared to the experimental surface area of 4.58cm² obtained by our method. The expected value for surface area of a quarter is calculated with the diameter measurement provided by the Royal Canadian Mint (“25 Cents Coins,” The Royal Canadian Mint, n.d.). The experimental value for surface area is provided by the contours in the script. This percent error can be attributed

to camera angle misalignment or lens distortion and is used to calculate the uncertainty of surface area values in **Table 2.2**.

The `pixelsPerMetric` value is a count of pixels corresponding to the user input diameter of the circular reference object. Our experimental results report 71.19 pixels per 2.388cm. This is equal to a pixel dimension of 0.034cm along each side meaning each pixel reflects a real-world area of $1.13 \times 10^{-3} \text{cm}^2$.

The output CSV holds measurements of surface area, and X and Y dimensions of each object (**Table 2.2**). The X and Y values are measured in centimetres, but do not equate to length and width values measured using a calliper (Andrefsky 2005). Rather, these values represent the minimum and maximum length and width of bounding box of minimum dimensions fitting the contour. Similar measurements have been considered to represent the intermediate axis of flakes, in prior lithic research (Brown 2001; Cadieux 2013). In some cases, these values are similar, but should not be used interchangeably.

Table 2.2: Output tabular results from experimental data. User entered diameter bolded.

X (cm)	Y (cm)	SA (cm²)
2.430	2.388	4.58 ±0.10
2.345	5.644	10.29 ±0.23
2.717	1.841	3.69 ±0.08
1.633	4.721	5.71 ±0.13
1.299	2.172	2.15 ±0.05
2.660	1.642	3.56 ±0.08
2.306	2.497	3.80 ±0.08
2.644	2.079	3.72 ±0.08
1.308	1.968	2.10 ±0.05
4.244	3.077	10.33 ±0.23
3.947	2.306	6.89 ±0.15
1.637	2.299	2.80 ±0.06
3.891	2.338	6.51 ±0.15
4.127	4.705	13.95 ±0.31
2.559	3.085	5.77 ±0.13
4.325	3.421	10.27 ±0.23
2.917	4.763	8.96 ±0.20
1.691	1.949	2.37 ±0.05
1.140	3.286	2.63 ±0.06
4.544	2.476	7.71 ±0.17
1.898	4.649	6.06 ±0.14
1.942	1.951	2.66 ±0.06
2.094	5.013	7.47 ±0.17
3.655	1.891	4.45 ±0.10
4.160	2.340	6.56 ±0.15

2.4 Applications & Limitations

We have presented the most rapid technique currently available for extracting surface area measurements from artefacts. This technique is lightweight, running on a python script that can be executed in a command prompt using in-line arguments. The script instructs the computer to translate the image to greyscale, blur the image, perform canny edge detection using thresholds defined by the range of values within the image, place contours around relatively homogenous groupings of pixels fitting a size criterion, and output the measurements to a CSV (**Figure 2.2**).

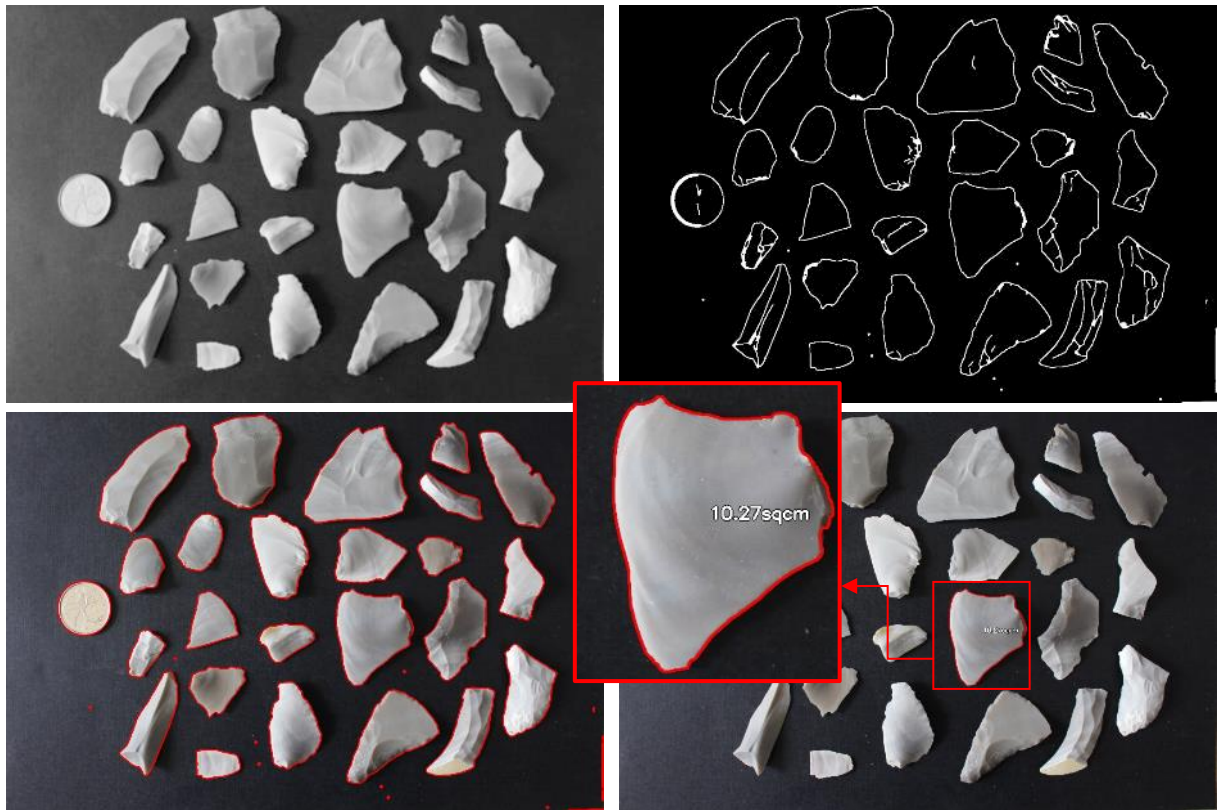


Figure 2.2: Process of surface area extraction from an image. Top Left - blurred composite greyscale image. Top Right – edge detection after dilation and erosion. Bottom Left – contours identified in the image using computer vision. Bottom Right & Inset – calculated surface area measurement of an artifact from the contour.

Our method is powerful, yet simple, and with careful consideration, has a variety of archaeological applications, including extracting information from scans of artefact images in published literature. The applications of the method presented not only apply to archaeology and artefact analysis, but can percolate through the disciplines of geography and geology – from where Byrd & Owens (1997) drew their inspiration.

Automated, rapid measurement of surface area also identifies a point of intersection for geologic, geographic, and archaeological research along past and present coastline contexts by considering how object shape influences its relocation by geomorphic processes. The

intersection is expressed in emerging relational studies of geomorphology and archaeology known as landscape geoarchaeology (Holliday 2009; Holliday *et al.* 2019; Contreras 2017; 2009). Flake shape often resembles that of beach shingles found within the swash-zone of coastal systems having a relatively small mass compared to 2D surface area. By creating a way of readily quantifying the geometry of swash-zone gravel shingles, geographers will be able to create more thorough conceptual and numerical models of how materials such as beach shingles and flakes are transported in coastal areas. Research in such areas will certainly provide insights into geoarchaeological problems of taphonomy, site-formation processes, and post-depositional movements of artefacts within coastal environments.

Deploying this tool on larger assemblages with well-defined spatial provenience can give insights into the relationships that surface area holds in relation to well-defined expected distributions of debitage in flintknapping areas (Kvamme 1988; 1997; 1998). Surface area can be used in combination with object mass, and material mass density to estimate the thickness and volume of materials (Cadieux 2013). Both applications present novel ways to observe patterns in spatial and non-spatial assemblages through attributes too complex to compute from traditional measurement techniques.

This technique does not come without some limitations. The ability of this method to measure objects comes from an apparent contrast between object and background. This means that employing this method on images with varying material types may provide inaccurate measurements between objects. One approach to solve this problem is to separate each assemblage based on material type. This way, consistent measurements and associated errors can be obtained for each material class.

Understanding what the measurements represent clarifies this method's limitations and applicability to other problems. The distinction between 2D and 3D surface area is key. A 2D surface area is measured only using the horizontal axis, while a 3D surface area uses the vertical (depth) axis in addition to horizontal. This effectively means a 2D surface area represents a footprint of an artefact viewed in planform. The relevance of this distinction is that our 2D surface area measurement is in fact a generalized potential area for lift or drag forces to be applied to the object in conceptualizing artefact transportation whether it be due to waves on a beach, currents in a river, or striking flakes from a core.

2.5 Conclusions

The opportunities for research provided by this technique are vast. The convenience offered by our automated, rapid artefact surface area measurement technique is instrumental in its service of accelerating data collection and analysis. Techniques such as this bridge digital analysis skills and computer literacy with the material culture remains of the past. By providing links to blog posts inspiring this publication, we are presenting sources of information that can be used to develop computer literacy in relation to programming and analysis.

Though still quite rudimentary, this technique could be applied as one step in a much larger research workflow. Automated metric extraction from unpublished images, and archival scans of artefacts offers an avenue for archival projects to benefit from this technique as well. The extracted contours could perceivably be one input layer into a deep learning algorithm determining typology from an image. Alternatively, surface area used as a proxy for lift and drag forces may be able to help identify a feeder source for artefacts redistributed within coastal areas by longshore drift. Countless present and future

applications are presented by this technique, and the authors encourage input into future developments by interested parties in any discipline.

Chapter 3 Microfossils, Remote Sensing, and GIS for Proxy-dating Coastal Archaeological Sites and Landscapes: A case from Minas Basin, Bay of Fundy, Canada

Tentatively to be submitted to the Journal of Archaeological Science

Abstract

An analysis employing previously published *Foraminifera* data spanning the Middle to Late Holocene from salt marsh deposits backing the coastal beach site of Oak Point (BgDc-07) on the southwestern shores of Minas Basin, Nova Scotia is provided.

Site formation and post-depositional processes are examined using Foraminifera data from three radiocarbon dated samples published as higher high water (HHW) sea level indicator points (SLIP). These data provide an elevation equivalent to the limit of high marsh, and highest astronomical tides (HAT) for the age interval of each sample. Two SLIPs represent past higher high marsh, and one represents lower high marsh.

Stumps of an *in-situ* drowned forest are exposed below the site, clustering in two loci. The first hold well rooted stumps showing through mudflats at the lower limit and along an erosional face at the upper limit. The erosional face contains rooted stumps of various sizes, indicating the forest was well established prior to relative sea level (RSL) rise draping the former forested surface with accretional layers of salt marsh sediments.

Calibrated SLIP ages, together with a hydrographic vertical separation (HyVSEP) surface, lidar derived digital elevation model (DEM), and global navigation satellite system (GNSS) and ground penetrating radar (GPR) surveys allow the production of geochronological boundaries indicating multiple *terminus post quem* and/or *terminus ante quem* boundary scenarios for the site and drowned forest.

Additionally, the geochronological boundaries allow relict geomorphological features to be proxy-dated for archaeological prospection and reconstruction of past morphodynamics of the landscape in the southwestern Minas Basin.

3.1 Introduction

Microfossil analysis in archaeological research repeatedly demonstrates its importance for reconstructing chronologies of archaeological sites and environmental conditions (e.g. [Griffiths et al., 2015](#); [Marriner et al., 2005](#); [Pint et al., 2015](#); [Vittori et al., 2015](#)). Recent developments in the analysis of microfossil assemblages have provided methods of differentiating cultural and natural shell deposits ([Rosendahl et al., 2007](#)), and adding provenance to lithic archaeological materials ([Quinn, 2008](#)) as well as to objects manufactured of fired or unfired clay, chalk, and lime ([Riquelme et al., 2012](#); [Wilkinson et al., 2008](#); [Williams et al., 2015](#)). Our work focuses on the use of microfossils consisting of the calcareous outer remains of foraminifera (foram), a type of single-celled organism primarily found in marine environments.

Foram studies are used globally to understand changes in sea level, salinity, and temperature their habitats at a species level ([Hayward, et al., 2020](#)). Understanding foram habitat preference plays a vital role in the interpretation of modern salt-marsh ecology, a process that has been used in combination with radiometric dating methods to delineate past RSL with a vertical accuracy of up to $\pm 0.15\text{m}$ ([Gehrels, 1994](#); [Murray-Wallace and Woodroffe, 2014](#); [Scott, 1977](#); [Scott and Medioli, 1978](#); [Smith et al., 1984](#)). In turn, foram microfossils are of great importance to understanding the geochronology of archaeological sites situated in coastal regions.

This article presents the application of a GIS and Jupyter Notebook based age-depth model to visualize date ranges of coastal archaeological sites spatially and temporally using foram data. Where foram data is already available, this method can be directly applied to surface exposures of artifacts or archaeological features exposed on salt marsh erosional

faces — examining site formation processes at a landscapes scale. We use GIS to produce geochronological boundary surfaces from microfossil-derived SLIPs. Spatial analysis of geochronological boundaries, GNSS and GPR survey data, a lidar derived DEM, and a HyVSEP surface reveal proxy dates for the deposition of a surface scatter of archaeological materials, and drowned forest at Oak Point in western Minas Basin. The method integrates modern and archival archaeological, geospatial, and chronometric data within a GIS to visualize the spatial relationship of past RSL, site formation processes, and post-depositional processes generating the exposure of archaeological materials visible today.

3.1.1 Study Area

The Bay of Fundy is a semidiurnal hypertidal system on the Atlantic coast of North America bounded on the southwest by the Gulf of Maine, west by New Brunswick, and north and east by Nova Scotia. The bay is bifurcated at its approach to the Cobequid Highlands flowing northeast to Chignecto Bay, and east-northeast to Minas Basin and Cobequid Bay (Figure 3.1). With the largest recorded tidal range in the world (Minas Basin: 16.3m) (O'Reilly et al., 2005) archaeological materials deposited at elevations close to mean sea level are more likely to be intertidal than those deposited in meso- or micro-tidal regions. Early written record of intertidal archaeological deposits observed in Bay of Fundy can be traced at present to 1607 when Marc Lescarbot is credited with remarking the “rude circular stone walls, which may still be seen standing on the stony beaches in the Bay of Fundy, and looking as if they had stood there three hundred years” (Gilpin, 1873).

Lescarbot was referring to the remains of features placed by ancestors of the Indigenous people who greeted him, the Mi'kmaq. Though his determination of age for the features is conservative, Lescarbot's observation fits quite well with contemporary models

of past RSL in Bay of Fundy. Reconstructions of past RSL in Bay of Fundy (Shaw et al., 2010; Vacchi et al., 2018) suggest the vast majority of archaeological sites approaching the modern marine limit will date to no earlier than 6 C¹⁴ ka with an increasing probability of these sites post-dating 3.4 C¹⁴ ka corresponding to a period of intense tidal range expansion. This event was caused by the proposed breaching of a naturally formed tidal-barrier at the mouth of the Minas Basin recorded in Mi'kmaw legend and place names (Rand and Webster, 1894; Sable, 2011; Shaw et al., 2010). Coastal archaeological sites of the Early Holocene are generally expected to be below lowest low water (LLW) along former Bay of Fundy coastlines prior to 6 C¹⁴ ka (Fader, 2005). Pleistocene coastal archaeological sites exist above highest astronomical tides (HAT) at elevations of up to 20m Canadian Geodetic Vertical Datum 2013 (CGVD2013) down to present mean sea level (0m CGVD2013) due to rapid isostatic adjustments and the movement of the glacial forebulge after the retreat of the Laurentide Ice Sheet combined with increasing eustatic sea levels (Dalrymple and Zaitlin, 1994; Dalton et al., 2020; Deal, 2015; Shaw et al., 2002; Stea, 2011, 1988).

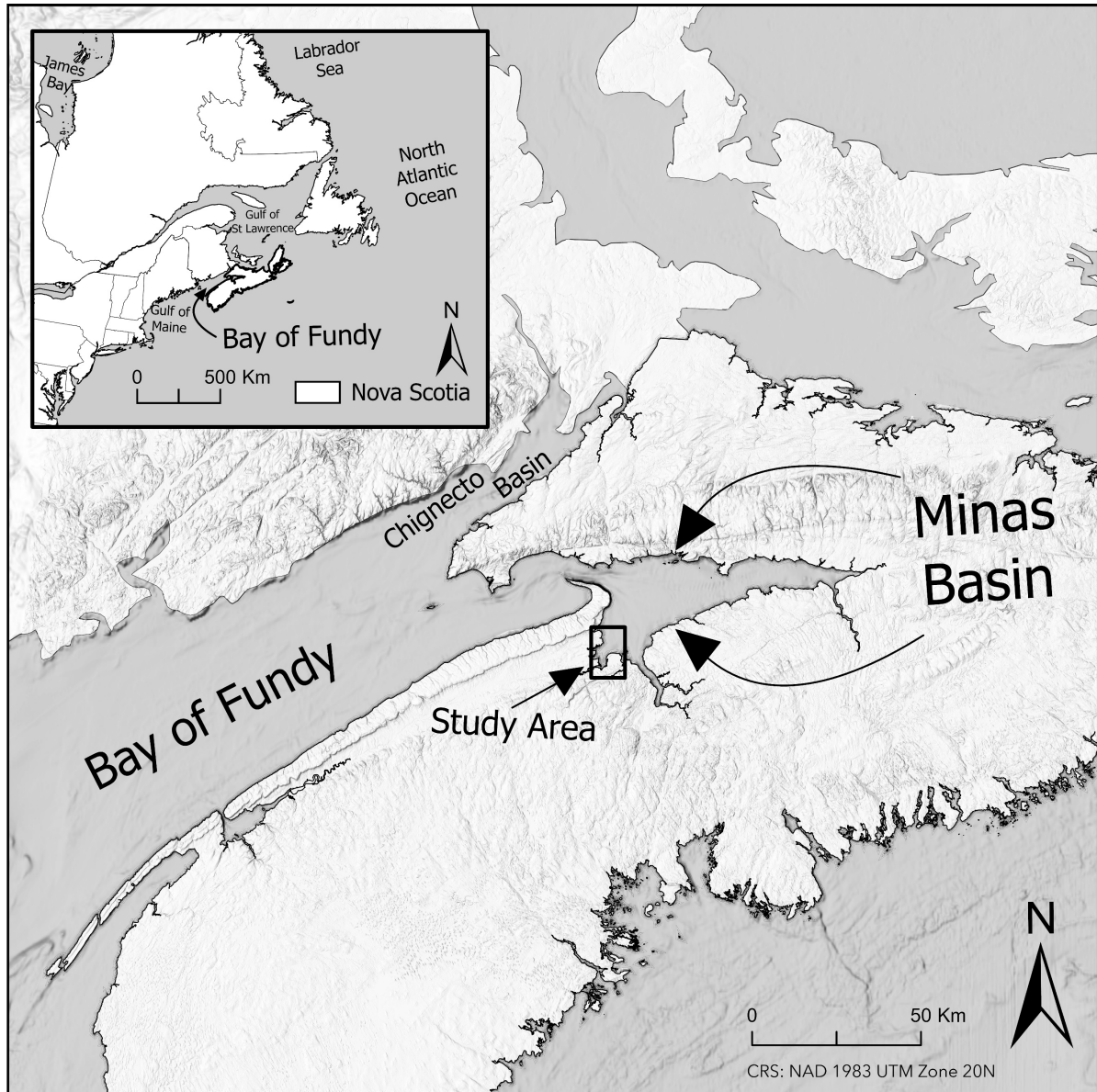


Figure 3.1: Location of southwest Minas Basin study area. Inset indicates location within northeastern North America.

Along the western coast of Minas Basin are a series of estuaries characterized by elevation and slope limited salt marsh deposits at their edges, many of which are now restricted to tidal flow. Originally dyked and drained for agriculture, former salt marshes within the Minas Basin are now home to a variety of land-uses beyond agriculture, including wastewater treatment, residential housing, and commercial enterprises.

Abandonment of former agricultural dykes has passively restored tidal flow to Kingsport marsh (Figure 3.2) providing a coastal buffer zone that protects a road at its posterior.

Oak Point is located at the confluence of the Habitant, Canard and Cornwallis River estuaries (Figure 3.2). The village of Kingsport borders Oak Point to the north and northeast. A tidal salt marsh occupying the northern outflow of the Habitant River flanks



Figure 3.2: Estuaries and places referenced in text in southwestern Minas Basin in relation to Oak Point.

Oak Point from the north through west, while tidal waters of the Minas Basin front Oak point from the southwest to the east.

The study area at Oak Point is characterized here as a salt marsh-estuarine environment fronted by a sandy beach deposit overlying erosional steppes along former marsh surfaces. Brush and post footings belonging to a former dyke alignment at the mouth of the Habitant River bisect the site (Figure 3.3a). Peat giving way in the foreshore fronting the former dyke exposes an ancient forest sealed by rising RSL (Figure 3.3b). Behind the former dyke remnants is an ebb-tidal delta and disjoint hook of a sand spit extending from Kingsport, curving around the head of a small tidal meander channel that stems from a larger tidal creek in the complex, hypertidal system (Dalrymple and Choi, 2007, p. 144; Hughes, 2012; Robin et al., 2020; Figure 3.3c; Figure 3.3e). The head of the meander channel is at the approximate centre of the lee side of the disjoint spit hook and faces the Minas Basin. The position of the disjoint hook at the head of this channel causes tides to simultaneously rise along both sides but drain dominantly with an ebb-dominated flow because it formed on a platform where the downdrift orientation of the shoreline changes abruptly (Davidson-Arnott et al., 2019, p. 347).

Mi'kmaw ties to Oak Point are noted by Mi'kmaq written and oral history (Piers, 2003), archaeological sites (Deal, 1991; Simonsen, 1978), local history (Eaton, 1910), and historical records (Pote et al., 1896). Late 19th century and early 20th century Mi'kmaq use of the area included porpoise hunting from an island (Paddy's Island) north of Oak Point (Piers, 2003; Figure 3.2), while historical records of that period suggests activities more reminiscent of those undertaken during *mawiomi* (Eaton, 1910; Young, 2016). Local history holds that "the Micmacs [sic] in old days held councils of war, yearly feasts, and

religious dances, and celebrated solemn marriage rites” at Oak Point (Eaton, 1910, p. 154). Observing that “councils of war” is an American Civil War period idiom meaning “a meeting held to decide what action to take in a serious or difficult situation” (“Council of War,” n.d.), the definition of *mawiomí* matches the description in the local history precisely as “ ‘a formal gathering.’ Examples include a traditional powwow, a religious (Christian) festival, feast or political gathering. Every *mawiomí* brings the L’nu [Mi’kmaq people] together in ceremony to discuss issues — local, regional, national, global — of common concern. The traditional St. Anne’s Day celebration at Potlotek, for example, is when the Santé Mawiomí meets to debate policy and agree on priorities” (Young, 2016, p. 96). Regardless of what activities manifested at the area, the Mi’kmaw Place Names Digital Atlas entry for the area is *Pka’wi’knk*, meaning “at the house covered in spruce rinds” or “at the spruce bark place” (2020).

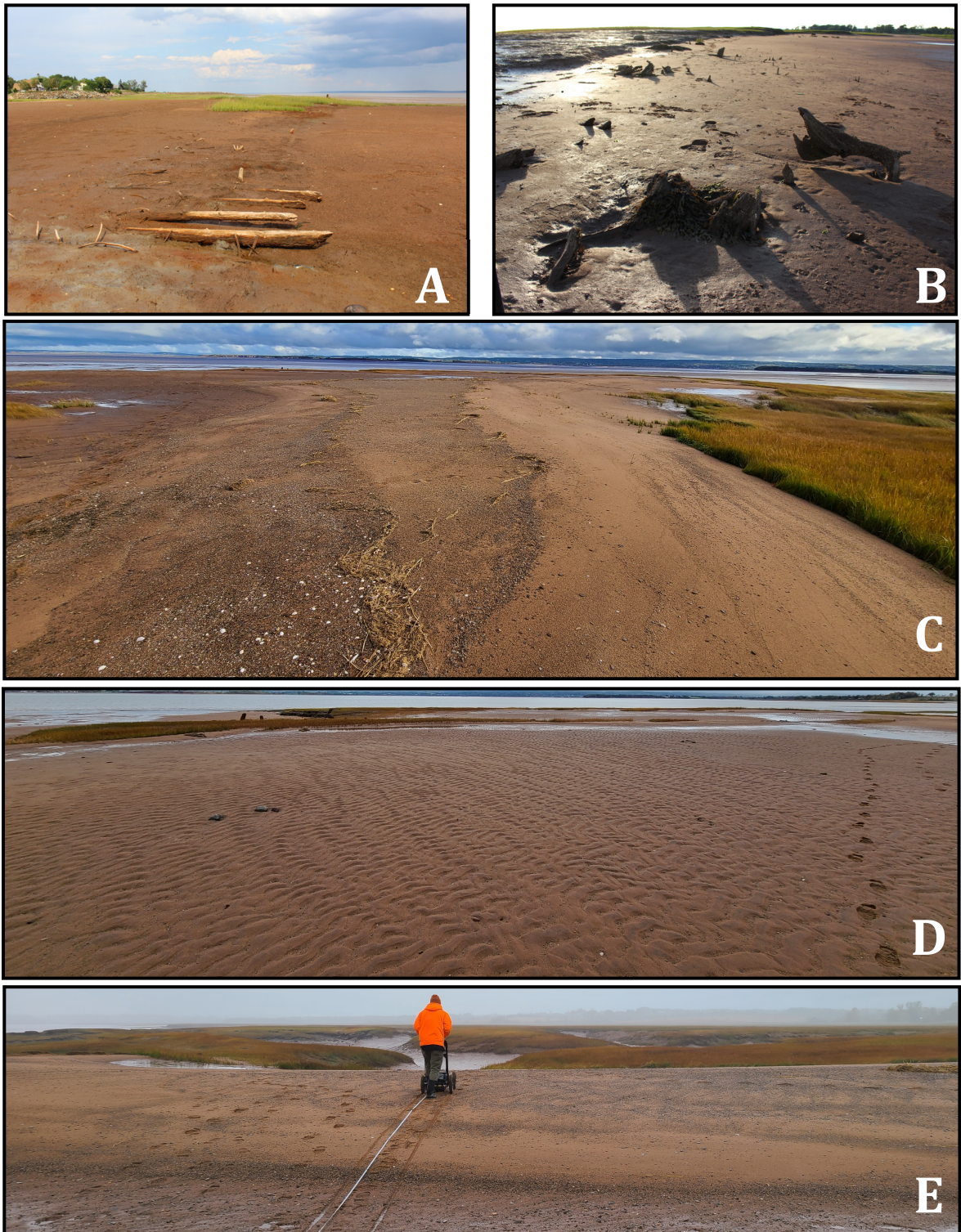


Figure 3.3: (A) Brush footing of past dyke alignment. (B) Drowned forest exposed through mud overburden at face of salt marsh peat. (C) Sand spit deposit showing strandlines present on both faces. (D) Sand ripples indicating dominant flow direction on scoured surface. Brush footing visible as linear feature of marsh grass crossing centre of photo. Sand spit hook termination visible at right of frame as elevated (lighter, dry) deposit. Drowned forest is located to the left of centre following the erosional face of salt marsh peat toward mudflats. See Figure 3.4 for location and direction of photographs. (E) GPR transect bisecting the sand spit from the limit of recent high tide toward the head of a meander channel from a larger tidal creek.

3.1.2 Past Research

A past research program cored salt marshes flanking the archaeological site to use foraminifera as indicators of past RSL (Scott and Greenberg, 1983; Smith et al., 1984; Figure 3.4). Samples were collected for microfossil identification and radiocarbon dating from sediments at the interface of the lowest layer of peat and a compacted substrate. Smith et al. (1984) provided a case-study in the Bay of Fundy on the use of marsh foraminifera as a high accuracy indicator of both sea level and tidal range.

Composition of marsh foraminifera assemblages deposited on tidal marshes were split into two groups to differentiate between high marsh and low marsh, zone 1 and zone 2, respectively (Scott and Medioli, 1980). The upper limit of zone 1 provides an accurate estimate of higher high water (HHW) elevation in mesotidal marshes of the Atlantic coast (5cm), but due to larger tidal ranges in upper Bay of Fundy the accuracy is decreased to 20cm at Kingsport (Scott and Medioli, 1980; Smith et al., 1984). Marsh grass species and forams cluster in regions of marsh primarily as a function of depth of saltwater at elevations approaching HAT, but foram assemblages respond to changes in RSL with every oscillation of the tides.

Foram assemblages in zone 1 at Kingsport were subdivided allowing 20cm accuracy to be obtained in two cases (Smith et al., 1984). Discrete surficial assemblages of forams in zone 1a characterized the upper portion of high marsh, while zone 1b characterized the lower high marsh. Vertical range of zone 1a was 20cm, while zone 1b was 55cm using the surface assemblages. Foram assemblages in the basal peat at cores 1 and 3 were zone 1a, and core 2 assemblages were zone 1b (Smith et al., 1984).

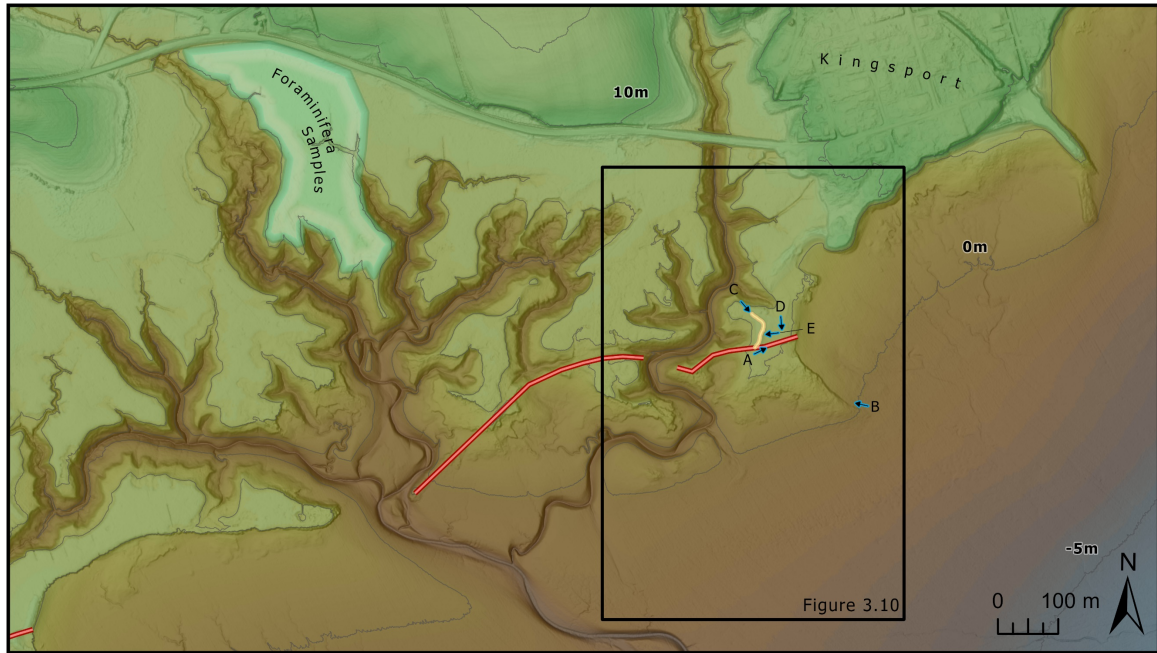


Figure 3.4: Overview of landscape directly adjacent to Oak Point site. Contours shown at 5 metre intervals in grey with -5m, 0m, and 10m labelled. Location and direction of photos in Fig. 3.3 are shown by labelled blue arrows. Digitized disjoint sand spit hook crest shown as a yellow line. Remnants of the past dyke alignment shown as red line. Approximate area of foram samples shown in labelled green boundary.

In foram studies the upper limit of microfossil deposits is used as a SLIP for HHW. As marine dwellers, foraminifera populations rapidly drop above the limit of tidal waters (Scott and Medioli, 1980). The HHW limit produced by the foram SLIP is equated HAT or marine limit (Gehrels, 1994, p. 995).

In 1988, Dr. Michael Deal began the *Western Minas Basin Project* designed to build the foundation for “the reconstruction of prehistoric and historic coastal resource exploitation and settlement patterning in the Minas Basin” (Deal, 1991). Deal built off of earlier archaeology in the region to frame and justify the baseline study of coastal archaeological resources in the Minas Basin (e.g.: Davis, 1980; Erskine, 1960; Simonsen, 1979, 1978). The survey resulted in the documentation of 35 archaeological sites in the western Minas Basin over the course of two years in 1988-89 (Deal, 1991).

The survey of Oak Point in 1988 recovered no evidence of archaeological resources on the site, but contextual documentation supported recording Oak Point as an archaeological site in the Maritime Archaeological Resource Inventory. Deal's report covered evidence noted by local histories (Deal, 1991; Eaton, 1910), Mi'kmaw language (Rand, 1902), and recent erosion of coastal shell middens from an eroding upland in Kingsport, adjacent to Oak Point (Simonsen, 1979). The negative evidence of archaeological remains suggested the site had either been destroyed by erosion or submerged in salt marsh peat and sands as RSL rose.

3.1.3 Current Research

The site remained uninvestigated for just over three decades until 2020 when the authors began a project to reassess coastal archaeological sites in the Minas Basin and Cobequid Bay for physical integrity and future vulnerability to erosion. An additional goal of this project is to collect high precision spatial data of the sites to gain accurate elevation values for coastal archaeological sites vulnerable to the impacts of RSL rise in Minas Basin and Cobequid Bay.

3.2 Materials & Methods

Geochronological boundaries visualized across Oak Point were created from corrected SLIP elevation and uncertainties calculated in a Jupyter Notebook. The Jupyter Notebook is available as Supplementary Data hosted through MyBinder to provide detailed, interactive reproduction of the methodology (Appendix B). Geochronological boundaries were created in ArcGIS Pro 2.8.0 to visually represent corrected SLIP elevations across horizontal space (ESRI Inc., 2020). Four pre-requisite datasets were collected and prepared in advance of deployment: 1) foram samples with associated radiocarbon dates, depth of

sample below HHW, and contemporary foram distribution for zonation. Additional data regarding dated material, matrix, and horizontal coordinates are preferable, but not mandatory; 2) HHW elevation data (e.g.: surveyed elevations or hydrographic vertical separation surface (HyVSEP)) for the study area (Robin et al., 2016); 3) Surveyed locations of archaeological materials or SLIPs representing a former marine limit; 4) lidar derived digital elevation model (DEM). These data must utilize a common vertical datum, in our case the vertical datum CGVD2013 was natively used in the HyVSEP and DEM elevation data acquired.

Table 3.1: Radiocarbon dates and corresponding depth data from Foram samples at Kingsport as reported in Scott & Greenberg, 1983 & Smith et al., 1984.

<i>Core</i>	<i>C¹⁴ BP</i>	<i>Sample ID</i>	<i>Material</i>	<i>Depth Below HHW (m)</i>
<i>Kingsport 1</i>	4430 ±235	GX-6810	Salt Marsh Peat	9.5
<i>Kingsport 2</i>	2905 ±220	GX-6811	Salt Marsh Peat	6.5
<i>Kingsport 3</i>	2355 ±180	GX-6812	Salt Marsh Peat	4.5

Supplementary Data holds information key to deployment of this workflow within an organized file directory. A formatted CSV titled AppendixA.csv and present in the /data folder of the Supplementary Data holds requisite data from Table 3.1. Appendix B is a Jupyter Notebook (Kluyver et al., 2016) documenting workflow computations with further details than described in text by annotating the Python 3 workflow with visual, interactive outputs. We combine HHW SLIP vertical uncertainty of data collected at Kingsport and defined by foram zonation (Smith et al., 1984) with the vertical uncertainty (±7.5cm) from the CANEAST derived HHW values (Robin et al., 2016).

This method is supplemented by a variety of small geoarchaeological analyses contextualizing recent landscape processes impacting Oak Point. An end point rate (EPR) of recent shoreline movements at Oak Point was provided by calculating the rate of positional change between digitized shorelines from historic aerial images (Himmelstoss et al., 2018). Geotagged photography and GNSS survey points of artifact distribution and geomorphology were examined visually, providing a qualitative illustration of recent post-depositional processes at Oak Point. Density of the surface scatter was analyzed in relation to the side of the sand spit hook to determine if and how artifacts are moving from tidal forces. Finally, a series of ground penetrating radar (GPR) transects were collected using a Sensors & Software Noggin 500 with a centre frequency of 500 MHz to illuminate the depth of the intertidal deposits and stratigraphic information at Oak Point.

3.2.1 Preparation of Foraminifera Data

Foram data had previously been collected adjacent to Oak Point, allowing us to move directly to preparation (Smith et al., 1984; Figure 3.4). For more information on the foram data collection process see: Gehrels, 1994; Scott, 1977; Scott and Medioli, 1980, 1978; Smith et al., 1984. Data points from the study at Kingsport marsh (Table 3.1) are reported in Shaw et al., 2010 and available in the supplementary dataset provided with Vacchi et al., 2018.

Radiocarbon dates were reported normalized to $\delta^{13}\text{C} = 25\text{‰}$. Dates were calibrated with IOSACal 1.4.0 using Python3 (Costa and Gutiérrez-Roig, 2018; Van Rossum, 2021). The newly released MARINE20 calibration curve was used to correct the date from normalized radiocarbon years before present (C^{14}BP) to calibrated years before present (calBP) (Heaton et al., 2020). Impacts from the marine reservoir effect were corrected using

a ΔR of -64 ± 90 from the Marine Reservoir Database (Reimer and Reimer, 2001). Suggested best-practice is to subtract the ΔR value from carbon dates before calibration (Alves et al., 2018, p. 296). The INTCAL20 radiocarbon calibration curve was used with terrestrial samples as needed (Reimer et al., 2020). Calibration curve files were imported into the IOSACal 1.4.0 distribution from OxCal (Ramsey, 2008, 2001, 1995).

An elevation for HHW at Oak Point was gathered, in our case, from the points used to develop the CANEAST HyVSEP surface. The elevation obtained from the HyVSEP point closest to Oak Point is 6.826m. Foram sample depths were provided as depth below HHW (in 1980). To discern 1980 HHW elevation at each foram sample, depth values were subtracted from the elevation of the closest HyVSEP point for each sample. These values represent the depth of the material below modern HHW at each sample location. Three linear equations illustrate the relationships of elevation of the samples over time (Table 3.2-2). The relationship between elevation of the youngest date (2.295m CGVD2013) and modern HHW (6.795m CGVD2013) was used to solve for the calendar year 1980 with $x = -30$, where 0 equals the year 1950. The result is a predicted HHW value of 6.703m for Kingsport in 1980, a RSL rise of 9.2cm. This value is used to correct for RSL rise since

Table 3.2: Linear relationships calculated describing change in elevation of samples over time.

<i>Sample</i>			
<i>Gx-6810</i>	<i>Gx-6811</i>	<i>Gx-6812</i>	<i>Modern</i>
<i>Linear Relationship</i>			
$y = -0.00167x + 4.6951$	$y = -0.00273x + 7.3886$	$y = -0.0023x + 6.6340$	

1980 at the Oak Point sand spit generating the data shown in Table 3. In addition, a positive offset of 0.2m was applied to the SLIP elevation derived from foram zone 1b (Gx-6811). The offset moves the upper limit of the zone 1b derived boundary to the upper limit of zone 1a.

3.2.2 Production of Geochronological Boundaries

Once the HHW data were corrected, a minimum and maximum elevation of high marsh for each date range is given using the vertical uncertainty of the foram indicators (Smith et al., 1984). The minimum and maximum elevations were used as limits in the Set Null geoprocessing tool in ArcGIS Pro. The tool was used to set values above the maximum and below the minimum elevations to Null values. This process was repeated for each of the data points. Output raster surfaces represent a salt marsh associated *terminus ante quem* for the deposition of archaeological materials deposited in terrestrial environments.

3.2.3 Archaeological Survey

An archaeological survey was undertaken at Oak Point twice in 2020. The first survey occurred on July 21st, and the second on October 14th when vegetation began to die-off. Both surveys followed a systematic approach using transect spacing of approximately 3m with a team of two. The extent of the summer survey was the beach deposit, and drowned forest. Our autumn survey extent did not include the lower section of drowned forest, focusing on the beach deposit.

All datapoints were surveyed with a Leica GS14 nRTK GNSS receiver from Saint Mary's University. Temporary numbers were ascribed for each artifact collected to

correlate the surveyed point with the physical object. Each artifact surveyed and collected was individually photographed in the field. Mean vertical positional error (1D) of the artifacts is 1.2 ± 0.9 cm, while the maximum is 2.6cm on one occasion. Horizontal error (2D) is smaller with a mean positional error of 0.7 ± 0.5 cm, and max of 1.5cm in one case.

The summer field survey included collection of high-precision point data of each visible stump in the drowned forest at Oak Point. 1D and 2D errors of the stumps are $1.2\text{cm} \pm 0.2$ and $0.8\text{cm} \pm 0.2$. Elevations have a range of 1.615m. The highest visible stump recorded is at 4.330m, and lowest is at 0.377m. A mean value of 1.751m and a median value of 1.156m for the 10 stumps surveyed. Locations of surveyed stumps are shown in [Figure 3.5](#).

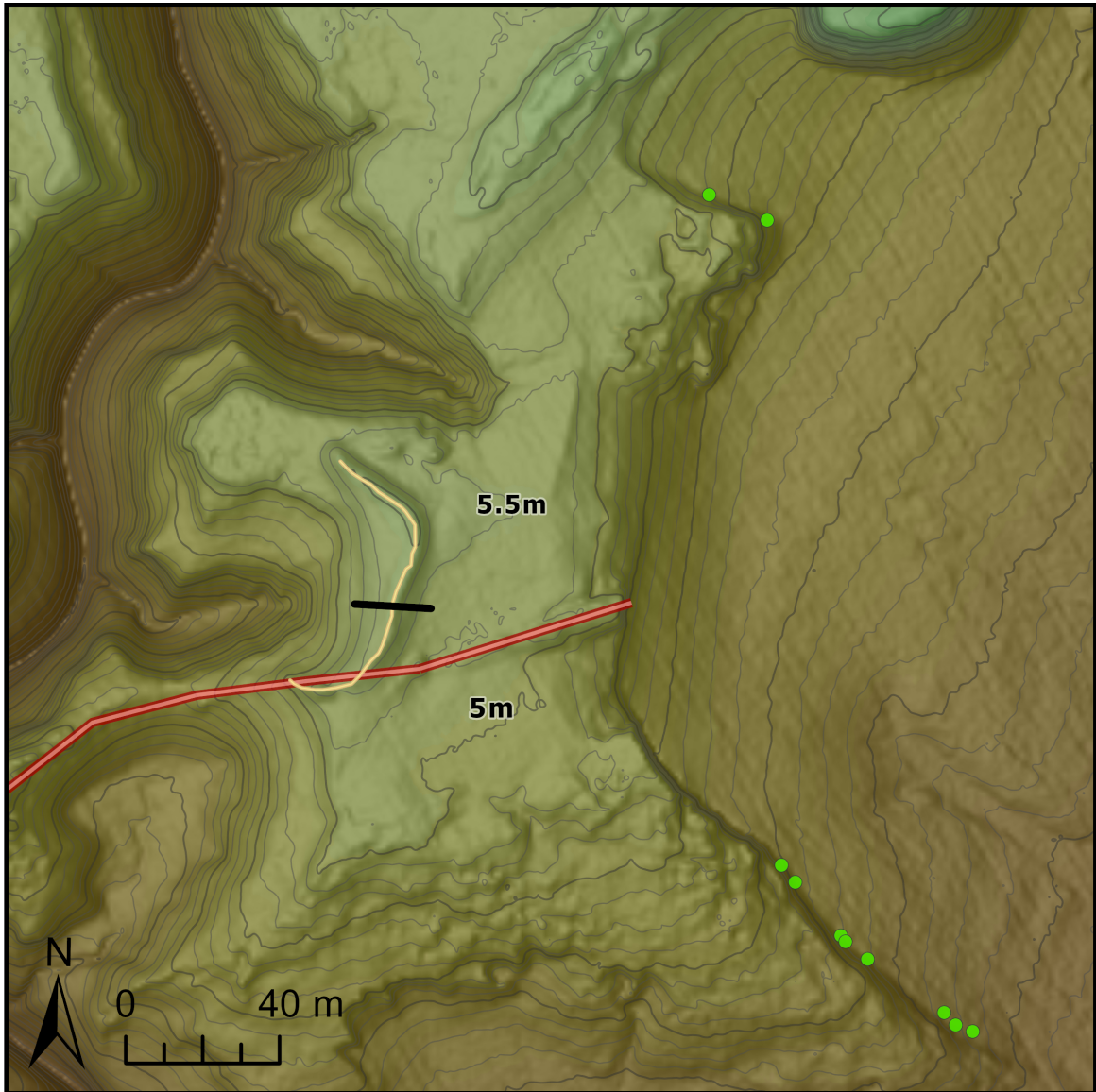


Figure 3.5: Location of the surveyed drowned forest at Oak Point shown as green points. Sand spit hook shown as yellow line. Dyke footing shown as red line. Location of GPR transect shown as black line.

3.2.4 Geoarchaeological Analysis

Four analyses were employed to understand the relationship of the intertidal artifact deposit at Oak Point to short and long term geomorphological processes at work in the landscape. Our analyses of Oak Point included (1) calculating the rate of inland migration of the sand

deposit, (2) measuring the spatial relationship between the sand spit hook and the surface artifact distribution, (3) a visual interpretation characterizing the morphodynamics by overlaying various spatial datasets, and (4) collecting data along selective transects with ground penetrating radar (GPR).

An EPR is used to describe the inland migration of the sand deposit. A series of EPRs were calculated from historic aerial images to see changes in the movement of sands over time. Lidar data collected in 2019 by the Province of Nova Scotia was used to digitize the crest of the sand spit hook at Oak Point. This feature was analyzed in relation to the spatial distribution of surveyed artifacts collected in 2020. Visual interpretation employed all amassed spatial datasets and background information from this project to highlight processes driving the present and past transformations of the landscape. Finally, our GPR survey non-invasively produced information contextualizing the near-surface sedimentological processes through selectively placed transects. Interpretation of the profiles follows a radar stratigraphy and radar facies approach to understanding the (re)working of sediments and archaeological materials at Oak Point (Conyers, 2016; Heteren et al., 2002; Shan et al., 2016).

Calculation of Sand Migration Rate

A series of historic aerial images dating to 1944 were acquired from the Province of Nova Scotia. Imagery from 2012 is the product of orthorectification of a series of aerial photos to the resolution of 0.25m/pixel with a reported root mean square error (RMSE) of 2.5 and a shoreline position error of 3.35m. Imagery used in this study captured prior to 2012 are scanned photographs rectified to the 2012 orthophoto.

Scanned photographs were georectified using a series of ground control points (GCPs) and a 1st Order Polynomial transformation. Placement of GCPs was carefully chosen to allow for static anthropogenic features on the marsh surface to line up as closely as possible between the series. Most GCPs landed on the marsh surface preserve accuracy at similar elevations to the beach deposit. The forward RMSE of all georeferenced imagery is below 1m, reported in [Table 3.3](#).

Additionally, georectified photos were visually inspected for quality control to ensure static features in the imagery lined up. The apparent inland extent of the sand deposit in the imagery series was digitized into a line feature class ([Figure 3.6](#)). The resulting data was analyzed using a procedure mimicking that of the Digital Shoreline Analysis System distributed by the United States Geological Survey ([Himmelstoss et al., 2018](#)).

Table 3.3: Relevant data resulting from air photo georectification.

Year	Photo ID	Resolution (m)	RMSE (m)
1944	A8719-33	0.58	0.96
1987	87304-038	0.50	0.54
2002	02308-079	0.50	0.59

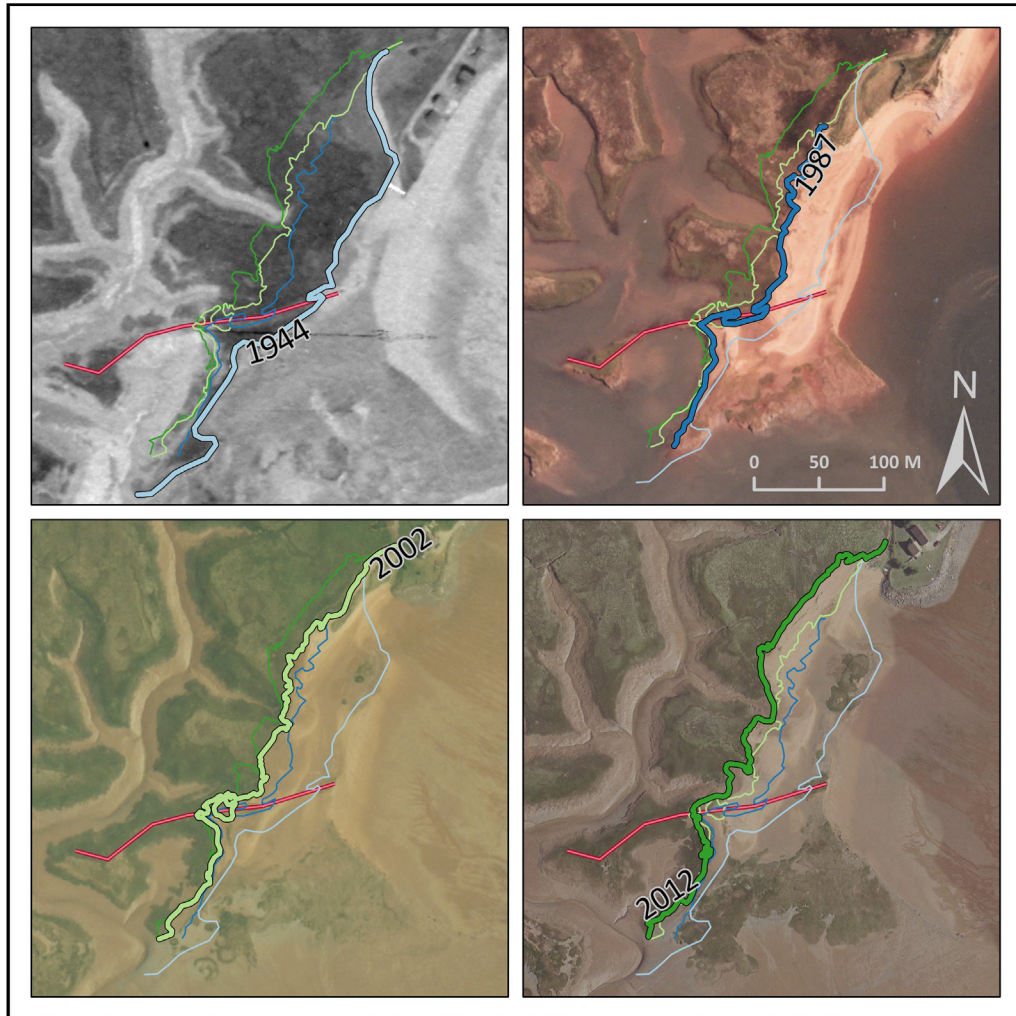


Figure 3.6: Movement of beach deposit at Oak Point since 1944. Base image matches year labelled and boldened line feature.

A trendline was created from the digitized shorelines using the Linear Directional Mean geoprocessing tool. A linear trendline varies from the curved baselines in DSAS but effectively smooths the baseline to the maximum shoreline length (Himmelstoss et al., 2018, p. 31). A series of vertices were created along the trendline spaced at a determined sampling distance using the Densify Line tool. Concerned with small scale changes, the distance used in here is 1m.

A baseline was created 200m seawards by modifying a copy of the trendline using the Offset tool accessed through the Modify Features button under the Edit tab. The process

was repeated with the direction setting in the opposite direction creating a backshore baseline landward by 200m (Figure 3.7). The backshore baseline ensures the transects extend through all features and contributes to serving the same function as the “Baseline Search Distance” attribute in a DSAS 5.0 baseline (Himmelstoss et al., 2018, p. 20).

The Feature Vertices to Point geoprocessing tool was then used to create point features at the vertices of the baseline features. Transects were created using both baselines in the Points to Line tool and the OBJECT_ID field as the Line Field. Choosing the Line Field ensures that transects were cast between corresponding points along each baseline.

The Intersect geoprocessing tool was selected to create point features at intersections of the transects and digitized extents of the sand deposit. Resulting features were dissolved from multi-part to single part points used as input features in the Point to Line geoprocessing tool. Only transects crossing two or more digitized extents can be converted to lines. The Spatial Join geoprocessing tool was used on the dissolved features with the original Intersect feature class to add ID fields.

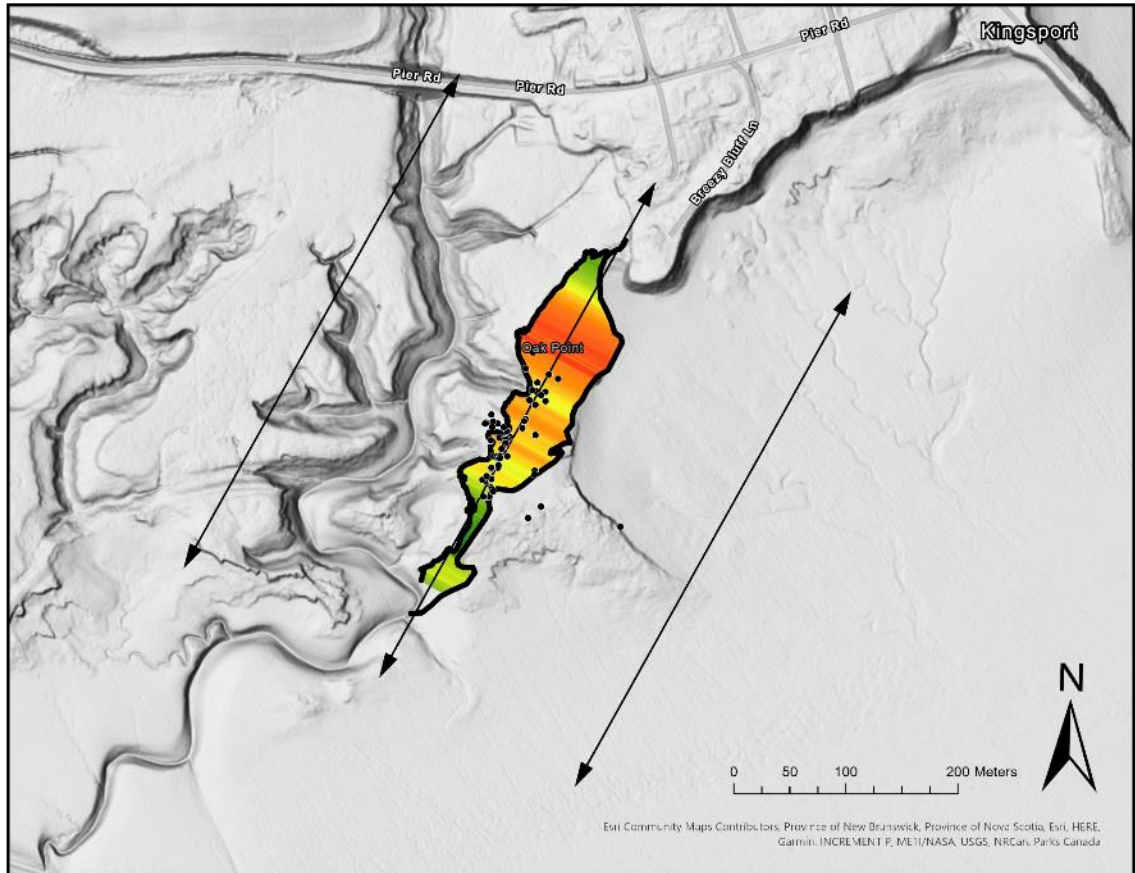


Figure 3.7: Trendline and baselines overlaying EPR of the sand deposit at Oak Point.

Our process resulted in a series of transects extending between the oldest and youngest digitized inland extent of the sand deposit. Transects were analyzed to determine net shoreline movement (in this case, sand deposit movement) and an end point rate (EPR) of change from 1944 to 2012 (Equation 3.2.1). The EPR along subsets of transects were examined to explore the movement of sands in relation to other features on the landscape and the surface scatter mapped and collected during field surveys.

Equation 1: End Point Rate equation modified to represent beach migration.

$$EPR = \frac{\text{Net Sand Deposit Movement}}{\Delta \text{Time}_{\text{youngest photo} \leftrightarrow \text{oldest photo}}}$$

Measuring Spatial Relationships

Digitization of the spit hook crest began by clipping the lidar derived DEM (1 meter resolution) to a polygon envelope of the platform where the sand spit hook rests. A slope surface was derived from the clipped DEM using “Degrees” as the cell value. The slope surface was classified using symbology making cells with high slope values transparent and those with low values (flat platform, lee side of spit hook & crest) opaque. The crest of the sand spit hook was then displayed as opaque cells following trending along the spit hook. Crest digitization uses the midpoint of each group of cells where a group is defined by one or more cells that are directly adjacent to each other (Figure 3.8).

Three fields were added to the artifact layer. One field differentiates artifacts located on the stoss and lee sides of the sand spit hook, while the remaining two hold values for distance to nearest artifact and distance to the spit hook crest. These values hold data necessary to compare the distribution of artifacts in relation to the hook, and along either side.

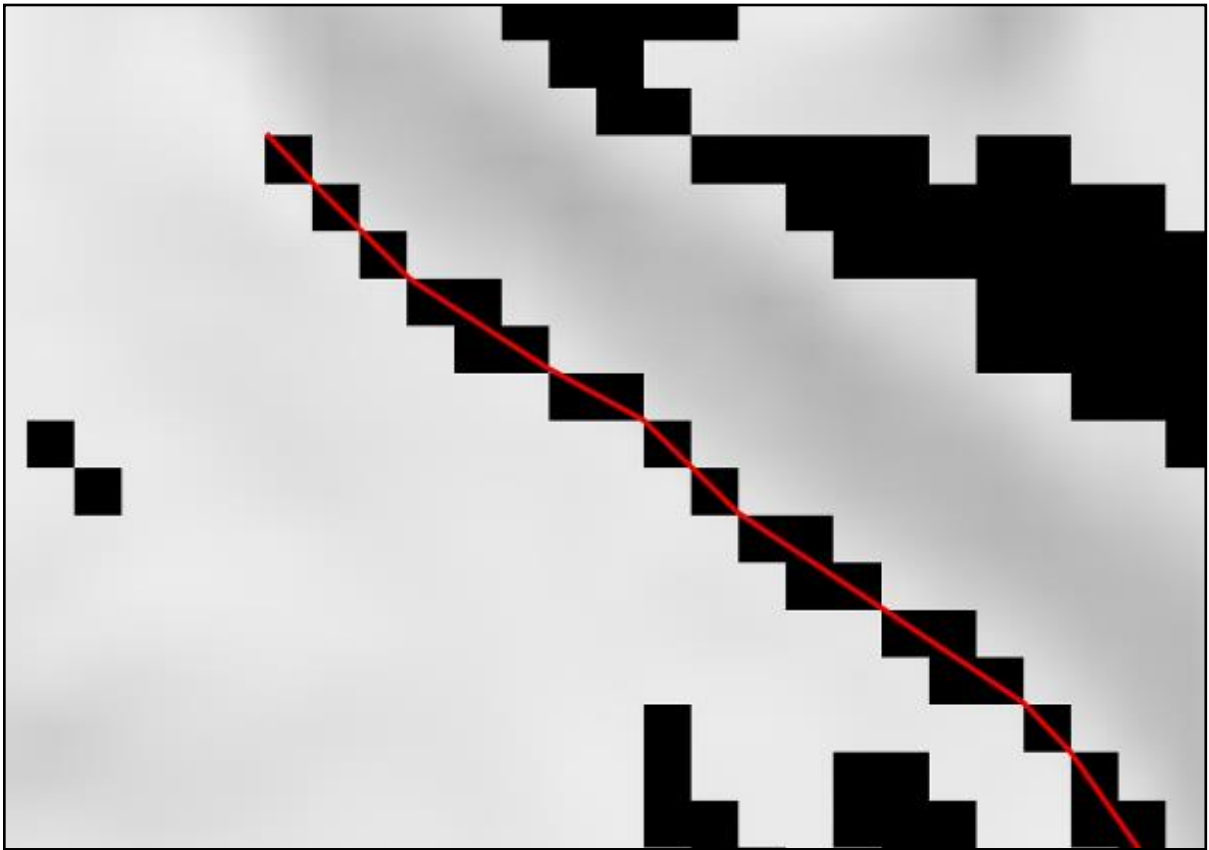


Figure 3.8: Example of spit hook crest digitization (red line). Square cells measure 1m².

Distance to the spit hook crest and nearest artifact are each calculated using the Near geoprocessing tool. Determining lee and stoss side of surface artifacts uses the Select by Polygon tool with a trace function allowing the polygon to trace the spit hook crest exactly. At the end of the spit hook crest, the polygon extends in a straight line beyond the artifact scatter continuing outside of the artifact scatter back to the place of beginning. Selected records are input into the field calculator, lee side artifacts are calculated using a value of 1. The selection is inverted, and stoss side was calculated to a value of 2, allowing grouping of the points by side. Artifact features symbolized by lee and stoss values for visual observation of the relationship between the artifacts and sand spit (Figure 3.9).

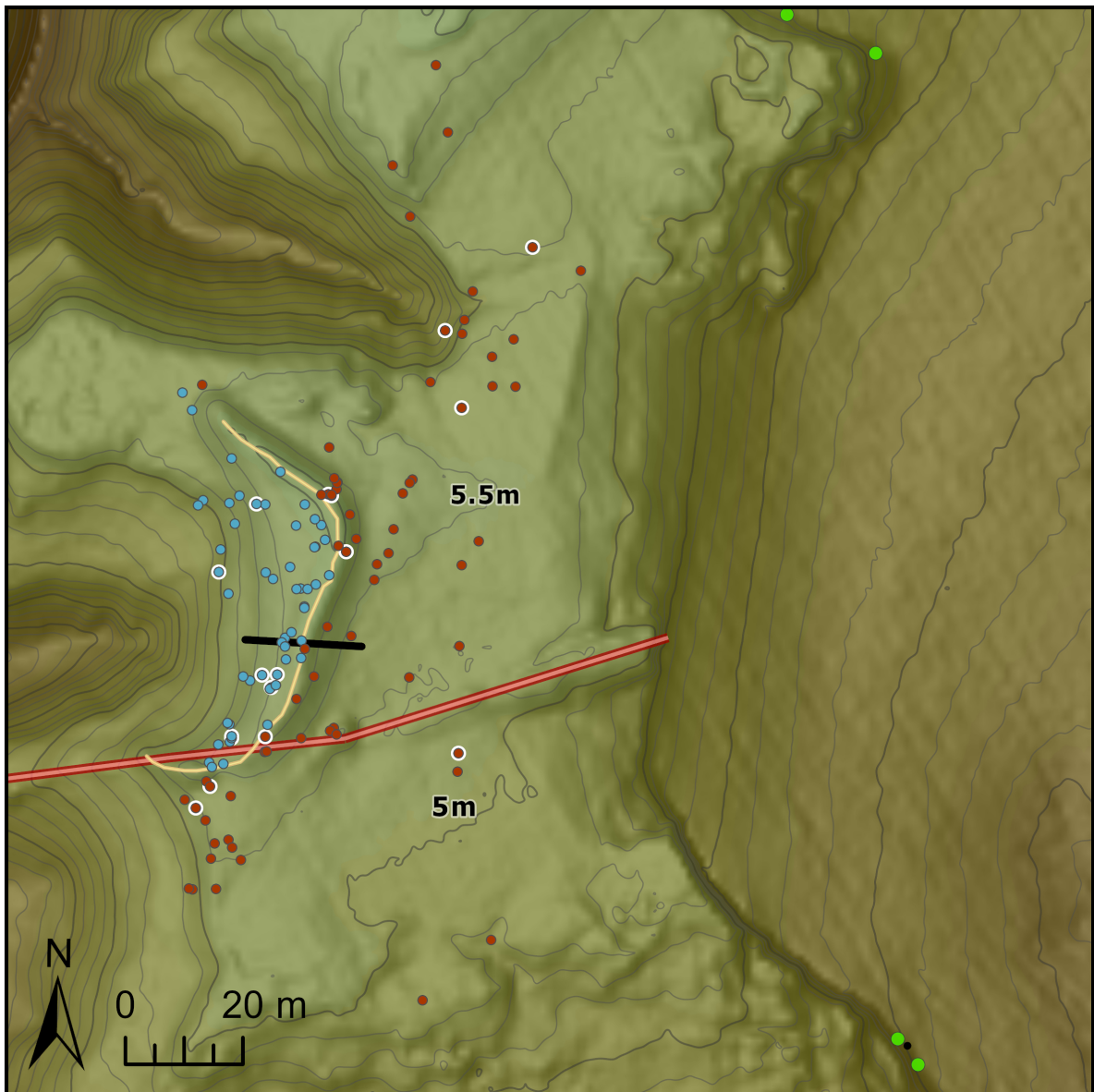


Figure 3.9: Distribution of artifacts in relation to lee (red point) and stoss (blue point) side of sand spit hook. White halo indicates non-debitage artifact. Dyke footing shown as red line. GPR transect shown as black line.

Characterizing Spatial Relationships

Observations were made in the field, and GIS of spatial relationships among geomorphic features on the present marsh-estuarine and beach landscapes in relation to the archaeological site and drowned forest landscape at Oak Point. General current direction was inferred through observation of lidar derived elevation and slope surfaces, geomorphic

features in geotagged photography, and aerial imagery. Artifact distribution was visually compared to the direction of currents, limits of vegetation, and topography to reveal glimpses of the ecomorphodynamic to archaeological deposit entanglement at Oak Point.

Ground Penetrating Radar Survey

Subsurface profiles were collected using ground penetrating radar in October 2020 to determine the sedimentological nature of the sand spit hook and estimate depth of the beach deposit at Oak Point. Data was collected on a total of four selectively placed transects across the beach deposit.

Data collection occurred along the sand spit hook transect directly after high tide and approaching low tide four hours later to obtain data under wet and dry beach conditions to isolate reflection surfaces of different resolutions. Our radar was equipped with a Leica GS14 GNSS receiver using nRTK corrections to obtain horizontal accuracies (<5cm). Our horizontal accuracies are smaller than the minimum calculated radar footprint dimension, 8cm, at the maximum estimated RDP of 6 (Neal, 2004, figure 10).

GPR data were processed in Sensors & Software EKKO_Project 5 (Sensors & Software Inc., 2018). Each line underwent the following baseline processing steps: time-zero correction, dewow, and background subtraction. Time-zero correction was applied using an absolute correction of 5mV, dewow was applied with a window length of 1.333m (default value), and an average background subtraction was applied for each individual line.

A bandpass filter was applied to the transects across the sand spit hook. Transects on the sand spit hook required separate velocity settings, as the velocity, resolution, and depth of penetration varies due to relative dielectric permittivity (RDP) differing with water content (Conyers, 2018, 2016; Neal, 2004; Neal and Roberts, 2000). Velocity of the radar wave during the first sand spit hook transect was estimated to be 0.9 nm/s. Our estimate assumed that most of the sand spit hook had not been submerged under the preceding tide propagating the radar wave at a velocity at the lower end of the range expected for unsaturated sands (Neal, 2004; Shan et al., 2016). Radar signals were expected to propagate slightly faster during the second survey, four hours later. We calibrated the velocity of the second transect by adding 0.15 nm/s to the velocity of the first line until depth of reflections at 40-50cm below surface landed at equivalent elevations. Velocity was estimated for the second transect at 1.05 nm/s, as waters slowly percolated out of the sand spit hook after tides lowered.

Interpretation of GPR reflections are based on the principles of radar stratigraphy (Neal, 2004). Radar surfaces are discrete high amplitude responses in a reflection profile. Radar facies are reflection configurations of radar surfaces segmented by continuity, shape, and dip of reflections and the relationships they share (Neal, 2004; Neal and Roberts, 2000; Shan et al., 2016). Radar surfaces and radar facies were interpreted from the GPR transect collected under drier conditions.

A vertically exaggerated reflection profile was exported as an image from EKKO_Project 5 and brought into ArcGIS Pro 2.7.0. The profile image was georeferenced to an arbitrary, planar coordinate system with x values equivalent to distance (metres) along the transect, and y values equivalent to elevation (metres CGVD2013). This allows the

reflection profile to be interpreted and measured at a 1:1 ratio with the vertical resolution of the exaggerated image.

The image was clipped to exclude high-frequency noise beyond the depth of penetration. Radar reflections were digitized to line features representing surfaces. Regions where radar surfaces exhibited similar reflection configuration patterns (Neal, 2004, fig. 23) were interpreted as discrete radar facies and digitized as polygon features. Radar stratigraphy was then considered in relation to known forcing functions acting on the sand spit hook to interpret response type.

3.3 Results

Surveys during the 2020 field season have (re)located the archaeological site at Oak Point. Radiocarbon dates from HHW SLIPs have been recalibrated with the new MARINE20 calibration curve (Table 3.4). Elevations from the HHW SLIPs at Kingsport have been converted to a modern geodetic datum (CGVD2013) providing a basis for relative dating of any in-situ archaeological materials at the site with the derived geochronological boundaries (Figure 3.10).

Table 3.4: Calibrated (MARINE20) radiocarbon dates and HHW elevations (CGVD2013) for Kingsport marsh.

<i>Sample ID</i>	<i>2σ range</i>			<i>1σ range</i>			<i>HHW</i>
	<i>Max</i>	<i>Min</i>	<i>Mean</i>	<i>Max</i>	<i>Min</i>	<i>Mean</i>	
<i>Gx-6810</i>	5270	3691	4480 \pm 790	4861	4065	4465 \pm 400	-2.766m \pm 0.20
<i>Gx-6811</i>	3333	1799	2565 \pm 765	2937	2162	2550 \pm 390	0.434m \pm 0.55
<i>Gx-6812</i>	2577	1281	1930 \pm 650	2218	1557	1890 \pm 330	2.234m \pm 0.20

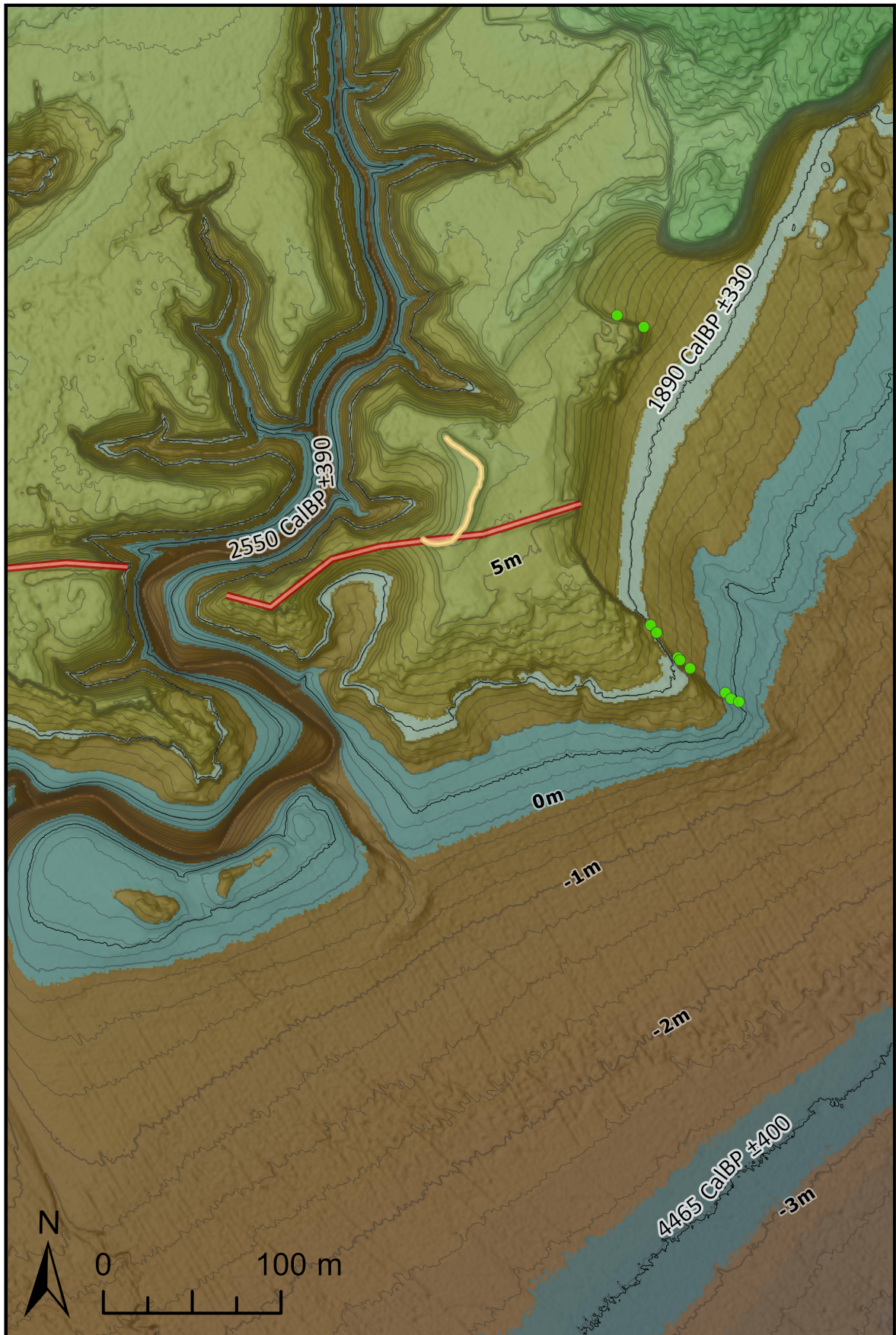


Figure 3.10: Geochronological boundaries in relation to features at Oak Point. Mean of each boundary shown by labelled contour.

Archaeological survey reveals the surficial scatter of lithics at Oak Point to extend for over 100m in the intertidal zone with the long axis running roughly shore-parallel. The scatter is most concentrated at the southwest adjacent to and near the crest of the sand spit hook (Figure 3.3c; Figure 3.3e). Lithics are less concentrated in scoured areas exhibiting sand ripple topography (e.g.: Figure 3.3d). A total of 125 objects were collected during the 2020 surveys.

EPR for the complete 68-year timespan of the series of aerial images shows the maximum inland migration of sands per year is 1.2m in the area north of the sand spit hook. The lowest EPR are observed along lateral extremities of the sand deposit. Excluding the southernmost section of the southern extremity, an observed maximum EPR of 0.20m grades into higher EPR values toward the centre of the sand deposit (Figure 3.11).

The spatial association of archaeological materials and the disjoint sand spit hook at Oak Point is apparent. Artifact distribution shows lee side clustering of artifacts that are also more closely associated with the crest of the spit hook than those stoss side (Figure 3.12). Most artifacts in close association with the spit hook are white quartz, while a larger diversity of materials is associated with the scatter northeast of the hook.

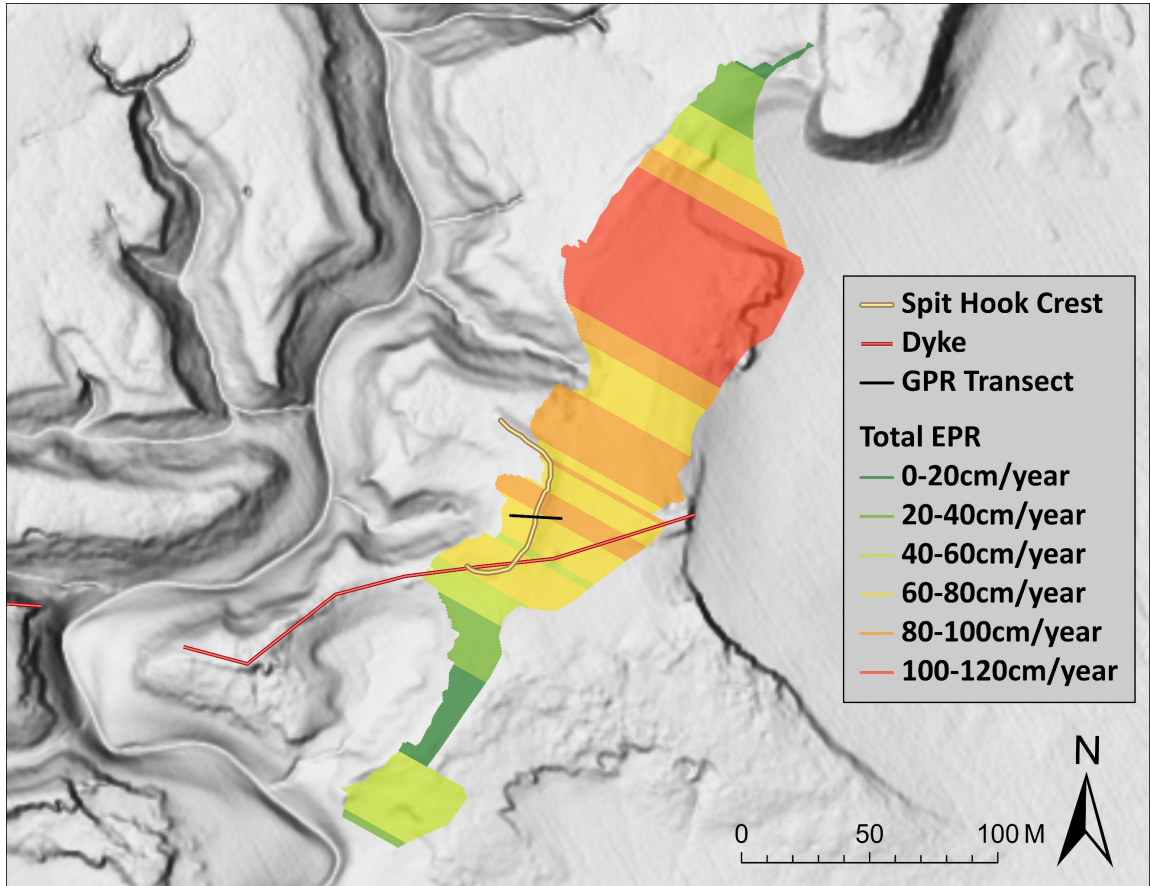


Figure 3.11: EPR calculations for the sand deposit at Oak Point.

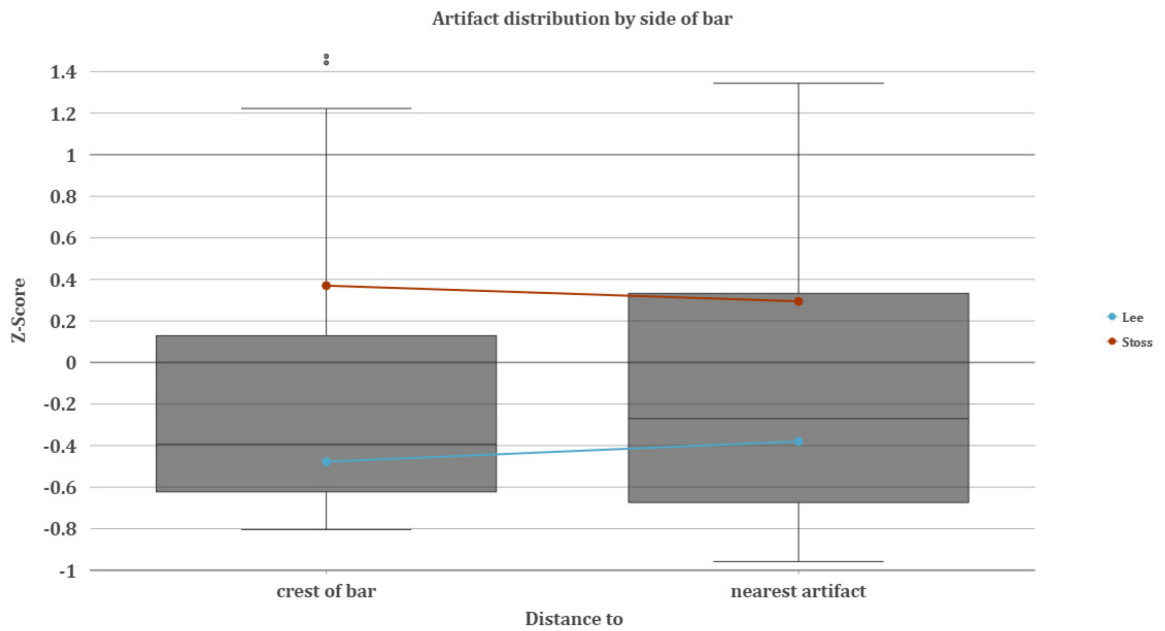


Figure 3.12: Artifact distribution by side of spit hook. Series one is distance to crest of spit hook, series 2 is distance to nearest artifact. Lee side in blue, stoss in red.

Interpretation of the GPR profile through facies reveals that the spit hook has been subject to frequent overtopping and frontal lapping erosion in recent times (Figure 3.13). Radar facies also indicate that seaward erosional forces were more significant in the past, prior to aggradation of a gentle beach slope to elevations allowing tidal waters and sediments to wash over the sand spit hook during HAT. This implies that if artifacts are coming from a deposit shoreward of the spit hook, deposition of the artifacts on the spit hook happened relatively recently. The horizontal location of radar facies in the following is references by metre.

Radar facies *f1-fus* is currently interpreted as a former upland surface extending from 0.7m to 17.7m along the bottom of the reflection profile. This facies expresses itself as a series of moderately continuous to discontinuous planar, horizontal, subparallel reflections dipping away from the topographical high at approximately 4.5m to 6.5m. Reflections transition to a series of discontinuous, oblique, chaotic convex forward dipping reflections from 4.5m towards the start of the profile. Reflection surfaces in *f1-fus* grade into chaotic noise at the lower limit. The upper boundary is characterized by erosional truncation in much of the profile, while between 11m and 16m attenuation rendered the upper boundary uncertain.

Radar facies *f2-sm* and *f3-sm* are interpreted as shallow salt marsh deposits that onlap *f1-fus*. The facies is a series of continuous planar to sinuous, horizontal, parallel to subparallel reflection surfaces. Below the upper boundary the facies is intruded by a series of discontinuous chaotic reflectors dipping from forward to backward from 7.5m to 12m, then forward again between 14m and 18m. This intrusion is interpreted as episodic deposition from spit hook migration and erosional contact with facies *f2-ecbr*.

Erosion of facies *f1-fus* is the interpreted source of material constituting radar facies *f2-ecbr*, *f3-ecbr*, and *f5-ecbr*. We tentatively interpret these facies as gently seaward sloping deposits bounded at the bottom by erosional contact surfaces. Discontinuity of reflections is interpreted as being the result of inclusions of coarser materials than in the overlying eroded beach ridge facies described below. The reflection surfaces are discontinuous, convex, and tangential, dipping away from surfaces at higher elevations and down lapping surfaces below.

Two radar facies are interpreted as scour and fill deposits, *f3-sf* and *f4-sf*, occur near the start of the profile. These facies fill troughs at the top of *f1-fus*. Facies *f3-sf* is a series of discontinuous, chaotic, dipping reflectors down lapping *f1-fus*, while *f4-sf* holds continuous, planar, horizontal, reflection surfaces onlapping *f1-fus*. We acknowledge the variation in reflectors in these radar facies but have grouped these based on the geometry they fill. Another interpretation of radar facies *f4-sf* is planar bedded beach deposit, as the facies fit this description as well.

Four interpreted eroded beach ridge facies occur on the seaward side of the spit hook, *f6-ecbr*, *f9-ecbr*, *f10-ecbr*, and *f12-ecbr*. These four facies are characterized by erosional upper surface boundaries, and down lapping onto surfaces below. The reflection configuration is a series of moderately continuous, sub-parallel and divergent, sinuous surfaces dipping away from the crest of the spit hook and former slip-faces.

Planar bedded beach deposits are the most abundant deposit on the stoss side of the sand spit hook. There are five polygons representing four chronological sequences of *f7-pbb* (x2), *f8-pbb*, *f11-pbb*, *f13-pbb*. These facies are highly related to facies interpreted as eroded beach ridge deposits, onlapping at lower and eroding at upper boundaries. The

series consists of continuous, subparallel, planar, horizontal reflection surfaces. At the surface, beach facies are scoured. We interpret the subparallel relationship as representative of scoured and sand rippled topography.

The last group of radar facies are overtop or overwash deposits: *f11-ot/ow*, *f13-ot/ow*, and *f14-ot/ow*. These facies express onlap and downlap at the lower boundaries, and toplap at upper boundaries. Reflection configuration consists of a series of continuous to moderately continuous, convex to sigmoidal, tangential reflection surfaces. Dip is strongly correlated with the slope of the underlying reflection surface.

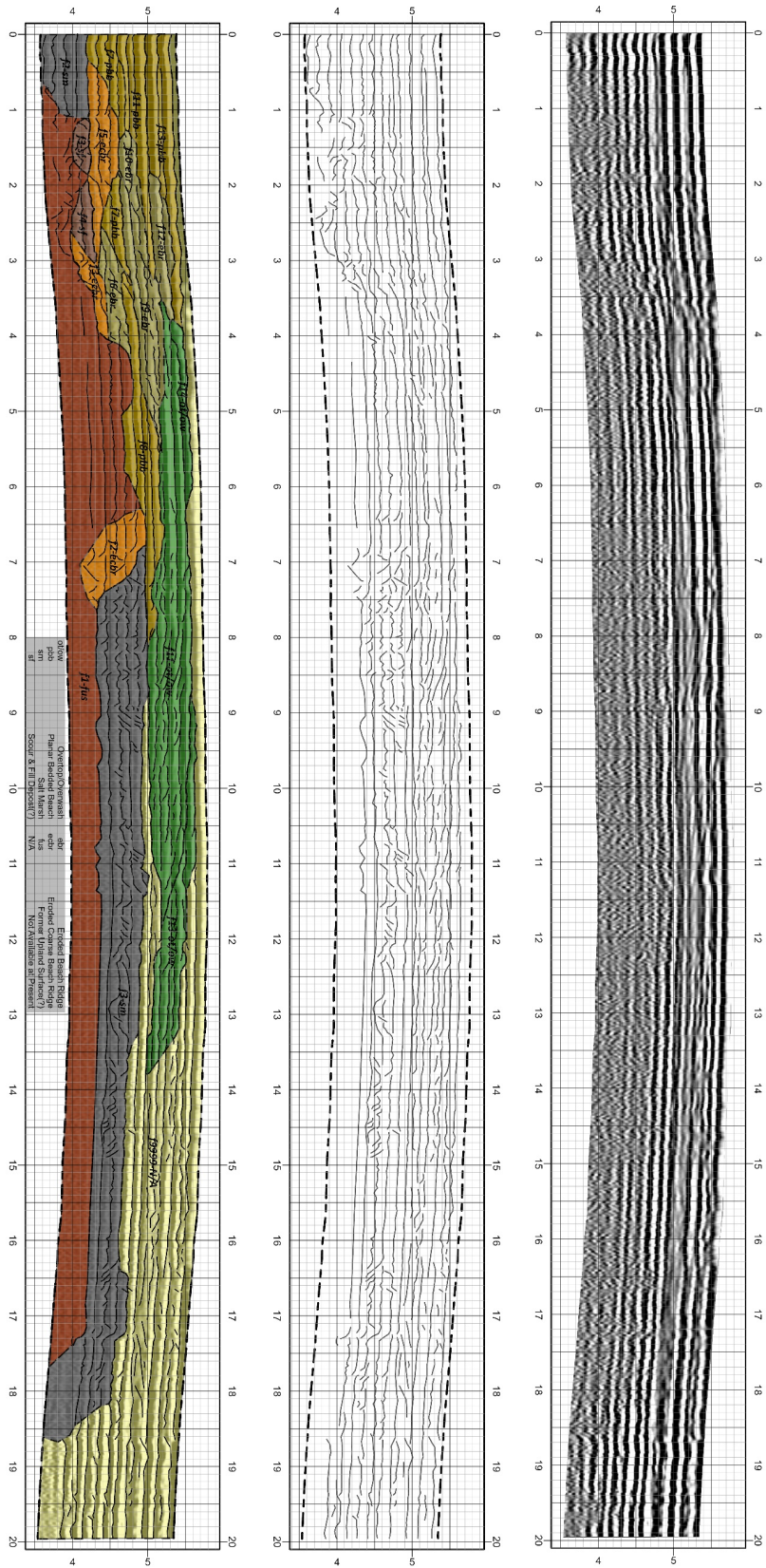


Figure 3.13: Radar surface (centre) and radar facies (left) interpretation of the reflection profile under drier conditions (right).

A visual interpretation of data amassed from Oak Point helps describe the landscape geoarchaeology in terms of morphodynamics and site formation processes. Flood tide flow direction and drainage during ebb is inferred through lidar derived topography, and field observations. Patterning in surface artifact distribution appears to represent how the disjoint hook at the distal end of the sand spit is growing. In effect, artifact distribution reveals that the location of a gyre occurring at the lee side of the spit hook during periods of sustained submergence during flood tide. Bidirectional flows in the gyre help pin artifacts at the lee side of the spit hook at Oak Point creating a distinct spiraling artifact distribution ([Figure 3.14](#)).



Figure 3.14: Oak Point geomorphology. Sand spit and dyke footing follow prior symbology. Also shown are artifacts (white points), /gyre in artifact distribution (black spiral line), current vectors (solid blue lines), drainage (small blue dashed lines), and eddy trajectory (dashed blue line with eddy symbol)

3.4 Discussion

The results indicate that age-depth model derived geochronological boundaries provide a valuable visual framework to guide further study of archaeological stratigraphy, deposition patterns, and the landscape geoarchaeology of coastal archaeological sites. When combined with field and GIS based geoarchaeological techniques, these geochronological boundaries help to characterize the relationship between archaeological materials and the long and short term morphodynamics of coastal archaeological sites.

Visualizing geochronological boundaries provides temporal reference points tied into elevations. Utilizing geochronological boundaries in combination with remote sensing techniques (e.g.: lidar, GPR) has provided insights into the landscape history at Oak Point. Proxy dating of the drowned forest acts as an analogue for considering the landscape prior to inundation/disturbance of archaeological sites on the landscape.

The sea-level curve for Oak Point shows that saltwater intrusion would have likely impacted the oldest surveyed stump of the antecedent forest ca. 2585 calBP at 0.377m CGVD2013. The stumps at the highest elevations were inundated by saltwater ca. 1000 calBP at 4.33m CGVD2013. Stumps in the lower antecedent forest hold a maximum age range for inundation spanning 2940 – 1560 calBP (Table 3.3-1; Figure 3.4.1).

Assuming the measured stump elevations represent the living tree location, death of all stumps post-dates the earliest date obtained from the deep cores (Smith et al., 1984). The implication is that the forest and archaeological site at Oak Point would be backed by a tidal marsh, though the forest would have been standing at 4465 ± 400 CalBP. During this period, Oak Point would have had a spur, or point, of land extending southwest of the sand spit hook, following the same orientation as the modern beach. This spur of land is noted

by a geomorphic feature of the antecedent landscape in the southwest of (Figure 3.14). The feature is highlighted by our boundaries as being at the limit of HHW ca. 2550 ±390 CalBP and lies at the same elevation as lower stumps from the drowned forest. Our geochronological boundaries provide corroborating evidence that this landform was a gently sloping coastal area in the antecedent landscape following the tidal expansion in the upper Bay of Fundy ca. 3400BP (Shaw et al., 2010).

Artifact deposition and distribution are closely related to the deposition and morphology of the sand spit hook. Strong currents from the Minas Basin are dampened as they move into the creek and up the channel to the lee side of the spit hook, while shoreward sand rippled surfaces and planar bedding in the spit hook imply turbulent flow from the beach front is a major source of material for the planar bedded beach (*pb*) and overtop/overwash (*ot/ow*) radar facies interpreted in the GPR data.

The crescent shape of the distal sand spit hook is partly due to weaker incoming current strength at the head of the meander channel. The dominant factor controlling the crescent shape is the gyre that forms at the apex of the crescent (Figure 3.14). The 1987 aerial photograph shows two large gyres seemingly originating at the Kingsport wharf (Figure 3.4, on right). The first gyre is shown at the wharf, and the second is shown at drowned forest near the bottom of the estimated trajectory shown in Figure 3.14. Excluding sections where the gyre transfers between meander channel channels over headlands, expansive circular surficial scouring of sediments occurs along the path of the gyre.

Artifact distribution follows a pattern expected and observed in other sediments on the spit hook. The coarser clasts in the sediment supply (artifacts) are closely associated with the lee side of the spit hook. Coarse clasts and artifacts on the surface are more tightly

clustered with increasing proximity to the crest of the spit hook during summer months (Figure 3.3c; Figure 3.9; Figure 3.12). This suggests that although the gyre is reworking surface materials, the outcome of the reworking seems to hold materials in place once they are relocated, likely by waves, to the disjoint sand spit hook.

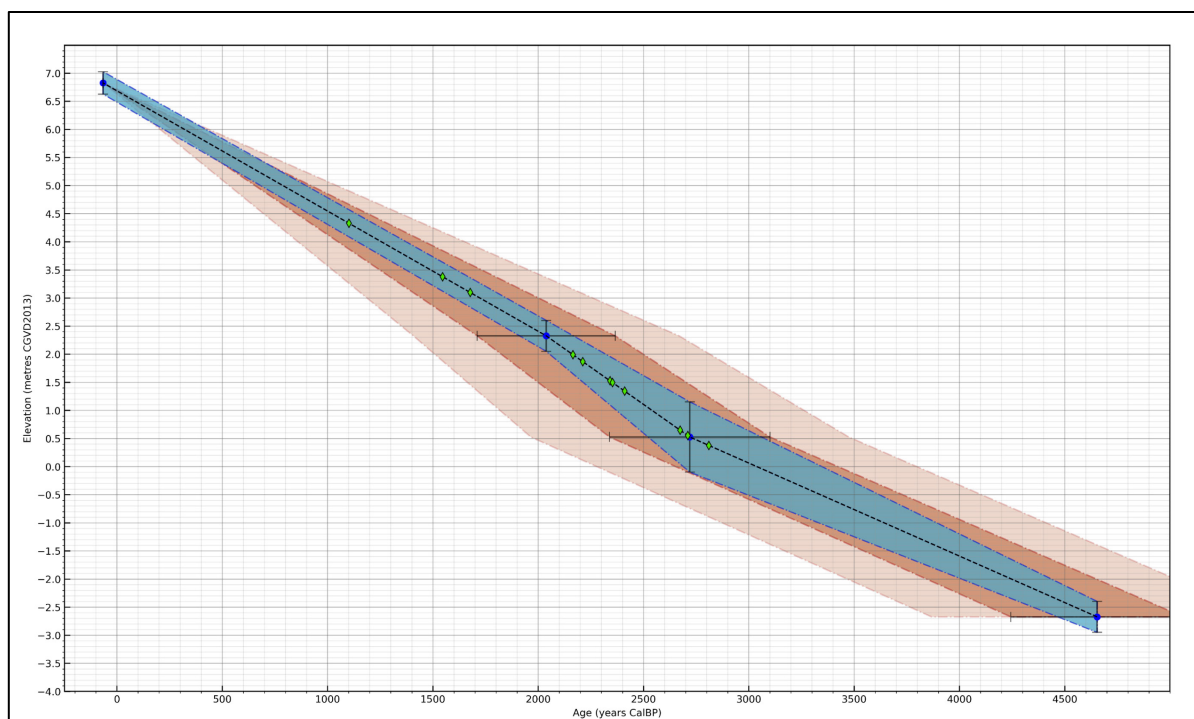


Figure 3.15: Predicted submergence dates of rooted stumps at Oak Point. Blue polygon shows SLIP uncertainty, red boundary shows age uncertainty.

Lee side artifact-to-artifact clustering is likely the product of artifact movement from overtop/overwash during a succession of storm events, the flood tide gyre, and deposition by ice during ebb tide in winter months. However, this does not ensure that are coming from the scoured surface or the eroding bed of the spit hook as artifacts may have been deposited on the lee side by the gyre prior to reworking during a storm. Association of lee side artifacts to the crest can be explained by size of the artifact, and the short distance the object would be moved from wave action if the gyre was responsible for originally depositing the objects near the top of the spit hook.

For either the gyre, or successive storm events to deposit materials in the same location, the materials are likely to come from the same source. For this reason, an in-situ or surficially scoured archaeological deposit is expected in association with the erosional

faces along the path of the gyre, the drowned forest, or the scoured sand deposit directly at the stoss side of the spit hook.

Lithics are primarily debitage accounting for 85.6% of the objects collected. Scrapers accounted for ten of the objects, and seven partial or complete bifaces have been identified. A nearly complete quartz projectile point preform is broken at the distal end then reworked producing a finely pressure flaked graver at the proximal end of the object. A complete quartz bipoint diagnostic of the transition from Early to Middle Woodland periods, and a roughly made unifacial projectile point manufactured from vein quartz are the only two complete projectile-like objects located in 2020. The quartz bipoint is similar in dimensions and style to a quartz bipoint identified within a feature dated to 2120 ± 60 C¹⁴ BP at the Oxbow Site in New Brunswick (Allen, 1980). Bipoints such as the one located at Oak Point appear in the Maine-Maritimes region at a time where trade-goods and burial customs originating in the Ohio River valley begin appearing in the region (Deal, 2015; Rutherford, 1990; Taché, 2011). Results support the inference that the bipoint from Oak Point may be used as a proxy for dating the archaeological deposit.

Here we find that HHW was less than 5m below the elevation of all artifacts surveyed during the period that bipoints like that at Oak Point were being produced at the Oxbow Site. If we assume that people are less likely to settle within 2m elevation of HHW to avoid flooding during extreme storm events, the erosional faces along the trajectory of the gyre are likely to be responsible for the artifacts. A lack of artifacts on scoured surface to the stoss of the sand spit suggests this area is less likely to be the source of any *in-situ* archaeological deposits.

Rooting the analysis in the ethnography and history of the region has provided valuable information contextualizing the landscape of Oak Point with more human understandings of the deep past. Oak Point is suggested to be part of a *mawiomi* landscape for ancestral Mi'kmaq, that the now drowned forest may have been implicated into in life. More evidence is needed to determine the temporal depth of this cultural landscape. Regardless of the date, the importance of an ancestral *mawiomi* landscape Mi'kmaq is heritage created from the intersection of the cultural and natural.

3.5 Conclusion

As a landscape geoarchaeology tool, geochronological boundaries provide a basis for proxy dating archaeological features and landscapes. The ability to visually date antecedent coastal features on lidar surfaces is a benefit that helps construct a landscape chronology, understand post depositional processes, contextualize site formation processes, and guide archaeological prospection. These boundaries are a natural progression from sea level curves or age-depth models for studying coastal archaeological sites and landscapes as they provide a spatial fix for higher high water in the past. The geo-temporal reference visually provided by these geochronological boundaries allows a degree of engagement with archaeological landscapes not possible with sea-level curves alone.

The resultant geochronological boundaries are created with relative ease with much processing occurring within a Jupyter Notebook, and can be used to guide age estimates of archaeological features and post-depositional processes. Additionally, these boundaries provide a basis for measuring distance from the marine limit, shown to be an important correlate for archaeological location modelling in other regions ([Lausanne et al., 2019](#); [Mackie, 2001](#); [Mackie et al., 2018](#)). The tool we have produced is best suited for landscape geoarchaeology of coastal regions that have experienced significant change in RSL since human occupation began in the region.

**Chapter 4 Landscape geoarchaeology of ice margins and
paleo-coastlines with GIS: A case study from Minas Basin,
Nova Scotia, Canada**

4.1 Introduction

The timing of late Pleistocene explorations and occupations of the Minas Basin by humans is constrained by the date at which ice sheets retreated, revealing a landscape topography like that of the modern day. Coastline location is one of the key differences between the landscape of Minas Basin today and early days of the most recent ice sheet retreat. A growing body of evidence supports a phenomenon placing coastal archaeological occupations within 5m elevation above the marine limit on moderately complex coastlines (Lausanne et al., 2019; Mackie, 2001; Mackie et al., 2018). A soft boundary for the end of the post-glacial high stand of relative sea levels exists sometime close to the Younger Dryas event (~11.96 – 13.16 ka CalBP) when eustatic sea level rise outpaced glacial isostatic adjustments (Reinig et al., 2020; Rivard et al., 2007; Stea, 1988; Stea and Mott, 2005, 2002, 1989). After this period, coastlines would begin to rapidly regress to a low stand in the early Holocene.

Determining locations where site formation processes favor preservation will help archaeologists pinpoint areas preferable for human occupation during early, likely relatively short-lived coastal occupations in the Minas Basin, Nova Scotia, Canada prior to the establishment of the late Pleistocene Debert-Belmont archaeological site complex (BiCu-01, BiCu-04, BiCu-06, BiCu-07, BiCu-08, & BiCu-10 – 24). The first, and most well studied of these sites (BiCu-01) provides a calibrated date range of 11.68 – 12.93 ka CalBP, constraining this occupation within the chronological boundaries of the Younger Dryas (Macdonald, 1965). The degree that geomorphological processes impacted archaeological materials at BiCu-01 is currently uncertain, though initial interpretations suggested that the vertical distribution of artifacts was heavily disturbed by natural

processes in all areas except where features were intruding into the laminated sands below (Macdonald, 1965, p. 16).

Defining the degree of influence of geomorphology and site-formation processes on archaeological deposits is integral for clarifying the agent(s) responsible for precise placement and distribution of archaeological materials. All anthropological interpretations constructed from distributions of archaeological materials are constrained by the degree of certainty held in humans being the primary agent responsible for those distributions. On a landscape scale, however, the influence of geomorphology and site-formation processes is fundamental to analyzing site distribution, and informing archaeological site prospection (Contreras, 2017; Holliday, 2009; Holliday et al., 2019; Lausanne et al., 2019; Mackie, 2001).

A modern technology frequently enabling remote archaeological site prospection is light detection and ranging, or lidar. Lidar data released in 2020 by the Government of Nova Scotia records topography at a resolution of 1m/pixel, allowing conceptual models of landscape change in the Bay of Fundy since the most recent deglaciation to be considered at higher spatial resolutions (Dalton et al., 2020; Shaw et al., 2006; Stea, 2004, 1988; Taylor and Shaw, 2016). The new data presents an opportunity to illustrate how lidar can increase spatial coherency between models of deglaciation and the observable landscape through exploratory identification of surficial features not visible at lower resolutions.

Archaeological research benefits from lidar assisted conceptualizations of late Pleistocene landscapes in northeastern North America prior to the Younger Dryas, as it helps approximate coastal regions where people are most likely to be. Coastal regions are

approximated applying corrections that account for both glacial isostatic adjustments and eustatic sea level. The adjusted lidar data models late Pleistocene sea-level on the modern landscape, allowing these coastal landscapes to be interpreted through landforms. The aim of this paper is to investigate the ability of this technique, developed on more recently deglaciated Arctic environments, to model late Pleistocene sea-level in a section of Minas Basin (Leverington et al., 2002).

Late Pleistocene relative sea-levels are modelled using a lidar derived digital elevation model (DEM) surface using raised marine limits in Minas Basin as a proxy for combined glacial isostatic adjustments and eustatic sea level change (Stea, 1988). The process produces a surface modelling the relative sea-level high directly following retreat of the Laurentide Ice Sheet from the Minas Basin (Dalrymple et al., 1992; Dalrymple and Zaitlin, 1994; Fader, 2005; Taylor, 2020). During the late Pleistocene, the waterbody that fronted the retreating Laurentide Ice Sheet in the Bay of Fundy was known as the De Geer Sea (Fader, 2005). Soon after the Laurentide Ice Sheet retreated into what is now the Minas Basin, rebounding glacial isostatic adjustments outpaced rising eustatic sea levels causing a drop in the relative sea-level of the De Geer Sea (Fader, 2005; Vacchi et al., 2018).

One careful consideration to be made when constructing and interpreting a marine emergence isosurface for Minas Basin is the duration of time since deglaciation has been much longer than that of the Arctic. Since deglaciation, the landscape of Minas Basin has been subject to geomorphological processes responsible for presenting the modern surficial landform configuration. Therefore, although the isosurface may be created of quantitative late Pleistocene samples, the surface is draped on modern topography which has been subject to geomorphological change.

In Minas Basin, a large portion of the paleogeographic record below modern high water has been lost during marine transgression (Amos, 1978; Swift, 1968). However, a record of raised marine deposits exists throughout the Minas Basin that are correlated to the retreat of the Laurentide Ice Sheet. In the following, corrections to lidar elevation surfaces are applied using isolines of marine emergence in the southwestern Minas Basin to develop a surface representing the deformed peri-glacial, and early post-glacial landscape (Leverington et al., 2002; Stea, 1988). This surface will be used to further detail how the observed trend of shorelines, surficial deposits, landforms, and glacial isostatic adjustments in the region relate to each other, and whether the De Geer Sea intruded in to the southern Minas Basin during the late Pleistocene (Dalton et al., 2020; Paradis et al., 2006; Rivard et al., 2012, 2007; Shaw et al., 2002; Stea, 2004, 1988).

4.2 Background

4.2.1 Project background

The past interface of water and land between 12.3 - 8kya became of primary interest for an archaeological resource impact assessment on the UNESCO Landscape of Grand Pré because there was little evidence in primary contexts from the archaeological record relating to this period (Fowler and Weatherbee, 2020). That a peri-glacial waterbody existed in the late glacial period is apparent, but the genesis, type, and spatiotemporal extents rely on small amounts of evidence in the southwestern Minas Basin (Rivard et al., 2012; Stea, 2004). Surrounding the landscape of Grand Pré, a series of terraces were noted in the DEM and mapped (Fowler and Weatherbee, 2020; **Figure 4.1**). The Canadian Soil Information Service (CANSIS) National Soils Database illustrated that larger terraces were fluvial deposits, glaciolacustrine deposits, or a mix of the two (Government of Canada,

n.d.). A rudimentary sequence was suggested for land emergence at a series of elevations from the terraces between 12.3 - 8kya (Fowler and Weatherbee, 2020).

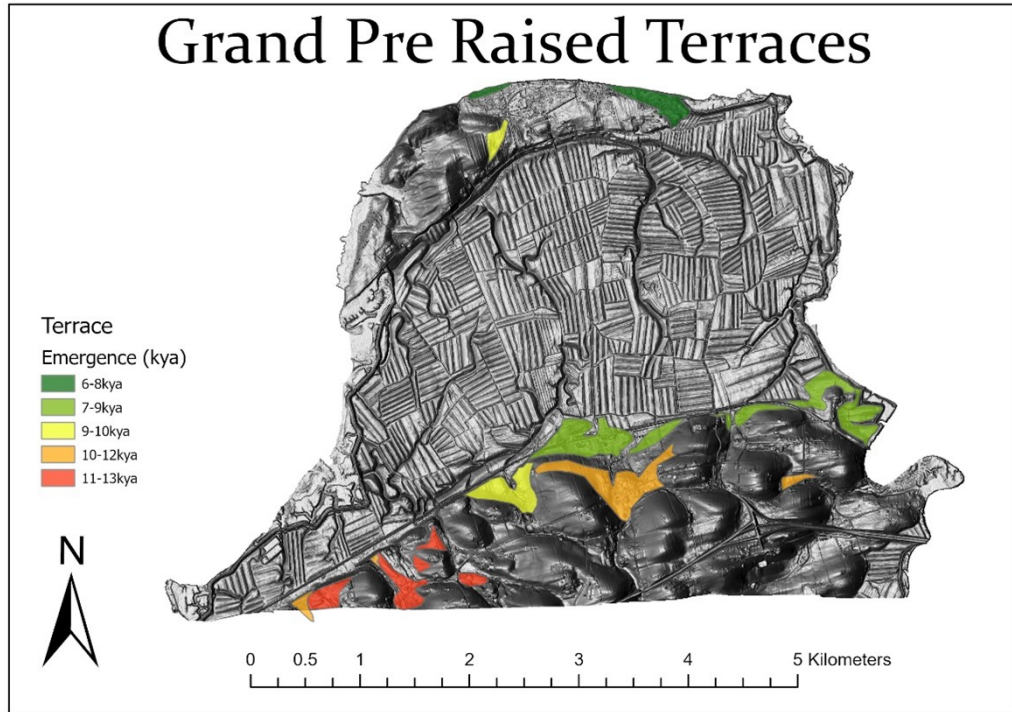


Figure 4.1: Rudimentary sequence for terrestrial emergence of terrace features at Grand Pré. Source: Fowler & Weatherbee, 2020.

There is a need for sub-regional analyses of environmental change in the late Pleistocene to refine models of human settlement patterns in the northeast (Lothrop et al., 2011, p. 564). One approach to elucidate information about the earliest settlers of recently deglaciated landscapes in late Pleistocene North America is that of landscape geoarchaeology, or “the relationship of [archaeological] sites to geomorphology” (Holliday, 2009, p. 317). Facilitation of surficial landscape geoarchaeology studies in the Maritimes region can be greatly expediated by the combination and interpretation of the spatial relationships between precise and accurate archaeological site location data, relict features in lidar derived surface models (Dupuis et al., 2018), and models of changes in

paleotopography (Leverington et al., 2002; Stea, 1988). These analyses are made possible by GIS, allowing for rapid observations of surficial geology in relation to paleotopography to help sequence events during the late Pleistocene that formed the lived environment of early people in the upper Bay of Fundy.

4.2.2 Previous research

Terraces identified on Long Island and Wolfville Ridge adjacent to Grand Pré do not stand alone as anomalous features in the broader landscape, though the date range in **Figure 4.1** likely underestimates the antiquity of the sequence (Fowler and Weatherbee, 2020; Rivard et al., 2012). It has also been demonstrated that sediments formerly interpreted as tills covering parts of the gently sloping landscape of southwestern Minas Basin are more likely sediments from supralittoral and littoral facies dating to the late Pleistocene to Early Holocene (Paradis et al., 2006; Rivard et al., 2012, 2007). Several authors:

recognize a nearshore facies that superficially resembles silty pebbly till. This is similar to those sediments associated with the paramarine basin in the Lawrencetown-Middleton area. We believe this unit was misidentified by Trescott (1968) as till because of the numerous pebbles, some striated, found at the surface (Fig. 18a). When this material is exposed in sections, it consists of massive silty clays without pebbles (Fig. 18b). We think pebbles are the result of wave washing of the adjacent tills on the North Mountain or protruding streamlined landforms, as well as deposition by ice rafting (Rivard et al., 2012, p. 32).

The deposits described above represent a late Pleistocene lake and/or a paramarine basin in the area. Such large bodies of water are sure to express themselves on even the modern landscape of today. These large, short lived water bodies have etched their own marks into modern topography throughout the southwestern Minas Basin in the form of

wave cut terraces, wave washed surfaces, sand wash limits, and raised beach ridges. In further describing this feature and their surficial geology, Rivard et al. (2012, p. 32) explain that during the terminal periods of the late Pleistocene, the:

[f]inal collapse of the ice drained the lake completely and allowed marine waters to invade the lower reaches of the Cornwallis, Canard, Pereau, and Habitant rivers. Marine clays occupy all areas below 15 to 20m a.s.l. These must have been estuarine environments that even today would be subjected to tidal processes if the rivers had not been dyked.

In relation to archaeology, these sediments are best contextualized as part of the terminal Pleistocene environment presented to the earliest known people to occupy the upper Bay of Fundy at the Debert-Belmont site complex (Macdonald, 1965; Rosenmeier et al., 2012). The innermost easternmost region of upper Bay of Fundy and Minas Basin, known as Cobequid, was suggested to have been deglaciated by 14.0 ¹⁴C ka BP based on dates from vibrocores south of Five Islands (Amos, 1978; Wightman, 1980). Expressed in calibrated years, the sample dates between 17.2–15.3 ka calBP at 1 σ using the Marine20 calibration curve in IOSACal (Costa, 2018; Heaton et al., 2020, p. 20; **Figure 4.2**). If correct, the southwest Minas Basin may have been relatively ice free for millennia prior to the end of the Pleistocene.

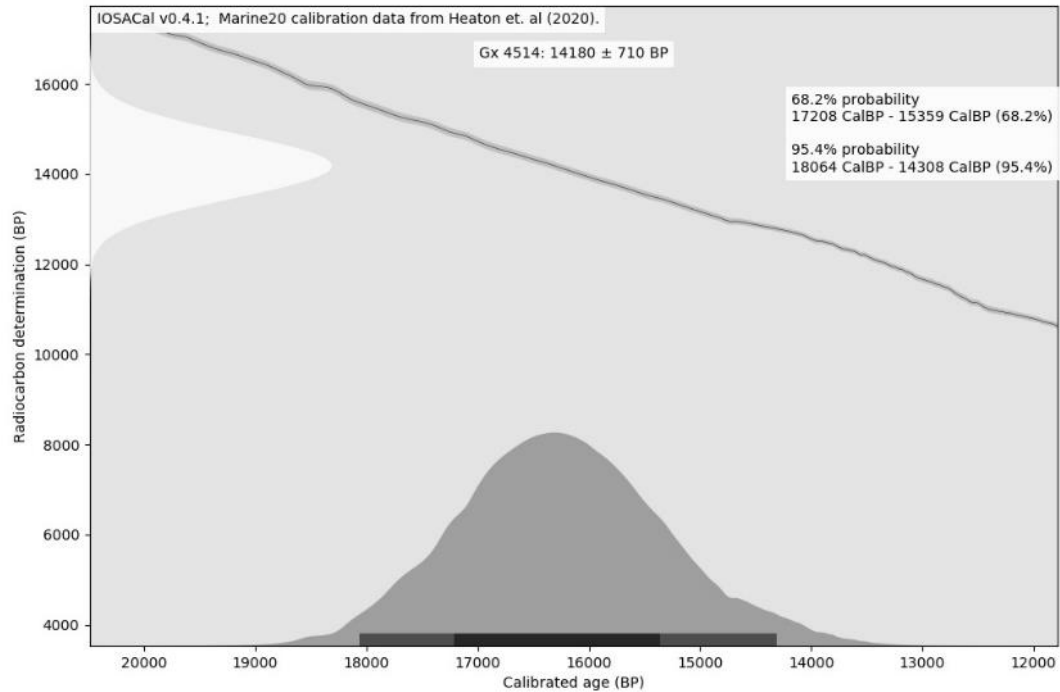


Figure 4.2: Probability distribution of calibrated dates for the deposition of the Minas Terrace south of Five Islands. SOURCE: (Amos, 1978; Wightman, 1980)

A later study provides more secure dating, noting that land-locked ice persisted at the Five Islands Formation until at least 13.0 ^{14}C ka BP (Stea, 2004). Most recently, GIS boundaries for the deglaciation of North America have been refined for use at a 1:1000000 scale for the first time since 2003 (Dalton et al., 2020; Dyke et al., 2003; **Figure 4.3**). The updated configuration suggests that from 15.5–14.2 ka CalBP there was a rapid retreat in the Laurentide Ice Sheet overlapping in time with glacial Meltwater Pulse 1A (~14.6 ka CalBP) (Dalton et al., 2020; Lin et al., 2021). Interpretation of multibeam bathymetry data the outer Bay of Fundy indicates ice retreat began after 18 ka CalBP (Shaw et al., 2014; Todd and Shaw, 2012). It is important to distinguish that the ice configuration does not represent the extent of seasonal sea-ice, and the authors recommend relying on local studies for the most accurate boundaries at higher resolutions (Dalton et al., 2020).

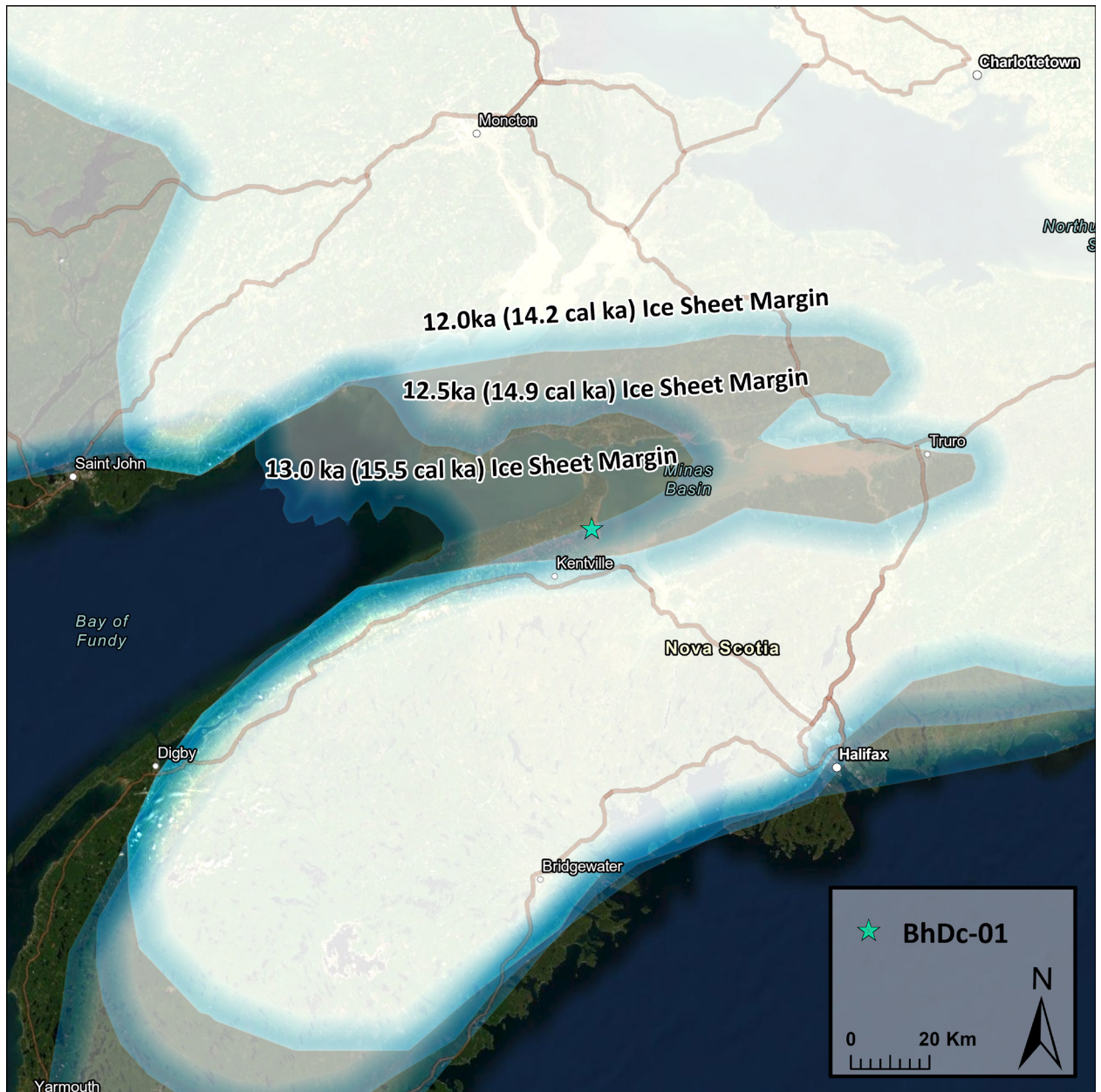


Figure 4.3: Continental-scale boundaries of the Laurentide Ice Sheet over the Maritimes from 15.5 to 14.2 ka CalBP. SOURCE: (Dalton et al., 2020)

4.3 Methods

Three processes contribute to this exploration of landscape geoarchaeology of late Pleistocene Minas Basin. Initially, published data (**Figure 4.4**) is re-used and analyzed using ArcGIS Pro 2.8.3 to reconstruct late Pleistocene coastal paleotopography, and hypothesize relative sea-level (Leverington et al., 2002). Next, the predicted relative sea

levels of the produced paleotopographic elevation model are used to discern relict coastal features and landscapes (Dupuis et al., 2018; Minár et al., 2020). Finally, the position of relict coastal features and the LIS margin over time is discussed in relation to archaeological materials in two examples: 1) a late Pleistocene age artifact in Minas Basin; 2) a large quartz blade located along a section of the predicted shoreline.

Throughout the paper, the paleotopographic surface model is visualized as a shaded relief image. The colour ramp used is indicative of the modelled 0m contour, or marine limit. To imply uncertainty in the model through visualization, the modelled marine limit is shown at the transition from sandy yellow to brown, while the sandy yellow and brown regions bordering this region encompass 5m in elevation.

4.3.1 Re-constructing the Minas Basin paleotopographic elevation model

In upper Bay of Fundy, the highest resolution map of the changing marine limit in the Terminal Pleistocene is found in a discussion paper about post-glacial changes in relative sea level in the Northumberland Strait (Stea, 1988; **Figure 4.4**). The figure shows isolines of marine emergence for upper Bay of Fundy, excluding the easternmost tip of Cobequid. Values shown on contours are the elevation at which the marine limit has been identified, providing a geospatial representation of the pace of GIA in relation eustatic sea level rise. Assuming a similar local impact of GIA per-unit-area as ice retreats, a rough estimate of the timing of this early succession of marine limits can be observed by comparing the location of the contours in **Figure 4.4** with the timing and extent of glaciers in **Figure 4.3**.

Published was re-used and analyzed using ArcGIS Pro 2.8.3 to reconstruct coastal paleotopography and a region of increased potential for human occupation within the

Minas Basin. A map was georeferenced to the North American Datum 1983 Universal Transverse Mercator Zone 20N projected coordinate system (Stea, 1988, figure 3). Contours and point features were digitized to create a database of marine emergence for the upper Bay of Fundy following methods in Leverington et al. (2002; **Figure 4.4a**) and utilizing the Canadian Geodetic Vertical Datum of 2013 (CGVD2013) to record elevations. This database was used to create a triangulated irregular network (TIN) from both point and line data in the database (**Figure 4.4b**). Points were classified as ‘Mass Points’, and contour lines were as ‘soft-break lines’. Constrained Delaunay was left unchecked. The TIN surface was then exported as two different resolution raster files (20m/pix; 1m/pix) to match a 20m provincial DEM (**Figure 4.4c**) and a 1m lidar derived DEM of Minas Basin and Cobequid (**Figure 4.4d**).

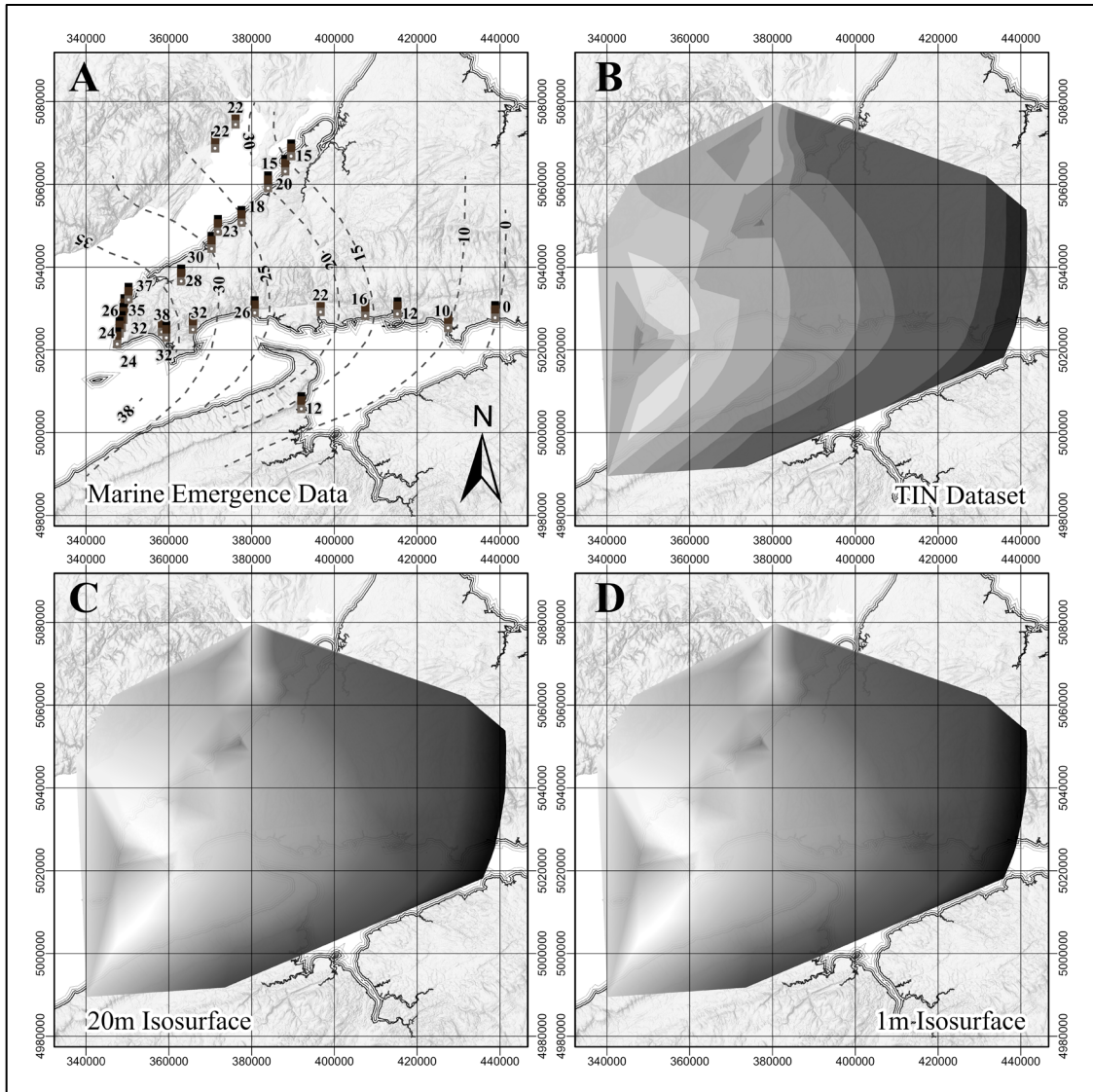


Figure 4.4: A) Digitized isolines of marine emergence data. B) TIN dataset created from marine emergence data. C) 20m isosurface of marine emergence. D) 1m isosurface of marine emergence.

Values in the 20m isosurface were subtracted from a 20m resolution DEM of the upper Bay of Fundy, while values in the 1m isosurface were subtracted from a 1m resolution DEM of Minas Basin. This process adjusts elevation values in the modern DEMs to a value of 0m elevation in areas where remnants of former shorelines are expected from 15.5–13.5 ka CalBP. The TIN surface was then subtracted from a lidar DEM of the Minas

Basin, to move the shoreline indicators shown in **Figure 4.4a** to an equal vertical reference of 0m. The elevation of 0m in the resulting marine limit derived paleotopographic elevation surface is temporally constrained between 15.5–13.5 ka CalBP for the Minas Basin.

An assumption is made that shoreline indicators would be more closely correlated with closer glacial margins, meaning shorelines get older as one moves from the upper to outer Bay of Fundy. A potentially problematic assumption for more result driven analyses, the identification of a baseline for future studies compliments the exploratory nature of the current study. This assumption, and inherent error in modelled ‘shoreline’ (0m elevation) position, are leveraged to help direct visual exploration of lidar data for the purpose of identifying coastal zone indicators in the model.

4.3.2 Identifying late Pleistocene relict coastal features

Visual inspection of the output surface was performed to identify relict coastal features and consider the accuracy of the modelled shorelines. First, contours were derived for both paleotopography elevation models at 0m. Contours were overlaid on a series of maps along with freely available Provincial and Federal surficial data, and pre-European entries to the Maritime Archaeological Resource Inventory to contextualize the late Pleistocene coastal zone. Base data for the map series was restricted to provincially available elevation data in 2019, meaning some areas of Southern Bight did not hold 1m lidar when maps were initially produced, and therefore use 20m base mapping. The series of 49 maps covers the extent of the paleotopographic elevation model from Huntington Point, North Mountain, to Southern Bight and available in **Appendix C**.

Relict coastal features have been identified in numerous recent studies of the Southern Bight (Paradis et al., 2006; Rivard et al., 2012, 2007; Stea, 2011). A guide on identifying surficial features from lidar data with a series of examples and descriptions is presented in a document for determining borrow pit potential (Dupuis et al., 2018). The descriptions of how features are identified are one of the most important characteristics of identifying surficial features.

Raised beach ridges are utilized as shoreline indicators. Many raised beaches previously documented exhibit a series of rhythmic, equivalently spaced, cusp and ridge landforms with an inter-ridge interval of 40-60m (e.g.: **Figure 4.4a**, in Paradis et al., 2006). Raised beach ridges in the Southern Bight have developed on deep deposits of extremely unconsolidated sediments that during formation held a degree of permafrost (Rivard et al., 2012). Inter-ridge distance was used to assess the interval of the rhythmic landforms because geomorphological processes have down and back wasted the cusps the melting of permafrost, shoreline recession, and millennia of surface water drainage potentially modifying the inter-cusp distance.

Relict features in the lidar data were considered in the context of the late Pleistocene to early Holocene marine regression in the Bay of Fundy. The highest relict coastal features in Southern Bight were considered micro- to mesotidal, transitioning into a macrotidal coastal system as the features approach modern high water (Dalrymple and Zaitlin, 1994). This conceptual model of tidal range during marine regression informs the interpretation of raised coastal features in order of descending elevation in Southern Bight.

4.3.3 Considering the landscape geoarchaeology of late Pleistocene Minas Basin

Multiple regions in the Minas Basin have produced isolated artifacts likely produced during the late Pleistocene to early Holocene marine regression. The spatial position of two of these artifacts was considered in relation to proximal relict coastal features and retreat of the Laurentide Ice Sheet to determine a *terminus post quem* for each (Figure 4.5). The local peri-glacial environment at each location differs, though the paleotopographic elevation surface allows for sequences of superimposed glacial and relict coastal features to help describe each region.

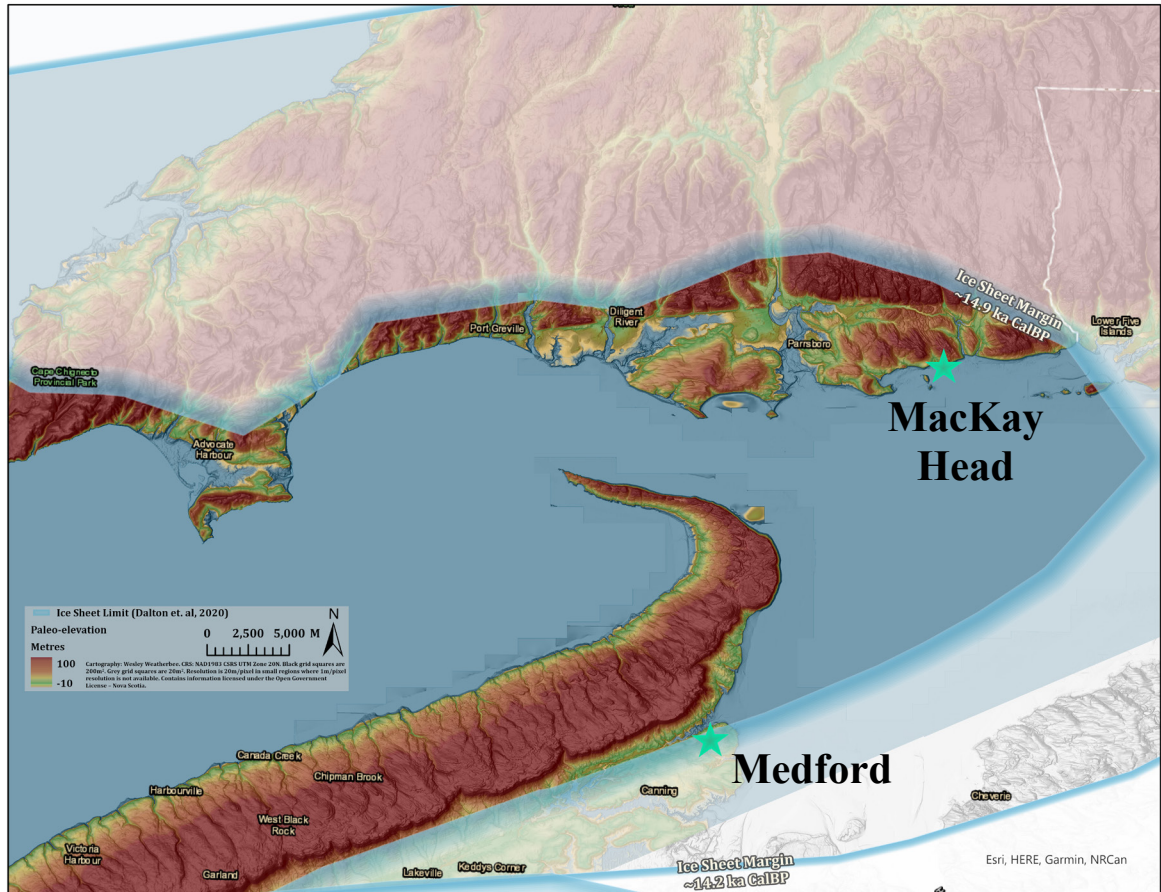


Figure 4.5: Location of finds described in the text in relation to the Laurentide Ice Sheet margin at ~14.9 ka CalBP.

Medford

The artifact originally located at Medford (BhDc-01) is a Debert style fluted projectile point was reported and mapped by George MacDonald during his 1960's investigations into the late Pleistocene Minas Basin (**Figure 4.6**). The Debert style fluted projectile point was reported to be made of a local “North Mountain Material” by John Erskine in a letter to MacDonald (Deal, 2020). The survey map produced by MacDonald was georeferenced to plot where the artifact was reported to be found in relation to the paleotopographic elevation model.

A brief archaeological surface survey was conducted on the property in October 2020. The area is now beneath a young apple orchard, surveyed to identify lithics moved to the surface by root driven bioturbation. Sediment profiles in exposed ditches were noted to inform landscape interpretation. A second survey area, recently cleared and ploughed by landowners provided a better horizontal view of surficial deposits. This region is noted on MacDonald's map (**Figure 4.6**) as "BUSH" and does not appear to have been investigated during later archaeological research by Dr. Michael Deal (Deal, 1991).

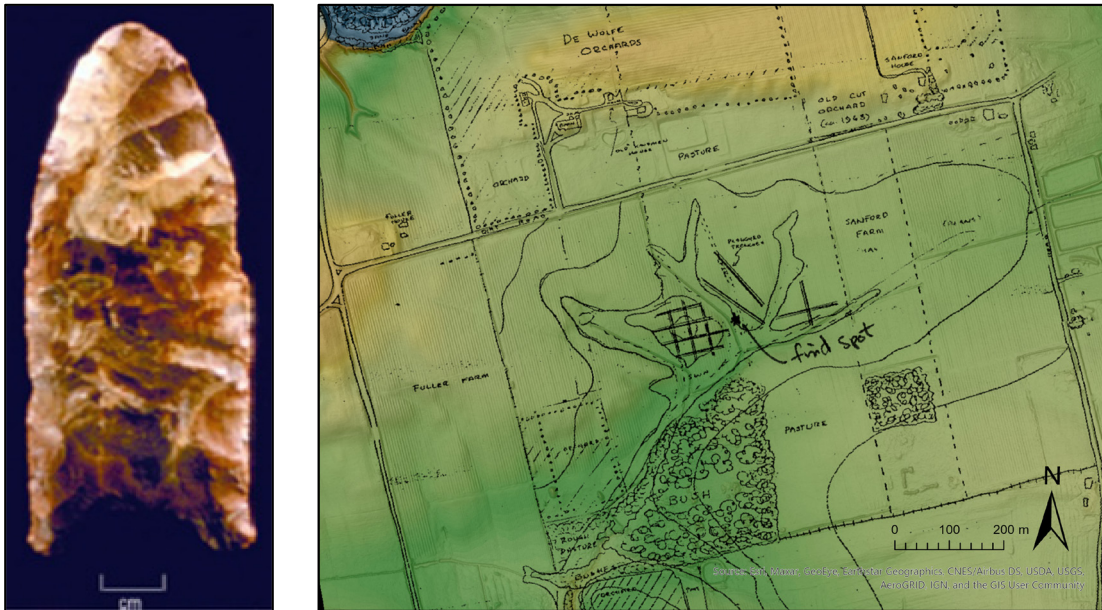


Figure 4.6: Artifact found at Medford (left), and section of georeferenced survey map produced by George MacDonald showing location of artifact as "find spot" (right). Images courtesy of Mike Deal, artifact image originally in Bonnicksen et al. (1991)

MacKay Head

A chance-find of an artifact collected at MacKay head is remarkably located in relation to this study (**Figure 4.7**). The artifact was collected by Dr. Danika van Proosdij

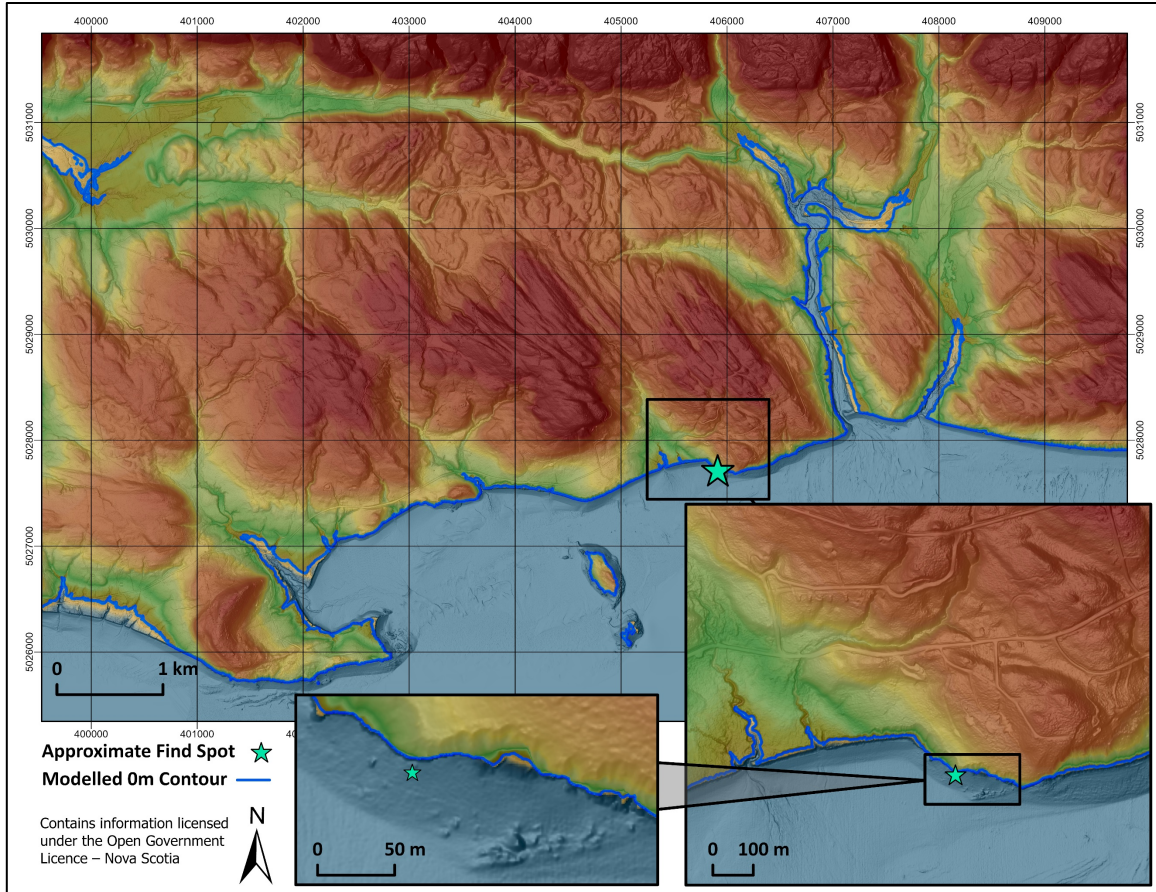


Figure 4.7: Location of find at MacKay Head, Minas Basin in relation to modelled marine limit.

in late July 2021 while observing coastal geology in the area between Two Islands and MacKay Head. The large quartz biface collected will be described in relation to late Pleistocene and early Holocene coastal geomorphology of the area to better contextualize the landscape geoarchaeology of this site.

4.4 Results

4.4.1 Paleotopographic Surface Model

The modelled paleotopographic surface indicates that the marine limit would have intruded the lower reaches of the Habitant and Canard River valleys (Rivard et al., 2012; **Figure 4.8**). However, as will be discussed, rhythmic surficial features are present in many regions above this (**Figure 4.9**). Understandings of the landscape emergence sequence and corresponding hydrological patterns during the late Pleistocene in the Southern Bight can be enhanced using paleotopographic surface models.

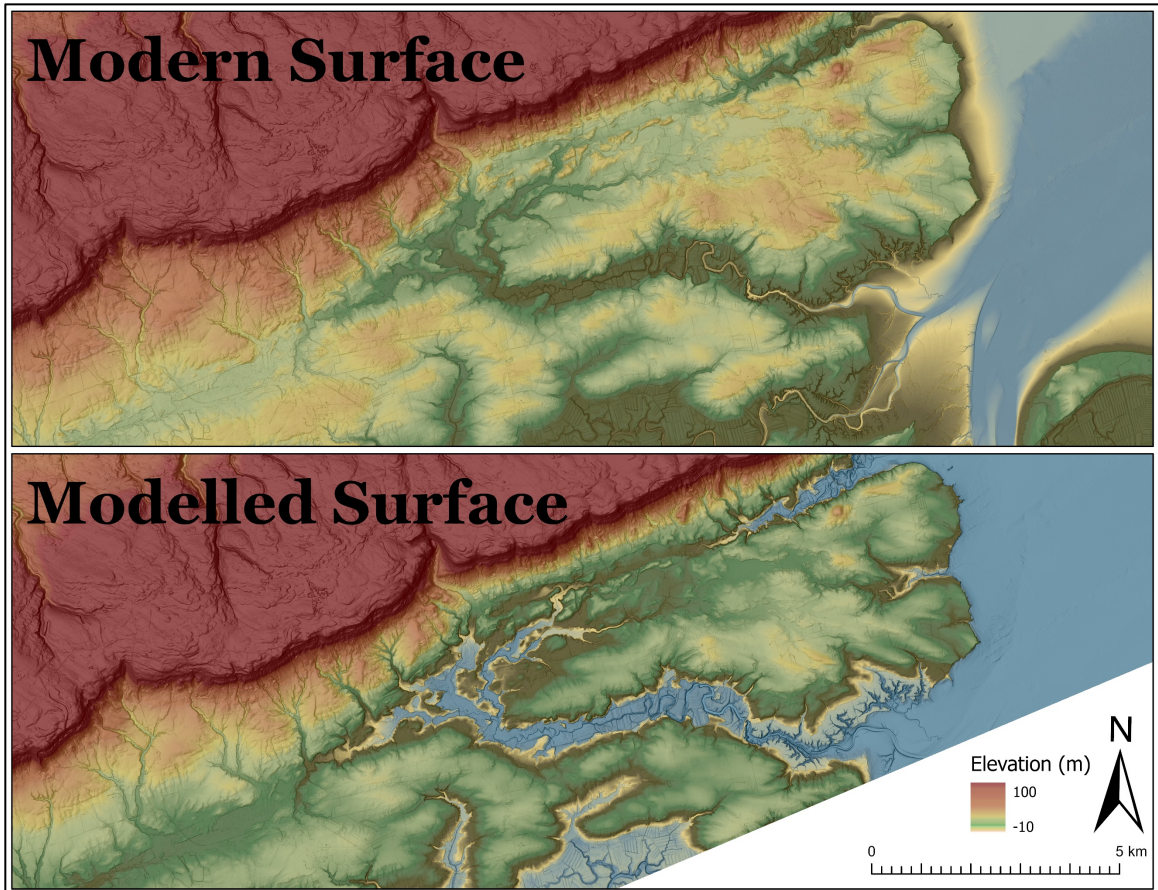


Figure 4.8: Overview of the change in elevation on modern and modelled paleotopographic surfaces derived from lidar.

The output 20m resolution paleotopographic surface model aids in the identification of larger scale coastal features at a landscape scale but is limited in its use on areas where the 0m contour intersects an area of lower slope (**Appendix C**). At a resolution of 20m the DEM cannot render subtle topographical changes such as beach ridges but provides a valuable reference of the areas where these features can be identified in aerial photography. If combined higher resolution aerial imagery, a 20m resolution surface has the potential to provide value as a tool for landscape geoarchaeology. This coarse resolution suffices to identify an area of focus for landscape geoarchaeological investigations of relict coastal features in higher resolution aerial photography.

Lidar data at a resolution of 1m/pixel resolution of the Minas Basin provides satisfactory results for visual investigation of landscape geoarchaeology when used to construct a paleotopographic surface model. The 0m contour invariably intersects what appear to be recessional raised beaches in the paleotopographic surface model along North Mountain (**Appendix C, Plate 1-12**). An important guiding principle for interpretation of the surface is the assumption that the highest shoreline indicators would be more closely correlated with closer glacial margins, meaning the marine limit should become older as one moves from the upper to outer Bay of Fundy. In many cases, the highest sea level indicators that can be identified on the shaded relief exist at elevations higher than the modelled limit of 0m. Post-depositional processes impacting some raised sea level indicators due to combined geomorphological changes, differential rates of local emergence, isostatic recovery of the landscape, and deflation from thawing ground ice therefore providing artificially low regions of marine limit in the Minas Basin.

4.4.2 Relict Coastal Features

A variety of raised rhythmic cusp and ridge landforms were identified, and a selection were selected for display (**Figure 4.9**). Some of these landforms were not identified in previous studies, and as the intent of the project is to present the surficial morphology of the raised coastal features in lidar they are not exhaustively highlighted in the Supplementary Data. The examples shown are presented to illustrate the landforms as shaded relief and in 3m contours to inform future coastal research in the Minas Basin (**Figure 4.9**). The elevations of the raised beach ridges can be used to develop a rudimentary sequence for the shorelines of the source waterbodies.

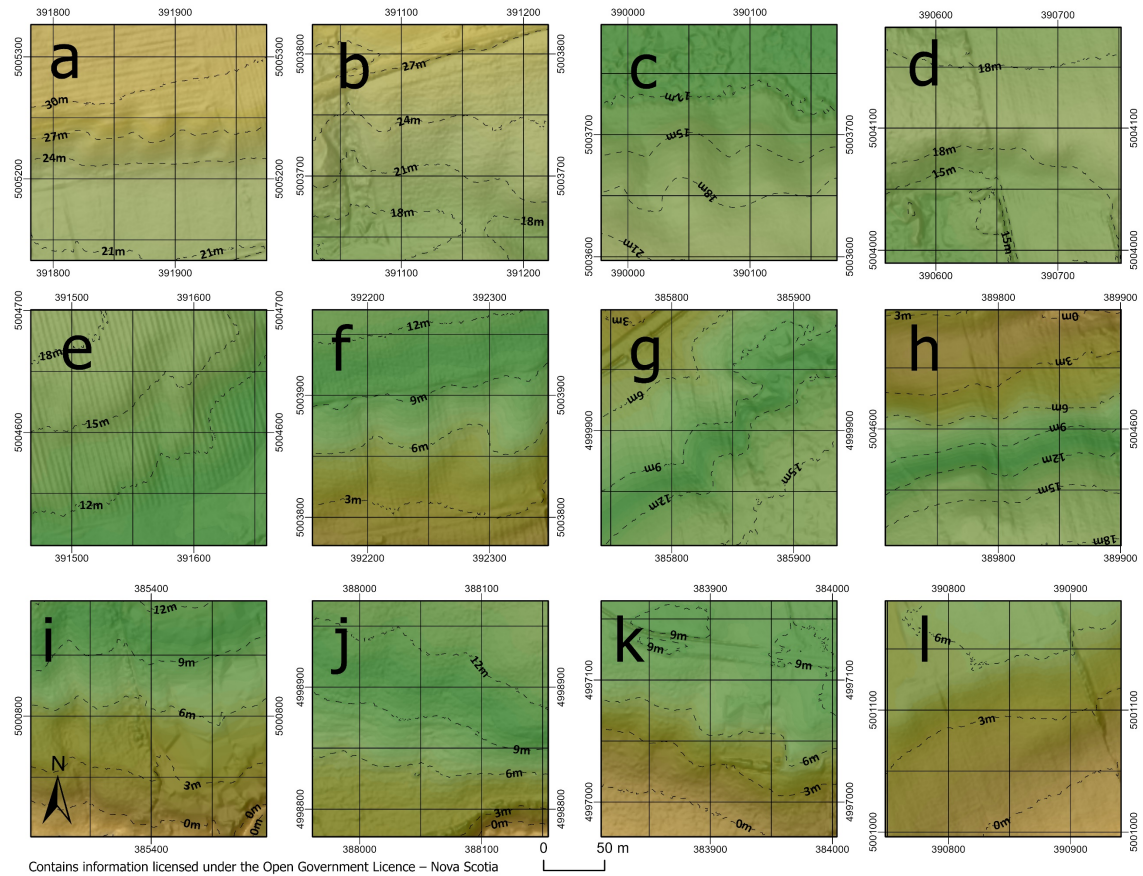


Figure 4.9: Selection of 12 areas visualized as shaded paleotopographic relief showing equivalently spaced, cusp-like rhythmic relief appearing on the slopes of regions of raised basin-like topography in Southern Bight. Contours at 3m interval represent elevation above marine limit defined by paleotopographic surface model.

The raised beach cusps shown have been deliberately clustered toward the Medford site (**Figure 4.9a-f, h**) as a function of proximity to the Debert/Vail style projectile reported from that location. These features, and other surficial coastal features are ubiquitous above the marshes in Southern Bight presenting themselves at elevations above the limit of modern high tide. Regardless of elevation, many cusps appear to illustrate a record of longshore direction (e.g.: eastward transport in **Figure 4.9a, f, j, k**), while others have overprinted, or been overprinted by terracing (e.g.: **Figure 4.9e, l**). Two of the sections exhibit what are interpreted as beach deposits preserved below the higher energy rhythmic cusp and ridge formations (**Figure 4.9f, j**). Modern coastlines indicate that high tide is

beginning to impact the lower reaches of late Pleistocene marine limit in Southern Bight, as these features exist at elevations descending to the limit of modern high tide.

4.4.3 Landscape Geoarchaeology

Relict coastal features identified in the lidar data provided the scale of analysis necessary for archaeological interpretations to begin to be developed in two areas where artifacts potentially dating to the late Pleistocene have been found. These artifacts are described in relation to geomorphological processes that would have created and subsequently modified the relict coastal features.

Medford

Archaeological survey at Medford in 2020 located four lithic objects, of which, one is a portion of a utilized lithic core (**Figure 4.10**). The objects were located downslope of the reported location of the Debert/Vail projectile point in the recently cleared land labelled “BUSH” in MacDonald’s 1965 map (**Figure 4.6; Appendix C, Plate 28**). These objects were located well above the modelled Late Pleistocene shoreline, even when considering the impacts of tidal range, and storm surge.

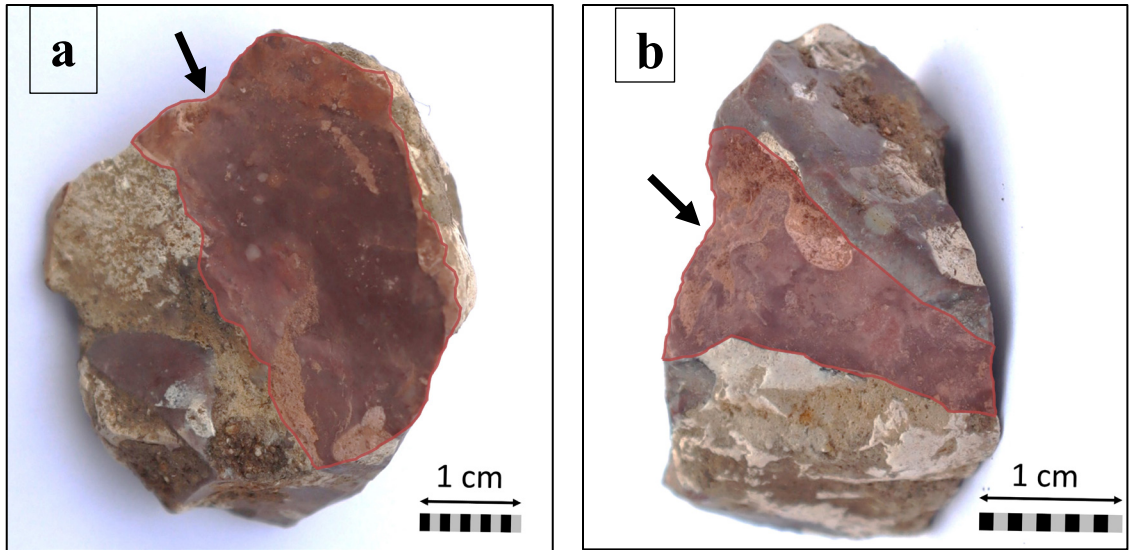


Figure 4.10: Images of the utilized core located in Medford showing flake scars highlighted in red. Arrows indicate location and direction of applied force.

The material of the utilized core is a locally available waxy chert from the North Mountain region, possibly from a source local to Blomidon. Colours are primarily purple to red, in a swirling configuration with circular regions of tan to caramel. A bright white cortex is present and has been removed by shallow flake scars on multiple faces. A 3D model of the utilized core displayed as a shaded mesh highlights worked regions of the object (**Figure 4.11**). The shaded mesh visualization (**Figure 4.11**) supplements the information shown in the imagery (**Figure 4.10**) by showing each object from a different perspective.

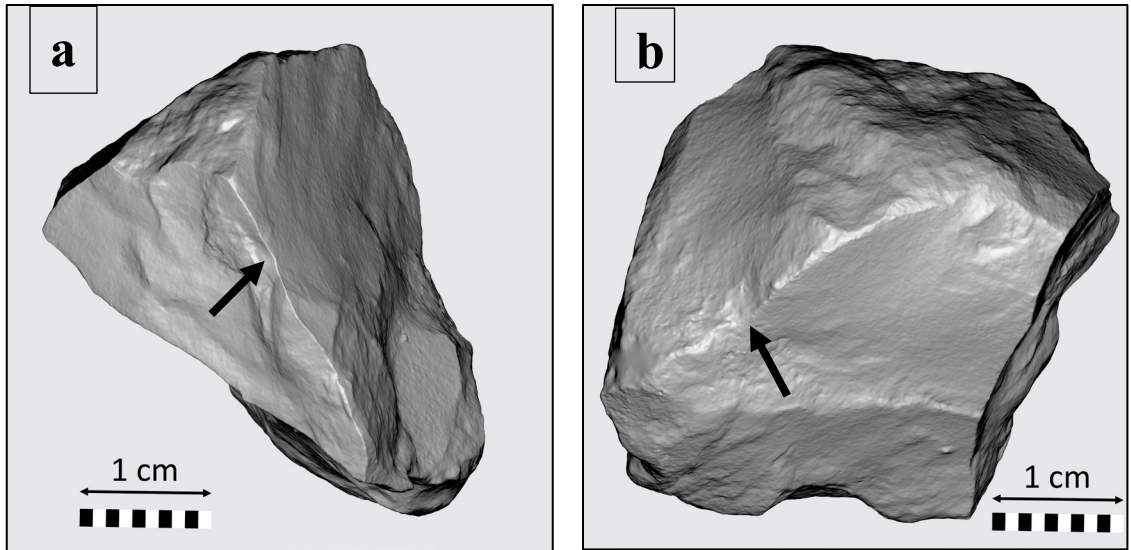


Figure 4.11: Shaded mesh visualization of the utilized core located in Medford showing flake scars. Arrows indicate location and direction of applied force.

MacKay Head

The large biface located at MacKay Head is located well below the marine limit modelled by the resultant paleotopographic surface model but is adjacent to a small section of preserved shoreline lying 2m below the modelled late Pleistocene marine limit. The artifact is manufactured from rutilated quartz appearing to be struck from a prepared core as a blade (**Figure 4.12; Figure 4.13**). There is a large degree of weathering from abrasion in the sediment heavy tides of the Minas Basin present on the artifact. Weathering has affected the ventral side of the artifact more severely than the dorsal, indicating the object was transported by sliding ventral-side-down in the sandy matrix of coastal Minas Basin for some time. A severely reworked, beveled, scraping edge is present on the medial edge of the artifact, while the lateral and distal ends have been bifacially resharpened.



Figure 4.12: Dorsal and medial view of the quartz blade collected at MacKay Head.



Figure 4.13: Ventral and lateral view of the quartz blade collected at MacKay Head.

The base of the artifact appears to have been deliberately ground flat to accommodate hafting. A bevelled and ground edge exists on the medial edge at the proximal end of the object deliberately abraded to accommodate a haft, also suggested by the ground base, and length of the tang below the reworked beveled edge. Subtle notches indicate the location of the haft and/or lashing. These notches appear at the midpoint on the medial edge and at the base of bifacial resharpening on the lateral edge.

4.5 Discussion

Literature review, observation, and exploratory analyses demonstrate that retreat of the Laurentide Ice Sheet into Minas Basin is closely correlated temporally, and spatially with human activities appearing in the Minas Basin during the Terminal Pleistocene (Borns, Jr., 2011; Macdonald, 1965; Rosenmeier et al., 2012; Stea, 2011). The basin geometry of the bedrock within Minas Basin, and topographic lows likely acted as controls on the configuration of supraglacial meltwater channels on the retreating LSI in upper Bay of Fundy during a sustained period of increased meltwater flows beginning near 16.8 ka CalBP (Shaw et al., 2006). Three large meltwater channels have their confluence near the Minas Passage at Cape Split in a conceptual model of deglaciation for the Maritimes region at 16.8 ka calBP (Shaw et al., 2006). Increased volumes of meltwater would contribute to rapid back and down wasting of the Laurentide Ice Sheet into the Minas Basin from 16.8–14.2 ka CalBP, allowing topographical highs to act as controls for emergent topography and configuration of meltwater drainage patterns.

The increased rate of ice retreat during the period from 16.8–14.2 ka CalBP is further intensified by the increase in sea levels brought by Meltwater Pulse 1A at 14.6 ka CalBP rapidly increasing sea levels, allowing relocation of stranded ice blocks from Minas Basin to the outer Bay of Fundy, preserving the recessional moraines used to sequence the retreat of the ice sheet (Todd and Shaw, 2012). The glaciodeltaic and glaciomarine facies along the north side of the Minas Basin are not present on the south side, with the exception of at Delhaven along the Pereau River (Swift and Borns, 1967). The distribution of the deltaic facies suggests that the meltwater output from the Cobequid Mountains on the north of Minas Basin was larger than that of South Mountain. Seasonal expansion of sea ice at

the confluence of the three major meltwater channels into Minas Basin, promoting divergence of meltwater likely responsible for the successions of glaciolacustrine deposits in Southern Bight, just beyond the higher energy glaciodeltaic facies.

Paleoclimate data indicates that summer temperatures nearing the end of the most intense retreat of the LIS margin (15.5–14.2 ka CalBP) during late Pleistocene reached highs resembling modern temperatures at Greenland (Miller and Elias, 2000). During summer months, the paleoclimate is modelled as presenting a -5C to 0C difference from modern summer temperatures. This suggests that the warming environment during the late Pleistocene promoted ice-walled lake formation during marine emergence, and that many forms of peri-glacial lakes similar to those observed forming on the Greenland Ice Sheet followed (Chudley et al., 2019; Leeson et al., 2015). Remnants of these supraglacial lakes are visible in southwestern Minas Basin in lidar data as lacustrine deposits at topographic highs superimposed on the weakly fluted morainal landscape in Medford with an expected upward fining of material from the base up to the top (**Figure 4.14; Appendix C, Plate 28; Figure 4.9a**). The relict surficial features left by supraglacial lakes are called ice-walled lake plains (Allred et al., 2014).

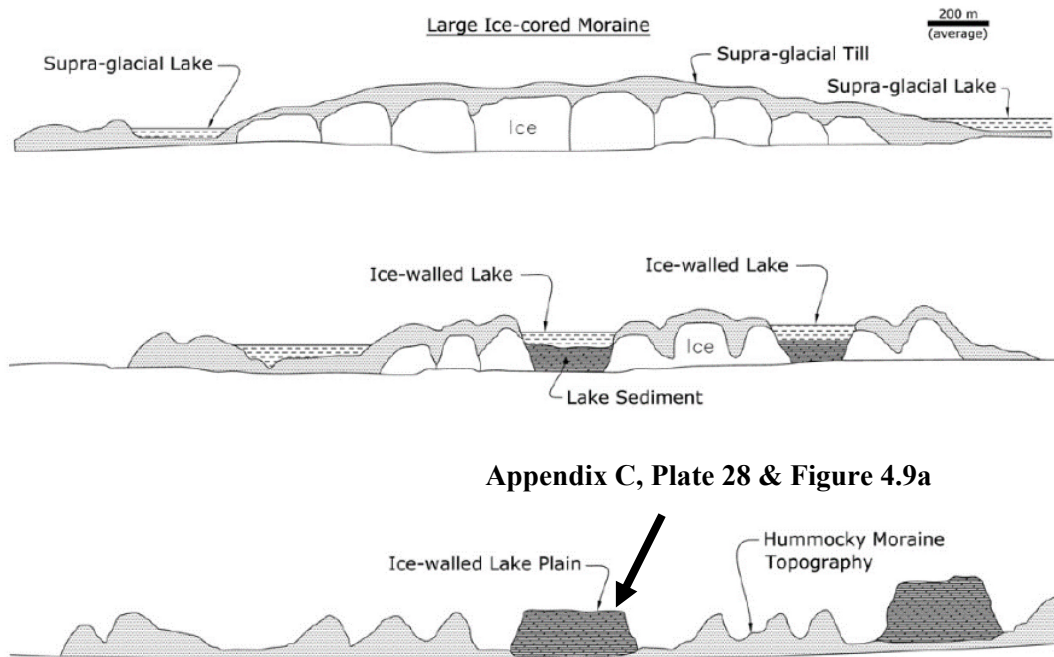


Figure 4.14: Conceptual model of landscape development on peri-glacial landscape at Medford. Modified from: Allred et al., 2014

The upward fining in ice-walled lake plain deposits is the product of the draining of the waterbody as the ice holding the water body melts. Heavier sediments fall to the lower sections of the deposit due to wave-action no longer relocating them to the shorelines. Smaller and lighter particles stay in suspension and are deposited with an inverse geometry of the lake bathymetry.

The isolated Debert/Vail style projectile point reported by George MacDonald in 1965 at Medford represents early human presence on the landscape of Minas Basin (Nash and Stewart, 1990). The location of the Medford site may represent a summer hunting camp close to the floe edge of retreating ice at the Laurentide Ice Sheet sometime after 14.9 ka calBP. The assumption being that the first inhabitants, who appear almost alongside the retreat of the Laurentide Ice Sheet, used similar seasonal resource allocation frameworks as modern arctic hunters.

4.5.1 Constraints on late Pleistocene coastal zone preservation

Huntington Point

The validation site at Huntington Point (**Appendix C, Plate 1**) is a plume shaped beach deposit with no obvious headland, rather it resembles a glacial outwash fan reworked by tides and wave action. At 1m resolution, the contour of marine emergence follows the geometry of relict beach ridges running parallel to the modern shoreline. The marine emergence contours of both models are located below (7.5-10m below) the highest visible escarpment from the beach, this is likely due to a combination of shoreline reworking since initial deposition, differential extents of wave-run up during varied paleoclimatic conditions, differential local glacial isostatic adjustments, and the resolution, accuracy, and completeness of the input paleotopographic database. Topographically, the late Pleistocene beach at Huntington Point exhibits what appear to be a regressive shoreline sequence expressed as a series of backshore beach ridges lowering in elevation. Backshore beach ridges should be oldest at the highest elevations, and youngest at elevations just above the modern marine limit. This lowering succession is likely indicative of the late Pleistocene lowering of RSL.

Scots Bay

The raised beach at Scots Bay resembles the crescent shape of the modern beach system below (**Appendix C, Plate 11-14**). A lowering succession of beach ridges visible at Scots Bay, like Huntington Point, indicate a falling RSL. However, the sequence at

Scots Bay has fewer backshore ridges, potentially suggesting an erosional environment. This raised beach system also exhibits an escarpment approximately 10m above the modelled shoreline. The raised beach at Scots Bay stratigraphically consists of “a cross bedded sand and red silt and horizontally laminated pebbly gravel” topping till (Taylor and Shaw, 2016, p. 7).

Kingsport

Kingsport validation site is located within the southwest Minas Basin south of North Mountain, unlike the previous three sites. This site holds terraces at 16m CGVD2013 noted as a marine limit by the Geologic Survey of Canada (Rivard et al., 2012; **Appendix C, Plate 32-34; Figure 4.9I**). This site also holds an escarpment at approximately 10m above the modelled shoreline. The escarpment above our modelled shoreline is interpreted as a Late Pleistocene period proglacial lake shoreline (Stea, 2011), but other interpretations can not be discounted. The lowering succession may also represent an early highstand marine shoreline following retreat of the Laurentide ice sheet (Rivard et al., 2012). There are beach ridges above and below the modelled shoreline at the south of the validation area (**Appendix C, Plate 35**). The sequence of these raised beach ridges in combination with the superimposition of terrace features suggest a regressive coastline indicative of lowering relative sea level during the late Pleistocene subsequently modified by the development of a glacial lake during the Younger Dryas period.

4.5.2 Landscape Geoarchaeology

Resulting from the discussion of the above section reveals that features representing a late Pleistocene falling relative sea level may be present in Minas Basin. Excluding those on what are interpreted as ice walled lake plains, these shoreline features exist at 15m elevation in the modelled paleotopographic surface. The earlier temporal limit of these features can be set between 14.9–14.2 ka calBP and a lowering succession of features suggests a marine regression may have occurred until the Younger Dryas period. Considering this interpretation, the landscape geoarchaeology of the lithics found at Medford and MacKay Head will be discussed in the following.

Medford

The discovery of a Debert/Vail type projectile point in 1920s by a farmhand lead to reporting of the find by John Erskine, exploratory trenching in 1965 by George MacDonald, excavation of 30 test pits measuring 50cm² to a depth of 50cm in 1988 under direction of Michael Deal, and a surficial survey of the area in 2020 in this project (Deal, 1991). Debert/Vail projectile point forms have been dated in contexts ranging from a maximum age of 13.3 ka CalBP to a minimum age of 10.6 ka CalBP (Lothrop et al., 2011). However, a regional study of the Early Paleoindian phase in the northeast indicates that biface forms related to the Early Paleoindian phase ended production around 12.2–12.1 ka CalBP (Lothrop et al., 2016).

Previous studies indicate that the Debert/Vail projectile point found at Medford may predate or be contemporary with the archaeological site complex in Debert and

Belmont. Medford became ice free just after 14.9 ka CalBP, permitting occupation in the area adjacent to the retreating floe edge of the Laurentide Ice Sheet. One interpretation considers that if the Debert/Vail projectile point at Medford were associated with the earliest populations making this style tool (~13.3 ka CalBP), the object would predate the occupations at Debert while being securely placed at the end of the supposed marine recession when the volume of late Pleistocene seasonal sea ice would be smallest. The implication here would be that families may have been using the floe edge of the ice sheet as a food acquisition landscape, like modern arctic hunters and that the Medford site lies upon a raised late Pleistocene marine coastline. Following the sea ice and landscape changes occurring during the late Pleistocene period and into the Younger Dryas provides a model for the continuation of people along the floe edge until establishing camp at Debert/Belmont for the remainder of the Younger Dryas.

A second interpretation considers post-glacial deformation of the landscape due to differential depths of ground-ice in the morainal landscape at Medford. The utilized core located in 2020 lies at an elevation lower than the reported projectile point, but these elevations may have once been more alike. The surficial glacial features at Medford appear to be a series of ice walled lake plains, not unlike pingos, left as topographical relief after permafrost differentially left the region. Differential depths of permafrost, as well as post-depositional site formation processes related to regressive coastal zones may have altered the landscape since the late Pleistocene. Differential depths of permafrost would produce differing rates and amounts of subsidence following deglaciation. The marine regression that occurred during this period would have pulled clasts along the waters edge lower and lower, as relative sea level dropped, artifacts present would surely be included here.

Aside from landscape, two attributes of the utilized core indicate that the object may be contemporary with, or from the same reduced material as the Debert/Vail style projectile point from Medford. The first is the type of material. Both objects are made of a reddish to purple material from North Mountain, with a circular section of white cortex-like material present. In the core, the white cortex-like section is present under flake scars, while the projectile point holds a circular section just above the midpoint (**Figure 4.6; Figure 4.10**). If these artifacts are produced by the same reduction process, then subsurface testing should produce more artifacts related to these objects. The second attribute of the utilized core indicating an Early Paleoindian age is the presence of a blade-like flake scar. These blade-like flakes are also referred to as burins. These types of flakes were present in the collection from the original Debert excavations by MacDonald and are generally indicative in this region of the Paleoindian period (Macdonald, 1965; **Figure 4.11b**).

A geomorphological interpretation of the heavily reworked Debert/Vail style projectile point reported from Medford and the utilized core located in 2020 is suggested by the distribution of these artifacts and surficial features. The position of the original find spot was at the top of a series of terraces (**Figure 4.9e**) and the core was located on a gently sloping smooth slope to the southeast. The location of the erosional terrace features in relation to the gently sloping location where the core was located suggests the feature is a depositional beach. If correct, this would indicate a clockwise circulation of sediments during the formation of these landforms.

MacKay Head

The artifact located at MacKay Head appears to be a manifestation of the final stages of marine regression following the Younger Dryas. The degree of resharpening, blade-like form, evidence of hafting, size, beveled edge, and basal grinding are suggestive of a Late Paleoindian phase date of manufacture. The object might best be considered as a curved knife or side scraper, with the most similar projectile morphology being Agate Basin, following Lothrop et al. (2016). During this period, if marine waters were present, the coastal geomorphology would be representative of a recessional, shallow water shoreline. A means to test this in the future would be to use Ground Penetrating Radar in combination with limited subsurface excavations to determine if modern transgressive facies overlie early Holocene recessional facies post-dating the marine limits set by the Five Islands Formation marine delta plain (Dalrymple and Choi, 2007; Stea, 2004; Wightman, 1980). Though the chance find of the blade at MacKay Head fits the modelled shoreline presented in the paleotopographic surface model, investigation of the source of this blade is limited by the scope of the current project. A tentative date range for this object can be placed between the early period of occupation in Minas Basin during the late Pleistocene and early Holocene transition but a relationship to more recent human activity up to Transitional Archaic period cannot be dismissed.

4.6 Conclusion

The paleotopographic surface model technique of analysis provides visualizations, that when used with lidar data can be leveraged to produce geomorphological interpretations that can help correct the modelled surface. As a tool for landscape

geoarchaeology, the surface model helps correlate surficial coastal features to isolated finds on the landscape. These data points are required to create geomorphological interpretations at scales relevant to archaeological analysis, and the above application has provided valuable information for relating the geomorphology to archaeology. The results of this initial exploration illustrate the need for an open-source database to be created to facilitate verification of, and iterative modelling of marine limits during deglaciation and at various timescales to support late Pleistocene landscape archaeology in the Minas Basin. Marine limit data and deglaciation data already exists and is published (Paradis et al., 2006; Shaw et al., 2014, 2006; Stea, 1988; Taylor, 2020; Taylor and Shaw, 2016; Todd and Shaw, 2012; Wightman, 1980), but has yet to be consolidated into a relative sea level specific database (e.g.: Vacchi et al., 2018).

Much work is still necessary on the landscape geoarchaeology of ice age humans in the Bay of Fundy to develop an understanding of their societies, culture, and subsistence strategies. This exploration of landscape geoarchaeology of Minas Basin provides baseline data for archaeologists to use when considering where people were during the late Pleistocene. The paleotopographic elevation model produces a productive digital baseline to identify the marine limit at the time of deglaciation, even with the caveat that the input data were not considered in a more precise context than as marine limits. The recent addition of lidar data to the remaining sections of Minas Basin and Bay of Fundy creates an opportunity for more directed exploratory, or systematic modelling to occur in the region, highlighting regions of heightened potential of holding late Pleistocene material culture to inform archaeological excavations.

Chapter 5 Conclusion

Modern technologies allow researchers to visualize, analyze, and ultimately interface with GIS, remote sensing data, and programmatic workflows in a manner not possible even a decade ago. Integration of increasingly large datasets from multiple technologies, and online open data repositories provide a ductile framework to investigate and share the results of regional landscape geoarchaeology studies within. This thesis works within this framework to present and share materials allowing conceptual models of coastal migration in the upper Bay of Fundy since deglaciation to be refined.

The objective of examining the dynamic coastal histories of upper Bay of Fundy was approached from a position sympathetic to the value of human observation in archaeology. In effect, the heuristic approaches presented here sidestep the prescription of a static spatial fix to the coast, emphasizing the value of modern remote sensing and visualization to inform human-scale observations and facilitate their remote production. It is this enrichment of human interaction with technology that helps field an answer to the research question of how effectively coastal histories in the upper Bay of Fundy can be narrated by integrating archaeological and ethnographic information using modern remote sensing and computer-assisted analyses?

Coastal histories can be narrated in a variety of manners, and the selective treatment of one or more aspects of natural and/or cultural histories will impact which details are emphasized. This thesis proposes that the most effective approach to narrating coastal histories by integrating archaeological and ethnographic information using modern remote sensing and computer-assisted analyses may currently be through the development of sub-regional conceptual models and heuristic tools guiding examination of the relationship of

people and the coast. The intention is to provide a set of tools guiding the development of more approaches to landscape geoarchaeology supplementing studies of relationships among archaeological sites and geomorphological systems.

The second chapter of this thesis provides an automated approach to deriving surface area from multiple artifacts in one image using computer vision using python. Here, the integration of technology and archaeology provides an approach that can be useful for examining geomorphological and archaeological questions. At a scale of individual objects, the automatically extracted surface area metric can be used as a measure of relative abundance studies of material culture as well as providing a means to derive how similarly shaped objects are to coastal beach shingles. This tool creates capacity for archaeologists to spend more time on activities requiring their direct intervention by reducing that spent on measurement.

The third chapter provides a method of integrating archaeological and ethnographic information using modern remote sensing and computer-assisted analyses at the coast through examination of the archaeological site of Oak Point in Minas Basin. An age-depth model written in python and available as an interactive online tool (**Appendix B**) calibrates radiocarbon dates, correlates elevation to the past limit of higher high water and provides an estimated date for input survey points. The limit of higher high water in the past is also combined with observations from archaeological survey and geomorphological research to develop geochronological boundaries for calibrated radiocarbon dates output from the online tool.

The final chapter examines late Pleistocene coastal history and landscape geoarchaeology of the Minas Basin using lidar data to model paleotopography through

marine limits. Visualizing high resolution lidar data in GIS and integrating it with regional literature detailing deglaciation guides the identification of surficial geomorphological features near the modelled marine limit. Identified relict geomorphological features are used in a landscape geoarchaeology exercise at Medford and MacKay Head to provide insights into how archaeological materials relate to the local geomorphology and suggest an interpretation of the coastal history at each. To promote utility, this chapter includes a large appendix (**Appendix C**) consisting of a series of 49 map plates to aid examination of raised, relict geomorphology and archaeology in Minas Basin.

As a student of landscape archaeology in Nova Scotia, coastal history has been a prominent theme in almost every research project I have had the pleasure of being involved in. The intention of this thesis is to provide a conceptual foundation that facilitates more detailed, refined studies of coastal histories in our region. The supplementary data provided has been deliberately amassed to support the objective of this thesis in providing information to help inform future landscape geoarchaeology and coastal history research in the Bay of Fundy and Minas Basin. It is certain that the integration of multiple datasets has enriched the discussion and interpretations provided within this thesis, and in sharing these processes I hope this data provides a similar benefit to other researchers.

Chapter 6 Bibliography

- “25 Cents Coins.” n.d. The Royal Canadian Mint. Accessed May 22, 2021.
<https://www.mint.ca/store/mint/about-the-mint/25-cents-5300010>.
- Allen, Patricia. 2005. “The Oxbow Site 1984 Metepenagiag Mi’kmaq First Nation Miramichi, New Brunswick.” *New Brunswick Manuscripts in Archaeology* 39. Fredericton, New Brunswick.
- Allen, Patricia Marlene. 1980. “The Oxbow Site : Chronology and Prehistory in Northeastern New Brunswick.” Masters, Memorial University of Newfoundland.
<https://research.library.mun.ca/7702/>.
- Allred, Kory, Wei Luo, Mike Konen, and B. Brandon Curry. 2014. “Morphometric Analysis of Ice-Walled Lake Plains in Northern Illinois: Implications of Lake Elongation by Wind-Induced Dual-Cycle Currents.” *Geomorphology* 220 (September): 50–57.
<https://doi.org/10.1016/j.geomorph.2014.05.022>.
- Amos, Carl L. 1978. “The Post Glacial Evolution of the Minas Basin, N.S.: A Sedimentological Interpretation.” *Journal of Sedimentary Petrology* 48 (3): 965–82.
- Andrefsky, William. 2005. *Lithics : Macroscopic Approaches to Analysis*. Vol. Second edition. Cambridge Manuals in Archaeology. Cambridge, UK: Cambridge University Press. <https://doi.org/10.1017/CBO9780511810244>.
- Black, David W. 2018. “...*Gathering Pebbles on a Boundless Shore...*” — *The Rum Beach Site and Intertidal Archaeology in the Canadian Quoddy Region*. Fredericton, New Brunswick: Department of Anthropology, University of New Brunswick.
- Borns, Jr., Harold W. 2011. “Overview of Palaeoecology/Palaeogeography of the Debert Palaeoindian Site, Debert, Nova Scotia.” In *Ta’n Wetapeski’k: Understanding From Where We Come. Proceedings of the 2005 Debert Research Workshop*, edited by Tim Bernard, Leah Morine Rosenmeier, and Sharon L. Farrell, 35–38. Debert, Nova Scotia, Canada: Eastern Woodland Print Communications.
- Bradski, G. 2000. “The OpenCV Library.” *Dr. Dobb’s Journal of Software Tools* 120: 122–25.

- Brown, Clifford T. 2001. "The Fractal Dimensions of Lithic Reduction." *Journal of Archaeological Science* 28 (6): 619–31. <https://doi.org/10.1006/jasc.2000.0602>.
- Byrd, John E., and Dalford D. Owens. 1997. "A Method for Measuring Relative Abundance of Fragmented Archaeological Ceramics." *Journal of Field Archaeology* 24 (3): 315–20. <https://doi.org/10.1179/009346997792208168>.
- Cadieux, Nicolas. 2013. "Size Matters: Measuring Debitage Area and Getting It Right with a Digital Scanner." *Lithic Technology* 38 (March): 46–70. <https://doi.org/10.1179/0197726113Z.00000000004>.
- Canny, J. 1986. "A Computational Approach to Edge Detection." *IEEE Transactions on Pattern Analysis and Machine Intelligence* 8 (6): 679–98. <https://doi.org/10.1109/TPAMI.1986.4767851>.
- Chudley, Thomas R., Poul Christoffersen, Samuel H. Doyle, Marion Bougamont, Charlotte M. Schoonman, Bryn Hubbard, and Mike R. James. 2019. "Supraglacial Lake Drainage at a Fast-Flowing Greenlandic Outlet Glacier." *Proceedings of the National Academy of Sciences* 116 (51): 25468–77. <https://doi.org/10.1073/pnas.1913685116>.
- Collins, M., R. Knutti, J. Arblaster, J.-L. Dufresne, T. Fichet, P. Friedlingstein, X. Gao, et al. 2013. "Long-Term Climate Change: Projections, Commitments and Irreversibility." In *Climate Change 2013: The Physical Science Basis. Contribution of Working Group I to the Fifth Assessment Report of the Intergovernmental Panel on Climate Change*, edited by T. F. Stocker, D. Qin, G.-K. Plattner, M. Tignor, S. K. Allen, J. Doschung, A. Nauels, Y. Xia, V. Bex, and P. M. Midgley, 1029–1136. Cambridge, UK: Cambridge University Press. <https://doi.org/10.1017/CBO9781107415324.024>.
- Contreras, Daniel A. 2009. "Reconstructing an Engineered Environment in the Central Andes: Landscape Geoarchaeology at Chavín de Huántar, Peru." In *The Archaeology of Anthropogenic Environments*, edited by Rebecca M. Dean. Center for Archaeological Investigations, Occasional Paper, No. 37. Board of Trustees, Southern Illinois University. <https://citeseerx.ist.psu.edu/viewdoc/download?doi=10.1.1.938.6003&rep=rep1&type=pdf>.

- . 2017. “(Re)Constructing the Sacred: Landscape Geoarchaeology at Chavín de Huántar, Peru.” *Archaeological and Anthropological Sciences* 9 (6): 1045–57. <https://doi.org/10.1007/s12520-014-0207-2>.
- Conyers, Lawrence B. 2018. *Ground-Penetrating Radar and Magnetometry for Buried Landscape Analysis*. SpringerBriefs in Geography. Springer International Publishing. <https://www.springer.com/gp/book/9783319708898>.
- Conyers, L.B. 2016. *Ground-Penetrating Radar for Geoarchaeology*. <https://doi.org/10.1002/9781118949993>.
- Costa, Stefano, Mario Gutiérrez-Roig, and Wesley Weatherbee. 2021. *IOSACal* (version 0.4.2). Python 3. <https://codeberg.org/steko/iosacal>.
- “Council of War.” n.d. In *Cambridge English Dictionary*. Cambridge University Press. Accessed September 23, 2020. <https://dictionary.cambridge.org/dictionary/english/council-of-war>.
- Dalrymple, R. W., C. L. Amos, and G. Yeo. 1992. “Nature and Evolution of the Tidal Sedimentation in the Minas Basin — Cobequid Bay Area, Bay of Fundy.” In *Guidebook. Geological Association of Canada, Annual Meeting, Wolfville, Trip A-8*.
- Dalrymple, Robert W., and Kyungsik Choi. 2007. “Morphologic and Facies Trends through the Fluvial–Marine Transition in Tide-Dominated Depositional Systems: A Schematic Framework for Environmental and Sequence-Stratigraphic Interpretation.” *Earth-Science Reviews* 81 (3): 135–74. <https://doi.org/10.1016/j.earscirev.2006.10.002>.
- Dalrymple, Robert W., and Brian A. Zaitlin. 1994. “High-resolution Sequence Stratigraphy of a Complex, Incised Valley Succession, Cobequid Bay — Salmon River Estuary, Bay of Fundy, Canada.” *Sedimentology* 41 (6): 1069–91. <https://doi.org/10.1111/j.1365-3091.1994.tb01442.x>.
- Dalton, April S., Martin Margold, Chris R. Stokes, Lev Tarasov, Arthur S. Dyke, Roberta S. Adams, Serge Allard, et al. 2020. “An Updated Radiocarbon-Based Ice Margin Chronology for the Last Deglaciation of the North American Ice Sheet Complex.” *Quaternary Science Reviews* 234 (April): 106223. <https://doi.org/10.1016/j.quascirev.2020.106223>.

- Davidson-Arnott, R., Bernard Bauer, and Chris 1974- Houser. 2019. *Introduction to Coastal Processes and Geomorphology*. Second edition. Cambridge, United Kingdom ; Cambridge University Press.
- Davis, Stephen A. 1980. "Coastal Erosion, Neglect, Disinterest Threatening Maritime Archaeology and Resources." In *Proceedings of the 1980 Conference on the Future of Archaeology in the Maritime Provinces*, 8:6–17. Halifax, Nova Scotia: Department of Anthropology, Saint Mary's University.
- Deal, Michael. 1991. "Collected Papers of the Western Minas Basin Project, 1988-1990." Halifax, Nova Scotia: Nova Scotia Museum.
- . 2015. *The Collection of Ages: A Prehistory of the Maritime Provinces*. Department of Archaeology, Memorial University of Newfoundland: Printing Services, Memorial University, St. John's.
- Dupuis, Martin, Antoine Leboeuf, Éric Vaillancourt, and Dominique Lachance. 2018. "A Guide to Surface Deposit and Borrow Pit Identification Using LiDAR." Secteur des forêts. Direction Des Inventaires Forestiers. Quebec: Ministère des Forêts, de la Faune et des Parcs. Bibliothèque et archives nationales du Québec 2018.
- Dyke, A.S., A. Moore, and L. Robertson. 2003. "Deglaciation of North America." Open File 5541. Geological Survey of Canada. Natural Resources Canada. GEOSCAN. <https://doi.org/10.4095/224887>.
- Eaton, Arthur Wentworth Hamilton. 1910. *The History of Kings County, Nova Scotia, Heart of the Acadian Land, Giving ...* The Salem Press Company. <http://archive.org/details/historykingscou00eatogooq>.
- Erskine, John S. 1960. "Shell-Heap Archaeology of Southwestern Nova Scotia." In *Proceedings of the Nova Scotia Institute of Science*, 24:339–75. Halifax, Nova Scotia: Nova Scotia Institute of Science.
- ESRI Inc. 2020. *ArcGIS Pro* (version 2.7.0). Environmental Systems Research Institute Incorporated. <https://www.esri.com/en-us/arcgis/products/arcgis-pro/>.

- Fader, Gordon. 2005a. “Glacial, Post Glacial, Present and Projected Sea Levels, Bay of Fundy.” Manuscript Report. Atlantic Marine Geological Consulting.
<https://novascotia.ca/nse/ea/whitespointquarry/09.Reference.Documents/17.Fader.GLACIAL.Sea.Level.Change.pdf>.
- . 2005b. “Marine Archaeology Offshore Digby Neck, Bay of Fundy.” Manuscript Report. Atlantic Marine Geological Consulting.
<https://novascotia.ca/nse/ea/whitespointquarry/09.Reference.Documents/14.Fader.Marine.Archaeology.pdf>.
- Fowler, Jonathan, and Wesley Weatherbee. 2020. “Grand-Pré Marsh (NS008) Phase 1 Archaeological Resource Impact Assessment.” Manuscript Report CBWES Report No. 33. Halifax, Nova Scotia: Nova Scotia Museum.
- Gehrels, W. Roland. 1994. “Determining Relative Sea-Level Change from Salt-Marsh Foraminifera and Plant Zones on the Coast of Maine, U.S.A.” *Journal of Coastal Research* 10 (4): 990–1009.
- Gilpin, J. Bernard (John Bernard). 1873. “On the Stone Age of Nova Scotia.” *Nova Scotian Institute of Science*. <https://DalSpace.library.dal.ca/handle/10222/11296>.
- Government of Canada, Agriculture and Agri-Food Canada. n.d. “Canadian Soil Information Service.” Accessed February 25, 2021. <https://sis.agr.gc.ca/cansis/>.
- Harris, Charles R., K. Jarrod Millman, Stéfan J van der Walt, Ralf Gommers, Pauli Virtanen, David Cournapeau, Eric Wieser, et al. 2020. “Array Programming with NumPy.” *Nature* 585: 357–62. <https://doi.org/10.1038/s41586-020-2649-2>.
- Hayward, Bruce, B.W., Le Coze, François, F., Vachard, Daniel, D., and Gross, Onno, O. 2020. “World Foraminifera Database.” *World Foraminifera Database*.
<https://doi.org/10.14284/305>.
- Heaton, Timothy J., Peter Köhler, Martin Butzin, Edouard Bard, Ron W. Reimer, William E. N. Austin, Christopher Bronk Ramsey, et al. 2020. “MARINE20—THE MARINE RADIOCARBON AGE CALIBRATION CURVE (0–55,000 CAL BP).” *Radiocarbon* 00 (00): 1–42. <https://doi.org/10.1017/RDC.2020.68>.

- Heteren, Sytze, Duncan FitzGerald, Paul Mckinlay, and Ilya Buynevich. 2002. "Radar Facies of Paraglacial Barrier Systems: Coastal New England, USA." *Sedimentology* 45 (January): 181–200. <https://doi.org/10.1046/j.1365-3091.1998.00150.x>.
- Himmelstoss, Emily A., Rachel E. Henderson, Meredith G. Kratzmann, and Amy S. Farris. 2018. "Digital Shoreline Analysis System (DSAS) Version 5.0 User Guide." USGS Numbered Series 2018–1179. *Digital Shoreline Analysis System (DSAS) Version 5.0 User Guide*. Vol. 2018–1179. Open-File Report. Reston, VA: U.S. Geological Survey. <https://doi.org/10.3133/ofr20181179>.
- Holliday, Vance T. 2009. "Geoarchaeology and the Search for the First Americans." *CATENA*, Developments in International Geoarchaeology, 78 (3): 310–22. <https://doi.org/10.1016/j.catena.2009.02.014>.
- Holliday, Vance T., Allison Harvey, Matthew T. Cuba, and Aimee M. Weber. 2019. "Paleoindians, Paleolakes and Paleoplayas: Landscape Geoarchaeology of the Tularosa Basin, New Mexico." *Geomorphology*, Human Geomorphological Interactions and the Legacy of Karl Butzer, 331 (April): 92–106. <https://doi.org/10.1016/j.geomorph.2018.08.012>.
- Hughes, Zoe J. 2012. "Tidal Channels on Tidal Flats and Marshes." In *Principles of Tidal Sedimentology*, edited by Richard A. Davis Jr. and Robert W. Dalrymple, 269–300. Dordrecht: Springer Netherlands. https://doi.org/10.1007/978-94-007-0123-6_11.
- Hunter, John D. 2007. "Matplotlib: A 2D Graphics Environment." *Computing in Science Engineering* 9 (3): 90–95. <https://doi.org/10.1109/MCSE.2007.55>.
- James, T. S., J. A. Henton, L. J. Leonard, A. Darlington, D. L. Forbes, and M. Craymer. 2014. "Relative Sea Level Rise Projections for Canada and the Adjacent Mainland United States." Open File 7377. Geological Survey of Canada.
- Kluyver, Thomas, Benjamin Ragan-Kelley, Fernando Pérez, Brian Granger, Matthias Bussonnier, Jonathan Frederic, Kyle Kelley, et al. 2016. "Jupyter Notebooks – a Publishing Format for Reproducible Computational Workflows." In *Positioning and Power in Academic Publishing: Players, Agents and Agendas*, edited by Fernando

- Loizides and Birgit Schmidt, 87–90. IOS Press. <https://doi.org/10.3233/978-1-61499-649-1-87>.
- Kvamme, Kenneth L. 1988. “A Simple Graphic Approach And Poor Man’s Clustering Technique For Investigating Surface Lithic Scatter Types.” *Plains Anthropologist* 33 (121): 385–94. <https://doi.org/10.1080/2052546.1988.11909418>.
- . 1997. “Patterns and Models of Debitage Dispersal in Percussion Flaking.” *Lithic Technology* 22 (2): 122–38. <https://doi.org/10.1080/01977261.1997.11754538>.
- . 1998. “Spatial Structure in Mass Debitage Scatters.” In *Surface Archaeology*, edited by A.P. Sullivan, 127–41. University of New Mexico Press, New Mexico. https://bcourses.berkeley.edu/files/54824839/download?download_frd=1.
- Land, Isacc. 2007. “Tidal Waves: The New Coastal History.” *Journal of Social History* 40 (3): 731–43. <https://doi.org/10.1353/jsh.2007.0051>.
- Lausanne, Alex L., Daryl W. Fedje, Quentin Mackie, and Ian J. Walker. 2019. “Identifying Sites of High Geoarchaeological Potential Using Aerial LIDAR and GIS on Quadra Island, Canada.” *The Journal of Island and Coastal Archaeology* 0 (0): 1–27. <https://doi.org/10.1080/15564894.2019.1659884>.
- Leeson, A. A., A. Shepherd, K. Briggs, I. Howat, X. Fettweis, M. Morlighem, and E. Rignot. 2015. “Supraglacial Lakes on the Greenland Ice Sheet Advance Inland under Warming Climate.” *Nature Climate Change* 5 (1): 51–55. <https://doi.org/10.1038/nclimate2463>.
- Leverington, David W., James T. Teller, and Jason D. Mann. 2002. “A GIS Method for Reconstruction of Late Quaternary Landscapes from Isobase Data and Modern Topography.” *Computers & Geosciences* 28 (5): 631–39. [https://doi.org/10.1016/S0098-3004\(01\)00097-8](https://doi.org/10.1016/S0098-3004(01)00097-8).
- Lewis, Paul H., and K. J. Goodson. 1990. “Images, Databases and Edge Detection for Archaeological Object Drawings.” *Computer Applications and Quantitative Methods in Archaeology*, 149.
- Lin, Yucheng, Fiona D. Hibbert, Pippa L. Whitehouse, Sarah A. Woodroffe, Anthony Purcell, Ian Shennan, and Sarah L. Bradley. 2021. “A Reconciled Solution of Meltwater Pulse 1A

- Sources Using Sea-Level Fingerprinting.” *Nature Communications* 12 (1): 2015.
<https://doi.org/10.1038/s41467-021-21990-y>.
- Lothrop, Jonathan C., Darrin L. Lowery, Arthur E. Spiess, and Christopher J. Ellis. 2016.
“Early Human Settlement of Northeastern North America.” *PaleoAmerica* 2 (3): 192–
251. <https://doi.org/10.1080/20555563.2016.1212178>.
- Lothrop, Jonathan C., Paige E. Newby, Arthur E. Spiess, and James W. Bradley. 2011.
“Paleoindians and the Younger Dryas in the New England-Maritimes Region.”
Quaternary International, HUMANS AND YOUNGER DRYAS: DEAD END, SHORT
DETOUR, OR OPEN ROAD TO THE HOLOCENE?, 242 (2): 546–69.
<https://doi.org/10.1016/j.quaint.2011.04.015>.
- Macdonald, George. 1965. *Debert: A Paleo-Indian Site in Nova Scotia*. Persimmon Press.
- Mackie, Quentin. 2001. *Settlement Archaeology in a Fjordland Archipelago: Network
Analysis, Social Practice and the Built Environment of Western Vancouver Island, British
Columbia, Canada since 2,000 BP: Network Analysis, Social Practice and the Built
Environment of Western Vancouver Island, British Columbia, Canada since 2,000 BP*.
BAR International Series 926. Oxford, UK: Archaeopress.
<https://doi.org/10.30861/9781841711713>.
- Mackie, Quentin, Daryl Fedje, and Duncan McLaren. 2018. “Archaeology and Sea Level
Change on the British Columbia Coast.” *Canadian Journal of Archaeology* 42 (1): 74–
91.
- Marriner, Nick, Christophe Morhange, Marcelle Boudagher-Fadel, Michel Bourcier, and
Pierre Carbonel. 2005. “Geoarchaeology of Tyre’s Ancient Northern Harbour,
Phoenicia.” *Journal of Archaeological Science* 32 (9): 1302–27.
<https://doi.org/10.1016/j.jas.2005.03.019>.
- McKinney, Wes. 2010. “Data Structures for Statistical Computing in Python.” *Proceedings of
the 9th Python in Science Conference*, 56–61. [https://doi.org/10.25080/Majora-92bf1922-
00a](https://doi.org/10.25080/Majora-92bf1922-00a).

- McLaren, Duncan, Andrew Martindale, Daryl Fedje, and Quentin Mackie. 2011. "Relict Shorelines and Shell Middens of the Dundas Island Archipelago." *Canadian Journal of Archaeology* 35 (1): 86–116.
- McPherron, Shannon P., and Harold L. Dibble. 1999. "Stone Tool Analysis Using Digitized Images: Examples from the Lower and Middle Paleolithic." *Lithic Technology* 24 (1): 38–52. <https://doi.org/10.1080/01977261.1999.11720944>.
- "Mi'kmaw Place Names Digital Atlas." 2020. Ta'n Weji-Sqalia'tiek. 2020. <https://www.mapdev.ca/placenames/>.
- Miller, Randall F., and Scott A. Elias. 2000. "Late-Glacial Climate in the Maritimes Region, Canada, Reconstructed from Mutual Climatic Range Analysis of Fossil Coleoptera." *Boreas* 29 (1): 79–88. <https://doi.org/10.1111/j.1502-3885.2000.tb01202.x>.
- Minár, Jozef, Ian S. Evans, and Marián Jenčo. 2020. "A Comprehensive System of Definitions of Land Surface (Topographic) Curvatures, with Implications for Their Application in Geoscience Modelling and Prediction." *Earth-Science Reviews* 211 (December): 103414. <https://doi.org/10.1016/j.earscirev.2020.103414>.
- Murray-Wallace, Colin V., and C. D. Woodroffe. 2014. "Palaeo-Sea-Level Indicators." In *Quaternary Sea-Level Changes : A Global Perspective*. Cambridge University Press. <https://web-b-ebshost-com.library.smu.ca/ehost/ebookviewer/ebook/ZTAwMHhuYV9fNjk2Mjk4X19BTg2?sid=0bc1283f-37cf-4cb4-9007-bc460d267735%40sessionmgr103&vid=0&format=EB&rid=1>.
- Nash, Ronald J., and Frances L. Stewart. 1990. "Melanson: A Large Micmac Village in Kings County, Nova Scotia." <https://ojs.library.dal.ca/NSM/article/view/4062>.
- Neal, A., and C. L. Roberts. 2000. "Applications of Ground-Penetrating Radar (GPR) to Sedimentological, Geomorphological and Geoarchaeological Studies in Coastal Environments." In *Coastal and Estuarine Environments: Sedimentology, Geomorphology, and Geoarchaeology*, edited by K Pye and J. R. L. Allen, 139–72. Special Publications 175. London: Geological Society.

- Neal, Adrian. 2004. "Ground-Penetrating Radar and Its Use in Sedimentology: Principles, Problems and Progress." *Earth-Science Reviews* 66 (August): 261–330.
<https://doi.org/10.1016/j.earscirev.2004.01.004>.
- O'Reilly, C.T., R. Solvason, and C. Solomon. 2005. "Where Are the World's Largest Tides?" In *Bedford Institute of Oceanography: 2004 in Review.*, edited by J. Ryan, 44–46. Dartmouth, NS; Ottawa: Fisheries & Oceans Canada, Bedford Institute of Oceanography ; Natural Resources Canada.
- Paradis, S. J., A. M. Bouldac, and R. R. Stea. 2006. "Surficial Geology, Annapolis Valley, Nova Scotia." Open File 5276. Geological Society of Canada.
- Pico, T., J. X. Mitrovica, and A. C. Mix. n.d. "Sea Level Fingerprinting of the Bering Strait Flooding History Detects the Source of the Younger Dryas Climate Event." *Science Advances* 6 (9): eaay2935. <https://doi.org/10.1126/sciadv.aay2935>.
- . n.d. "Sea Level Fingerprinting of the Bering Strait Flooding History Detects the Source of the Younger Dryas Climate Event." *Science Advances* 6 (9): eaay2935. <https://doi.org/10.1126/sciadv.aay2935>.
- Piers, Harry. 2003. *Harry Piers Ethnology Papers*. Edited by Ruth Whitehead. Vol. Volume 3. Halifax, NS: Nova Scotia Museum. <http://library2.smu.ca/xmlui/handle/01/28117>.
- Pint, Anna, Martin Seeliger, Peter Frenzel, Stefan Feuser, Ercan Erkul, Christopher Berndt, Christina Klein, Felix Pirson, and Helmut Brückner. 2015. "The Environs of Elaia's Ancient Open Harbour – a Reconstruction Based on Microfaunal Evidence." *Journal of Archaeological Science* 54 (February): 340–55. <https://doi.org/10.1016/j.jas.2014.06.011>.
- Pote, William, J. F. (John Fletcher) Hurst, and Charles Morris. 1896. *The Journal of Captain William Pote, Jr., during His Captivity in the French and Indian War from May, 1745, to August, 1747*. New York : Dodd, Mead & Co.
<http://archive.org/details/journalofcaptain00pote>.
- Quinn, Patrick Sean. 2008. "The Occurrence and Research Potential of Microfossils in Inorganic Archaeological Materials." *Geoarchaeology* 23 (2): 275–91.
<https://doi.org/10.1002/gea.20213>.

- Ramsey, C. Bronk. 2008. "Radiocarbon Dating: Revolutions in Understanding*." *Archaeometry* 50 (2): 249–75. <https://doi.org/10.1111/j.1475-4754.2008.00394.x>.
- Ramsey, Christopher Bronk. 1995. "Radiocarbon Calibration and Analysis of Stratigraphy: The OxCal Program." *Radiocarbon* 37 (2): 425–30. <https://doi.org/10.1017/S0033822200030903>.
- . 2001. "Development of the Radiocarbon Calibration Program." *Radiocarbon* 43 (2A): 355–63. <https://doi.org/10.1017/S0033822200038212>.
- Rand, Silas Tertius. 1902. *Rand's Micmac Dictionary from Phonographic Word-Lists*. Charlottetown: Patriot Publishing. <https://www.islandlives.ca/islandora/object/ilives%3A230896#page/1/mode/2up>.
- Rand, Silas Tertius, and Helen L. (Helen Livermore) Webster. 1894. *Legends of the Micmacs*. New York; London : Longmans, Green. http://archive.org/details/cihm_12305.
- Reimer, P. J., and R. W. Reimer. 2001. "A Marine Reservoir Correction Database and On-Line Interface." *Radiocarbon* 43 (2A): 461–63. <https://doi.org/10.1017/S0033822200038339>.
- Reimer, Paula J., William E. N. Austin, Edouard Bard, Alex Bayliss, Paul G. Blackwell, Christopher Bronk Ramsey, Martin Butzin, et al. 2020. "The IntCal20 Northern Hemisphere Radiocarbon Age Calibration Curve (0–55 Cal KBP)." *Radiocarbon* 62 (4): 725–57. <https://doi.org/10.1017/RDC.2020.41>.
- Reinig, Frederick, Adam Sookdeo, Jan Esper, Michael Friedrich, Giulia Guidobaldi, Gerhard Helle, Bernd Kromer, et al. 2020. "Illuminating Intcal During the Younger Dryas." *Radiocarbon* 62 (4): 883–89. <https://doi.org/10.1017/RDC.2020.15>.
- Riquelme, Francisco, Jesús Alvarado-Ortega, Martha Cuevas-García, José Luis Ruvalcaba-Sil, and Carlos Linares-López. 2012. "Calcareous Fossil Inclusions and Rock-Source of Maya Lime Plaster from the Temple of the Inscriptions, Palenque, Mexico." *Journal of Archaeological Science* 39 (3): 624–39. <https://doi.org/10.1016/j.jas.2011.10.022>.
- Rivard, C., Deblonde C., Boivin R., Bolduc A., Paradis S. J., Paradis D., Liao S., et al. 2007. "Canadian Groundwater Inventory: Hydrogeological Atlas of the Annapolis Valley, Nova

- Scotia.” Open File 5541. Geological Survey of Canada. Natural Resources Canada. GEOSCAN. <https://doi.org/10.4095/224887>.
- Rivard, C., D. Paradis, S. J. Paradis, A. M. Bouldac, A. Blackmore, I. Spooner, C. Deblonde, et al. 2012. “Canadian Groundwater Inventory: Regional Hydrogeological Characterization of the Annapolis Valley Aquifers.” Bulletin 598 5541. Geological Survey of Canada. Natural Resources Canada. GEOSCAN. <https://doi.org/10.4095/224887>.
- Robin, Catherine, Shannon Nudds, Phillip MacAulay, André Godin, Bodo De Lange Boom, and Jason Bartlett. 2016. “Hydrographic Vertical Separation Surfaces (HyVSEPs) for the Tidal Waters of Canada.” *Marine Geodesy* 39 (2): 195–222. <https://doi.org/10.1080/01490419.2016.1160011>.
- Robin, Nicolas, Franck Levoy, Edward J. Anthony, and Olivier Monfort. 2020. “Sand Spit Dynamics in a Large Tidal-Range Environment: Insight from Multiple LiDAR, UAV and Hydrodynamic Measurements on Multiple Spit Hook Development, Breaching, Reconstruction, and Shoreline Changes.” *Earth Surface Processes and Landforms* 45 (11): 2706–26. <https://doi.org/10.1002/esp.4924>.
- Rosebrock, Adrian. 2015a. “My Imutils Package: A Series of OpenCV Convenience Functions.” *PyImageSearch* (blog). 2015. <https://www.pyimagesearch.com/2015/02/02/just-open-sourced-personal-imutils-package-series-opencv-convenience-functions/>.
- . 2015b. “Zero-Parameter, Automatic Canny Edge Detection with Python and OpenCV.” *PyImageSearch* (blog). 2015. <https://www.pyimagesearch.com/2015/04/06/zero-parameter-automatic-canny-edge-detection-with-python-and-opencv/>.
- . 2016. “Measuring Size of Objects in an Image with OpenCV.” *PyImageSearch* (blog). March 28, 2016. <https://www.pyimagesearch.com/2016/03/28/measuring-size-of-objects-in-an-image-with-opencv/>.
- Rosendahl, Daniel, Sean Ulm, and Marshall I. Weisler. 2007. “Using Foraminifera to Distinguish between Natural and Cultural Shell Deposits in Coastal Eastern Australia.”

- Journal of Archaeological Science* 34 (10): 1584–93.
<https://doi.org/10.1016/j.jas.2006.11.013>.
- Rosenmeier, Leah Morine, Scott Buchanan, Ralph Stea, and Gordon Brewster. 2012. “New Sites and Lingering Questions at the Debert and Belmont Sites, Nova Scotia.” In *Late Pleistocene Archaeology & Ecology in the Far Northeast*, edited by Claude Chapdelaine, 1st ed., 113–34. College Station: Texas A&M University Press.
- Rutherford, Douglas. 1990. “Reconsidering the Middlesex Burial Phase in the Maine-Maritimes Region.” *Canadian Journal of Archaeology/Journal Canadien D'Archéologie* 14: 169–81.
- Sable, Trudy. 2011. “Legends as Maps.” In *Ta’n Wetapeski’k: Understanding From Where We Come. Proceedings of the 2005 Debert Research Workshop*, edited by Tim Bernard, Leah Morine Rosenmeier, and Sharon L. Farrell, 157–72. Debert, Nova Scotia, Canada: Eastern Woodland Print Communications.
- Scott, D. B. 1977. “Distributions and Population Dynamics of Marsh-Estuarine Foraminifera with Applications to Relocating Holocene Sea-Level.” Ph.D., Halifax, Nova Scotia: Dalhousie University. <https://DalSpace.library.dal.ca/handle/10222/75098>.
- Scott, D. B., K. Brown, E. S. Collins, and F. S. Medioli. 1995. “A New Sea-Level Curve from Nova Scotia: Evidence for a Rapid Acceleration of Sea-Level Rise in the Late Mid-Holocene.” *Canadian Journal of Earth Sciences* 32 (12): 2071–80.
<https://doi.org/10.1139/e95-160>.
- Scott, D. B., and David A. Greenberg. 1983. “Relative Sea-Level Rise and Tidal Development in the Fundy Tidal System.” *Canadian Journal of Earth Sciences* 20 (10): 1554–64.
<https://doi.org/10.1139/e83-145>.
- Scott, D. B., and F. S. Medioli. 1978. “Vertical Zonations of Marsh Foraminifera as Accurate Indicators of Former Sea-Levels.” *Nature* 272 (5653): 528–31.
<https://doi.org/10.1038/272528a0>.
- Scott, D. B., and F. S. Medioli. 1980. “Quantitative Studies of Marsh Foraminiferal Distributions in Nova Scotia: Implications for Sea Level Studies.” *Cushman Foundation for Foraminiferal Research Special Publication No. 17*, 57.

- Scott, D. B., and F. S. Medioli. 1986. "Foraminifera as Sea-Level Indicators." In *Sea-Level Research: A Manual for the Collection and Evaluation of Data*, edited by Orson van de Plassche, 435–56. Dordrecht: Springer Netherlands. https://doi.org/10.1007/978-94-009-4215-8_15.
- Sensors & Software Inc. 2018. *EKKO_Project* (version 5.3). Mississauga, Ontario: Sensors & Software Incorporated. <https://www.sensoft.ca/products/ekko-project>.
- Shan, Xin, Xinghe Yu, Peter D. Clift, Chengpeng Tan, Shunli Li, Zhixing Wang, and Dongxu Su. 2016. "Ground-Penetrating Radar Study of Beach-Ridge Deposits in Huangqihai Lake, North China: The Imprint of Washover Processes." *Frontiers of Earth Science* 10 (1): 183–94. <https://doi.org/10.1007/s11707-015-0501-z>.
- Shaw, J, P Gareau, and R Courtney. 2002. "Palaeogeography of Atlantic Canada 13–0kyr." *Quaternary Science Reviews* 21 (16–17): 1861–78. [https://doi.org/10.1016/S0277-3791\(02\)00004-5](https://doi.org/10.1016/S0277-3791(02)00004-5).
- Shaw, J., D. J. W. Piper, G. B. J. Fader, E. L. King, B. J. Todd, T. Bell, M. J. Batterson, and D. G. E. Liverman. 2006. "A Conceptual Model of the Deglaciation of Atlantic Canada." *Quaternary Science Reviews* 25 (17): 2059–81. <https://doi.org/10.1016/j.quascirev.2006.03.002>.
- Shaw, John, Carl L. Amos, David A. Greenberg, Charles T. O'Reilly, D. Russell Parrott, and Eric Patton. 2010. "Catastrophic Tidal Expansion in the Bay of Fundy, Canada." *Canadian Journal of Earth Sciences* 47 (8): 1079–91. <https://doi.org/10.1139/E10-046>.
- Shaw, John, Brian J. Todd, and Michael Z. Li. 2014. "Geologic Insights from Multibeam Bathymetry and Seascapes Maps of the Bay of Fundy, Canada." *Continental Shelf Research, Geoscience and Habitat Mapping for Marine Renewable Energy*, 83 (July): 53–63. <https://doi.org/10.1016/j.csr.2013.12.015>.
- Simonsen, B. O. 1978. "Attrition of Coastal Archaeological Resources in the Maritime Provinces of Canada." 2. Reports in Archaeology. Halifax, NS: Council of Maritime Premiers.

- . 1979. “Attrition of Coastal Archaeological Resources in the Maritime Provinces of Canada: A Management Study.” 3. Reports in Archaeology. Halifax, NS: Council of Maritime Premiers.
- Smith, D.A., D. S. Scott, and F. S. Medioli. 1984. “Marsh Foraminifera in the Bay of Fundy: Modern Distribution and Application to Sea-Level Determinations.” *Maritime Sediments and Atlantic Geology*, Publication No. 17, Centre for Marine Geology, Dalhousie University, 20: 127–42.
- Smith, Harlan I., and W. J. Wintenburg. 1929. “The Archaeology of Merigomish Harbour, Nova Scotia.” In *Some Shell-Heaps in Nova Scotia*, Facsimile Edition (1973), Bulliten No. 47:1–104. Anthropological Series 9. National Museum of Man, Ottawa, Ontario: F. A. Acland.
- Stea, R. R. 1988. “Holocene Sea Levels, Paleoceanography, and Late Glacial Ice Configuration near the Northumberland Strait, Maritime Provinces: Discussion.” *Canadian Journal of Earth Sciences* 25 (2): 348–50. <https://doi.org/10.1139/e88-035>.
- Stea, Rudolph R. 2004. “The Appalachian Glacier Complex in Maritime Canada.” In *Developments in Quaternary Sciences*, edited by J. Ehlers and P. L. Gibbard, 2:213–32. Quaternary Glaciations-Extent and Chronology. Elsevier. [https://doi.org/10.1016/S1571-0866\(04\)80199-4](https://doi.org/10.1016/S1571-0866(04)80199-4).
- Stea, Rudolph R., and Robert J. Mott. 1989. “Deglaciation Environments and Evidence for Glaciers of Younger Dryas Age in Nova Scotia, Canada.” *Boreas* 18 (2): 169–87. <https://doi.org/10.1111/j.1502-3885.1989.tb00388.x>.
- . 2002. “DEGLACIATION OF NOVA SCOTIA: STRATIGRAPHY AND CHRONOLOGY OF LAKE SEDIMENT CORES AND BURIED ORGANIC SECTIONS.” <https://doi.org/10.7202/004871ar>.
- . 2005. “Younger Dryas Glacial Advance in the Southern Gulf of St. Lawrence, Canada: Analogue for Ice Inception?” *Boreas* 34 (3): 345–62. <https://doi.org/10.1111/j.1502-3885.2005.tb01106.x>.
- Stea, Rudolph (Ralph). 2011. “Geology and Palaeoenvironmental Reconstruction of the Debert-Belmont Site.” In *Ta’n Wetapesksi’k: Understanding From Where We Come*.

- Proceedings of the 2005 Debert Research Workshop*, edited by Tim Bernard, Leah Morine Rosenmeier, and Sharon L. Farrell, 55–76. Debert, Nova Scotia, Canada: Eastern Woodland Print Communications.
- Swift, Donald J. P. 1968. “Coastal Erosion and Transgressive Stratigraphy.” *The Journal of Geology* 76 (4): 444–56.
- Swift, Donald J. P., and Harold W. Borns. 1967. “A Raised Fluvio-marine Outwash Terrace, North Shore of the Minas Basin, Nova Scotia.” *The Journal of Geology* 75 (6): 693–710.
- Taché, Karine. 2011. “New Perspectives on Meadowood Trade Items.” *American Antiquity* 76 (1): 41–80.
- Taylor, Conrad Aaron. 2020. “Paleogeography, Sea-Level Change and the Peopling of the Maritimes: An Archaeological Perspective.” Ph.D., Halifax, Nova Scotia: Dalhousie University. <https://DalSpace.library.dal.ca/handle/10222/80055>.
- Todd, Brian J., and John Shaw. 2012. “Laurentide Ice Sheet Dynamics in the Bay of Fundy, Canada, Revealed through Multibeam Sonar Mapping of Glacial Landscapes.” *Quaternary Science Reviews* 58 (December): 83–103. <https://doi.org/10.1016/j.quascirev.2012.10.016>.
- Vacchi, Matteo, Simon E. Engelhart, Daria Nikitina, Erica L. Ashe, W. Richard Peltier, Keven Roy, Robert E. Kopp, and Benjamin P. Horton. 2018. “Postglacial Relative Sea-Level Histories along the Eastern Canadian Coastline.” *Quaternary Science Reviews* 201 (December): 124–46. <https://doi.org/10.1016/j.quascirev.2018.09.043>.
- Van Rossum, Guido. 2021. *Python 3 Reference Manual*. Wilmington, Delaware: Python Software Foundation. <https://docs.python.org/3.7/download.html>.
- Virtanen, Pauli, Ralf Gommers, Travis E. Oliphant, Matt Haberland, Tyler Reddy, David Cournapeau, Evgeni Burovski, et al. 2020. “SciPy 1.0: Fundamental Algorithms for Scientific Computing in Python.” *Nature Methods* 17: 261–72. <https://doi.org/10.1038/s41592-019-0686-2>.
- Vittori, Cecile, Ilaria Mazzini, Ferréol Salomon, Jean-Philippe Goiran, Simona Pannuzi, Carlo Rosa, and Angelo Pellegrino. 2015. “Palaeoenvironmental Evolution of the Ancient

- Lagoon of Ostia Antica (Tiber Delta, Italy).” *Journal of Archaeological Science* 54 (February): 374–84. <https://doi.org/10.1016/j.jas.2014.06.017>.
- Weatherbee, Wesley. 2020. “A Quarter and a Camera — Measuring Relative Abundance of Artifacts with Computer Vision in Python.” DigitalArchNS. February 18, 2020. <https://www.digitalarchns.com/measureartifacts/>.
- Westley, Kieran, Trevor Bell, M. A. P. Renouf, and Lev Tarasov. 2011. “Impact Assessment of Current and Future Sea-Level Change on Coastal Archaeological Resources— Illustrated Examples From Northern Newfoundland.” *The Journal of Island and Coastal Archaeology* 6 (3): 351–74. <https://doi.org/10.1080/15564894.2010.520076>.
- Wightman, Daryl M. 1980. “Late Pleistocene Glaciofluvial and Glaciomarine Sediments on the North Side of the Minas Basin, Nova Scotia.” Ph.D., Halifax, Nova Scotia: Dalhousie University. <https://DalSpace.library.dal.ca/handle/10222/75120>.
- Wilkinson, Ian P., Mark Williams, Jeremy R. Young, Samantha R. Cook, Michael G. Fulford, and Graham K. Lott. 2008. “The Application of Microfossils in Assessing the Provenance of Chalk Used in the Manufacture of Roman Mosaics at Silchester.” *Journal of Archaeological Science* 35 (8): 2415–22. <https://doi.org/10.1016/j.jas.2008.03.010>.
- Williams, Mark, Ian Wilkinson, Jeremy Taylor, Ian Whitbread, Rebecca Stamp, Ian Boomer, Emma Yates, and Christopher Stocker. 2015. “Microfossil-Determined Provenance of Clay Building Materials at Burrough Hill Iron Age Hill Fort, Leicestershire, England.” *Journal of Archaeological Science* 54 (February): 329–39. <https://doi.org/10.1016/j.jas.2014.03.028>.
- Young, Tuma. 2016. “L’nuwita’simk: A Foundational Worldview for a L’nuwey Justice System.” *Indigenous Law Journal* 13 (May). <https://jps.library.utoronto.ca/index.php/ilj/article/view/26700>.

Supplementary Data

7.1 Appendix A: Automated Rapid Artefact Surface Area Measurement from Imagery with Computer Vision

Acknowledgements

Authors would like to acknowledge the author of the original post inspiring this application and publication, Adrian Rosebrock. Without the effective communication of computer programming topics at PyImageSearch this may not have been possible. The corresponding author would also like to express his gratitude for family, friends, colleagues, and Saint Mary's University for facilitating an environment allowing this idea to come to fruition, even during COVID-19 restrictions.

Data accessibility statement

All data and hosted repository are licensed by the corresponding author under a [Creative Commons Attribution 4.0 International License](#). Data is an open-source release hosted at Codeberg and indexed on Zenodo. Please cite use of supplementary data in publications employing or modifying this technique with the following citation:

Weatherbee, Wesley J., Fowler, Jonathan, and van Proosdij, Danika. 2021. "Supplementary Data: Automated Rapid Artefact Surface Area Measurement from Imagery with Computer Vision". Zenodo. <http://doi.org/10.5281/zenodo.4792203>.

List of supplementary files

Supplementary data for this article is available as an organized directory containing the Python script, input, and output data used in this article:

Supplementary data repository

[Supplementary Data: artifact-area-v0.1](#)

This repository contains Supplementary Data accompanying the publication *Automated Rapid Artefact Surface Area Measurement from Imagery with Computer Vision* submitted to the *Journal of Lithic Studies*. Please download the complete repository for easiest deployment of the script.

7.2 Appendix B: Microfossils, Remote Sensing, and GIS for Proxy-dating Coastal Archaeological Sites and Landscapes

This Jupyter Notebook is intended to replicate the production of geochronological *terminus ante quem* boundaries for the Kingsport marsh as described in the associated article. Loading this **AppendixB** Jupyter Notebook as a Binder through the following link allows for this document to be navigated interactively, increasing reproducibility of the workflow employed to create the geochronological boundaries.


Interactive Online Version:

<https://mybinder.org/v2/gh/weslyfe/past-hhw/main?urlpath=tree/AppendixB.ipynb>

A generalized procedure for the notebook is detailed as follows:

1. [Import Packages](#)
2. [CSV Data Import, Preparation, and Jupyter Functionality](#)
3. [Correct for Marine Reservoir Effect & Radiocarbon Calibration](#)
4. [Calculate *Terminus Ante Quem* Date of Sea Level Proxy Observations](#)
5. [Visualize Result](#)

Click a link above to jump to that section but take note that the code within the sections cannot run without first running all prior cells of code. For ease of use, we recommend running all cells by selecting the **Run All** command under the **Cell** dropdown of the menu bar at the top of the window prior to jumping to a section.

Alternatively, the notebook can be navigated cell by cell by pressing the  **Run** button on the toolbar above or using the keyboard shortcut **Shift + Enter** or **Shift + Return** to run the currently selected cell and move to the next.

Import Packages

The first step is to import the required Python packages to replicate the method presented in the associated article. Running the following cell imports the required packages.

In [1]:

```
import datetime
import iosacal as iCal
import json
import matplotlib.pyplot as plt
import numpy as np
import pandas as pd
import re

from iosacal.text import single_text
from ipyleaflet import (basemaps, CircleMarker,
                        FullScreenControl, GeoJSON,
                        LayerGroup, LayersControl,
                        LocalTileLayer, Map,
                        MeasureControl, ScaleControl,
                        Polyline)
from ipywidgets import HTML

%matplotlib inline
```

Data Import, Preparation, and Jupyter Functionality

Following the data preparation steps outlined in the methods section of the associated article, we have placed a CSV titled `AppendixA` within the `/data` folder. The following cell will display the `AppendixA.csv` file as a table.

First, the `AppendixA` CSV is loaded into a `pandas` data frame called `AppendixA`. Next, table formatting, cell alignment, and styles to be applied when we call the variable `Table`. `Table` is called in the last line and our formatted CSV is shown below.

In [2]:

```
#read CSV file to pandas dataframe
AppendixA = pd.read_csv("./data/AppendixA.csv")

#create table style
Table = AppendixA.style.format({"error": lambda x: "±{: .1f}".format(abs(x))},...)

#show stylized table
Table
```

Out[2]:

	ID	date	error	core_depth	modern_HHW	HHW_corrected	HHW_error
0	Gx-6810	4430.0 C14BP	±215.0	9.50m	-	-	±0.200m
1	Gx-6811	2905.0 C14BP	±220.0	6.50m	-	-	±0.550m
2	Gx-6812	2355.0 C14BP	±180.0	4.50m	-	-	±0.200m

Missing data in data frames can easily be replaced with data from other sources.

First, a new data frame called `hhwDf` is created holding data read from the CSV file `hhw.csv`. This file holds 3D locations of higher high-water samples from the CANEAST HyVSEP surface (Robin et al., 2016). `NaN` or `Null` values are filled with an initial value of 0 using the function `fillna(0)`. The zeros are replaced with values from a newly defined `hhwDf` data frame holding data from the `hhw.csv` file. The cell below performs this procedure to fill the values in `modern_HHW` with values from the `hhw.csv` file included in the `/data` directory.

In [3]:

```
#create hhw data frame from hhw.csv
hhwDf = pd.read_csv("./data/hhw.csv")

#fill empty values with zeros then
#replace with hhw values from hhwDf
AppendixA['modern_HHW'].fillna(0)
AppendixA['modern_HHW'] =
hhwDf.iloc[0:3,3]

#show stylized table
Table
```

Out[3]:

	ID	date	error	core_depth	modern_HHW	HHW_corrected	HHW_error
0	Gx-6810	4430.0 C14BP	±215.0	9.50m	6.805m	-	±0.200m
1	Gx-6811	2905.0 C14BP	±220.0	6.50m	6.796m	-	±0.550m
2	Gx-6812	2355.0 C14BP	±180.0	4.50m	6.795m	-	±0.200m

Adjustment of uncertainty to include higher high-water values

The values that loaded to the `AppendixA` data frame include a vertical uncertainty in the column `HHW_error`. This uncertainty reflects the vertical extent of the marsh zone indicated by Foraminifera within each radiocarbon dated sample (Scott and Greenberg, 1983; Smith et al., 1984). The convenience of combining documentation and calculations in Jupyter Notebooks is illustrated in the following example by updating the `HHW_error` field that stores elevation uncertainties accumulated in the analysis.

Not yet reported in the above table are uncertainties associated with values in the `modern_HHW` column. The reported bulk accuracy of the CANEAST dataset from where these points were derived is 7.5cm (Robin et al., 2016). The same publication notes that inconsistencies appear greater in the Bay of Fundy (Robin et al., 2016, fig. 5). Though the difference between tide station and modelled lower low water elevation shown in our southwestern Minas Basin study area is within the range of reported uncertainty. Therefore,

we can be reasonably confident that the values and uncertainty provided by the CANEAST dataset reflect true uncertainty of higher high-water at the time of publication, 2016.

The following cell performs two calculations then displays the formatted Table data frame in the output. Calculations are shown below:

1. add vertical uncertainty of `modern_HHW` points to uncertainty of foram derived high-water elevations in `HHW_error`.
2. subtract `modern_HHW` from the depth of foram samples in `core_depth`.

The first calculation combines errors accumulated in later steps to `HHW_error` for storage. The second calculation provides the elevation (vertical datum: CGVD2013) of the equivalent high-water from the CANEAST dataset. By structuring the code to overwrite values in the initial data frame with newly calculated excess variable creation is avoided.

In [4]:

```
#replace values in HHW error column with the sum of itself and 0.0075 metres
AppendixA["HHW_error"] = AppendixA["HHW_error"] + 0.075

#calculate adjusted hhw value as difference between
#modern_HHW and core_depth
AppendixA["HHW_corrected"] = AppendixA["modern_HHW"]-AppendixA["core_depth"]

#show stylized table
Table
```

Out[4]:

	ID	date	error	core_depth	modern_HHW	HHW_corrected	HHW_error
0	Gx-6810	4430.0 C14BP	±215.0	9.50m	6.805m	-2.695m	±0.275m
1	Gx-6811	2905.0 C14BP	±220.0	6.50m	6.796m	0.296m	±0.625m
2	Gx-6812	2355.0 C14BP	±180.0	4.50m	6.795m	2.295m	±0.275m

Foraminifera sample `Gx-6811` was identified as representing marsh Zone 1b, in the lower portion of high marsh (Smith et al., 1984). These marsh zones were identified through

surface sampling vegetation and Foraminifera along transects within the marsh (Smith et al., 1984). Marsh zone 1b was defined at Kingsport as having a vertical range of 55cm, and a maximum of 75cm below high tide. This means that at a minimum, the upper limit of Zone 1b will be 20cm below the limit of high-water.

To adjust for the vertical position of sample Gx-6811 in marsh Zone 1b, an offset of 20 cm is added. This increases the elevation in the `HHW_corrected` field to represent the high-water mark defining the limit of marsh Zone 1a. The cell below performs this correction, then displays the updated values in our `AppendixA` data frame.

In [5]

```
#apply positive offset to account for the upper
#limit of zone 1b being 20cm below high-water
AppendixA.iloc[1:2,5] = AppendixA.iloc[1:2,5]+0.2

#show formatted table
Table
```

Out [5]

	ID	date	error	core_depth	modern_HHW	HHW_corrected	HHW_error
0	Gx-6810	4430.0 C14BP	±215.0	9.50m	6.805m	-2.695m	±0.275m
1	Gx-6811	2905.0 C14BP	±220.0	6.50m	6.796m	0.496m	±0.625m
2	Gx-6812	2355.0 C14BP	±180.0	4.50m	6.795m	2.295m	±0.275m

Equating sample depth below higher high-water to Oak Point

Due to the higher high-water elevation values included in `hhwDf` being from a single dataset (Robin et al. 2016), and equivalent value for `HHW_corrected` at Oak Point can be obtained for each sample by correcting for differences in high-water elevation between each sample and high-water at Oak Point. The correction sets the

`HHW_corrected` value to be equal to the depth below higher high-water if the samples were taken at Oak Point.

The following cell performs this correction in three steps:

1. calculate difference between modern higher high-water at each sample and Oak Point.
2. replace `AppendixA` values in `modern_HHW` with the higher high-water value for Oak Point.
3. add calculated values in `hhwAdj` to the `HHW_corrected` values.

The final line of code in the cell shows the adjustments in the table.

In [6]:

```
#calculate adjustment values for  
#difference between high-water at  
#Oak Point and sample Location  
hhwAdj = (hhwDf.loc[3].at['hhw']-AppendixA['modern_HHW'])  
  
#replace sample modern_HHW values  
#with Oak Point hhw value  
AppendixA['modern_HHW'] = hhwDf.loc[3].at['hhw']  
  
#add difference to HHW_corrected to  
AppendixA['HHW_corrected'] = AppendixA['HHW_corrected'] + hhwAdj  
  
#show stylized table  
Table
```

Out [6]:

	ID	date	error	core_depth	modern_HHW	HHW_corrected	HHW_error
0	Gx-6810	4430.0 C14BP	±215.0	9.50m	6.827m	-2.673m	±0.275m
1	Gx-6811	2905.0 C14BP	±220.0	6.50m	6.827m	0.527m	±0.625m
2	Gx-6812	2355.0 C14BP	±180.0	4.50m	6.827m	2.327m	±0.275m

One final functionality of Jupyter Notebooks important in effective step-by-step communication of programmatic methods is the `Toggle Line Numbers` command accessed through the `View` dropdown in the menu bar. This can also be quickly toggled by

using the keyboard shortcut `Shift + L` to turn lines in a cell on and off. As specific lines of code in cells are referenced when explaining the procedures, this functionality will be of benefit to the reader.

With the functionality of Jupyter Notebooks shown in the first step of this analysis. The next step is to prepare the radiocarbon dates for calibration.

Correct for Marine Reservoir Effect & Radiocarbon Calibration

Now that we have our CSV holding the necessary data to begin, we need to correct for marine reservoir effect, then calibrate our radiocarbon dates. Mentioned in the associated article, the ΔR of -64 ± 90 (obtained from [CALIB](#)) is subtracted from each radiocarbon date before calibration occurs (Alves et al., 2018, p. 293). The cell below will perform this calculation. As per usual, when addition or subtraction between two values with reported errors, the errors are summed.

In [7]:

```
#apply marine resevoir correction to date and error values in table
AppendixA["date"] = AppendixA["date"] - (-64)
AppendixA["error"] = AppendixA["error"] + (90)

#show stylized table
Table
```

Out[7]:

	ID	date	error	core_depth	modern_HHW	HHW_corrected	HHW_error
0	Gx-6810	4494.0 C14BP	±305.0	9.50m	6.827m	-2.673m	±0.275m
1	Gx-6811	2969.0 C14BP	±310.0	6.50m	6.827m	0.527m	±0.625m
2	Gx-6812	2419.0 C14BP	±270.0	4.50m	6.827m	2.327m	±0.275m

Calibrating sample data

The python package IOSACal is used in the following to calibrate the radiocarbon dates obtained from samples at Kingsport.

Records from the CSV file are used as input for a loop calibrating the input dates in the following radiocarbon calibration. The output is a short report and a probability distributionplot for each of the calibrations.

To prepare for this process we create variables to hold the inputs and outputs of the calibration in the following cell. The first three lines of code define the variables `s`, `d`, and `e` as values from specified columns in our data frame (`ID`, `date`, & `error`). The following two lines initialize empty lists, `cal68` and `cal95`, that will store the minimum and maximum date of each confidence interval for each sample.

In [8]:

```
#create variables for sample id, date, and date error
s = AppendixA.ID.values
d = AppendixA.date.values
e = AppendixA.error.values

#create a list to hold min and max values of probability distributions
cal68 = []
cal95 = []
```

A lot worthy of explanation happens in the following cell. The details of the process are described in the text below, as well as line by line with inline `#comments`.

First, the relative directory to save the output probability distribution plots is defined as `dir` at the top of the cell.

The `for` loop iterating over all records in `AppendixA` is initialized with a header statement on `line 5`. The header defines the parameters of our loop and describes the

conditions to be met `for` the loop to stop. This header instructs the computer to iterate the body of the loop below `for` the number of times equal to the `range` of the `shape` attribute of `AppendixA` in column `[0]`. The `range` of `AppendixA.shape[0]` is equal to the number of records in the first column of `AppendixA`. The loaded example from Kingsport contains three samples directing the loop iterate `for` a total of three times with the provided data.

`Line 6` begins the body of the loop by defining a variable called `r` as equal to the values of `date` (`d`), `error` (`e`), and `ID` (`s`). The variables are designated as radiocarbon dated samples to be calibrated with the function `R`. The `i` in square brackets following `d`, `e`, and `s` is a reference to the value of `date`, `error`, and `ID` for the input record with an index matching the current iteration of the loop. the resulting `r` variable now holds a list containing the three values for each of the three samples.

`Line 11` passes the values of the list stored in `r` to the `calibrate` method in `IOSACal`. By suffixing `.calibrate()` to `r`, values in `r` will be calibrated using the selected calibration curve. The calculated values are saved in the variable `cal_r`. The `'marine20'` calibration curve is called in the parentheses of the `calibrate()` function.

`Line 14` creates a report for the calibration, saved to the variable `report`. The report is created using the `single_text` function outputting the report as text below the cell.

`Line 17` searches the output report text for numeric digits, storing them in as a list in the variable called `findDigits`. `Line 22` and `line 23` append the min and max values from `findDigits` for the 68% and 95% confidence intervals, using the position in the list

for reference. These lines take advantage of the consistent structure IOSACal uses for reporting to allow us to directly use the outputs in further analysis.

Line 26 and line 29 then print the report stored in our report variable below our code, creating and saving a visualization of the calibration to the directory /SupplementaryData/output as a JPG image named by ID.

In [9]:

```
#define the output directory
dir= r"./output/"

#begin for loop iterating through all input records
for i in range(AppendixA.shape[0]):

#sort date, error, and sample id records and add
#input radiocarbon sample list
r = iCal.R(d[i], e[i], s[i])

#calibrate dates with the calibration curve shown in quotes
cal_r = r.calibrate('marine20')

#create text based output report for radiocarbon calibration
report = (single_text(cal_r))

#add all integer only words of one of more digits in the report to a list
findDigits = [int(s) for s in re.findall(r'\b\d+\b', report)]

#append the resulting list values to new lists
#68% confidence interval values are location 7 and 8
#95% confidence interval values are location 13 and 14
cal68.append(findDigits[7:9])
cal95.append(findDigits[13:15])

#print report for current sample as output
print(report)

#show probability distribution plot as inline plot below output
iCal.iplot(cal_r, output = dir + s[i] + ".jpg")
```

Out[9]:

```
# Gx-6810
```

Calibration of Gx-6810: 4494 ± 305 BP##

Calibrated age

Marine20 calibration data from Heaton et. al (2020).

68.2% probability

* 4861 CalBP - 4065 CalBP (68.2%)

95.4% probability

* 5270 CalBP - 3691 CalBP (95.4%)

IOSACal v0.4.1

Gx-6811

Calibration of Gx-6811: 2969 ± 310 BP

Calibrated age

Marine20 calibration data from Heaton et. al (2020).

68.2% probability

* 2937 CalBP - 2162 CalBP (68.2%)

95.4% probability

* 3333 CalBP - 1799 CalBP (95.4%)

IOSACal v0.4.1

Gx-6812

Calibration of Gx-6812: 2419 ± 270 BP

Calibrated age

Marine20 calibration data from Heaton et. al (2020).

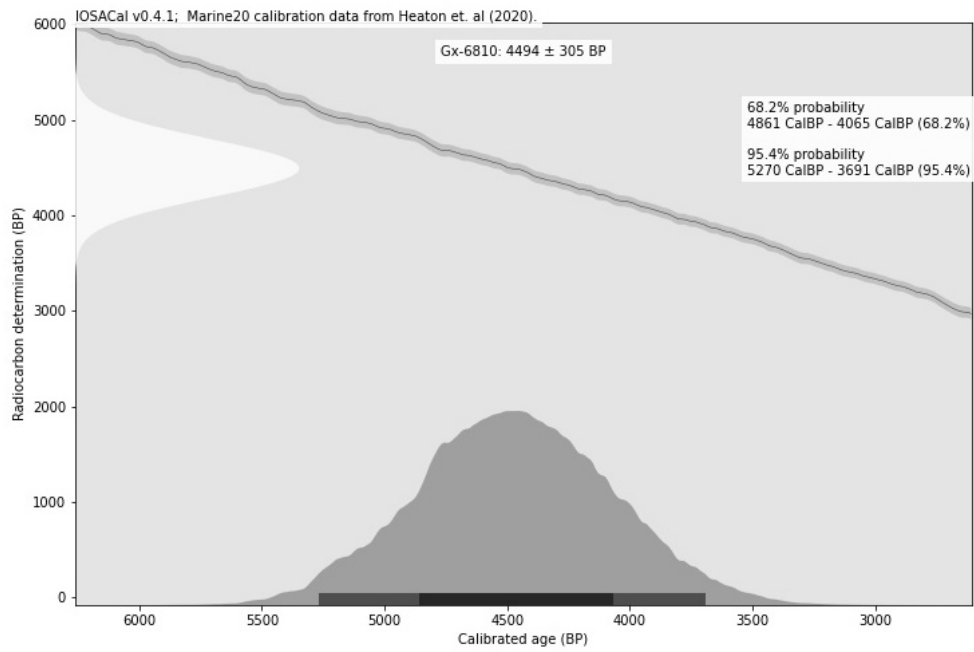
68.2% probability

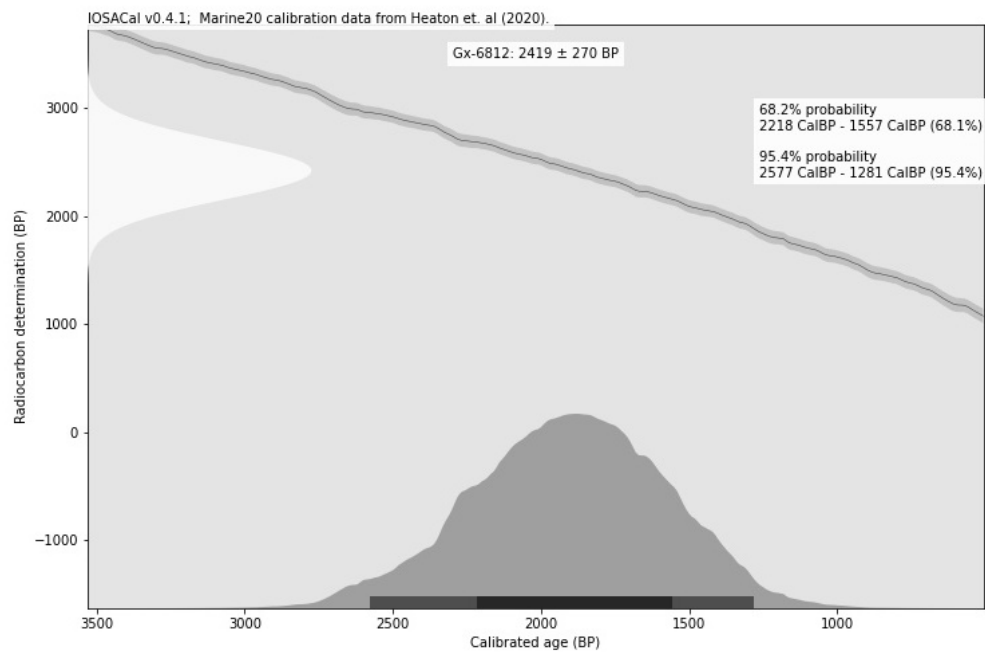
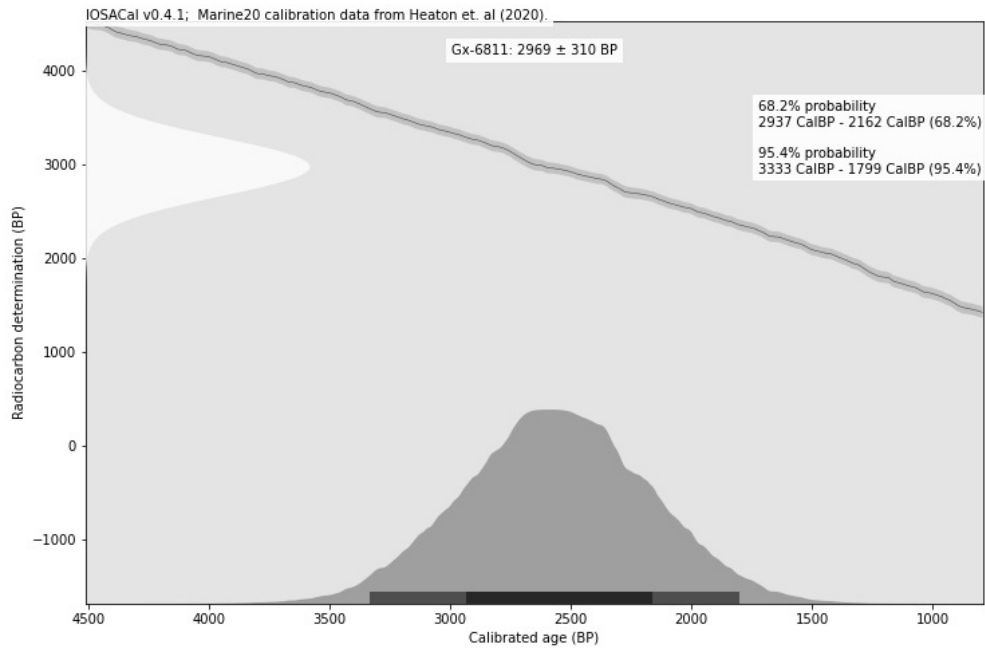
* 2218 CalBP - 1557 CalBP (68.1%)

95.4% probability

* 2577 CalBP - 1281 CalBP (95.4%)

IOSACal v0.4.1





After performing radiocarbon calibration, output lists are each cast to a `numpy array` on `line 2`, `line 3`, `line 4`, and `line 5` to perform the following calculations. These values are put into a `for` loop that iterates for `i` number of times on `line 8`. The

number of iterations is set to equal `range(AppendixA.shape[0])` once again, allowing the number of iterations to dynamically match the number of samples in the input data.

Within the `for` loop, simple calculations run for 1σ (68%) and 2σ (95%) confidence intervals on `line 11` and `line 12`, and `line 15` and `line 16`, respectively. These calculations retrieving minimum, maximum, mean and uncertainty values for each sample in calibrated years before present (CalBP). Values are then appended to variables `cal195Date`, `cal195Mean`, `cal195Err`, `d`, and `e` stored for use in later steps.

In [10]:

```
#create array objects to hold values not created above
cal68Date = np.array(cal68)
cal195Date = np.array(cal195)
cal195Mean = np.array(d)
cal195Err = np.array(e)

#begin for loop iterating through all input records
for i in range(AppendixA.shape[0]):

    #calculate mean and uncertainty for 68% confidence intervals
    d[i] = (cal68Date[i,0]+cal68Date[i,1])/2
    e[i] = (cal68Date[i,0]-cal68Date[i,1])/2

    #calculate mean and uncertainty for 95% confidence intervals
    cal195Mean[i] = (cal195Date[i,0]+cal195Date[i,1])/2
    cal195Err[i] = (cal195Date[i,0]-cal195Date[i,1])/2
```

A new data frame called `calDates` is created in the following cell. The `calDates` data frame holds our radiocarbon calibration results. Aside from the `numpy` array stored in `calMean` on `line 7`, all code in the following cell functions only to prepare data for and display the new data frame formatted to display the date range, mean, and uncertainty at both confidence intervals for all samples calibrated. These values are shown in the table below, stylized following standard conventions for display of radiocarbon calibration results.

In [11]:

```
#define columns of radiocarbon calibration table
cols = ['2'+'\u03C3'+ ' Max Age', '2'+'\u03C3'+ ' Min Age']
cols2 = ['1'+'\u03C3'+ ' Max Age', '1'+'\u03C3'+ ' Min Age']
cols3 = ['2'+'\u03C3'+ ' Mean Age', '2'+'\u03C3'+ ' Uncertainty',
         '1'+'\u03C3'+ ' Mean Age', '1'+'\u03C3'+ ' Uncertainty']

#create an array holding mean date and uncertainty at each confidence interval
calMean = np.column_stack((cal195Mean,cal195Err,d,e))

#create variable to hold an int of the number of records
numRecs = len(AppendixA)

#load cal95 list to a data frame and add column titles
calDates = pd.DataFrame(cal95)
calDates.columns = cols

#add remaining datasets and column titles
calDates.reindex(columns=calDates.columns.tolist() + cols2)
calDates[cols2] = cal68
calDates.reindex(columns=calDates.columns.tolist() + cols3)
calDates[cols3] = calMean.reshape(numRecs,4)
calDates.insert(0, "Sample ID", AppendixA.iloc[0:numRecs,0])

#stylize and show full results of radiocarbon calibration in a table
calDates.style.hide_index().set_properties([], **{'text-align': 'center'}).format...
```

Out [11]:

Sample ID	2 σ Max	2 σ Min	1 σ Max	1 σ Min	2 σ Mean	2 σ Uncertainty	1 σ Mean	1 σ Uncertainty
Gx-6810	5270 CalBP	3691 CalBP	4861 CalBP	4065 CalBP	4480 CalBP	± 789	4463 CalBP	± 398
Gx-6811	3333 CalBP	1799 CalBP	2937 CalBP	2162 CalBP	2566 CalBP	± 767	2549 CalBP	± 387
Gx-6812	2577 CalBP	1281 CalBP	2218 CalBP	1557 CalBP	1929 CalBP	± 648	1887 CalBP	± 330

Calculate Terminus Ante Quem Date of Sea Level Proxy Observations

With radiocarbon calibration complete, calculation of the geochronological *terminus ante quem* elevation boundaries can begin. The first calculation will provide the slope of the line connecting each high-water elevation-calibrated date coordinate pair in our samples. But first, a data frame called `coordData` is prepared to iteratively perform calculations on.

The table in the `coordData` data frame holds the mean value and uncertainty of all calibrated sample dates at both confidence intervals, the calculated higher high-water values. A record is appended to the end of the samples list to reference modern higher high-water at the study area, Oak Point.

In [12]:

```
#create list from past hhw values at Oak Point in AppendixA
hhw = list(AppendixA.iloc[0:3,5])
hhw.append(hhwDf.loc[3].at['hhw'])

#define the year today and year of hhw publication
yrToday = datetime.datetime.now().year
yrPub = 2016

#define modern date and errors to append to new data frame
confToday = [[1950-yrPub,0,1950-yrPub,0]]

#create data frame holding mean values
#and errors of calibrated dates for input
#in past sea level calculations
coordData = pd.DataFrame(calMean)

#join the AppendixA table and drop
#unnecessary columns
coordData=coordData.join(AppendixA)
coordData=coordData.drop(['ID', 'date', 'error', 'core_depth', 'modern_HHW'],axis=1)

#add a new record for the confidence
coordData = coordData.append(confToday)

#fill empty values with zeros
coordData = coordData.fillna(0)

#replace zeros with data from hhw list object
coordData.iloc[3:4,4] = coordData.iloc[3:4,4] + float(hhw[3])

#add uncertainty from hhw dataset
#to modern hhw error
coordData.iloc[3:4,5] = coordData.iloc[3:4,5] + 0.075

#reset the index values dropping old values
coordData = coordData.reset_index(drop=True)
```

Next, the coordinate pairs are used to calculate slope and intercept of the line connecting samples with sequential dates. Individual coordinates are defined below as `x1`,

`x2` , `y1`, and `y2` coordinates. Variable `x1` represents the radiocarbon equivalent date for the year of data publication, 2016, where the value 0 is equal to the year 1950.

We use our coordinate pairs from our table to derive the equation for the linear relationship between the most recent of the radiocarbon dated samples (`Gx-6812`, `HHW_corrected`) and modern HHW for that sample (`Gx-6812`, `modern_HHW`). The equation is later used to solve for the HHW at each of a series of surveyed proxies of past marine limits. At Oak Point, these proxies are elevations of rooted stumps of a drowned forest exposed during low tide conditions, and an interface of salt marsh peat and former terrestrial sediments.

First, four lists are initialized as `mList`, `bList`, `oldList`, and `yngLst` to hold values for slope, y-intercept, elevations from the older dates, and elevations from the younger dates, respectively. The number of iterations of a `while` loop is set to the number of records in `coordData` by storing the length of the index in the variable `iters`. The variable `i` is used to hold the current iteration and begins at the value `1`. A confidence interval can be selected if necessary, with the variable `interval`. In the following we select the 68% confidence interval, but the code is written to accommodate the 95% confidence interval as well.

Within the loop, coordinate data from the `coordData` data frame is stored to the `x1`, `x2`, `y1`, and `y2` variables. The values are sorted into coordinate pairs of date and elevation and held in the list `coords`. A `numpy` `zip()` function is then used to sort `coords` into `x_coords` and `y_coords` lists. The coefficient matrix, `A`, is created from the coordinate lists and used as a parameter for the least squares method, `lstsq()`.

Resulting from `lstsq()` are two derived values for slope, `m`, and intercept, `b`, of the equation, printed below. During each iteration of the loop the values of the coordinate pairs are appended the list objects `mList`, `bList`, `oldList`, and `yngList`. These values are used to provide an estimate of age for each past sea level elevation proxy observation provided in the `geojson` file at `/data/rslPoints.geojson` .

In [13]:

```
#create lists for slope, intercept, and
#elevation of older and younger coordinates
#in each coordinate pair
mList, bList, oldList, yngList = [],[],[],[]

#define number of iterations as equal
#to the number of records input
iters = len(coordData.index)

#set i to 1
i = 1

#selected interval for calculations#to be completed on
interval = 68

#begin while loop iterating the data
#until the total number of records is reached
while i < iters:

    #if the interval is equal to 95 use 95% C.I., else
    # use 68% C.I. to define x1 and x2 as the dates used
    if interval == 95:
        x1 = coordData.loc[iters-i].at[0]
        x2 = coordData.iloc[iters-i-1,0]
    else:
        x1 = coordData.loc[iters-i].at[2]
        x2 = coordData.loc[iters-i-1].at[2]

    #define y1 and y2 as higher high-water vales#at the chosen dates
    y1 = coordData.loc[iters-i].at["HHW_corrected"]
    y2 = coordData.loc[iters-i-1].at["HHW_corrected"]

    #define the list of coordinate pairs
    coords = [(x1,y1),(x2,y2)]

    #re-arrange the lists then add to an array
    x_coords, y_coords = zip(*coords)
    A = np.vstack([x_coords,np.ones(len(x_coords))]).T

    #define variables m and b as the result of least-squares
    #regression using the input coordinate pairs
    m, b = np.linalg.lstsq(A, y_coords, rcond=None)[0]
    yngList.append(x1)
    oldList.append(x2)
    mList.append(m)
    bList.append(b)

    #print the equation
    print("Equation for {:.0f} to {:.0f} CalBP is y = {:.5f}x + {:.5f}".format(...
    i+=1
```

Out [13]:

Equation for -66 to 1887 CalBP is $y = -0.00230x + 6.67493$

Equation for 1887 to 2549 CalBP is $y = -0.00272x + 7.45782$

Equation for 2549 to 4463 CalBP is $y = -0.00167x + 4.78865$

Load and solve for date of sea level proxies

The final step in this analysis is to use the elevation of the surveyed sea level indicator points to solve for the year that high-water submerged that upland feature.

The following cell provides an overview of the process used to interpolate the date that high-water submerged undated sea level proxy observations using surveyed elevations. The cell that follows creates a list value to hold the interpolated dates called `indAge`. A `for` loop iterates through the `mList` and `bList` objects that were filled after correcting HHW elevation. The loop passes input elevation values from the `indElev` list through a set of conditional statements interpolating the value with the correct equation. The interpolated value is then appended the `indAge` list.

A `geojson` file is loaded and the `['features']` of the file are read to the variable `features`. Two empty lists are also created to store indicator elevation, `indElev`, and uncertainty, `zErr` of each input record. Date values from `coordData` are used to are loaded to the `x` list object, and associated uncertainties at 68% and 95% confidence intervals are stored in `dateErr` and `err95`. The `y` list object holds the corrected high-water values from `coordData`, and the uncertainties are held in the list `error`. The `rs1Points` are then iterated over within a `for` loop. Within the `for` loop three conditions are set to decide which equation to use when solving for date of the indicator. This set number of three

`if/else` conditional statements is the one of the only places needing modification if more samples are calibrated within this notebook.

In [14]:

```
#Load geojson file containing surveyed but undated
#rsl indicator points
with open(r"./data/rs1Points.geojson", 'r') as f:
    data = json.load(f)

#reference geojson feature ID as variable 'features'
features = data['features']
indAge = []
indElev = []
zErr = []

#Load x values to plot from the OakPoint data frame
#then append the modern date relative to 1950
x = list(coordData[2])

#Load date uncertainty values to plot from the OakPoint
#data frame then append the modern date uncertainty
dateErr = list(coordData[3])
err95 = list(coordData[1])

#Load y values to plot from the OakPoint data frame
#then append the modern high-water and uncertainty
y = list(coordData['HHW_corrected'])
error = list(coordData['HHW_error'])

#for each sample decide which equation to solve with
#using corrected elevation of past hhw
for i in range(len(features)):

    if features[i]['properties']['OHeight'] >= y[2]:
        indAge.append((features[i]['properties']['OHeight']-bList[0])/mList[0])
    elif features[i]['properties']['OHeight'] >= y[1]:
        indAge.append((features[i]['properties']['OHeight']-bList[1])/mList[1])
    elif features[i]['properties']['OHeight'] >= y[0]:
        indAge.append((features[i]['properties']['OHeight']-bList[2])/mList[2])
```

Visualize Result

An interactive map frame powered by iPyLeaflet is prepared by running the proceeding code block. The map frame is centered on the Oak Point study area at Kingsport marsh.

On line 1 `mapFrame` defines the map frame then the following data and user interface functionalities are added for visualization:

- ESRI satellite imagery base map.
- custom map tile layer from the lidar base maps shown in the article.
- measurement functionality.
- full-screen toggle button.
- dynamic scale bar.
- layer toggle functionality.

In [15]:

```
#initialize map as "mapFrame"
mapFrame = Map(basemap=basemaps.Esri.WorldImagery,
               center=(45.1562107, -64.36996), zoom=15, max_zoom=18)

#Load and add Local tile Layer
basemap = LocalTileLayer(name="Shaded Relief", tms = True, attribution="Conta..."
mapFrame.add_layer(basemap)

#Load and add measurement function, fullscreen and layer toggle, and a visual sc
measure = MeasureControl(position='topleft', active_color = 'orange',
                          primary_length_unit = 'meters')
mapFrame.add_control(measure)
measure.completed_color = 'red'
mapFrame.add_control(FullScreenControl(position='topright'))
mapFrame.add_control(LayersControl(position='topleft'))
mapFrame.add_control(ScaleControl(position='topright', metric=True))
```

Creation of the map data

The map frame created above will display datasets to help explore the output calculations after running this notebook. The extent of the shaded relief mirrors that of Figure 1 in the associated article presenting a high-resolution maximum zoom level of 18 throughout.

The shaded relief layer was created from Lidar derived digital elevation models at 1m resolution from the Province of Nova Scotia. The layer is a series of compressed `.png`

tiles within an organized folder directory using naming conventions relating to geolocation. This directory is located at `/minasBase` off the Binder root folder.

The `/minasBase` directory was automatically created from a Map Tile Package (`.tpk`) file exported from ArcGIS Pro. With the help of python modules `tpkutils` and `mbutil`, the `.tpk` was converted to a `.mbtiles`, MapBox tile package file then extracted to the `/minasBase` directory.

Optimization of the map tiles is responsible for the high zoom level display presented in this Binder. An original file count for the `/minasBase` map tiles directory exceeded 5 million, which was not appreciated by GitHub or Binder. However, with the help of native python modules, the file count was reduced to approximately 26500 by removing any `.png` images in the directory that were a size of 190 bytes or smaller files of this size contained no image data, only a transparency layer.

Plotting surveyed elevations of sea level proxy observations with calculated dates

Surveyed points have been gathered at Oak Point of a series of past relative sea level proxies. Below we will load and visualize these survey points to the map frame.

To differentiate the values a `Popup` method is used to visualize the `properties.Code` property of the points when a point is clicked. All loaded vector data can be found within the `/data` directory, and shaded relief in the `/minasBase` directory.

Note: the following cell (In [16]) is too large to fit on one page. As a result of thesis formatting, the cell has been split in to two separate blocks. The interactive, online version of this notebook does not have the cells split.

In [16]:

```
#create variables from hhw csv to plot the high-water values in the map frame
hhwSmp = pd.read_csv("./data/hhw.csv", usecols=["ID"])
hhwZ = pd.read_csv("./data/hhw.csv", usecols=["hhw"])
hhwCoords = pd.read_csv("./data/hhw.csv", usecols=["lon", "lat"])
hhw = hhwSmp.join(hhwZ)

#Load geojson files containing digitized dyke footing and spit hook
with open(r"./data/dyke.geojson", 'r') as f:
    dyke = json.load(f)
with open(r"./data/spitHook.geojson", 'r') as f:
    hook = json.load(f)

#redefine the list of indicator elevations as an empty list
indElev = []

#create Layer group referencing json records within the map frame
rslGroup = LayerGroup(name="RSL Indicators", layers=())
hhwGroup = LayerGroup(name="HHW Samples", layers=())

#Loop over geojson features
for i in range(len(features)):
    location=(features[i]['geometry']['coordinates'][1], features[i]['geometry'] ...
    indicators = features[i]['properties']['Code']
    indElev.append(features[i]['properties']['OHeight'])
    zErr.append(features[i]['properties']['zError'])
    indA = str(indicators)
    indB = str(features[i]['properties']['OHeight']) + "m CGVD2013"
    indC = str(indAge[i]) + " years CalBP"
    html = "" + "<p><b>Indicator type: </b>"" + f"{indA}" + "" + "<br><b>Elevation: ...
    rslPoint = CircleMarker( radius=4, color="#000000", location=location, weig...

    # Popup associated to a Layer
    rslPoint.popup = HTML(html)
    rslGroup.add_layer(rslPoint)

#Loop over HHW sample points
for i in range(hhw.shape[0]):
    location = hhwCoords.loc[i].at["lon"], hhwCoords.loc[i].at["lat"]
    descA = str(hhwSmp.loc[i].at["ID"])
    descB = str(hhwZ.loc[i].at["hhw"]) + "m CGVD2013"
    html = "" + "<p><b>ID: </b>"" + f"{descA}" + "" + "<br> <b>Elevation: </b>"" + ...
    hhwPoint = CircleMarker( radius=4, color="#000000", location=location, weig...

# Popup associated to a Layer
hhwPoint.popup = HTML(html)
hhwGroup.add_layer(hhwPoint)

#add dyke Layer twice making one line thicker, creating custom symbology
dykeA = GeoJSON(data=dyke, name="Dyke footing", style={'opacity': 1, 'weight': 1, ...
dykeB = GeoJSON(data=dyke, name="Dyke footing", style={'opacity': 0.6, 'weight': ...
symDyke = LayerGroup(name="Dyke footing", layers=(dykeB, dykeA))
```



```

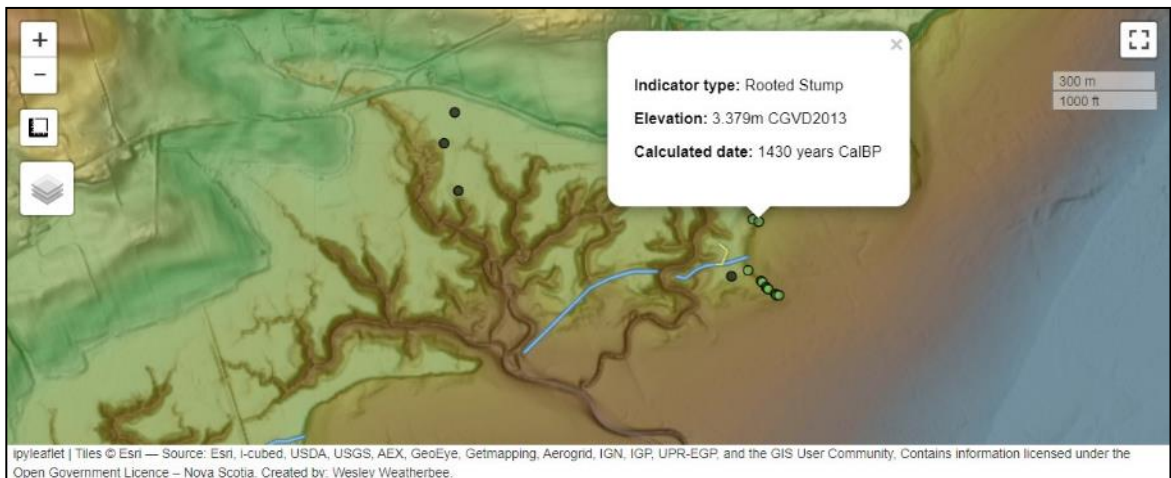
#add hook layer twice making one line thicker, creating custom symbology
hookA = GeoJSON(data=hook, name="Spit hook", style={'opacity': 1, 'weight': 1, '...
hookB = GeoJSON(data=hook, name="Spit hook", style={'opacity': 0.5, 'weight': 5, '...
symHook = LayerGroup(name="Spit hook", layers=(hookB, hookA))

#add group layers created from combined rslPoint, spit hook, and dyke layers
mapFrame.add_layer(symDyke)
mapFrame.add_layer(symHook)
mapFrame.add_layer(rslGroup)
mapFrame.add_layer(hhwGroup)

#call and display the map frame
mapFrame

```

Out [16]:



Note: the above image holds the place of an interactive map when running the online version of the notebook linked at the beginning.

Next, we create a plot of our observations intercepting a relative sea level curve derived from the input data. The plot uses the same custom style as found in the associated article.

The cell below converts the lists above in to `numpy array` objects, obtains the values from the `geojson` indicator points we stored in variables previously, and plots the values using custom style parameters.

In [17]:

```
#use the seaborn style colorblind in the plot
plt.style.use('seaborn-colorblind')

#define method to round values to the nearest 5
def myround(x, base=5):
    return int(base * round(float(x)/base))

#define x, y, errors, indicator elevation, z-error,
#calculated date, and date error
x = np.array(x)
dateErr = np.array(dateErr)
y = np.array(y)
error = np.array(error)
err95 = np.array(err95)
indAge = np.array(indAge)

#plot points, errorbars, interpolated rsl indicator age, and errorbar bounds
plt.plot(x, y, 'bo', x, y, 'k', linewidth=1.25, linestyle='dashed')
plt.plot(indAge, indElev, 'd', color='#4CE600', markersize=6, markeredgewidth=0.
plt.fill_between(x, y-x-err95, y-x+err95, alpha=0.2, edgecolor='#A80000', facecolo...
plt.fill_between(x, y-x-dateErr, y-x+dateErr, alpha=0.4, edgecolor='#A80000', facec...
plt.errorbar(x,y,error,dateErr, alpha=0.6, color='#1B2ACC', linewidth=0, elinew...
plt.fill_between(x, y-error, y+error, alpha=0.75, edgecolor='#1B2ACC', facecolo...

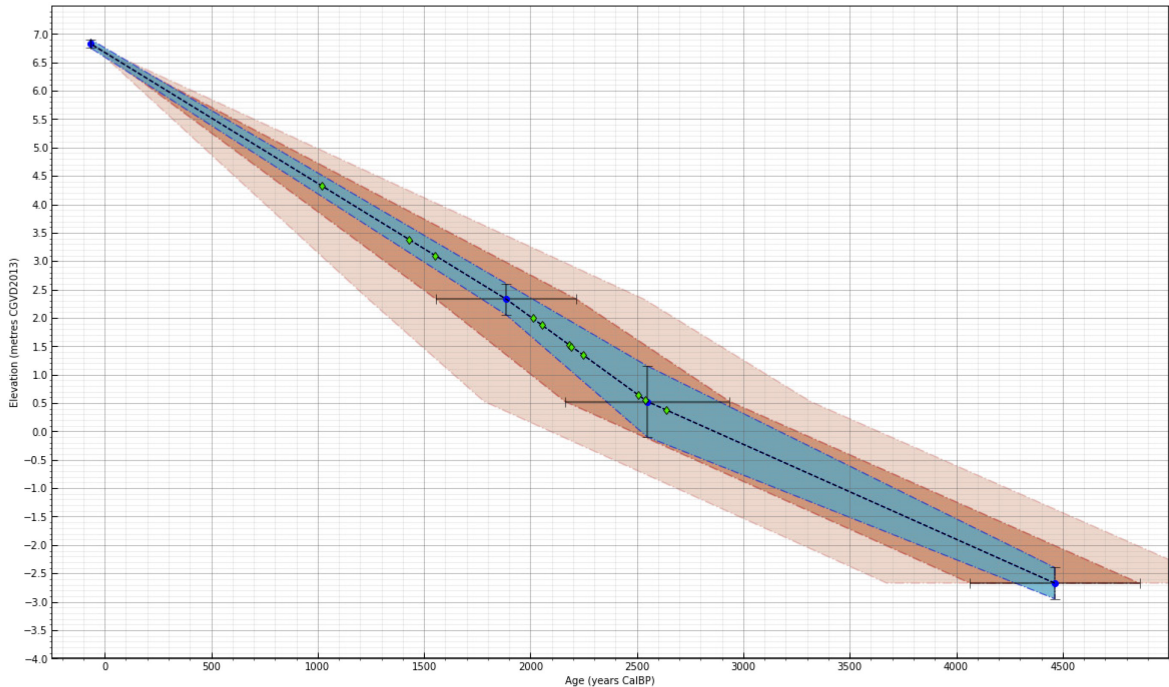
#stylize ticks, gridlines, bounds, and axis labels
plt.xticks(np.arange(0,5000, step=500))
plt.yticks(np.arange(-4,7.5, step=0.5))
plt.axhline(-4,color='black')
plt.axvline(-250,color='black')
plt.axhline(7.5,color='black')
plt.axvline(5000,color='black')
plt.tick_params(direction='in', length=6, width=1, colors='black',grid_color='gr...
plt.xlabel('Age (years CalBP)')
plt.ylabel('Elevation (metres CGVD2013)')
plt.xlim(-250, 5000)
plt.ylim(-4, 7.5)

# Show the major grid lines with dark grey lines
plt.grid(b=True, which='major', color='#666666')

# Show the minor grid lines with very faint and almost transparent grey lines
plt.minorticks_on()
plt.grid(b=True, which='minor', color='#999999', alpha=0.2)

#plot the figure and set the size
fig = plt.gcf() fig.set_size_inches(20, 12)
plt.savefig(r'./output/seaLevelCurve.png', edgecolor='black', dpi=400)
```

Out [17]:



The result of our above plot shows the relative sea-level curve for Oak Point. The calibrated dates were produced with the calibration curve used in the above process, and elevations were corrected using HHW points from a CHS grid surface for higher high-water. Uncertainties associated with each point are shown with vertical and horizontal bars.

A linear model is used to show interpolated uncertainty bounds over time. The light red boundary shows uncertainty of the radiocarbon calibration in the 95% confidence interval, while the 68% confidence interval is opaquer. Shown in blue boundary is uncertainty associated with the foram assemblage derived relative sea level indicator points.

There it is. The convenience of Jupyter Notebooks, functionality of Python, and accessibility of MyBinder interactively produces *terminus ante quem* elevations from case study observations of coastal archaeological sites and landscapes at Oak Point.

References

- Alves, E.Q., Macario, K., Ascough, P., Bronk Ramsey, C., 2018. The Worldwide Marine Radiocarbon Reservoir Effect: Definitions, Mechanisms, and Prospects. *Reviews of Geophysics* 56, 278–305. <https://doi.org/10.1002/2017RG000588>
- Brochart, D., Granger, B., Dafna, I., Grout, J., Weston, J., Tuloup, J., Breddels, M., Meireles, M., Renou, M., Bektas, M., Bugnion, P., Corlay, S., Fasuke, V.T., 2021. `jupyter-widgets/ipyleaflet`. Jupyter Widgets.
- Costa, S., Gutiérrez-Roig, M., 2018. IOSACal: An open source radiocarbon (14C) calibration software. Written in Python. Zenodo.
- Harris, C.R., Millman, K.J., van der Walt, S.J., Gommers, R., Virtanen, P., Cournapeau, D., Wieser, E., Taylor, J., Berg, S., Smith, N.J., Kern, R., Picus, M., Hoyer, S., van Kerkwijk, M.H., Brett, M., Haldane, A., Fernández del Río, J., Wiebe, M., Peterson, P., Gérard-Marchant, P., Sheppard, K., Reddy, T., Weckesser, W., Abbasi, H., Gohlke, C., Oliphant, T.E., 2020. Array programming with NumPy. *Nature* 585, 357–362. <https://doi.org/10.1038/s41586-020-2649-2>
- Heaton, T.J., Köhler, P., Butzin, M., Bard, E., Reimer, R.W., Austin, W.E.N., Ramsey, C.B., Grootes, P.M., Hughen, K.A., Kromer, B., Reimer, P.J., Adkins, J., Burke, A., Cook, M.S., Olsen, J., Skinner, L.C., 2020. MARINE20—THE MARINE RADIOCARBON AGE CALIBRATION CURVE (0–55,000 CAL BP). *Radiocarbon* 00, 1–42. <https://doi.org/10.1017/RDC.2020.68>
- Hunter, J.D., 2007. Matplotlib: A 2D Graphics Environment. *Computing in Science Engineering* 9, 90–95. <https://doi.org/10.1109/MCSE.2007.55>
- McKinney, W., 2010. Data Structures for Statistical Computing in Python. *Proceedings of the 9th Python in Science Conference* 56–61. <https://doi.org/10.25080/Majora-92bf1922-00a>
- McNeely, R., Dyke, A.S., Southon, J.R., 2006. Canadian marine reservoir ages, preliminary data assessment (Open File No. 5049), Geological Survey of Canada. Natural Resources Canada.
- Robin, C., Nudds, S., MacAulay, P., Godin, A., Boom, B.D.L., Bartlett, J., 2016. Hydrographic Vertical Separation Surfaces (HyVSEPs) for the Tidal Waters of Canada. *Marine Geodesy* 39, 195–222. <https://doi.org/10.1080/01490419.2016.1160011>
- Scott, D.B., Greenberg, D.A., 1983. Relative sea-level rise and tidal development in the Fundy tidal system. *Can. J. Earth Sci.* 20, 1554–1564. <https://doi.org/10.1139/e83-145>
- Smith, D.A., Scott, D.S., Medioli, F.S., 1984. Marsh foraminifera in the Bay of Fundy: modern distribution and application to sea-level determinations. *Maritime Sediments and Atlantic Geology*, Publication No. 17, Centre for Marine Geology, Dalhousie University 20, 127–142.

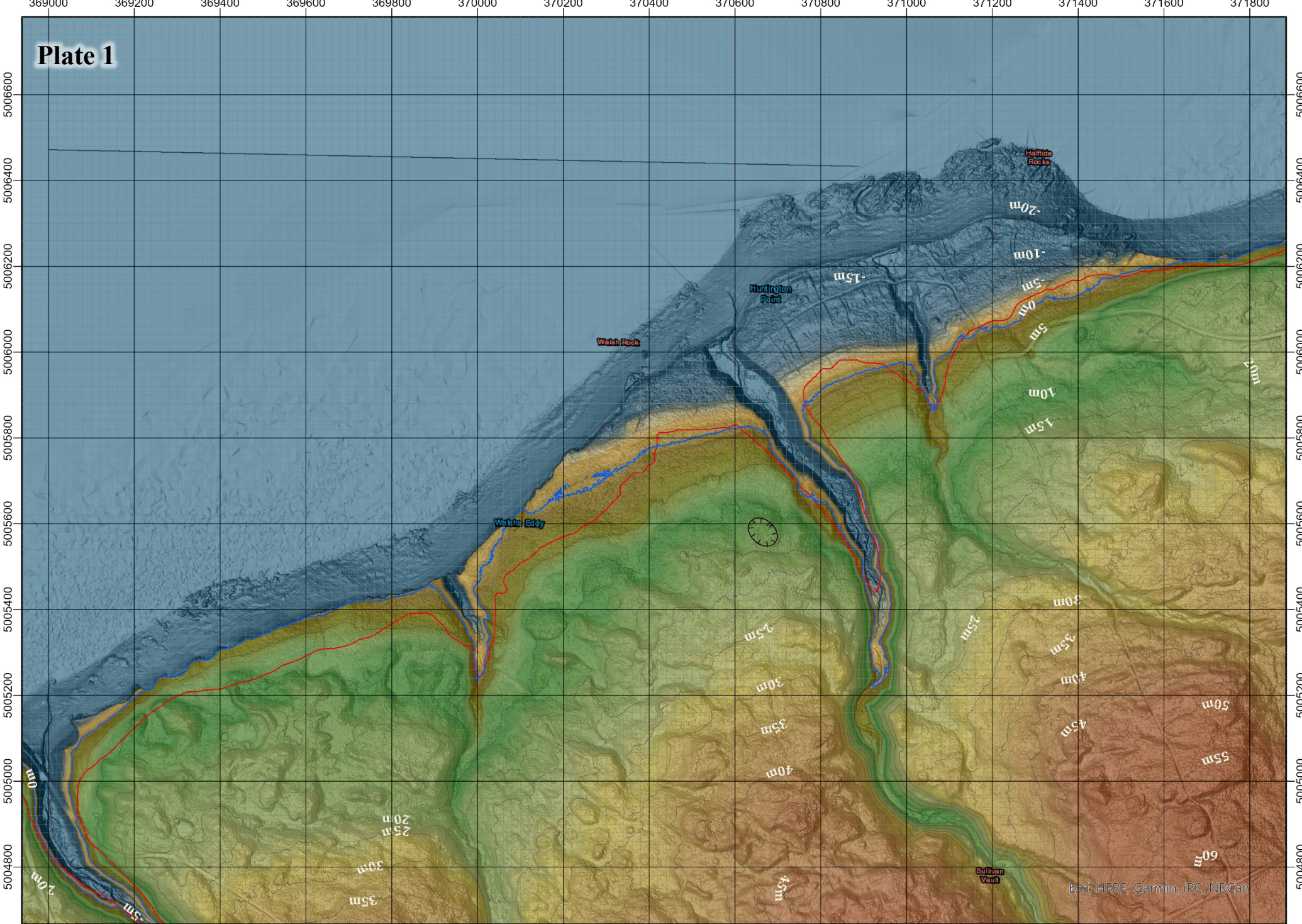
7.3 Appendix C: Landscape geoarchaeology of ice margins and paleo-coastlines with GIS

The following is an automated series of 49 maps covering the section of coastline along the south of Minas Basin from Huntington Point through to the mouth of the Cornwallis River. The maps are bounded to the east by the agricultural marsh of Grand Pré and by the summit of land to the south of the Canard River valley.

The colour ramp in the series imitates a generalized hypothetical coastal zone with a 10m tidal range. In this hypothetical coastal zone 0m elevation is the predicted mean water level. Yellow intertidal sandy deposits exist from -5m to 0m elevation, while elevations below -5m are blue, indicating subtidal. A change to yellowish brown colour at 0m indicates intertidal features above mean water level up to 5m. The change from yellowish brown to a pale light green occurs at 5m elevation and indicates the change from the intertidal to supratidal zone. The pale light green changes to a darker green at 10m elevation, then following a slower gradual change through yellow to red, then dark red as elevations increase through 100m elevation.

The colour ramp should only be used as a general means to reference elevations above the predicted 0m elevation of the isosurface. Mean water level and tidal range of the hypothetical coastal zone as indicated by the colour ramp cannot be considered as factual. However, the colour ramp does provide a valid base layer aiding visual validation of the predicted 0m elevation of the isosurface, and a logical tidal range to visually reference.

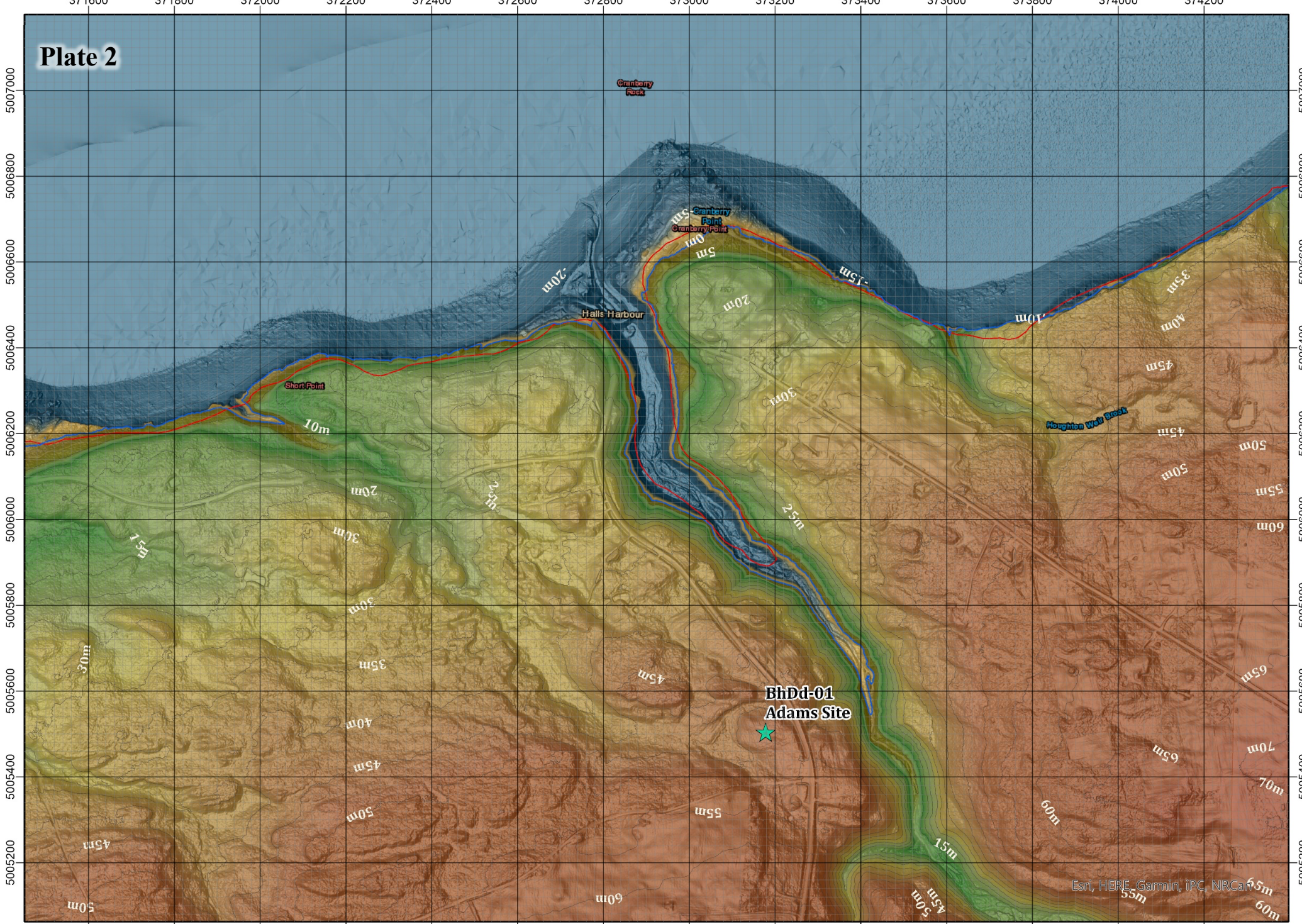
Plate 1



Reference Section	Artifacts from 2020	Lacustrine Limit (Paradis et. al, 2006)	Nearshore Deposits (Paradis et. al, 2006)	Paleo-elevation
Dated Sample (Dalton et. al, 2020)	Raised Beach Cusps (This Study)	Raised Beach Ridge (Paradis et. al, 2006)	Ice Sheet Limit (Dalton et. al, 2020)	<p>Metres</p> <p>100 -10</p>
Archaeological Site	Modelled Marine Limit (1m)	Raised Terrace (Paradis et. al, 2006)	Modelled Marine Limit (20m)	
Delta	Ring Features (This Study)	<p>Cartography: Wesley Weatherbee, CRS: NAD1983 CSRS UTM Zone 20N. Black grid squares are 200m². Grey grid squares are 20m². Contains information licensed under the Open Government License - Nova Scotia.</p> <p>0 100 200 M</p>		

Esri, HERE, Garmin, IPC, NRCan

Plate 2



Reference Section	Mineral Occurrence	Artifacts from 2020	Lacustrine Limit (Paradis et al., 2006)	Nearshore Deposits (Paradis et al., 2006)	Ice Sheet Limit (Dalton et al., 2020)	<p>Cartography: Wesley Weatherbee. CRS: NAD1983 CSRS UTM Zone 20N. Black grid squares are 200m². Grey grid squares are 20m². Contains information licensed under the Open Government License - Nova Scotia.</p> <p>Metres</p>
Dated Sample (Dalton et al., 2020)	Raised Beach Cusps (This Study)	Raised Beach Ridge (Paradis et al., 2006)	Raised Terrace (Paradis et al., 2006)	Ring Features (This Study)	Contour (5m)	

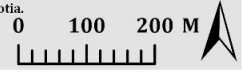
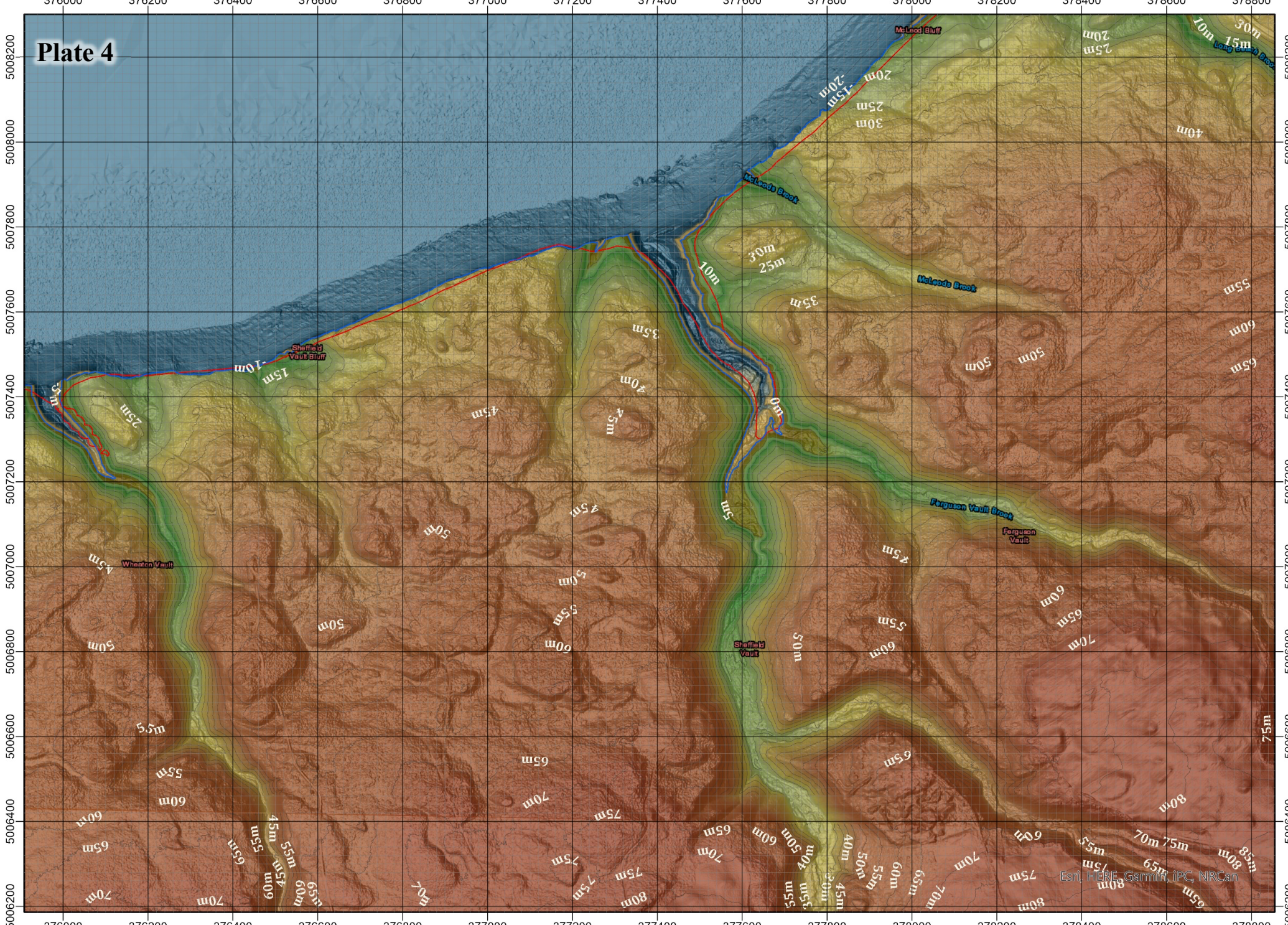


Plate 3



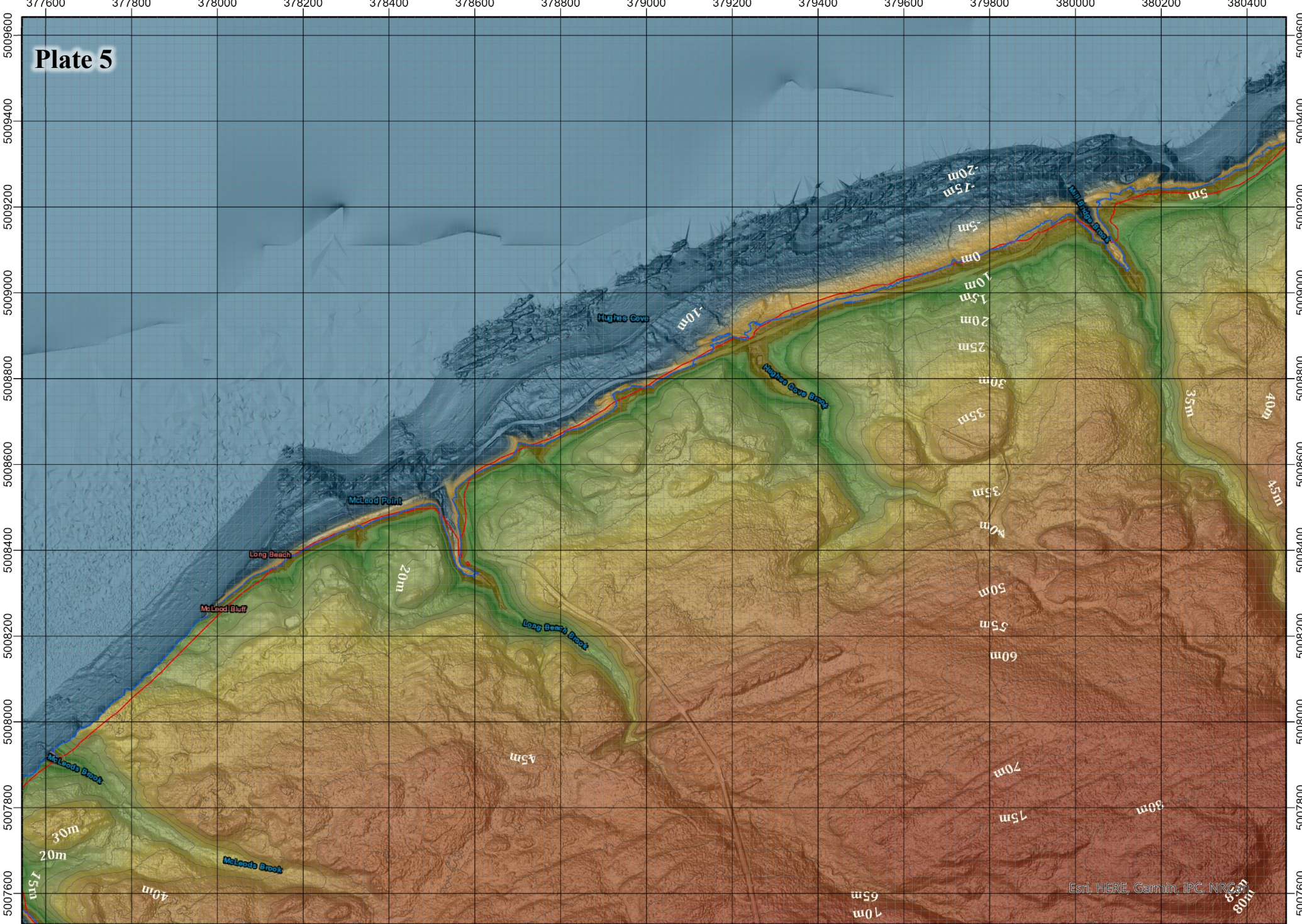
Reference Section	Artifacts from 2020	Lacustrine Limit (Paradis et. al, 2006)	Nearshore Deposits (Paradis et. al, 2006)	Ice Sheet Limit (Dalton et. al, 2020)	<p>Cartography: Wesley Weatherbee. CRS: NAD1983 CSRS UTM Zone 20N. Black grid squares are 200m². Grey grid squares are 20m². Contains information licensed under the Open Government License - Nova Scotia.</p> <p>Esri, HERE, Garmin, IPOL, NRCan</p>
Mineral Occurence	Dated Sample (Dalton et. al, 2020)	Raised Beach Cusps (This Study)	Raised Beach Ridge (Paradis et. al, 2006)	Raised Terrace (Paradis et. al, 2006)	
Delta	Archaeological Site	Modelled Marine Limit (1m)	Ring Features (This Study)	Modelled Marine Limit (20m)	<p>Metres</p> <p>0 100 200 M</p> <p>Contour (5m)</p>

Plate 4



Reference Section	Mineral Occurrence	Artifacts from 2020	Lacustrine Limit (Paradis et al, 2006)	Nearshore Deposits (Paradis et al, 2006)	Ice Sheet Limit (Dalton et al, 2020)	<p>Cartography: Wesley Weatherbee. CRS: NAD1983 CSRS UTM Zone 20N. Black grid squares are 200m². Grey grid squares are 20m². Contains information licensed under the Open Government License - Nova Scotia.</p> <p>Esri, HERE, Garmin, iPC, NRCAN</p>
Delta	Archaeological Site	Dated Sample (Dalton et al, 2020)	Raised Beach Cusps (This Study)	Raised Beach Ridge (Paradis et al, 2006)	Raised Terrace (Paradis et al, 2006)	
			Modelled Marine Limit (1m)	Ring Features (This Study)		<p>Metres</p> <p>0 100 200 M</p> <p>Contour (5m)</p>

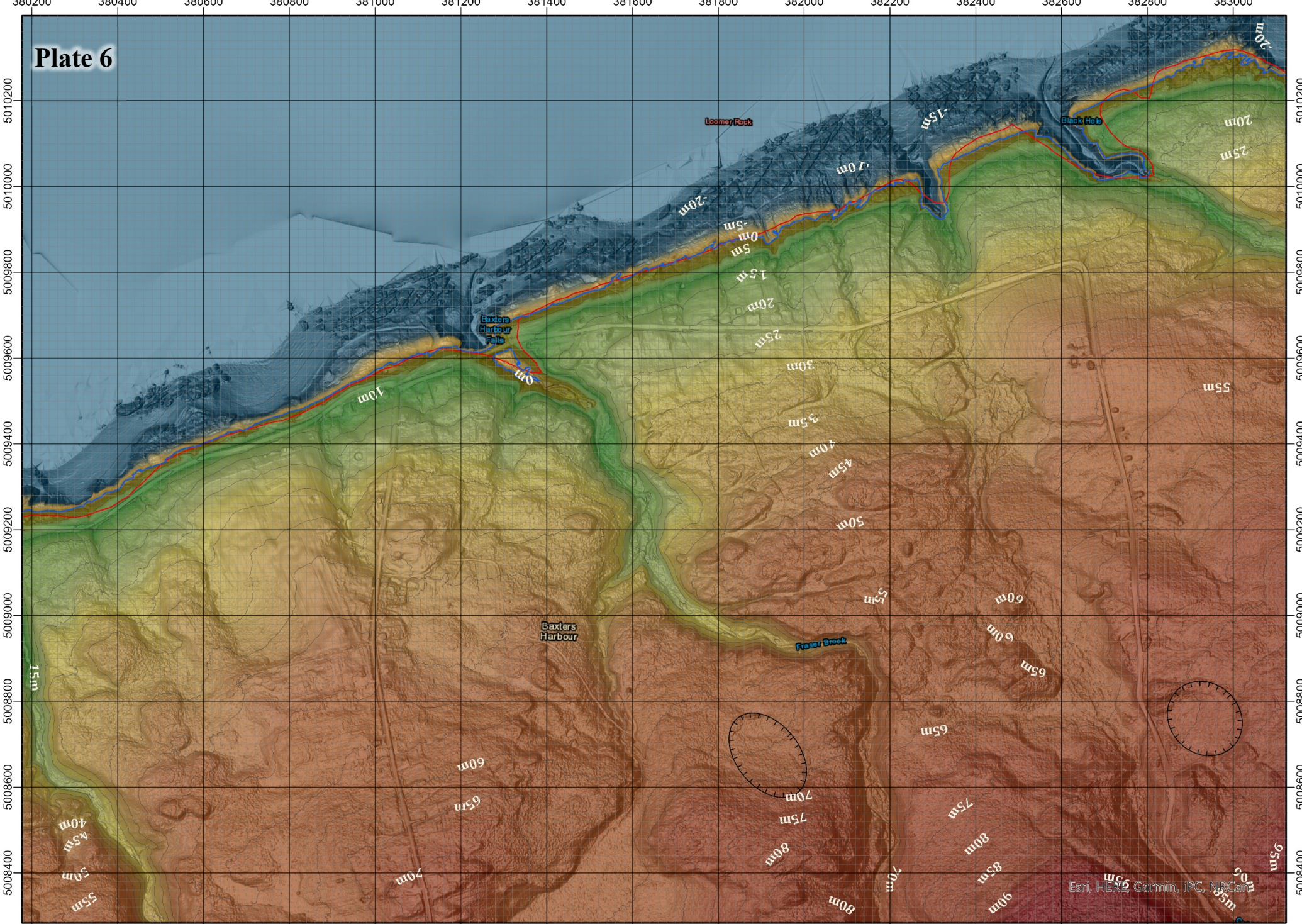
Plate 5



Reference Section	Artifacts from 2020	Lacustrine Limit (Paradis et. al, 2006)	Nearshore Deposits (Paradis et. al, 2006)	Paleo-elevation Metres 100 -10
Dated Sample (Dalton et. al, 2020)	Raised Beach Cusps (This Study)	Raised Beach Ridge (Paradis et. al, 2006)	Ice Sheet Limit (Dalton et. al, 2020)	
Delta	Archaeological Site	Modelled Marine Limit (1m)	Raised Terrace (Paradis et. al, 2006)	Cartography: Wesley Weatherbee, CRS: NAD1983 CSRS UTM Zone 20N. Black grid squares are 200m ² . Grey grid squares are 20m ² . Contains information licensed under the Open Government License - Nova Scotia.
	Modelled Marine Limit (20m)	Ring Features (This Study)		

Esri, HERE, Garmin, IPC, NRC

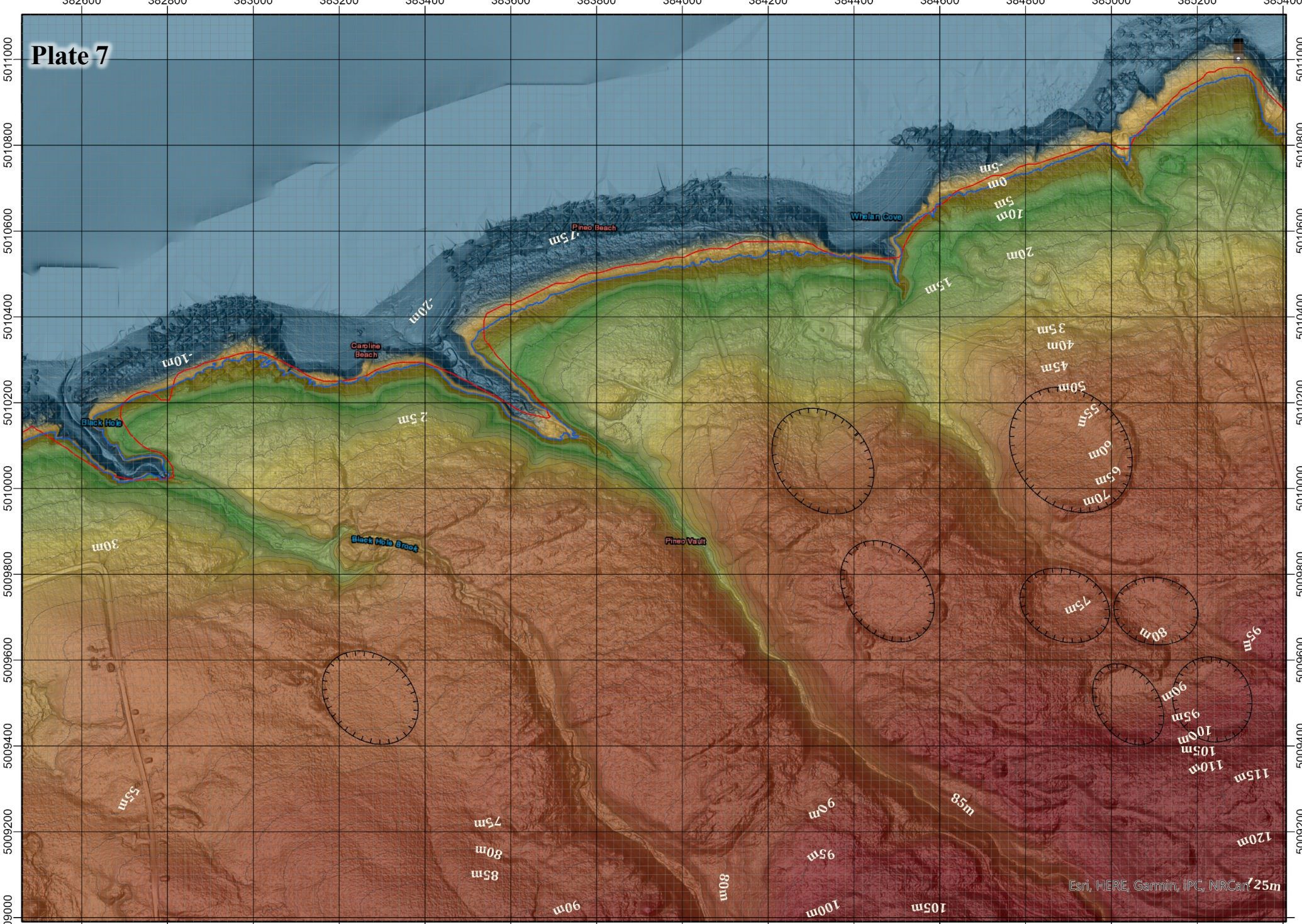
Plate 6



Reference Section	Artifacts from 2020	Lacustrine Limit (Paradis et. al, 2006)	Nearshore Deposits (Paradis et. al, 2006)	Paleo-elevation
Dated Sample (Dalton et. al, 2020)	Raised Beach Cusps (This Study)	Ice Sheet Limit (Dalton et. al, 2020)	Raised Beach Ridge (Paradis et. al, 2006)	Metres
Archaeological Site	Modelled Marine Limit (1m)	Raised Terrace (Paradis et. al, 2006)	Ring Features (This Study)	0 100 200 M
Delta	Modelled Marine Limit (20m)			N

Cartography: Wesley Weatherbee. CRS: NAD1983 CSRS UTM Zone 20N. Black grid squares are 200m². Grey grid squares are 20m². Contains information licensed under the Open Government License - Nova Scotia.

Plate 7



Reference Section	Mineral Occurrence	Artifacts from 2020	Lacustrine Limit (Paradis et. al, 2006)	Nearshore Deposits (Paradis et. al, 2006)	Ice Sheet Limit (Dalton et. al, 2020)	Paleo-elevation	Cartography: Wesley Weatherbee. CRS: NAD1983 CSRS UTM Zone 20N. Black grid squares are 200m ² . Grey grid squares are 20m ² . Contains information licensed under the Open Government License - Nova Scotia.
Delta	Dated Sample (Dalton et. al, 2020)	Raised Beach Cusps (This Study)	Raised Beach Ridge (Paradis et. al, 2006)	Raised Terrace (Paradis et. al, 2006)	Ring Features (This Study)	Metres 100 -10	

N
 0 100 200 M
 Contour (5m)

Plate 8

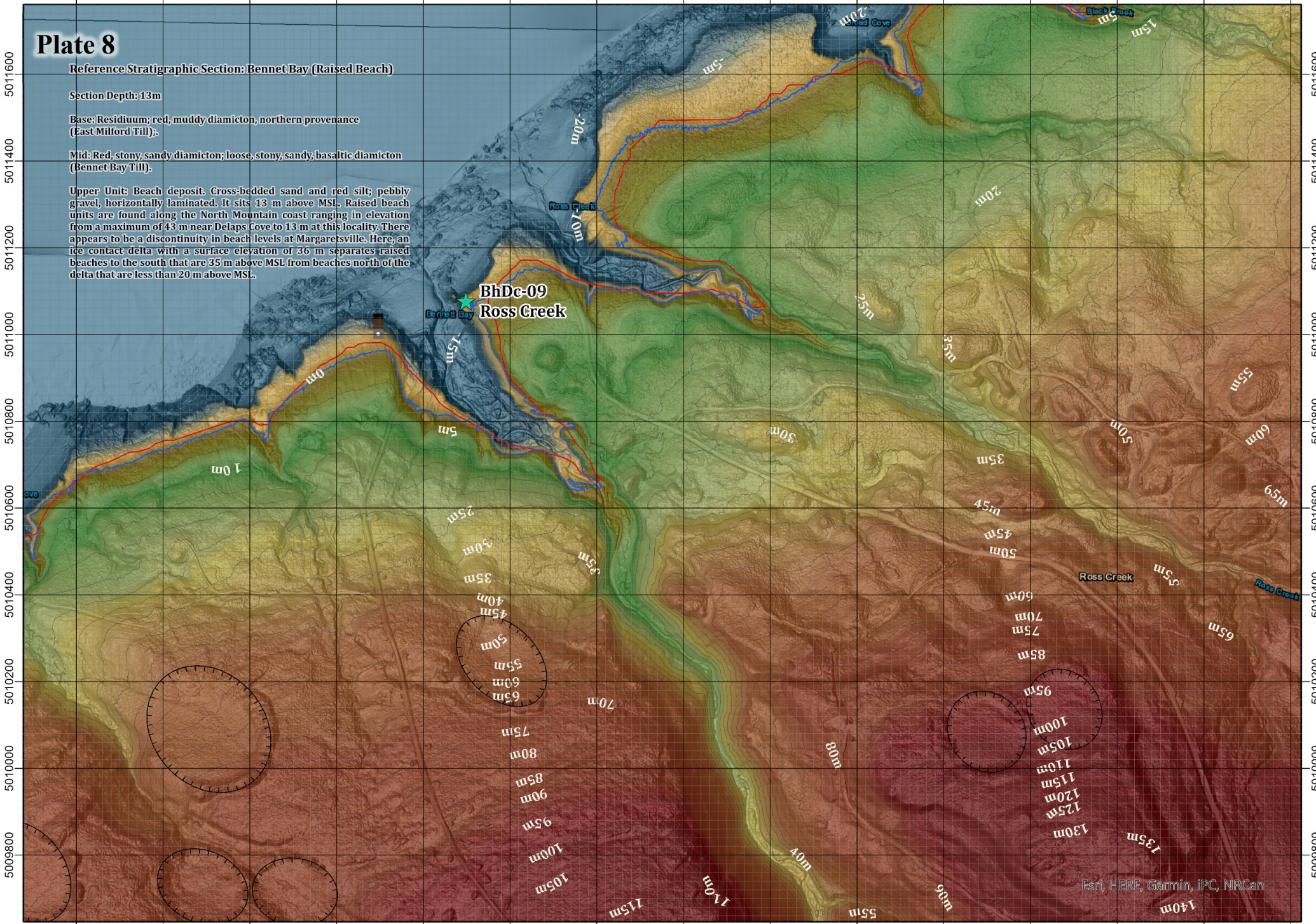
Reference Stratigraphic Section: Bennet Bay (Raised Beach)

Section Depth: 13m

Base: Residuum; red, muddy diamicton, northern provenance (East Milford Till).

Mid: Red, stony, sandy diamicton; loose, stony, sandy, basaltic diamicton (Bennet Bay Till).

Upper Unit: Beach deposit. Cross-bedded sand and red silt; pebbly gravel, horizontally laminated. It sits 13 m above MSL. Raised beach units are found along the North Mountain coast ranging in elevation from a maximum of 43 m near Delaps Cove to 13 m at this locality. There appears to be a discontinuity in beach levels at Margaretsville. Here, an ice contact delta with a surface elevation of 36 m separates raised beaches to the south that are 35 m above MSL from beaches north of the delta that are less than 20 m above MSL.



Reference Section	Mineral Occurrence	Artifacts from 2020	Lacustrine Limit (Paradis et al, 2006)	Nearshore Deposits (Paradis et al, 2006)	Paleo-elevation	Cartography: Wesley Weatherbee. CRS: NAD1983 CSRS UTM Zone 20N. Black grid squares are 200m ² . Grey grid squares are 20m ² . Contains information licensed under the Open Government License - Nova Scotia.
Dated Sample (Dalton et al, 2020)	Raised Beach Cusps (This Study)	Modelled Marine Limit (1m)	Ice Sheet Limit (Dalton et al, 2020)	Raised Terrace (Paradis et al, 2006)	Metres 100 -10	
Delta	Archaeological Site	Modelled Marine Limit (20m)	Ring Features (This Study)	Contour (5m)		

Esri, HERE, Garmin, iPC, NRCAN

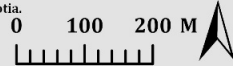
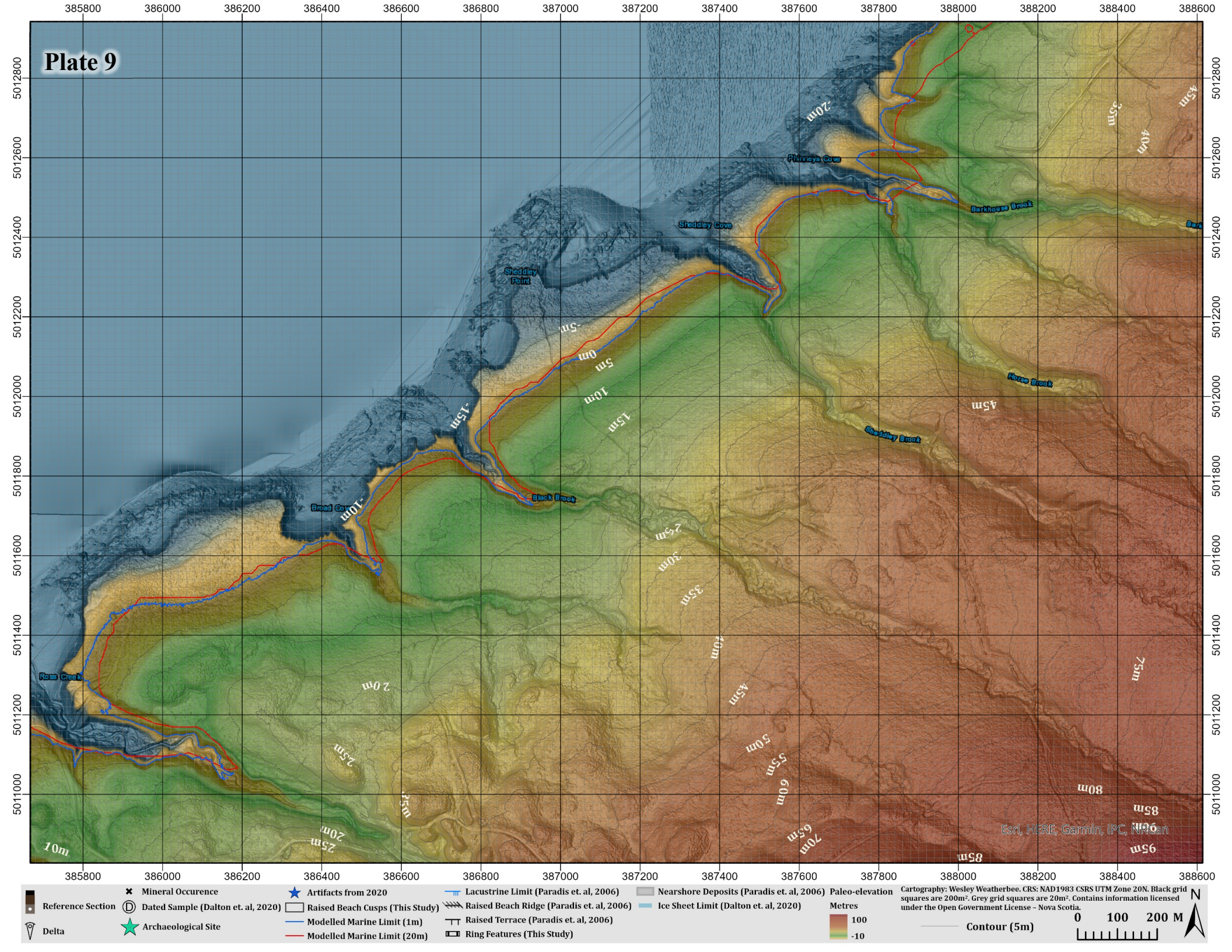


Plate 9

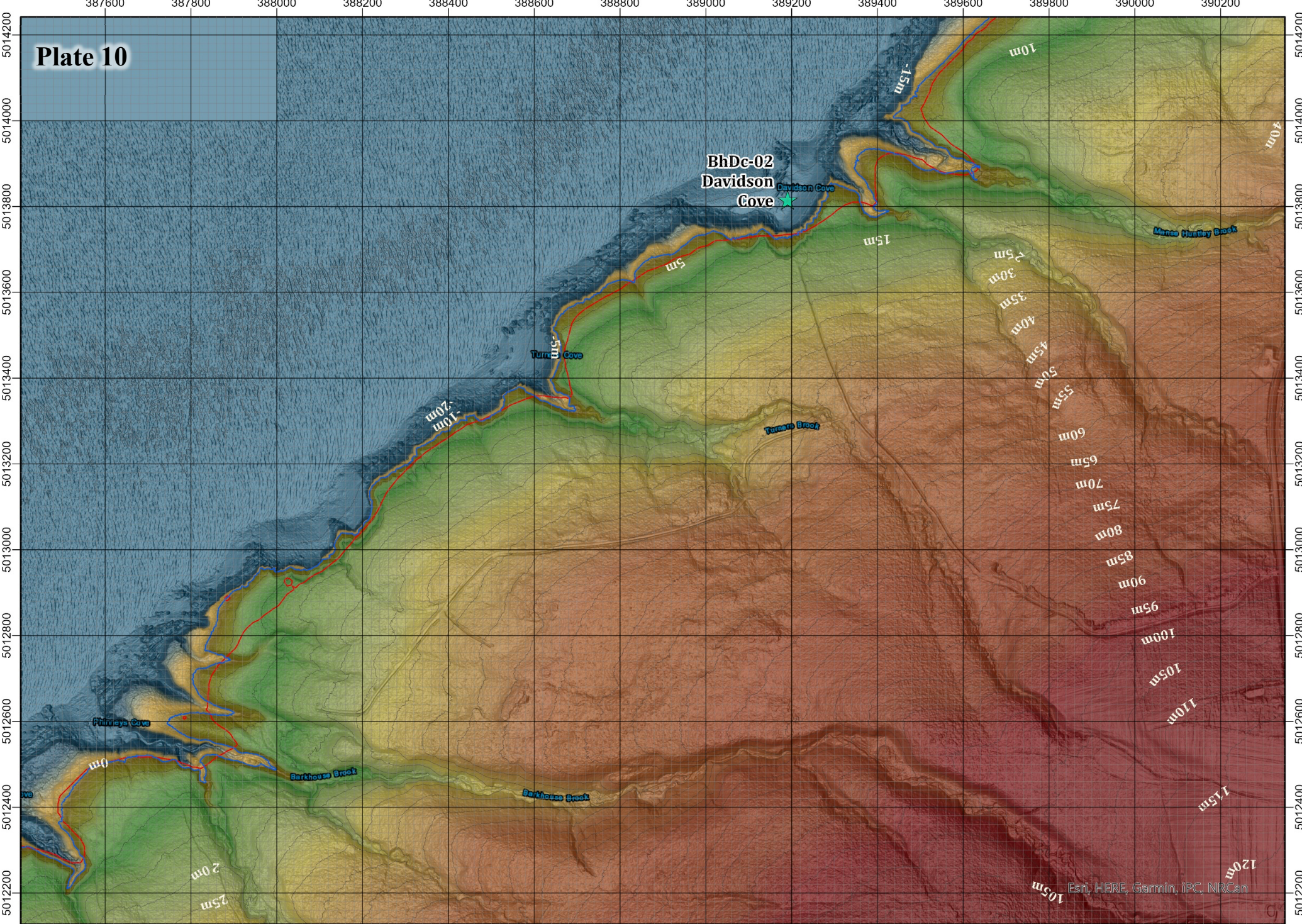


Reference Section	Mineral Occurrence	Artifacts from 2020	Lacustrine Limit (Paradis et. al, 2006)	Nearshore Deposits (Paradis et. al, 2006)	Ice Sheet Limit (Dalton et. al, 2020)	Paleo-elevation
Dated Sample (Dalton et. al, 2020)	Raised Beach Cusps (This Study)	Raised Terrace (Paradis et. al, 2006)	Raised Beach Ridge (Paradis et. al, 2006)	Ring Features (This Study)	Modelled Marine Limit (1m)	Contour (5m)
Delta	Archaeological Site	Modelled Marine Limit (20m)				0 100 200 M

Metres
100
-10

Cartography: Wesley Weatherbee. CRS: NAD1983 CSRS UTM Zone 20N. Black grid squares are 200m². Grey grid squares are 20m². Contains information licensed under the Open Government License - Nova Scotia.

Plate 10

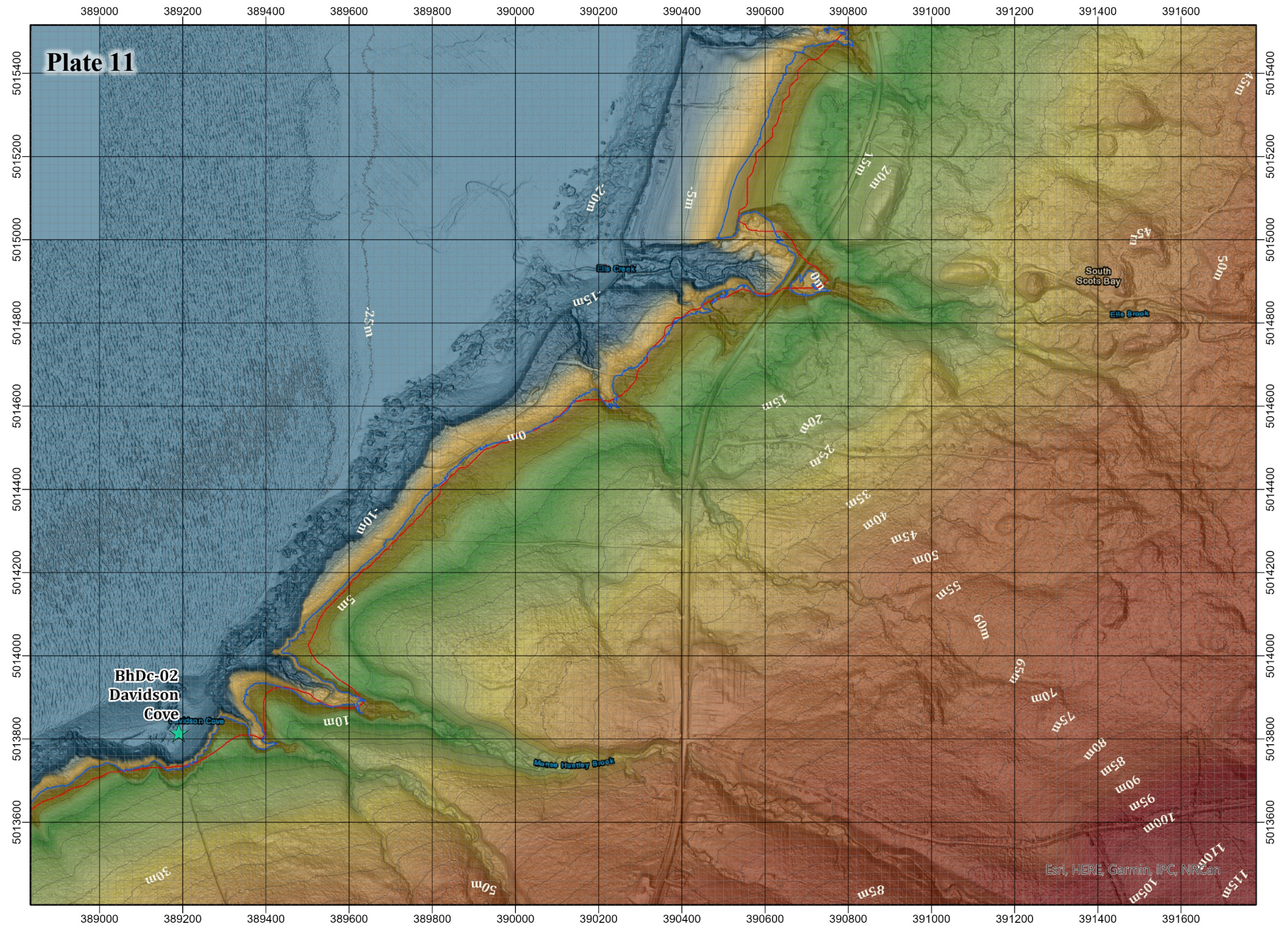


Reference Section	Mineral Occurrence	Artifacts from 2020	Lacustrine Limit (Paradis et. al, 2006)	Nearshore Deposits (Paradis et. al, 2006)	Paleo-elevation
Dated Sample (Dalton et. al, 2020)	Raised Beach Cusps (This Study)	Modelled Marine Limit (1m)	Raised Beach Ridge (Paradis et. al, 2006)	Ice Sheet Limit (Dalton et. al, 2020)	Contour (5m)
Delta	Archaeological Site	Modelled Marine Limit (20m)	Raised Terrace (Paradis et. al, 2006)	Ring Features (This Study)	0 100 200 M

Cartography: Wesley Weatherbee. CRS: NAD1983 CSRS UTM Zone 20N. Black grid squares are 200m². Grey grid squares are 20m². Contains information licensed under the Open Government License - Nova Scotia.

Esri, HERE, Garmin, IPC, NRCan

Plate 11



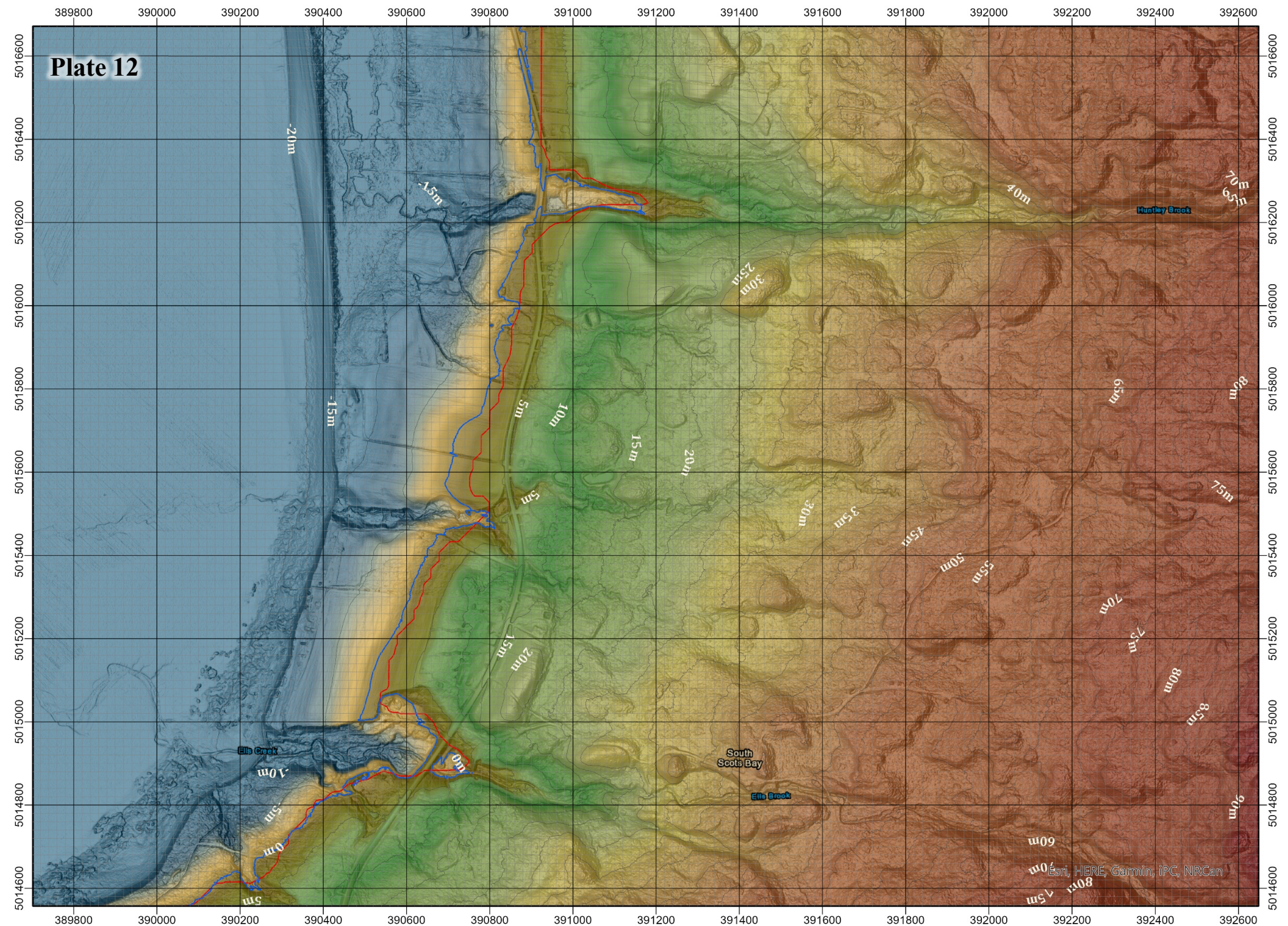
Reference Section	Mineral Occurrence	Artifacts from 2020	Lacustrine Limit (Paradis et al, 2006)	Nearshore Deposits (Paradis et al, 2006)	Paleo-elevation
Dated Sample (Dalton et al, 2020)	Raised Beach Cusps (This Study)	Raised Beach Ridge (Paradis et al, 2006)	Modelled Marine Limit (1m)	Ice Sheet Limit (Dalton et al, 2020)	Metres
Archaeological Site	Modelled Marine Limit (20m)	Raised Terrace (Paradis et al, 2006)	Ring Features (This Study)		100 -10
Delta					Cartography: Wesley Weatherbee, CRS: NAD1983 CSRS UTM Zone 20N. Black grid squares are 200m ² . Grey grid squares are 20m ² . Contains information licensed under the Open Government License - Nova Scotia.

Esri, HERE, Garmin, iPC, NRCan

Contour (5m)

0 100 200 M

Plate 12



Reference Section	Mineral Occurrence	Artifacts from 2020	Lacustrine Limit (Paradis et. al, 2006)	Nearshore Deposits (Paradis et. al, 2006)	Paleo-elevation
Dated Sample (Dalton et. al, 2020)	Raised Beach Cusps (This Study)	Modelled Marine Limit (1m)	Raised Beach Ridge (Paradis et. al, 2006)	Ice Sheet Limit (Dalton et. al, 2020)	
Delta	Archaeological Site	Modelled Marine Limit (20m)	Raised Terrace (Paradis et. al, 2006)	Ring Features (This Study)	

Metres

-10
100

Contour (5m)

0 100 200 M

N

Cartography: Wesley Weatherbee. CRS: NAD1983 CSRS UTM Zone 20N. Black grid squares are 200m². Grey grid squares are 20m². Contains information licensed under the Open Government License - Nova Scotia.

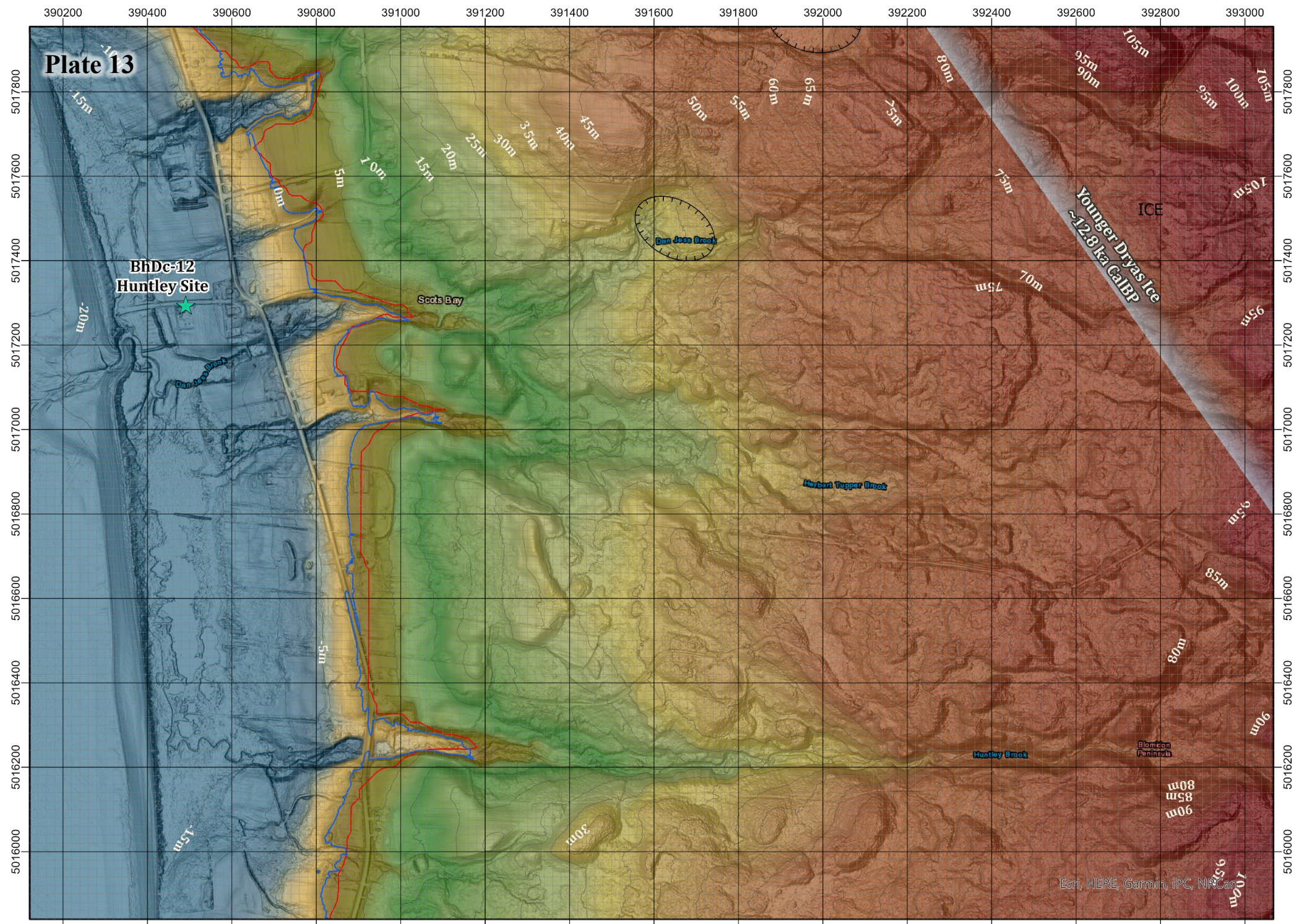


Plate 13

**BhDc-12
Huntley Site**

Scots Bay

Dan Jesse Brook

Herbert Tupper Brook

Huntley Brook

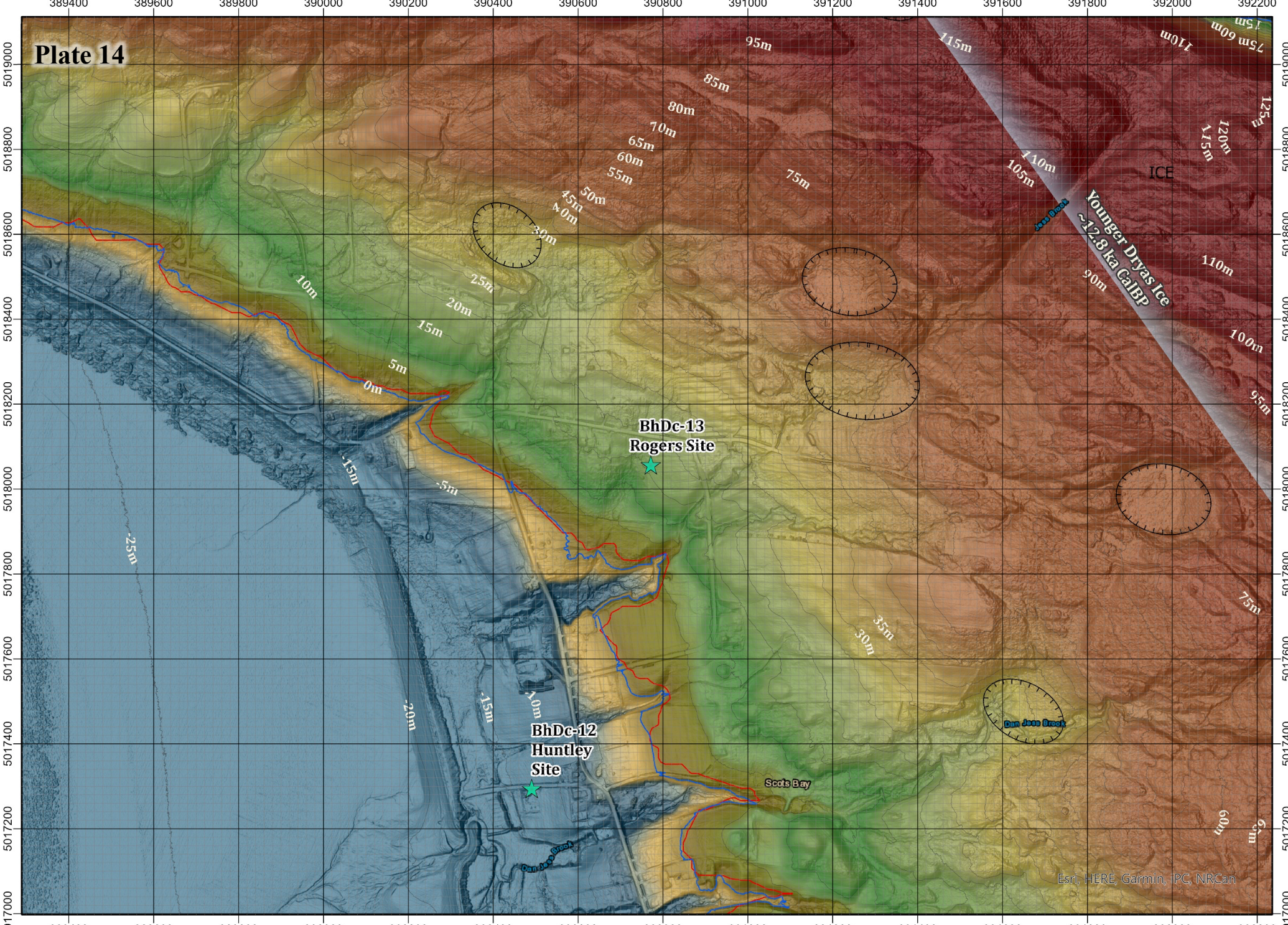
Blomkon
Famineus

Younger Dryas Ice
~12.8 ka CalBP

ICE

Reference Section	Mineral Occurrence	Artifacts from 2020	Lacustrine Limit (Paradis et. al, 2006)	Nearshore Deposits (Paradis et. al, 2006)	Paleo-elevation Metres 100 -10	<p>Cartography: Wesley Weatherbee, CRS: NAD1983 CSRS UTM Zone 20N. Black grid squares are 200m². Grey grid squares are 20m². Contains information licensed under the Open Government License - Nova Scotia.</p> <p>Esri, HERE, Garmin, IPC, NRCAN</p>
Delta	Archaeological Site	Raised Beach Cusps (This Study)	Raised Beach Ridge (Paradis et. al, 2006)	Ice Sheet Limit (Dalton et. al, 2020)	<p>Contour (5m)</p> <p>0 100 200 M</p>	
		Modelled Marine Limit (1m)	Raised Terrace (Paradis et. al, 2006)	Ring Features (This Study)		

Plate 14



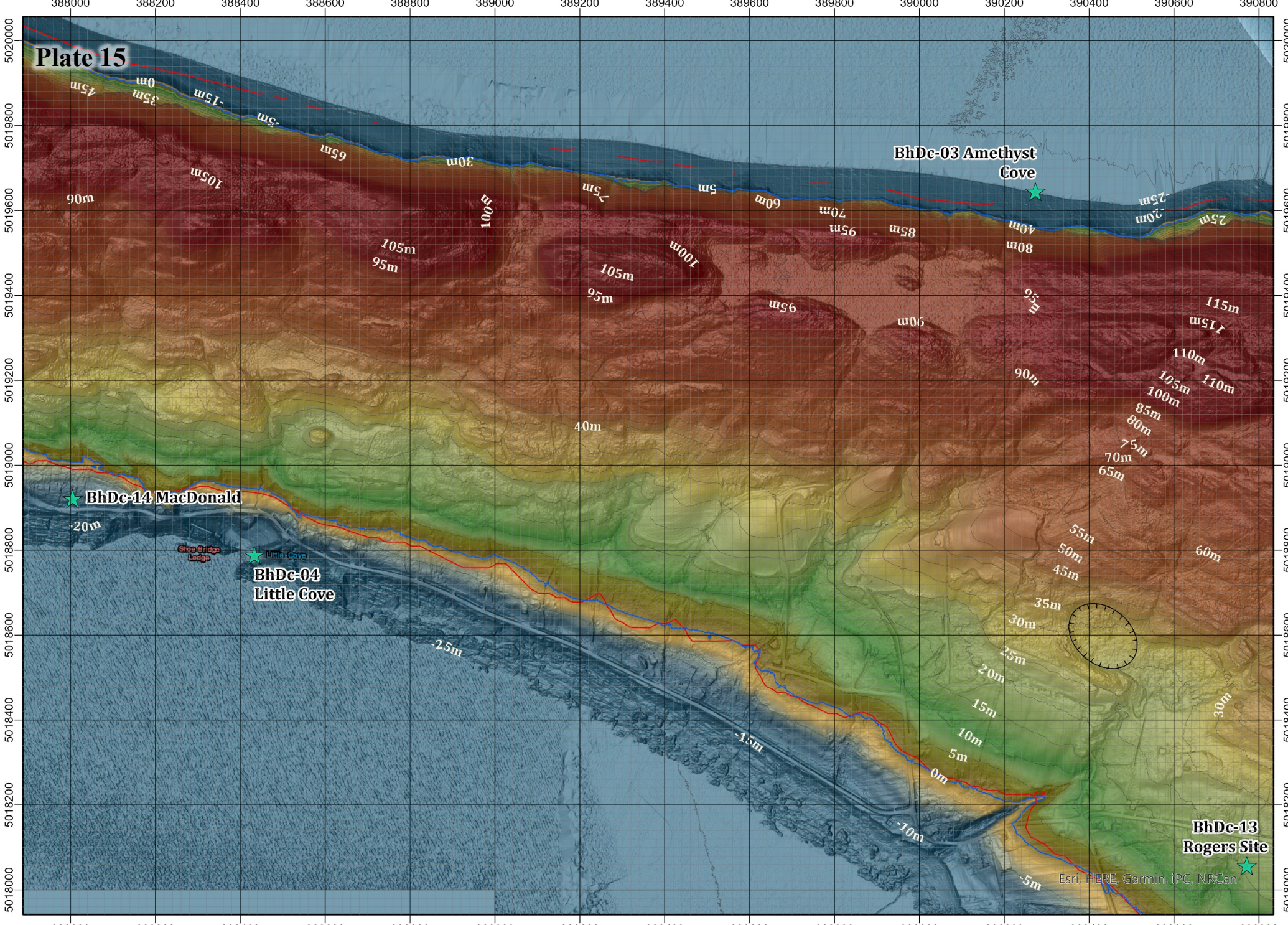
Reference Section	Mineral Occurrence	Artifacts from 2020	Lacustrine Limit (Paradis et. al, 2006)	Nearshore Deposits (Paradis et. al, 2006)	Paleo-elevation
Dated Sample (Dalton et. al, 2020)	Raised Beach Cusps (This Study)	Raised Beach Ridge (Paradis et. al, 2006)	Ice Sheet Limit (Dalton et. al, 2020)	Delta	<p>Metres</p>
Archaeological Site	Modelled Marine Limit (1m)	Raised Terrace (Paradis et. al, 2006)	Ice Sheet Limit (Dalton et. al, 2020)	Ring Features (This Study)	

Cartography: Wesley Weatherbee, CRS: NAD1983 CSRS UTM Zone 20N. Black grid squares are 200m². Grey grid squares are 20m². Contains information licensed under the Open Government License - Nova Scotia.

0 100 200 M

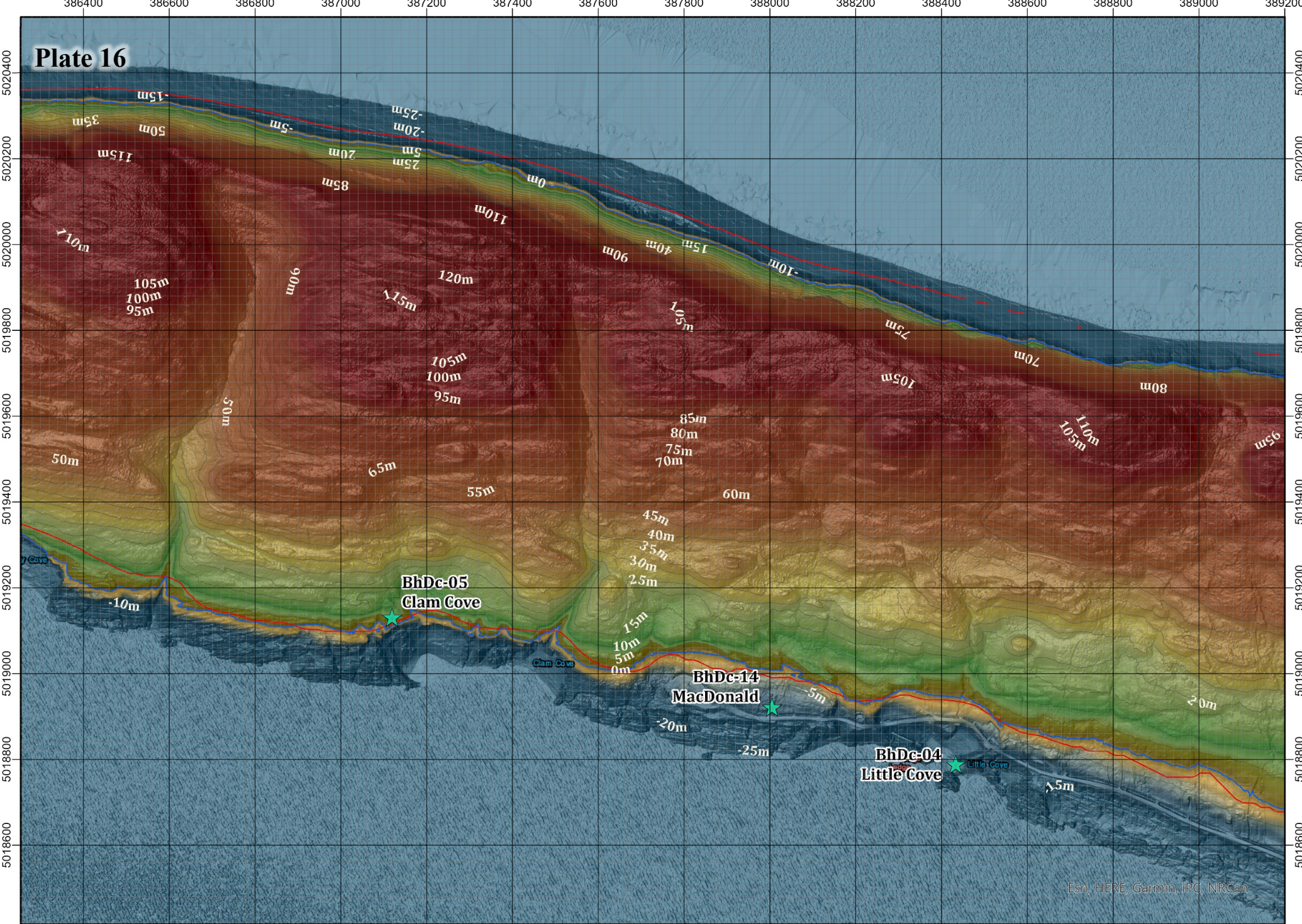
Contour (5m)

Esri, HERE, Garmin, IPC, NRCAN



Reference Section	Mineral Occurrence	Artifacts from 2020	Lacustrine Limit (Paradis et. al, 2006)	Nearshore Deposits (Paradis et. al, 2006)	Paleo-elevation
Dated Sample (Dalton et. al, 2020)	Raised Beach Cusps (This Study)	Raised Beach Ridge (Paradis et. al, 2006)	Ice Sheet Limit (Dalton et. al, 2020)	Metres	Cartography: Wesley Weatherbee, CRS: NAD1983 CSRS UTM Zone 20N. Black grid squares are 200m ² . Grey grid squares are 20m ² . Contains information licensed under the Open Government License - Nova Scotia.
Archaeological Site	Modelled Marine Limit (1m)	Raised Terrace (Paradis et. al, 2006)	Modelled Marine Limit (20m)	-10	
Delta	Ring Features (This Study)				N 0 100 200 M

Plate 16

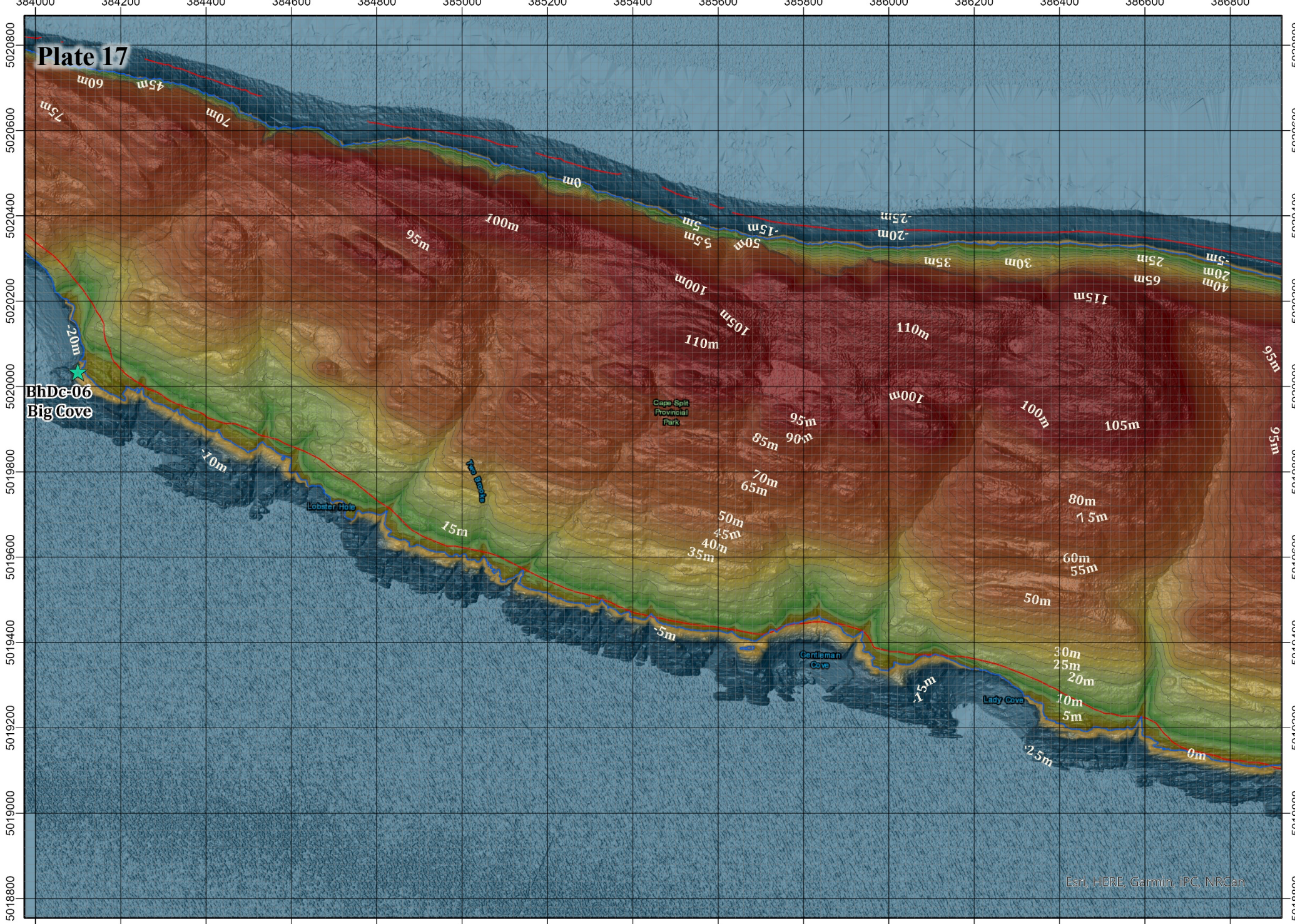


Reference Section	Mineral Occurrence	Artifacts from 2020	Lacustrine Limit (Paradis et. al, 2006)	Nearshore Deposits (Paradis et. al, 2006)	Paleo-elevation
Dated Sample (Dalton et. al, 2020)	Raised Beach Cusps (This Study)	Raised Beach Ridge (Paradis et. al, 2006)	Ice Sheet Limit (Dalton et. al, 2020)	Ring Features (This Study)	Contour (5m)
Delta	Archaeological Site	Modelled Marine Limit (1m)	Raised Terrace (Paradis et. al, 2006)		
	Modelled Marine Limit (20m)				

Metres
100
-10

Cartography: Wesley Weatherbee. CRS: NAD1983 CSRS UTM Zone 20N. Black grid squares are 200m². Grey grid squares are 20m². Contains information licensed under the Open Government License - Nova Scotia.

0 100 200 M



Legend

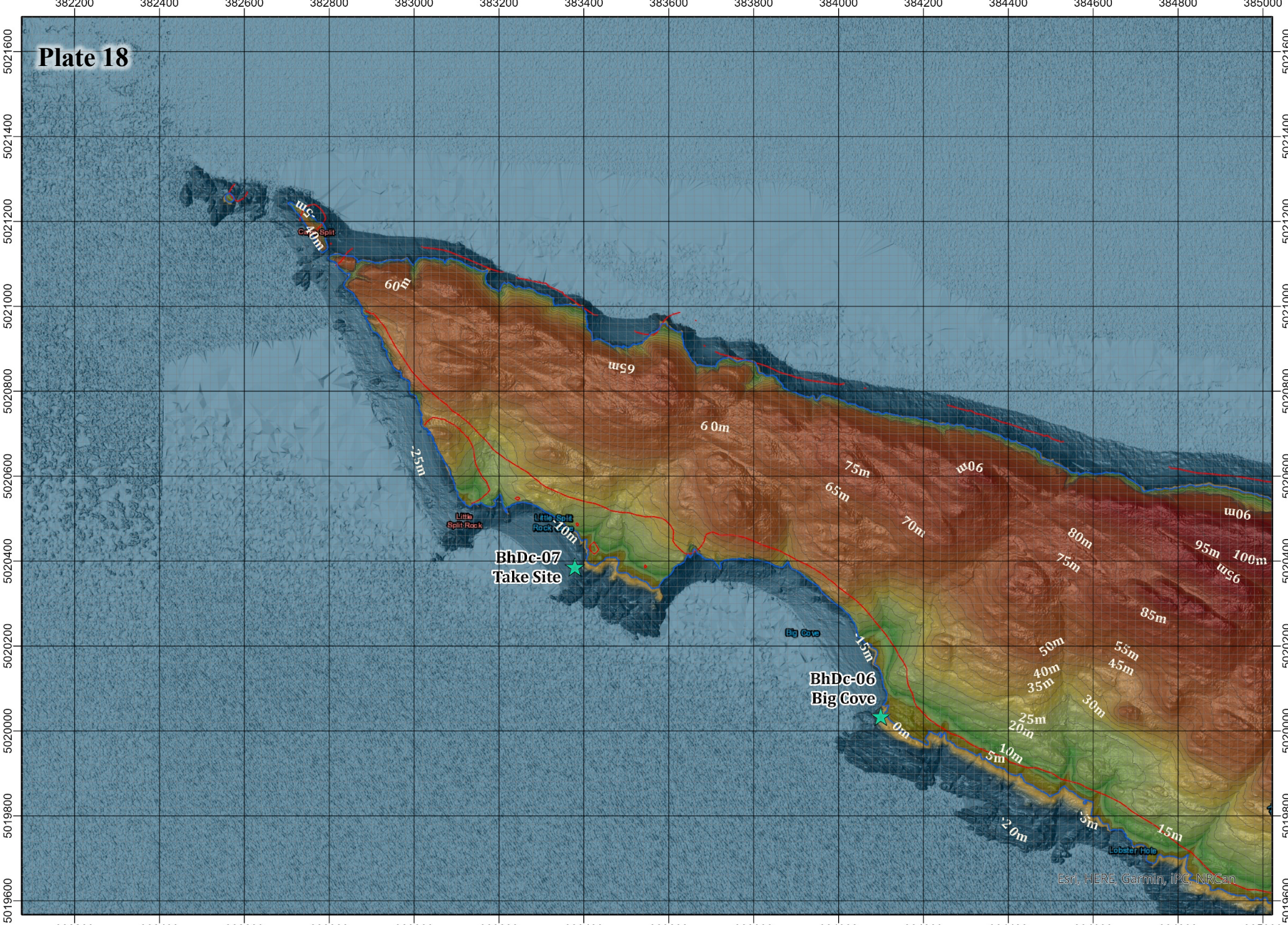
Reference Section	Mineral Occurrence	Artifacts from 2020	Lacustrine Limit (Paradis et al, 2006)	Nearshore Deposits (Paradis et al, 2006)	Paleo-elevation
Dated Sample (Dalton et al, 2020)	Archaeological Site	Raised Beach Cusps (This Study)	Ice Sheet Limit (Dalton et al, 2020)	Raised Beach Ridge (Paradis et al, 2006)	Contour (5m)
Delta		Modelled Marine Limit (1m)	Raised Terrace (Paradis et al, 2006)	Ring Features (This Study)	
		Modelled Marine Limit (20m)			

Cartography: Wesley Weatherbee. CRS: NAD1983 CSRS UTM Zone 20N. Black grid squares are 200m². Grey grid squares are 20m². Contains information licensed under the Open Government License - Nova Scotia.

Scale: 0 100 200 M

Source: Esri, HERE, Garmin, IPC, NRCAN

Plate 18

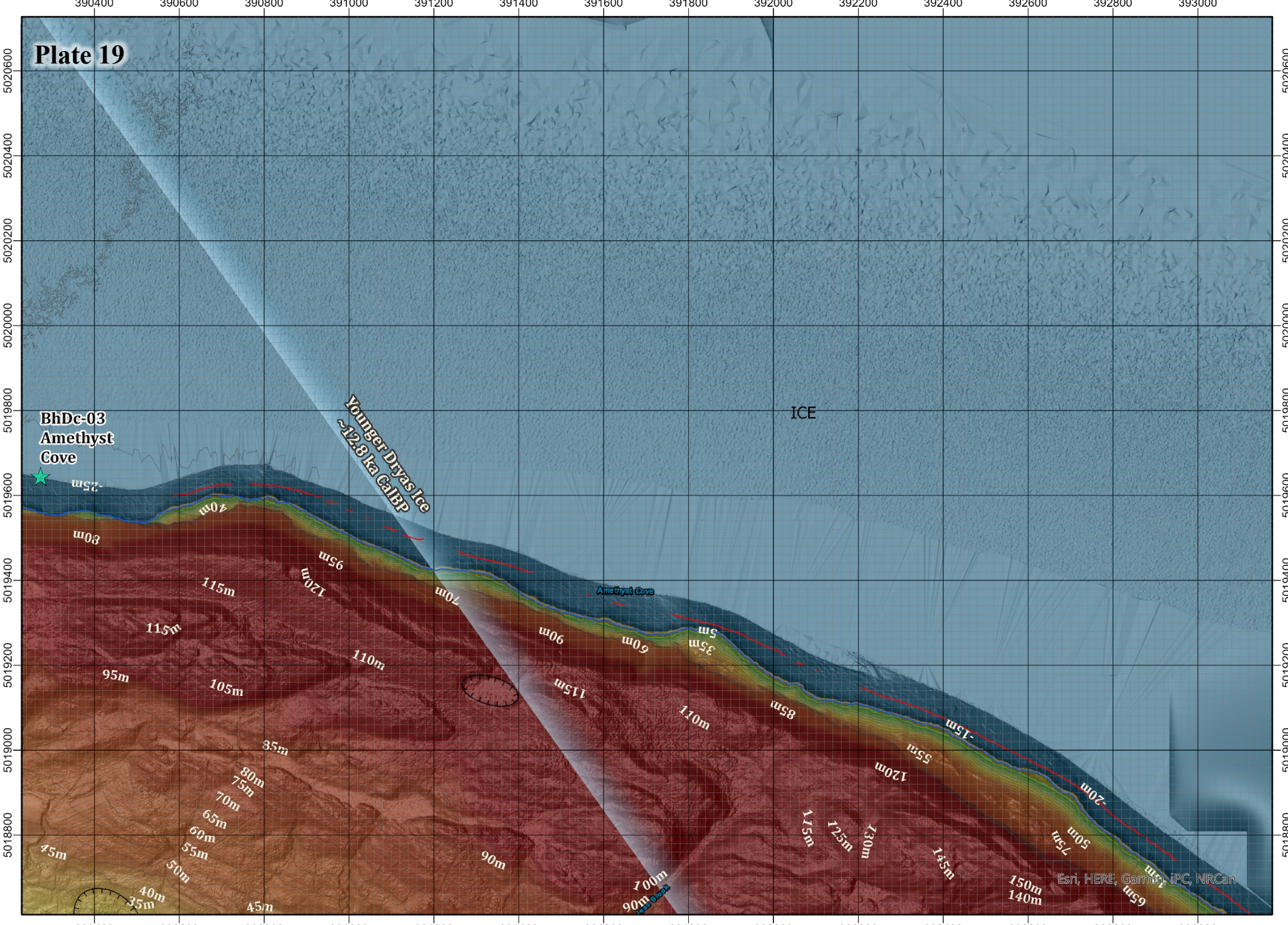


Reference Section	Mineral Occurrence	Artifacts from 2020	Lacustrine Limit (Paradis et. al, 2006)	Nearshore Deposits (Paradis et. al, 2006)	Metres 100 -10
Dated Sample (Dalton et. al, 2020)	Raised Beach Cusps (This Study)	Raised Beach Ridge (Paradis et. al, 2006)	Ice Sheet Limit (Dalton et. al, 2020)	Modelled Marine Limit (1m)	
Delta	Archaeological Site	Modelled Marine Limit (20m)	Raised Terrace (Paradis et. al, 2006)	Ring Features (This Study)	Contour (5m) 0 100 200 M

Cartography: Wesley Weatherbee, CRS: NAD1983 CSRS UTM Zone 20N. Black grid squares are 200m². Grey grid squares are 20m². Contains information licensed under the Open Government License - Nova Scotia.

Esri, HERE, Garmin, iPC, NRCAN

Plate 19



Reference Section	Mineral Occurrence	Artifacts from 2020	Lacustrine Limit (Paradis et. al, 2006)	Nearshore Deposits (Paradis et. al, 2006)	Paleo-elevation
Dated Sample (Dalton et. al, 2020)	Archaeological Site	Raised Beach Cusps (This Study)	Modelled Marine Limit (1m)	Ice Sheet Limit (Dalton et. al, 2020)	<p>Cartography: Wesley Weatherbee, CRS: NAD1983 CSRS UTM Zone 20N. Black grid squares are 200m². Grey grid squares are 20m². Contains information licensed under the Open Government License - Nova Scotia.</p> <p>0 100 200 M</p>
Delta	Modelled Marine Limit (20m)	Raised Beach Ridges (Paradis et. al, 2006)	Ring Features (This Study)	Raised Terrace (Paradis et. al, 2006)	

Plate 20

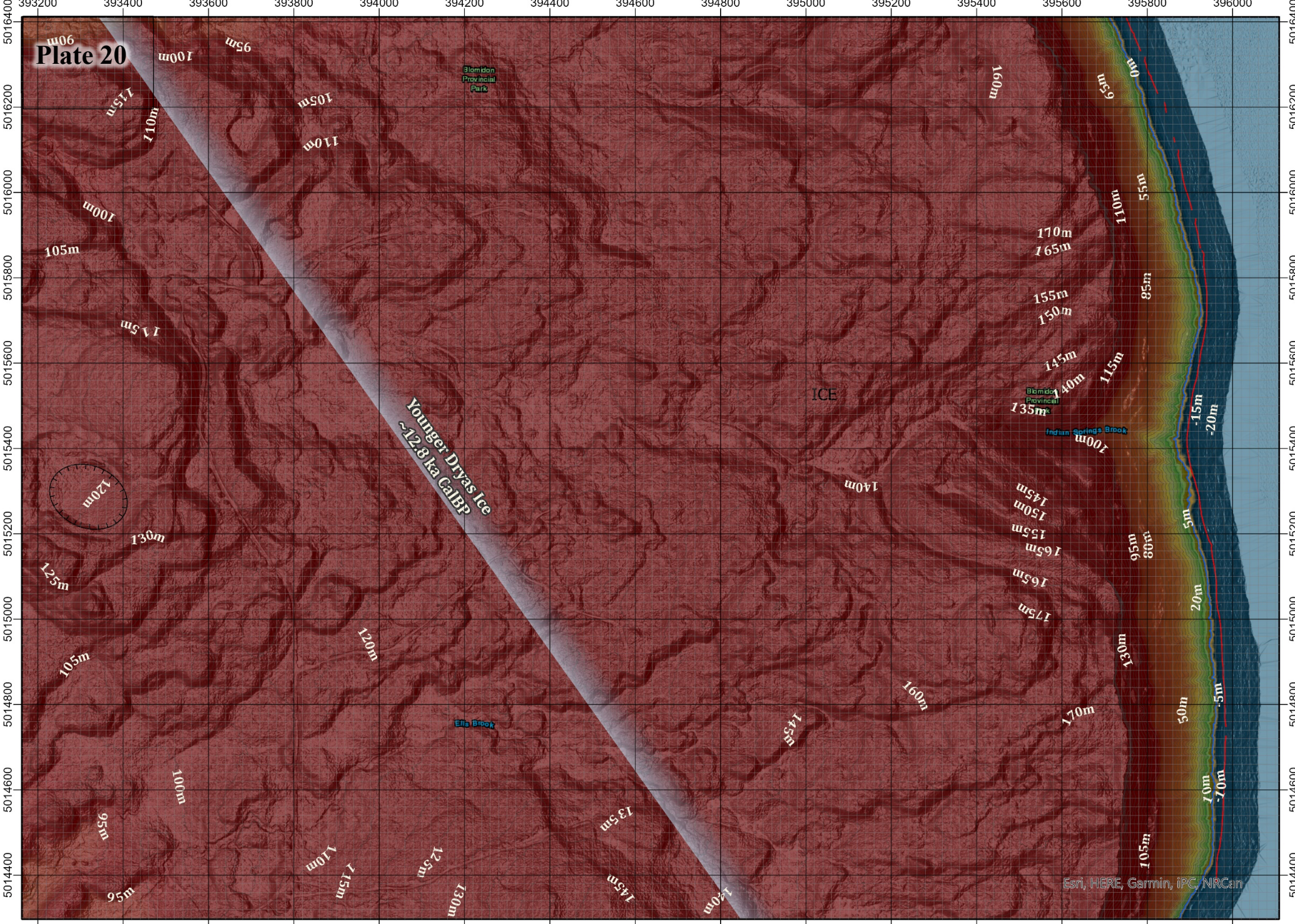
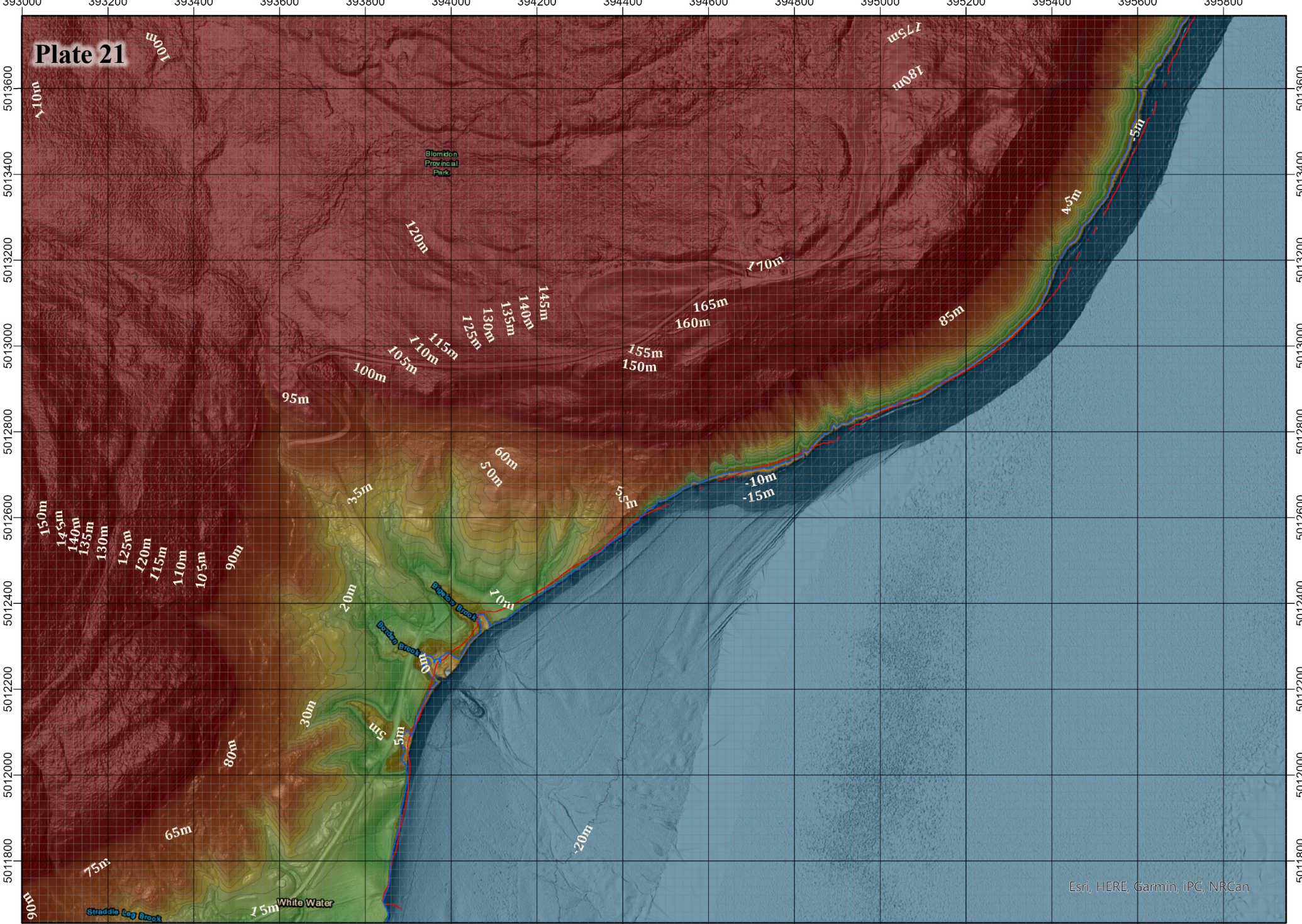


Plate 21

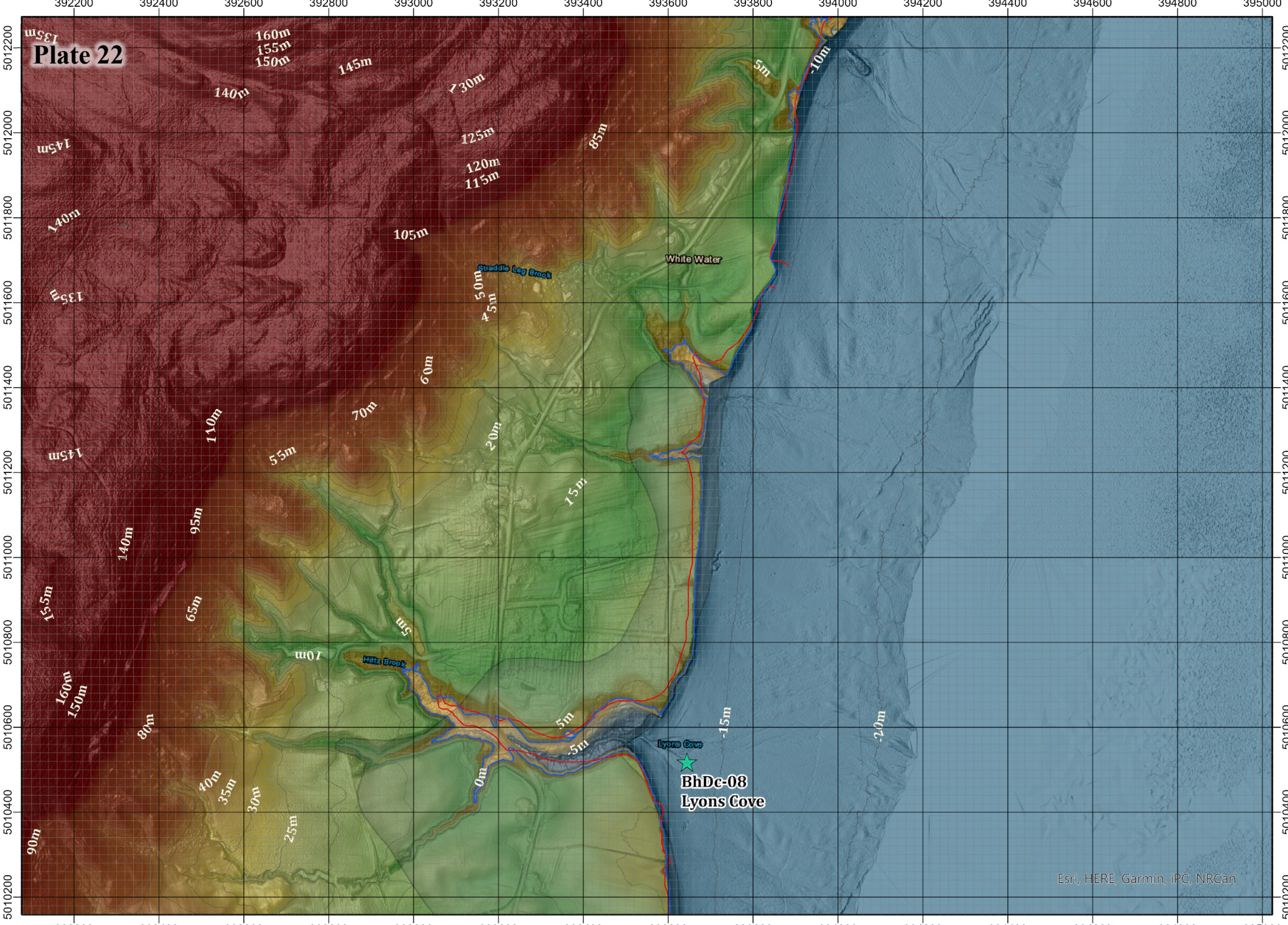


Reference Section	Artifacts from 2020	Lacustrine Limit (Paradis et. al, 2006)	Nearshore Deposits (Paradis et. al, 2006)	Paleo-elevation	<p>Cartography: Wesley Weatherbee. CRS: NAD1983 CSRS UTM Zone 20N. Black grid squares are 200m². Grey grid squares are 20m². Contains information licensed under the Open Government License - Nova Scotia.</p> <p>0 100 200 M</p>
Dated Sample (Dalton et. al, 2020)	Raised Beach Cusps (This Study)	Raised Beach Ridge (Paradis et. al, 2006)	Ice Sheet Limit (Dalton et. al, 2020)	<p>Metres</p> <p>100</p> <p>-10</p>	
Archaeological Site	Modelled Marine Limit (1m)	Raised Terrace (Paradis et. al, 2006)	Modelled Marine Limit (20m)		
Delta	Ring Features (This Study)				

Esri, HERE, Garmin, IPC, NRCan

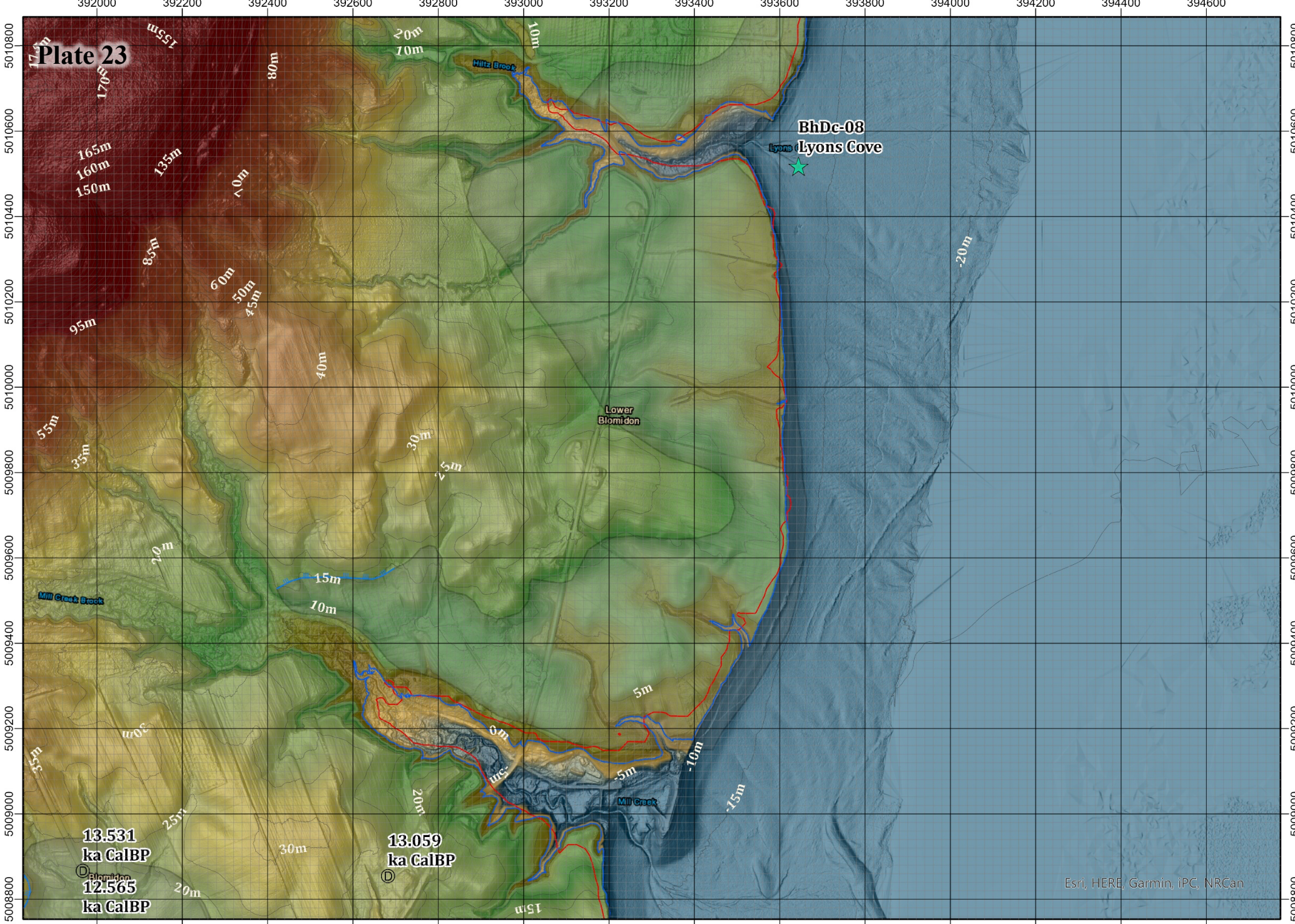


Plate 22



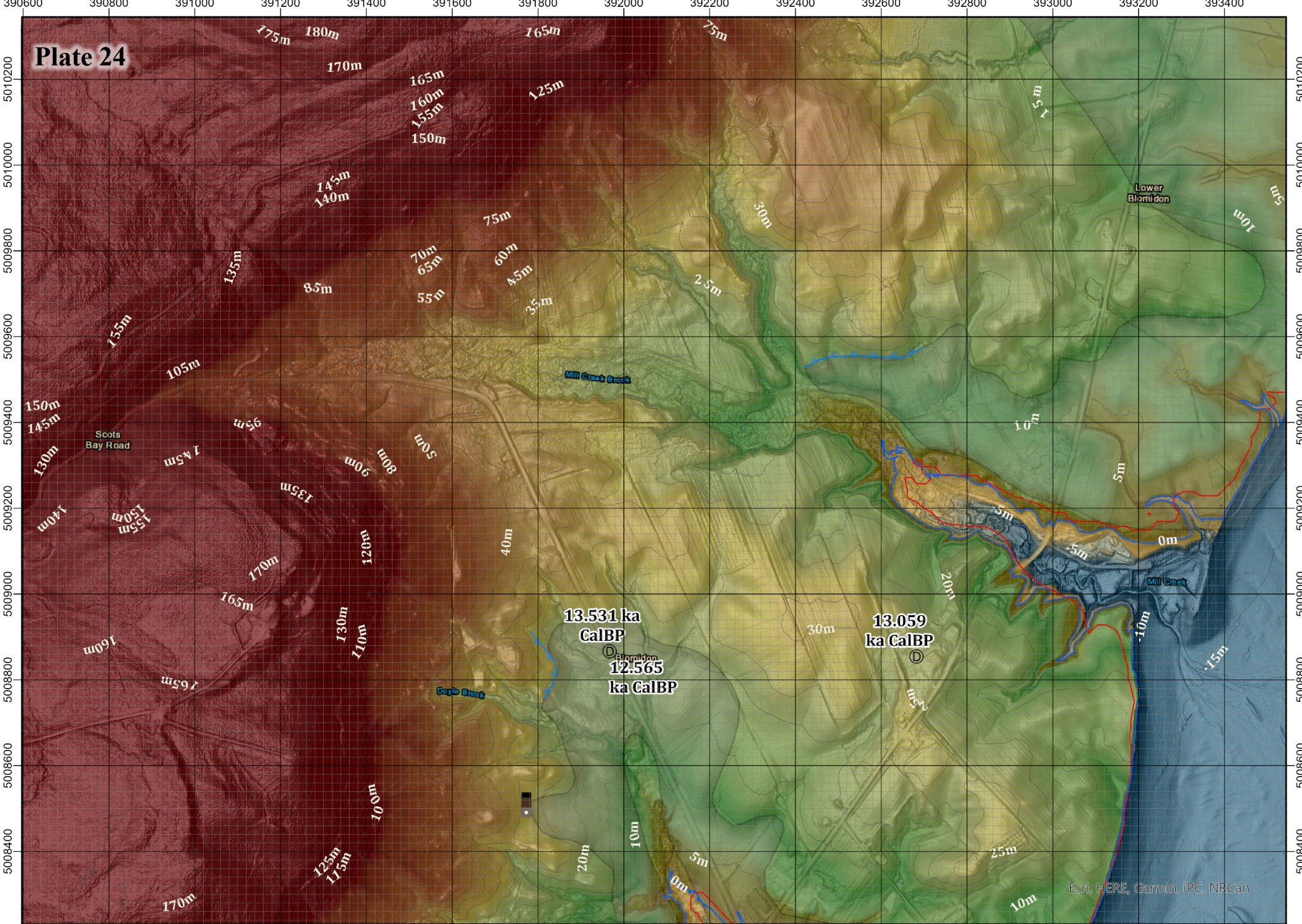
Esri, HERE, Garmin, IPC, NRCan

Reference Section	Mineral Occurrence	Artifacts from 2020	Lacustrine Limit (Paradis et. al, 2006)	Nearshore Deposits (Paradis et. al, 2006)	Palco-elevation Metres 100 -10
Dated Sample (Dalton et. al, 2020)	Raised Beach Cusps (This Study)	Modelled Marine Limit (1m)	Ice Sheet Limit (Dalton et. al, 2020)	Delta	
Delta	Archaeological Site	Modelled Marine Limit (20m)	Raised Beach Ridge (Paradis et. al, 2006)	Raised Terrace (Paradis et. al, 2006)	Cartography: Wesley Weatherbee, CRS: NAD1983 CSRS UTM Zone 20N. Black grid squares are 200m ² . Grey grid squares are 20m ² . Contains information licensed under the Open Government License - Nova Scotia. 0 100 200 M
			Ring Features (This Study)		



<ul style="list-style-type: none"> Reference Section Delta 	<ul style="list-style-type: none"> Mineral Occurrence Dated Sample (Dalton et. al, 2020) Archaeological Site 	<ul style="list-style-type: none"> Artifacts from 2020 Raised Beach Cusps (This Study) Modelled Marine Limit (1m) Modelled Marine Limit (20m) 	<ul style="list-style-type: none"> Lacustrine Limit (Paradis et. al, 2006) Raised Beach Ridge (Paradis et. al, 2006) Raised Terrace (Paradis et. al, 2006) Ring Features (This Study) 	<ul style="list-style-type: none"> Nearshore Deposits (Paradis et. al, 2006) Ice Sheet Limit (Dalton et. al, 2020) 	<p>Metres</p> <p>0 100 200 M</p> <p>Contour (5m)</p>	<p>Cartography: Wesley Weatherbee, CRS: NAD1983 CSRS UTM Zone 20N. Black grid squares are 200m². Grey grid squares are 20m². Contains information licensed under the Open Government License - Nova Scotia.</p> <p>Esri, HERE, Garmin, IPC, NRCan</p>
--	---	---	---	--	--	---

Plate 24



Reference Section	Artifacts from 2020	Lacustrine Limit (Paradis et. al, 2006)	Nearshore Deposits (Paradis et. al, 2006)	Paleo-elevation
Dated Sample (Dalton et. al, 2020)	Raised Beach Cusps (This Study)	Raised Beach Ridge (Paradis et. al, 2006)	Ice Sheet Limit (Dalton et. al, 2020)	Contour (5m)
Archaeological Site	Modelled Marine Limit (1m)	Raised Terrace (Paradis et. al, 2006)	Ring Features (This Study)	0 100 200 M
Delta	Modelled Marine Limit (20m)			N

Cartography: Wesley Weatherbee, CRS: NAD1983 CSRS UTM Zone 20N. Black grid squares are 200m². Grey grid squares are 20m². Contains information licensed under the Open Government License - Nova Scotia.

Esri, HERE, Garmin, IPC, NRCan

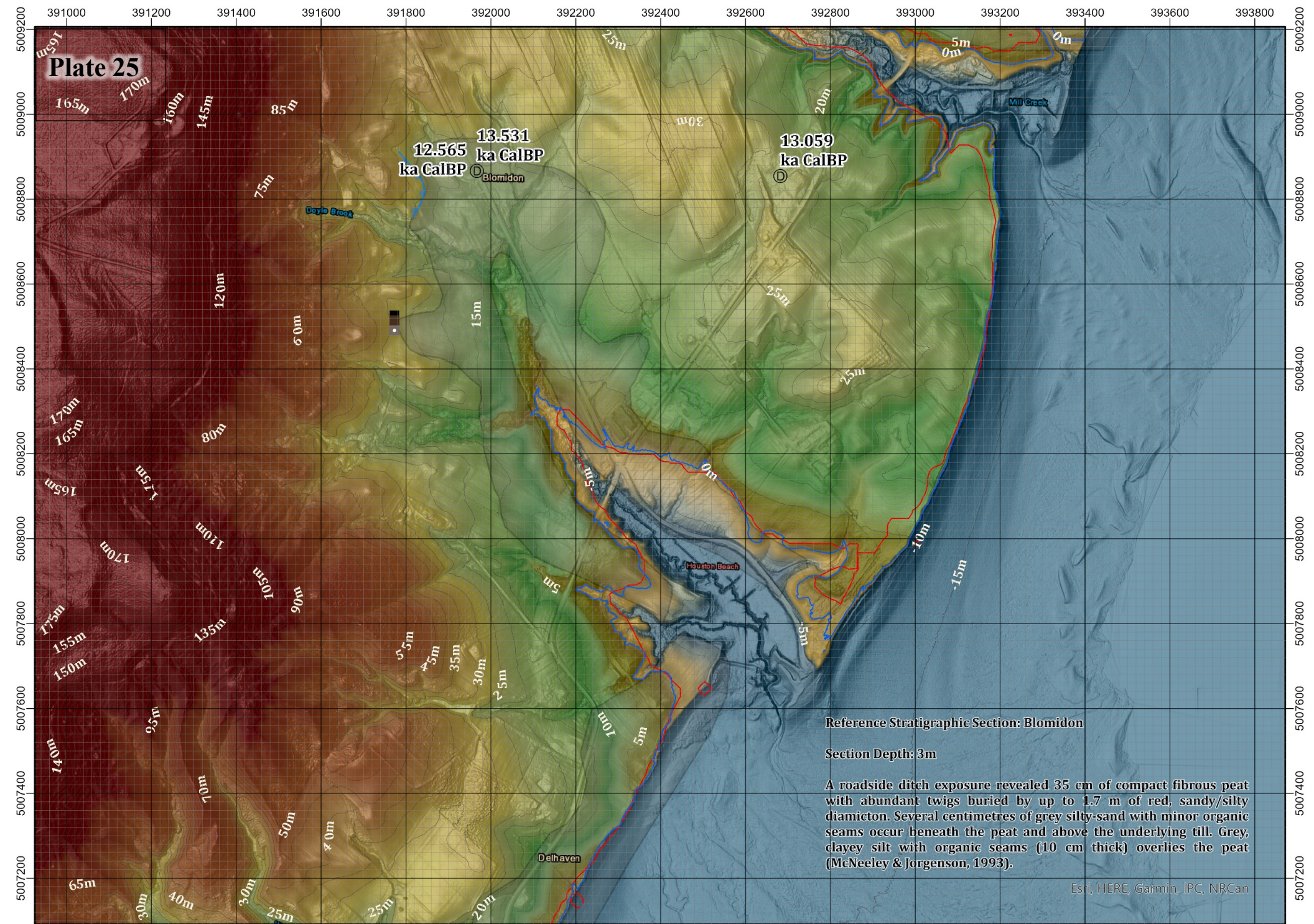


Plate 25

12.565 ka CalBP
 13.531 ka CalBP
 13.059 ka CalBP

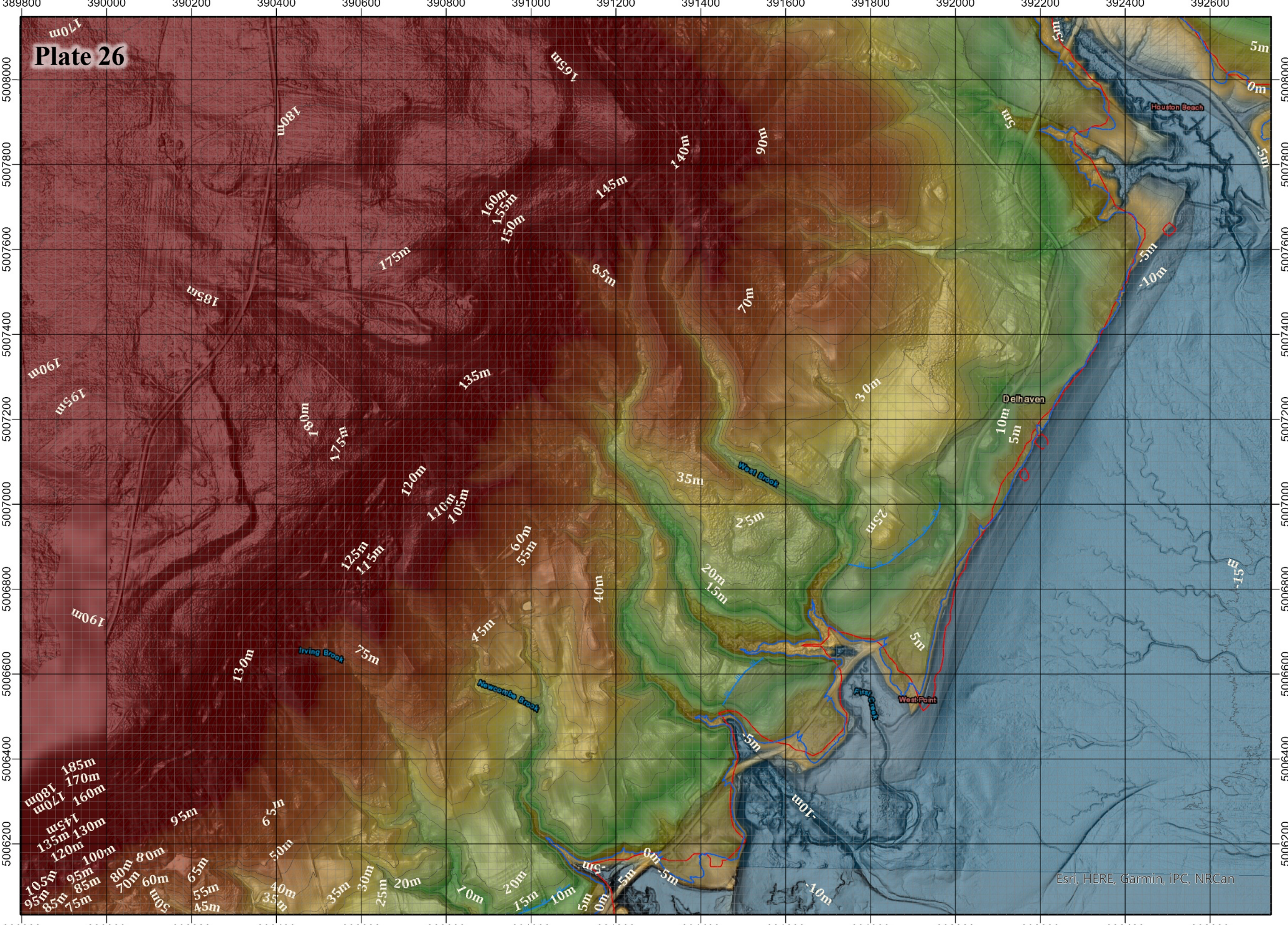
Reference Stratigraphic Section: Blomidon
 Section Depth: 3m

A roadside ditch exposure revealed 35 cm of compact fibrous peat with abundant twigs buried by up to 1.7 m of red, sandy/silty diamicton. Several centimetres of grey silty-sand with minor organic seams occur beneath the peat and above the underlying till. Grey, clayey silt with organic seams (10 cm thick) overlies the peat (McNeeley & Jorgenson, 1993).

Esri, HERE, Garmin, IPC, NRCan

<ul style="list-style-type: none"> Reference Section Dated Sample (Dalton et al, 2020) Archaeological Site Delta 	<ul style="list-style-type: none"> Artifacts from 2020 Raised Beach Cusps (This Study) Modelled Marine Limit (1m) Modelled Marine Limit (20m) 	<ul style="list-style-type: none"> Lacustrine Limit (Paradis et al, 2006) Raised Beach Ridge (Paradis et al, 2006) Raised Terrace (Paradis et al, 2006) Ring Features (This Study) 	<ul style="list-style-type: none"> Nearshore Deposits (Paradis et al, 2006) Ice Sheet Limit (Dalton et al, 2020) 	<p>Palaeo-elevation</p> <p>Metres</p> <p>0 100 200 M</p> <p>Contour (5m)</p>	<p>Cartography: Wesley Weatherbee, CRS: NAD1983 CSRS UTM Zone 20N. Black grid squares are 200m². Grey grid squares are 20m². Contains information licensed under the Open Government License - Nova Scotia.</p>
--	---	--	--	--	---

Plate 26

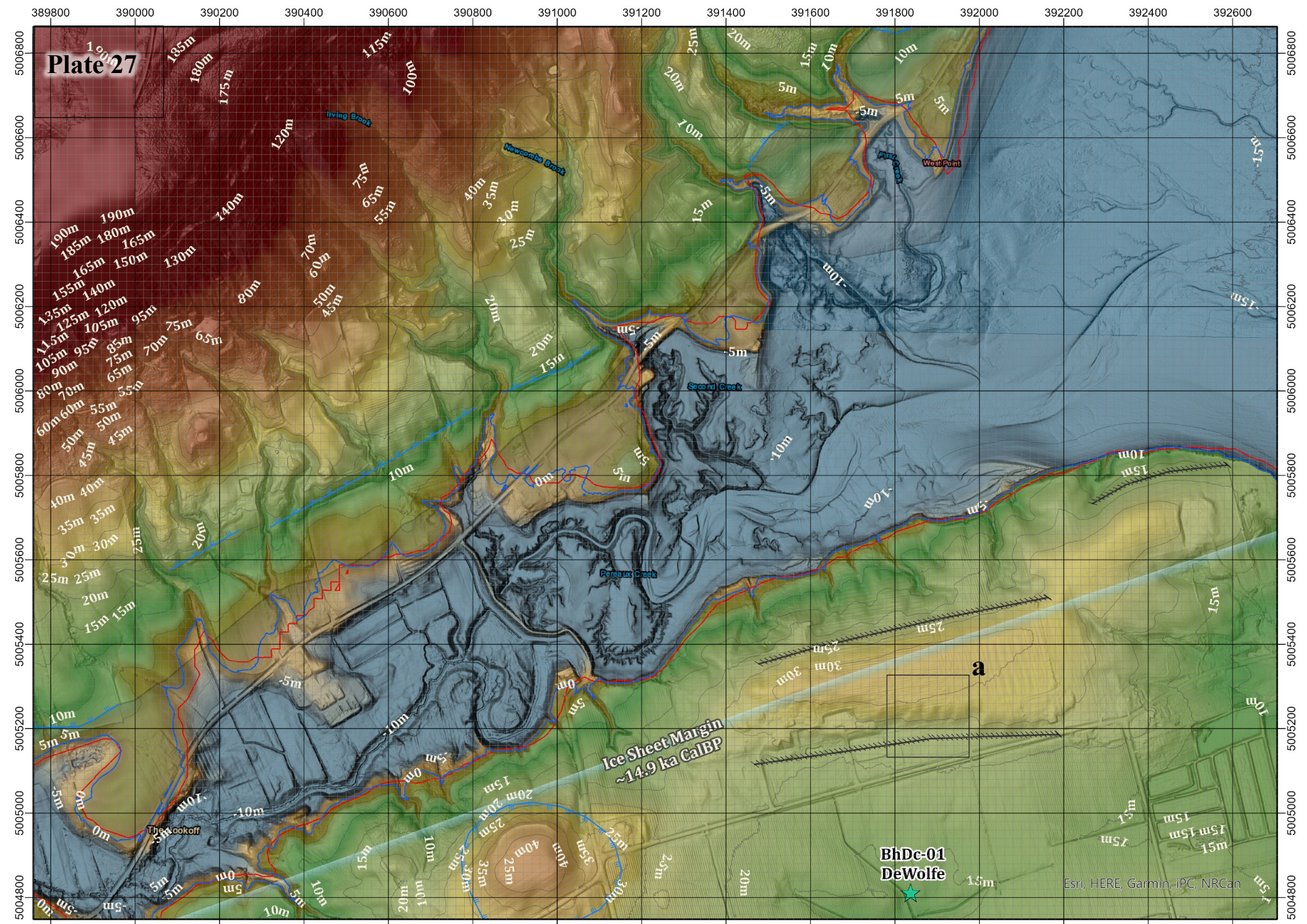


Reference Section	Artifacts from 2020	Lacustrine Limit (Paradis et. al, 2006)	Nearshore Deposits (Paradis et. al, 2006)	Paleo-elevation
Dated Sample (Dalton et. al, 2020)	Raised Beach Cusps (This Study)	Raised Beach Ridge (Paradis et. al, 2006)	Ice Sheet Limit (Dalton et. al, 2020)	Metres
Archaeological Site	Modelled Marine Limit (1m)	Raised Terrace (Paradis et. al, 2006)	Ring Features (This Study)	N
Delta	Modelled Marine Limit (20m)			0 100 200 M

Cartography: Wesley Weatherbee. CRS: NAD1983 CSRS UTM Zone 20N. Black grid squares are 200m². Grey grid squares are 20m². Contains information licensed under the Open Government License - Nova Scotia.

Esri, HERE, Garmin, IPC, NRCan

Plate 27



Reference Section	Dated Sample (Dalton et al, 2020)	Artifacts from 2020	Lacustrine Limit (Paradis et al, 2006)	Nearshore Deposits (Paradis et al, 2006)	Paleo-elevation
Delta	Archaeological Site	Modelled Marine Limit (1m)	Modelled Marine Limit (20m)	Raised Beach Cusps (This Study)	Raised Beach Ridge (Paradis et al, 2006)
		Ring Features (This Study)	Raised Terrace (Paradis et al, 2006)	Ice Sheet Limit (Dalton et al, 2020)	

Metres

 100
 -10

Contour (5m)

 0 100 200 M

Cartography: Wesley Weatherbee. CRS: NAD1983 CSRS UTM Zone 20N. Black grid squares are 200m². Grey grid squares are 20m². Contains information licensed under the Open Government License - Nova Scotia.

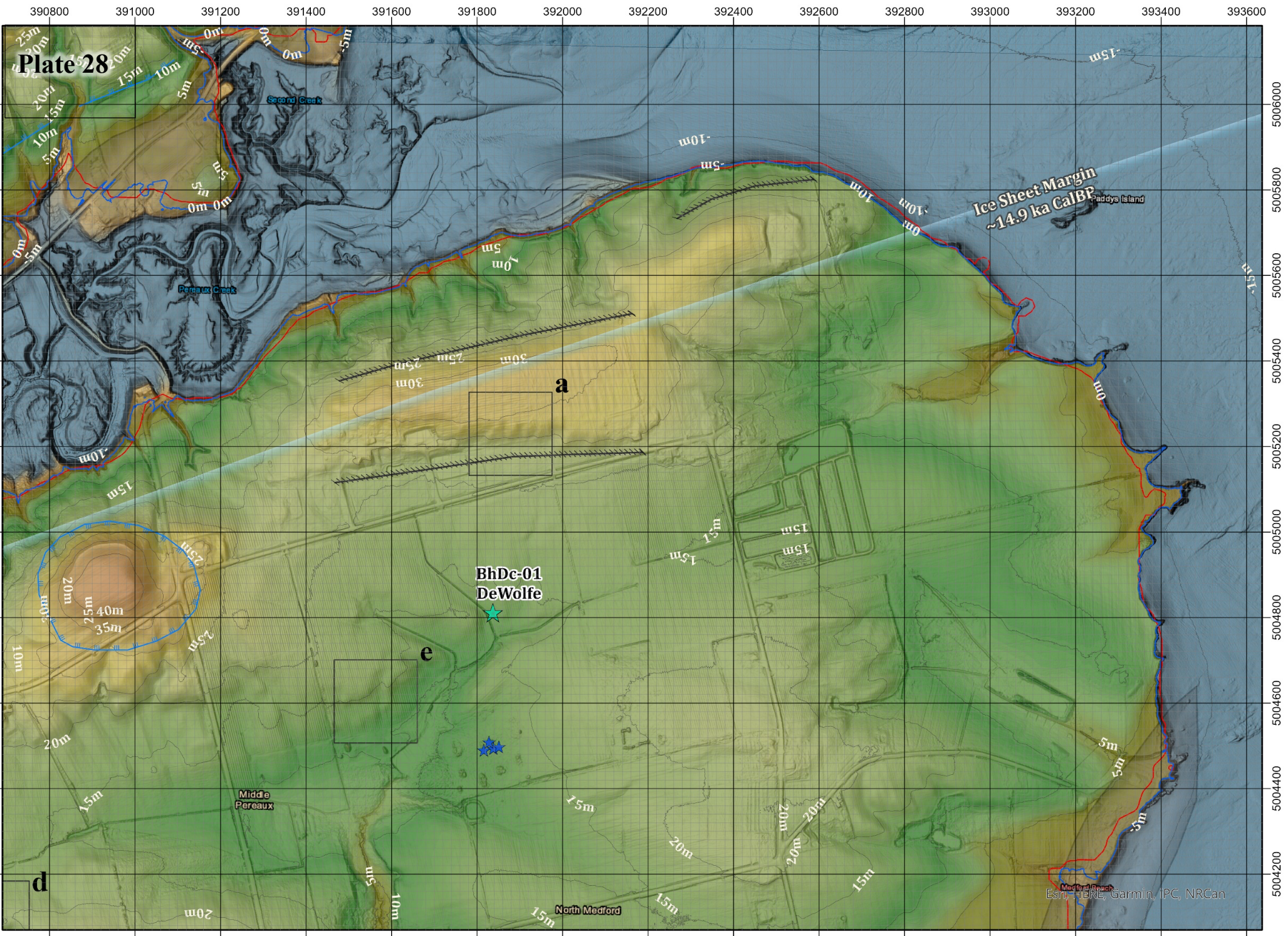


Plate 28

**Ice Sheet Margin
~14.9 ka CalBP**

**BhDc-01
DeWolfe**

Esri, HERE, Garmin, IPC, NRCan

Reference Section	Mineral Occurrence	Artifacts from 2020	Lacustrine Limit (Paradis et. al, 2006)	Nearshore Deposits (Paradis et. al, 2006)	Paleo-elevation
Dated Sample (Dalton et. al, 2020)	Raised Beach Cusps (This Study)	Raised Beach Ridge (Paradis et. al, 2006)	Ice Sheet Limit (Dalton et. al, 2020)	Raised Terrace (Paradis et. al, 2006)	Metres
Delta	Archaeological Site	Modelled Marine Limit (1m)	Ring Features (This Study)		100 -10
					Contour (5m)

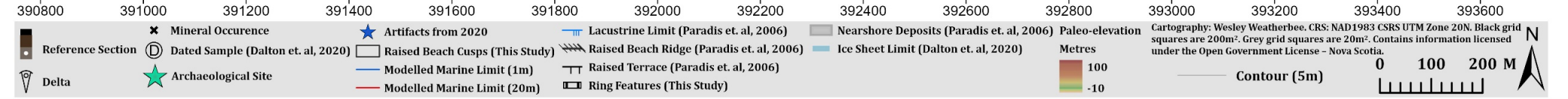
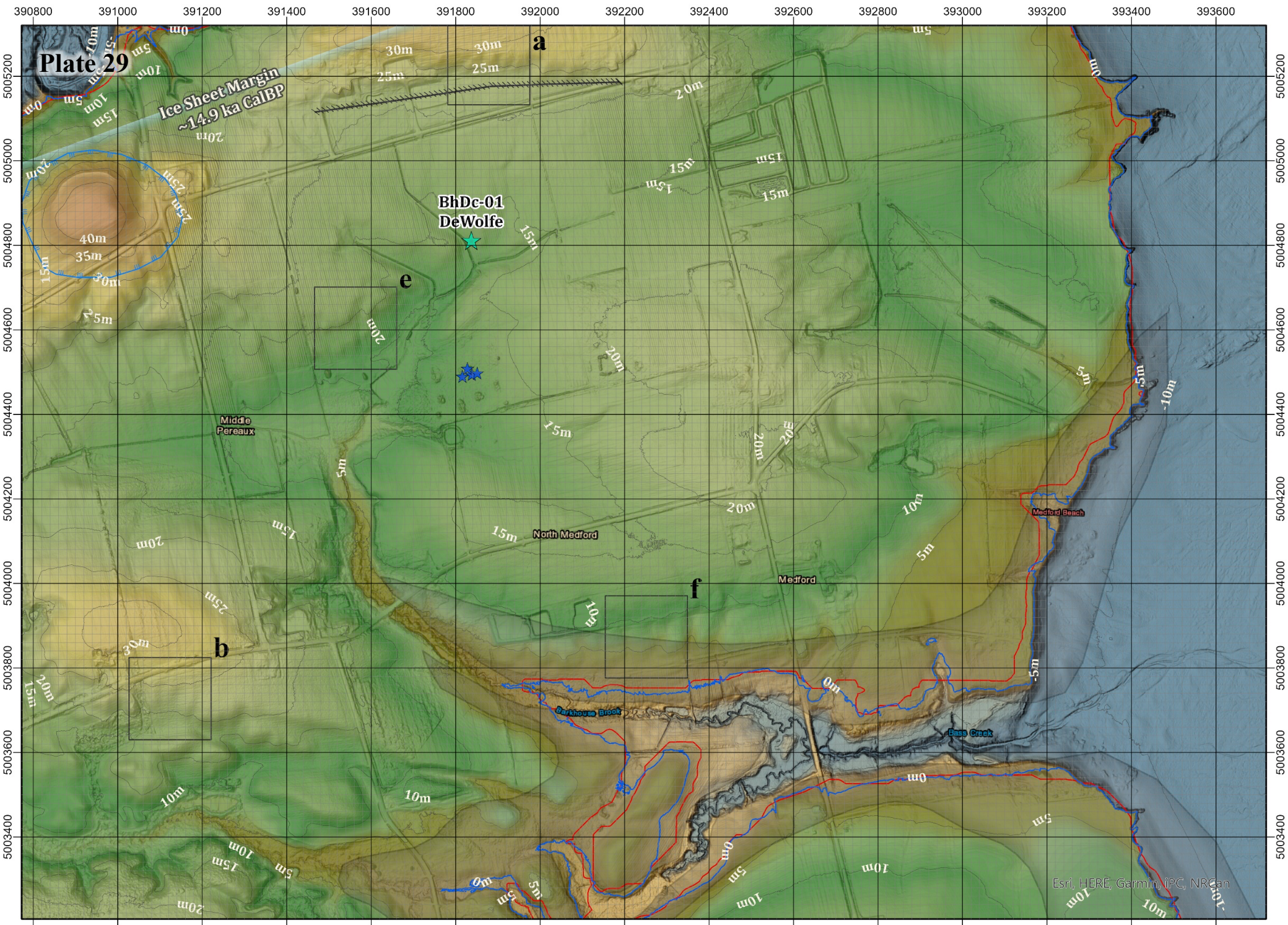
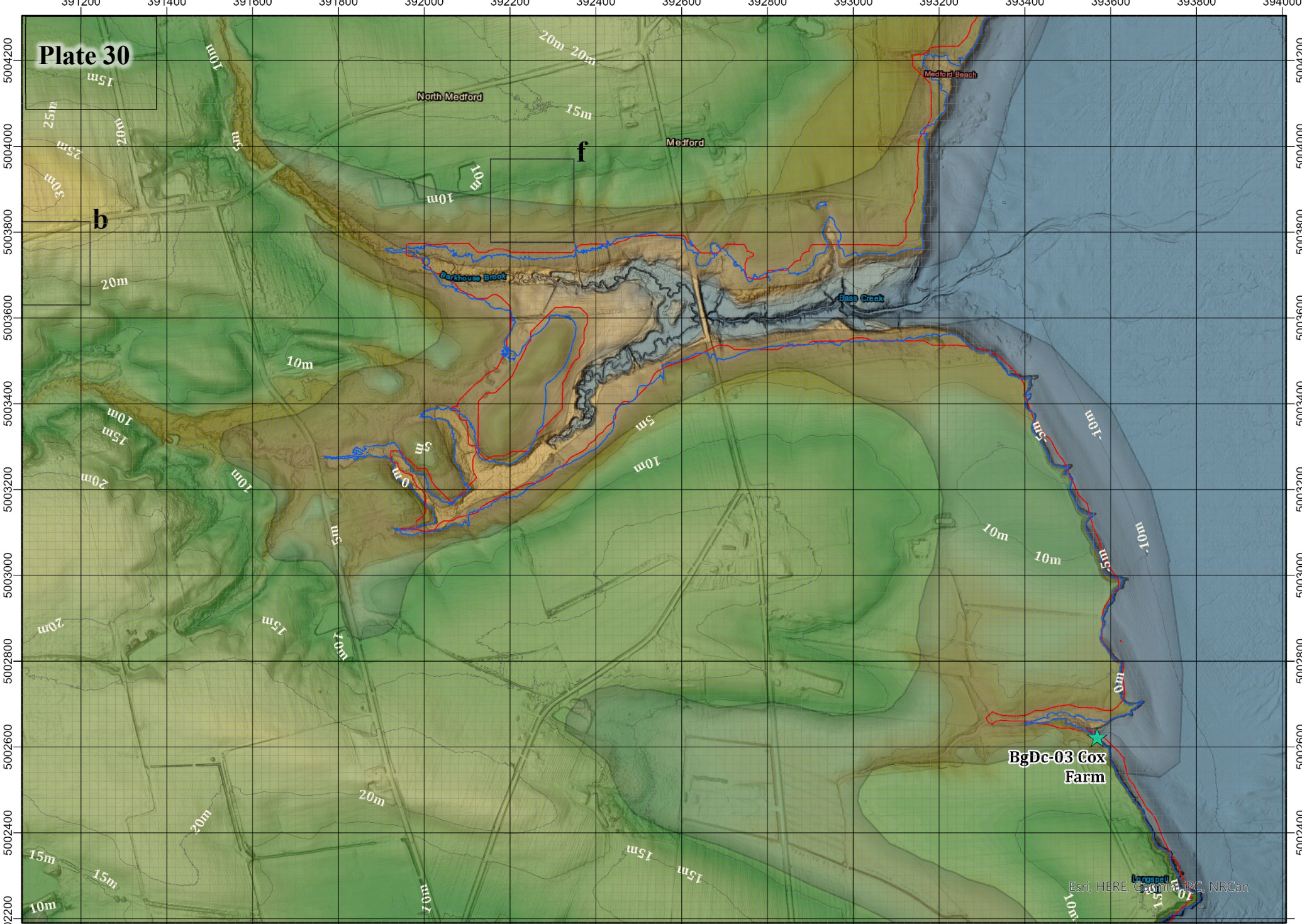


Plate 30



Reference Section	Mineral Occurrence	Artifacts from 2020	Lacustrine Limit (Paradis et. al, 2006)	Nearshore Deposits (Paradis et. al, 2006)	Paleo-elevation Metres
Dated Sample (Dalton et. al, 2020)	Raised Beach Cusps (This Study)	Raised Beach Ridge (Paradis et. al, 2006)	Ice Sheet Limit (Dalton et. al, 2020)	Modelled Marine Limit (1m)	
Delta	Archaeological Site	Raised Terrace (Paradis et. al, 2006)	Ring Features (This Study)	Modelled Marine Limit (20m)	 0 100 200 M

Cartography: Wesley Weatherbee. CRS: NAD1983 CSRS UTM Zone 20N. Black grid squares are 200m². Grey grid squares are 20m². Contains information licensed under the Open Government License - Nova Scotia.

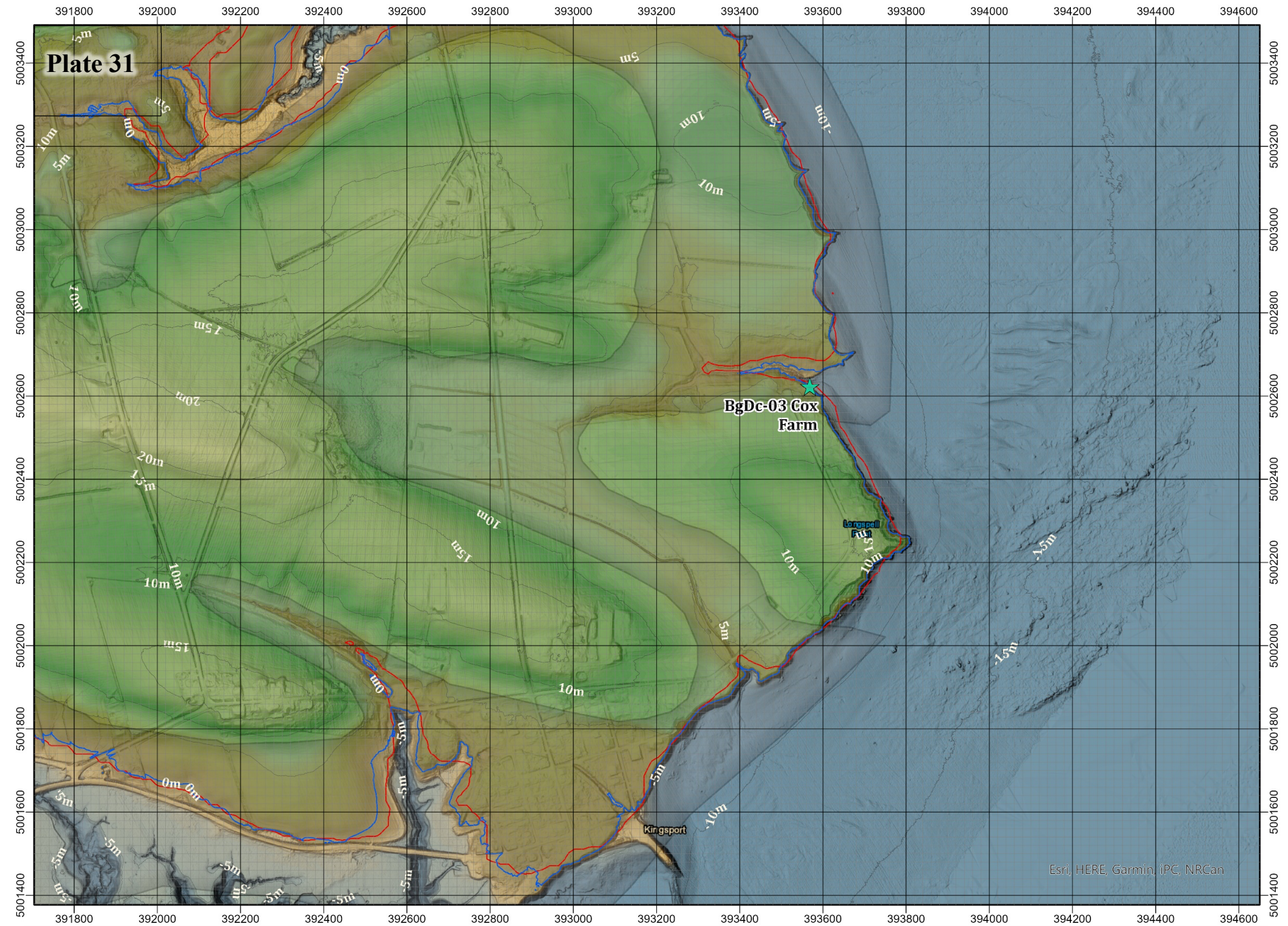


Plate 31

BgDc-03 Cox Farm

Longspell Farm

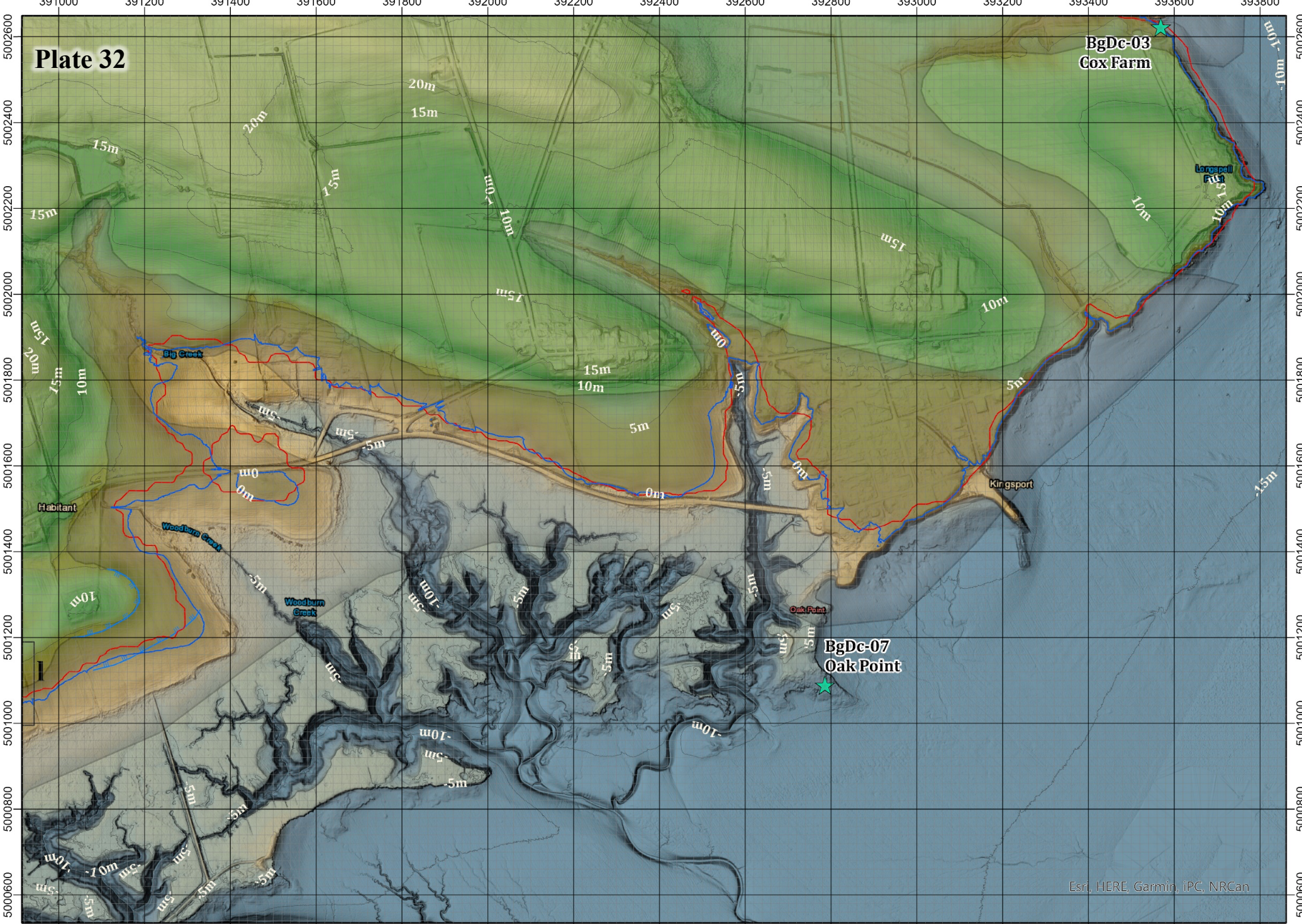
Kingsport

Esri, HERE, Garmin, IPC, NRCan

Reference Section	Mineral Occurrence	Artifacts from 2020	Lacustrine Limit (Paradis et. al, 2006)	Nearshore Deposits (Paradis et. al, 2006)	Paleo-elevation Metres 100 -10
Dated Sample (Dalton et. al, 2020)	Raised Beach Cusps (This Study)	Raised Beach Ridge (Paradis et. al, 2006)	Ice Sheet Limit (Dalton et. al, 2020)	Modelled Marine Limit (1m)	<p>0 100 200 M</p>
Delta	Archaeological Site	Raised Terrace (Paradis et. al, 2006)	Modelled Marine Limit (20m)	Ring Features (This Study)	

Cartography: Wesley Weatherbee. CRS: NAD1983 CSRS UTM Zone 20N. Black grid squares are 200m². Grey grid squares are 20m². Contains information licensed under the Open Government License - Nova Scotia.

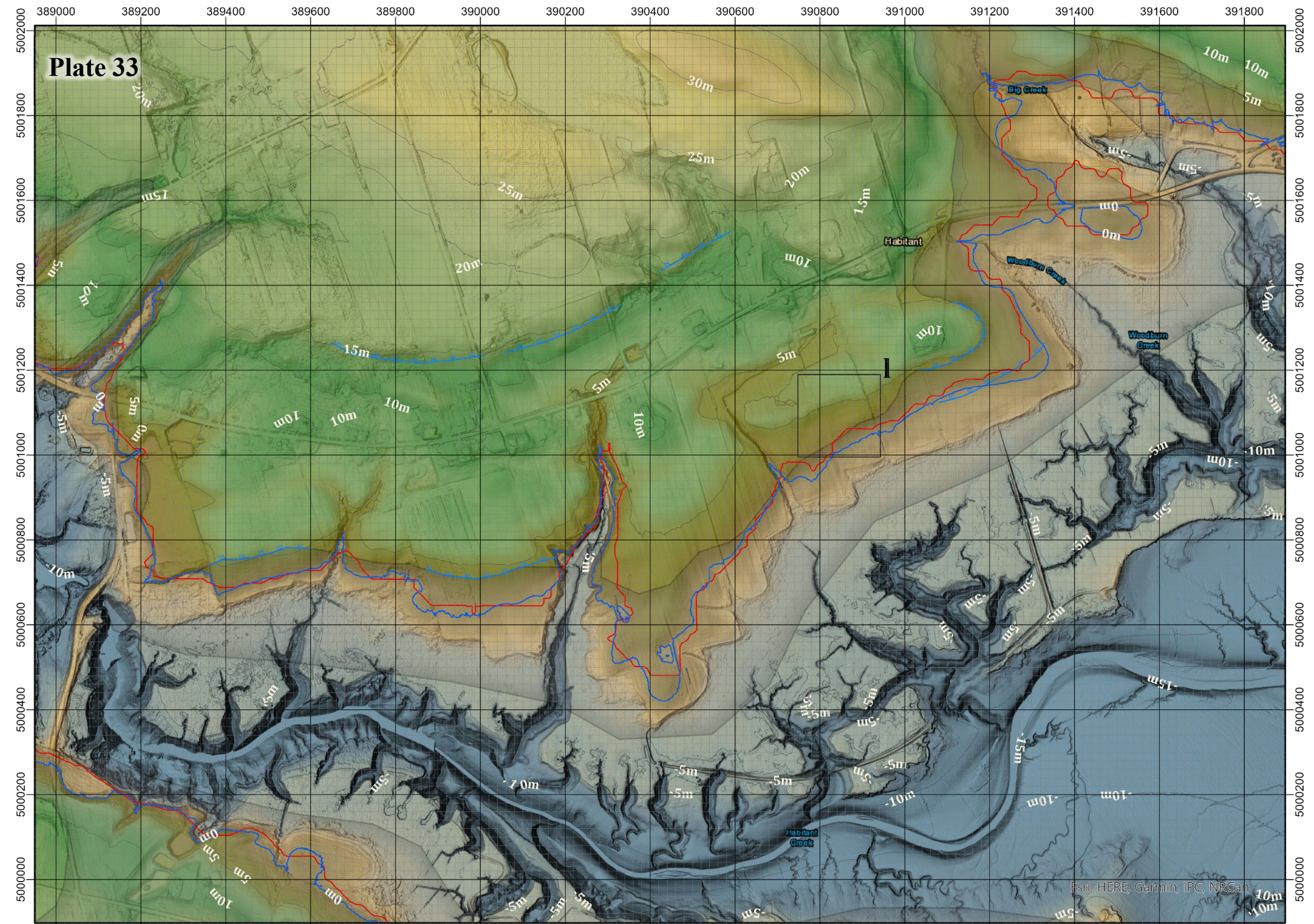
Plate 32



Reference Section	Mineral Occurrence	Artifacts from 2020	Lacustrine Limit (Paradis et al, 2006)	Nearshore Deposits (Paradis et al, 2006)	Paleo-elevation
Dated Sample (Dalton et al, 2020)	Raised Beach Cusps (This Study)	Modelled Marine Limit (1m)	Ice Sheet Limit (Dalton et al, 2020)	Raised Beach Ridge (Paradis et al, 2006)	<p>Metres</p> <p>0 100 200 M</p>
Delta	Archaeological Site	Modelled Marine Limit (20m)	Ring Features (This Study)	Raised Terrace (Paradis et al, 2006)	

Cartography: Wesley Weatherbee. CRS: NAD1983 CSRS UTM Zone 20N. Black grid squares are 200m². Grey grid squares are 20m². Contains information licensed under the Open Government License - Nova Scotia.

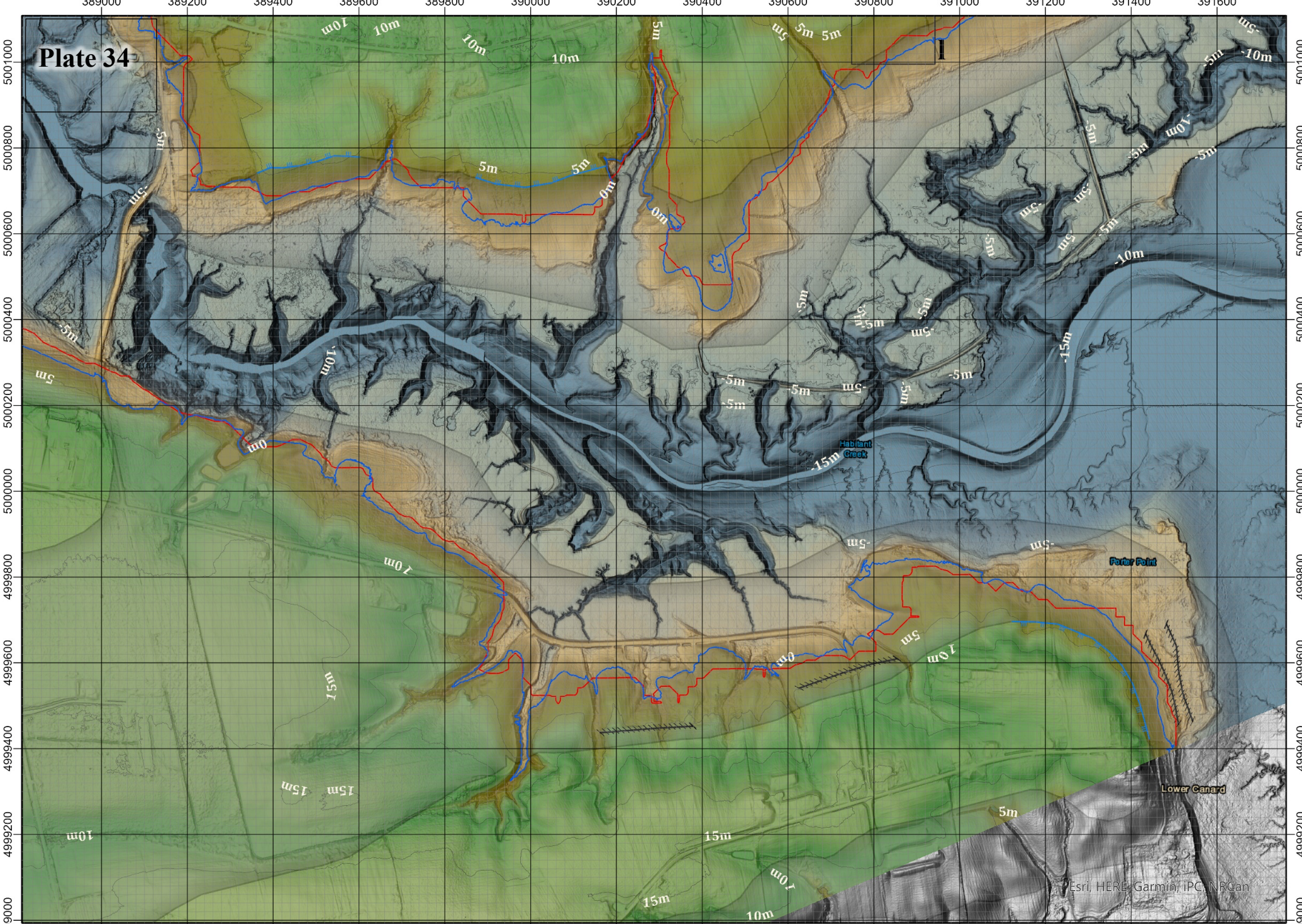
Plate 33



Mineral Occurrence	Artifacts from 2020	Lacustrine Limit (Paradis et al., 2006)	Nearshore Deposits (Paradis et al., 2006)	Paleo-elevation
Reference Section	Dated Sample (Dalton et al., 2020)	Raised Beach Cusps (This Study)	Raised Beach Ridge (Paradis et al., 2006)	Ice Sheet Limit (Dalton et al., 2020)
Delta	Archaeological Site	Modelled Marine Limit (1m)	Raised Terrace (Paradis et al., 2006)	Metres
	Modelled Marine Limit (20m)	Ring Features (This Study)		0 100 200 M

Cartography: Wesley Weatherbee. CRS: NAD1983 CSRS UTM Zone 20N. Black grid squares are 200m². Grey grid squares are 20m². Contains information licensed under the Open Government License - Nova Scotia.

Plate 34



Reference Section	Mineral Occurrence	Artifacts from 2020	Lacustrine Limit (Paradis et. al, 2006)	Nearshore Deposits (Paradis et. al, 2006)	Paleo-elevation
Dated Sample (Dalton et. al, 2020)	Raised Beach Cusps (This Study)	Modelled Marine Limit (1m)	Ice Sheet Limit (Dalton et. al, 2020)	Raised Beach Ridge (Paradis et. al, 2006)	<p>Cartography: Wesley Weatherbee. CRS: NAD1983 CSRS UTM Zone 20N. Black grid squares are 200m². Grey grid squares are 20m². Contains information licensed under the Open Government License - Nova Scotia.</p> <p>0 100 200 M</p>
Archaeological Site	Modelled Marine Limit (20m)	Raised Terrace (Paradis et. al, 2006)	Ring Features (This Study)	Delta	

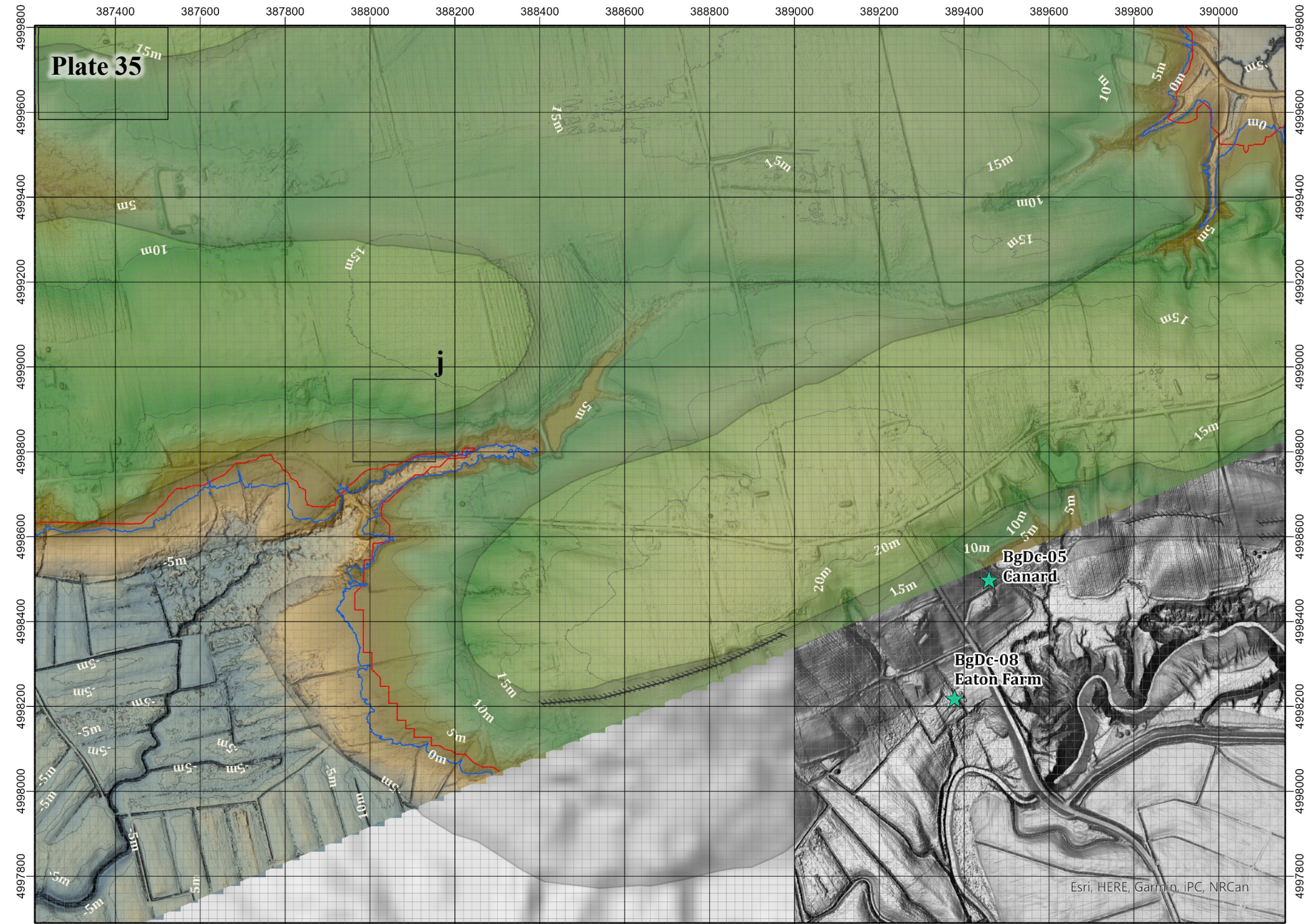


Plate 35

j

**BgDc-05
Canard**

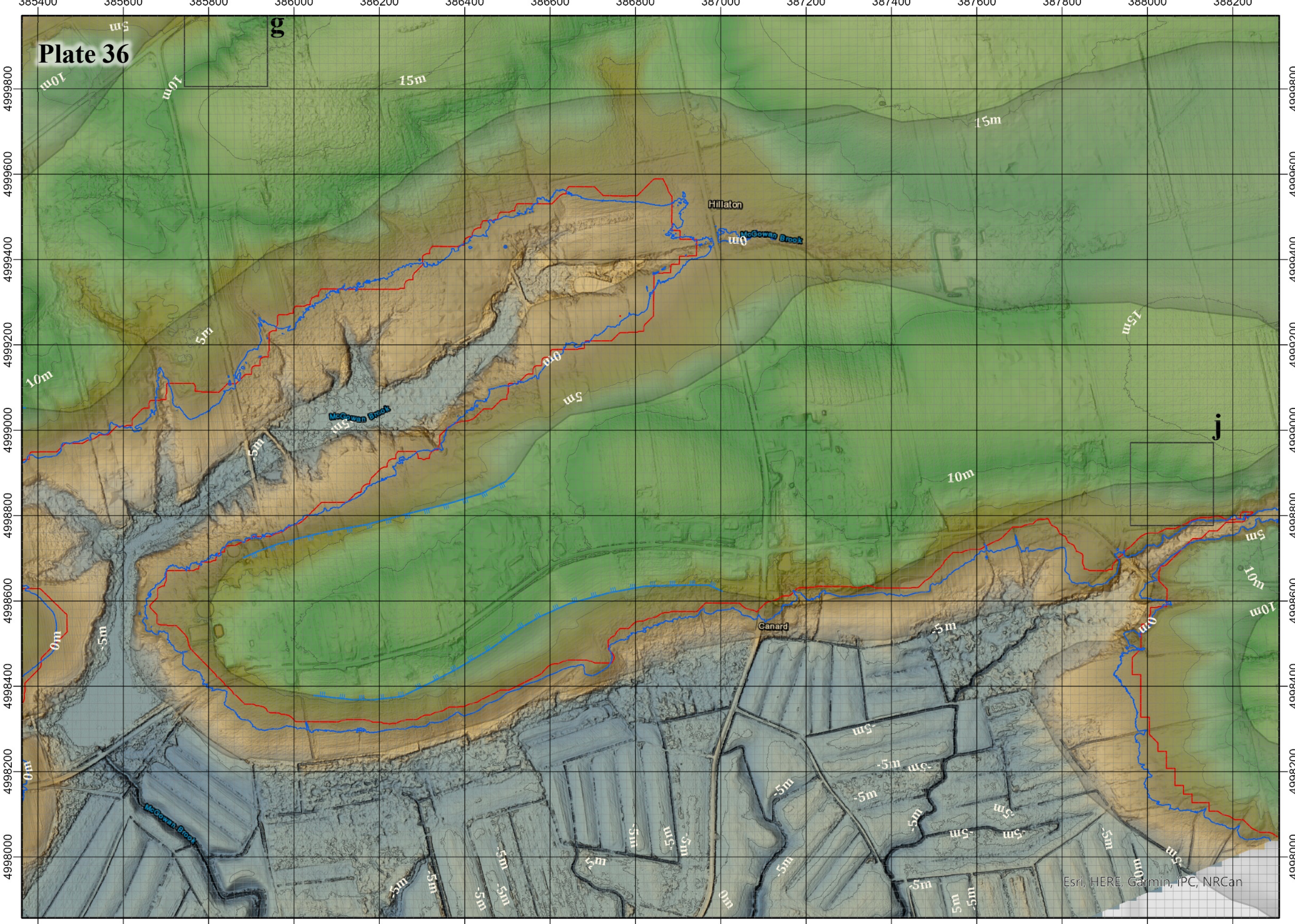
**BgDc-08
Eaton Farm**

Esri, HERE, Garmin, IPC, NRCan

Reference Section	Mineral Occurrence	Artifacts from 2020	Lacustrine Limit (Paradis et. al, 2006)	Nearshore Deposits (Paradis et. al, 2006)	Paleo-elevation
Delta	Dated Sample (Dalton et. al, 2020)	Raised Beach Cusps (This Study)	Raised Beach Ridge (Paradis et. al, 2006)	Ice Sheet Limit (Dalton et. al, 2020)	Contour (5m)
Archaeological Site	Modelled Marine Limit (1m)	Raised Terrace (Paradis et. al, 2006)	Ring Features (This Study)	Modelled Marine Limit (20m)	0 100 200 M

Cartography: Wesley Weatherbee. CRS: NAD1983 CSRS UTM Zone 20N. Black grid squares are 200m². Grey grid squares are 20m². Contains information licensed under the Open Government License - Nova Scotia.

Plate 36



Reference Section	Artifacts from 2020	Lacustrine Limit (Paradis et al, 2006)	Nearshore Deposits (Paradis et al, 2006)	Ice Sheet Limit (Dalton et al, 2020)
Mineral Occurrence	Dated Sample (Dalton et al, 2020)	Raised Beach Ridge (Paradis et al, 2006)	Raised Terrace (Paradis et al, 2006)	Ring Features (This Study)
Delta	Archaeological Site	Modelled Marine Limit (1m)	Modelled Marine Limit (20m)	
Raised Beach Cusps (This Study)				

Metres

100
-10

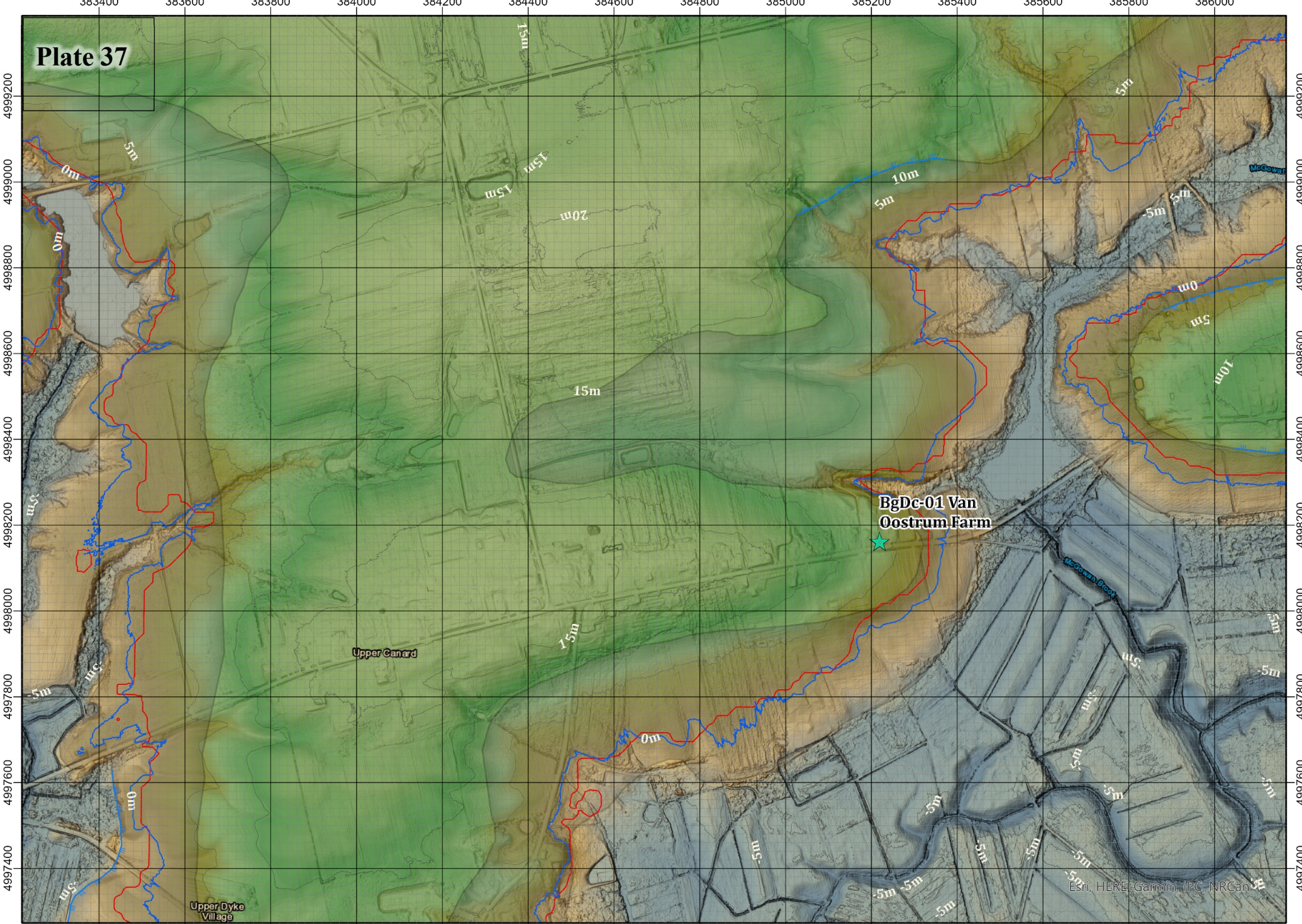
Contour (5m)

0 100 200 M

Cartography: Wesley Weatherbee. CRS: NAD1983 CSRS UTM Zone 20N. Black grid squares are 200m². Grey grid squares are 20m². Contains information licensed under the Open Government License - Nova Scotia.

Esri, HERE, Garmin, IPC, NRCan

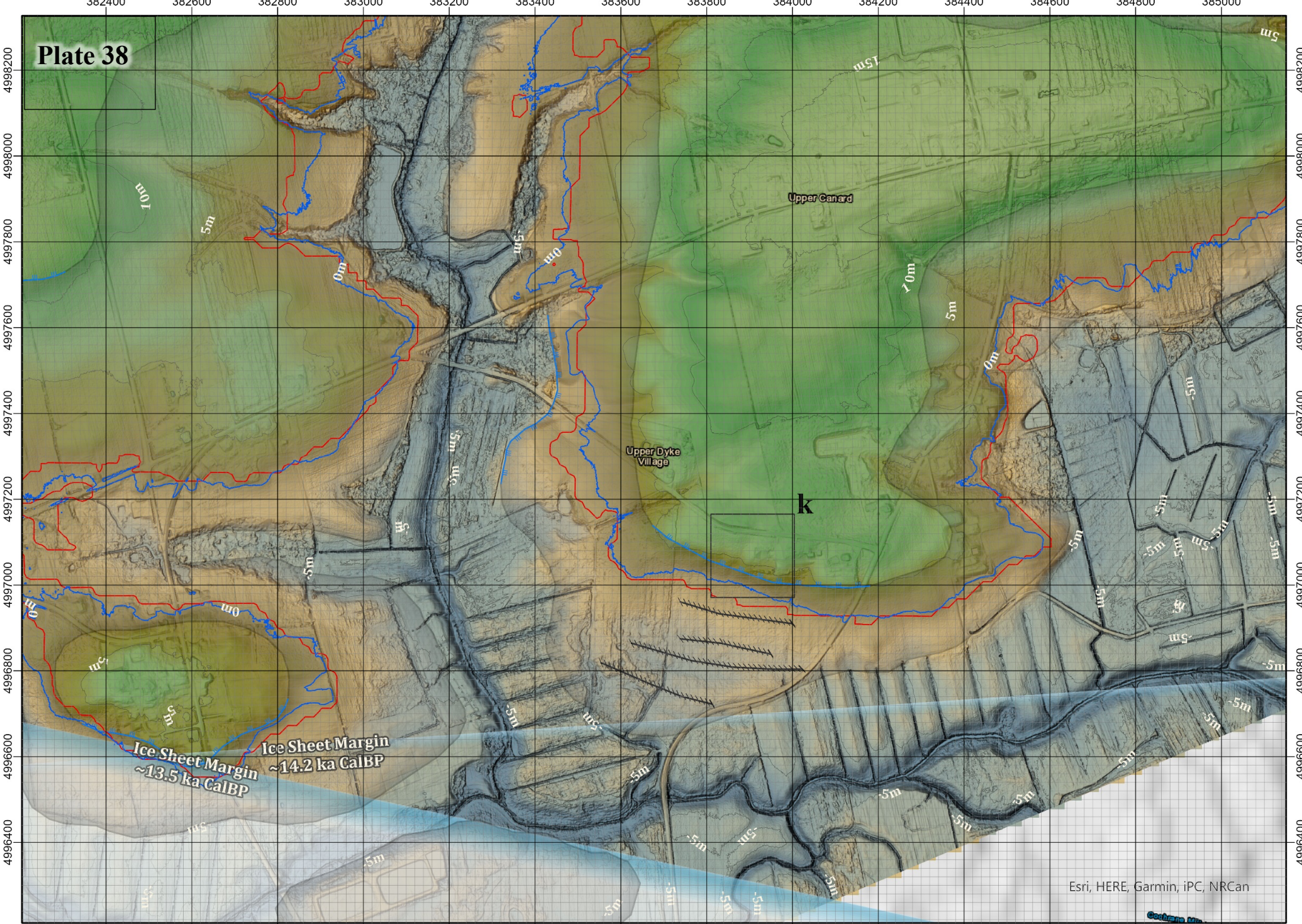
Plate 37



Reference Section	Mineral Occurrence	Artifacts from 2020	Lacustrine Limit (Paradis et. al, 2006)	Nearshore Deposits (Paradis et. al, 2006)	Paleo-elevation
Dated Sample (Dalton et. al, 2020)	Dated Sample (Dalton et. al, 2020)	Raised Beach Cusps (This Study)	Raised Beach Ridge (Paradis et. al, 2006)	Ice Sheet Limit (Dalton et. al, 2020)	Contour (5m)
Delta	Archaeological Site	Modelled Marine Limit (1m)	Raised Terrace (Paradis et. al, 2006)	Ring Features (This Study)	

Cartography: Wesley Weatherbee. CRS: NAD1983 CSRS UTM Zone 20N. Black grid squares are 200m². Grey grid squares are 20m². Contains information licensed under the Open Government License - Nova Scotia.

Plate 38

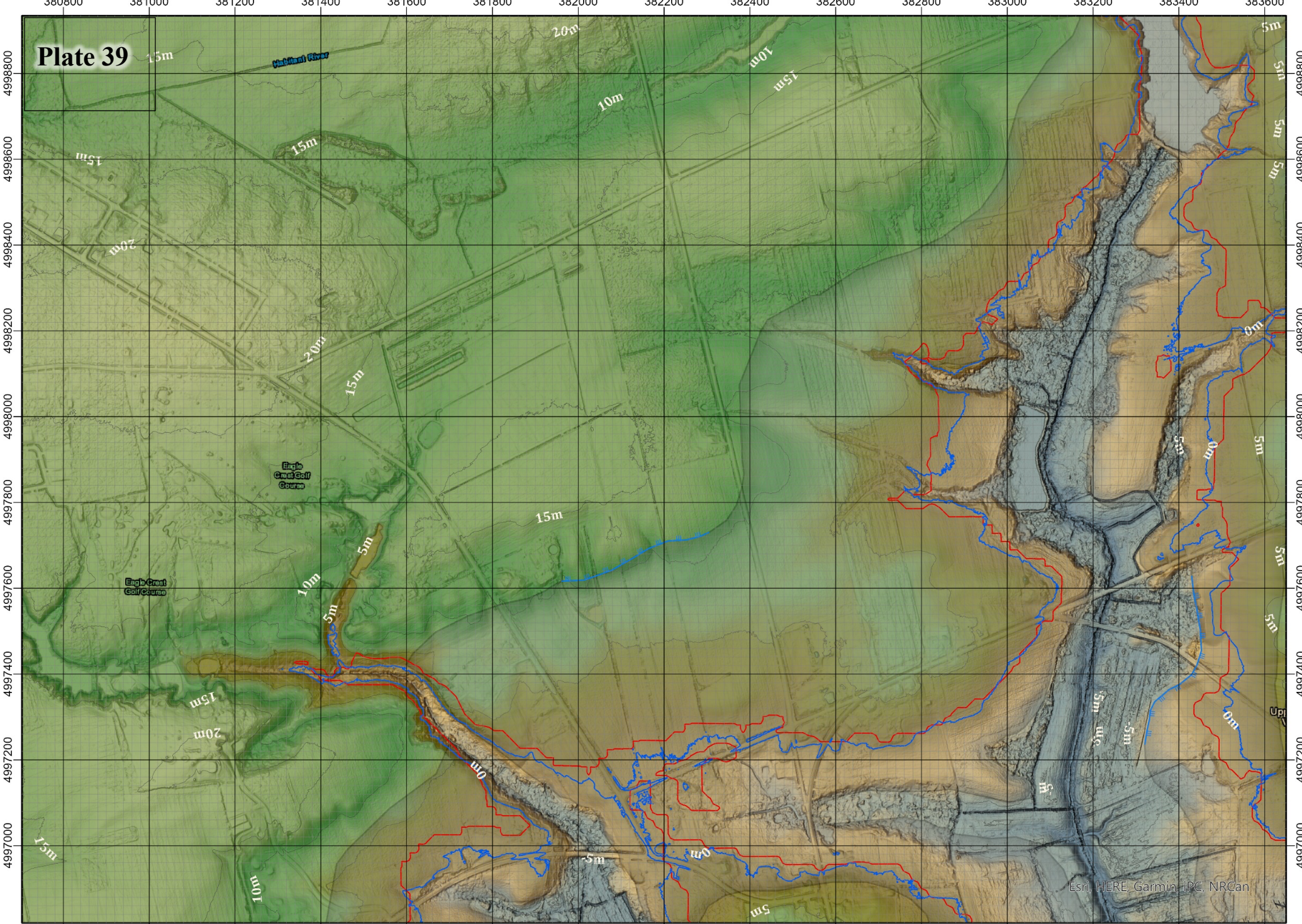


Reference Section	Artifacts from 2020	Lacustrine Limit (Paradis et. al, 2006)	Nearshore Deposits (Paradis et. al, 2006)	Paleo-elevation
Dated Sample (Dalton et. al, 2020)	Raised Beach Cusps (This Study)	Raised Beach Ridge (Paradis et. al, 2006)	Ice Sheet Limit (Dalton et. al, 2020)	Metres
Archaeological Site	Modelled Marine Limit (1m)	Raised Terrace (Paradis et. al, 2006)	Ring Features (This Study)	0 100 200 M
Delta				N

Cartography: Wesley Weatherbee. CRS: NAD1983 CSRS UTM Zone 20N. Black grid squares are 200m². Grey grid squares are 20m². Contains information licensed under the Open Government License - Nova Scotia.

Esri, HERE, Garmin, iPC, NRCan

Plate 39



Reference Section	Mineral Occurrence	Artifacts from 2020	Lacustrine Limit (Paradis et. al, 2006)	Nearshore Deposits (Paradis et. al, 2006)	Ice Sheet Limit (Dalton et. al, 2020)	Metres 100 -10	Cartography: Wesley Weatherbee. CRS: NAD1983 CSRS UTM Zone 20N. Black grid squares are 200m ² . Grey grid squares are 20m ² . Contains information licensed under the Open Government License - Nova Scotia.
Delta	Dated Sample (Dalton et. al, 2020)	Raised Beach Cusps (This Study)	Raised Beach Ridge (Paradis et. al, 2006)	Raised Terrace (Paradis et. al, 2006)	Ring Features (This Study)		

Esri, HERE, Garmin, IPC, NRCan

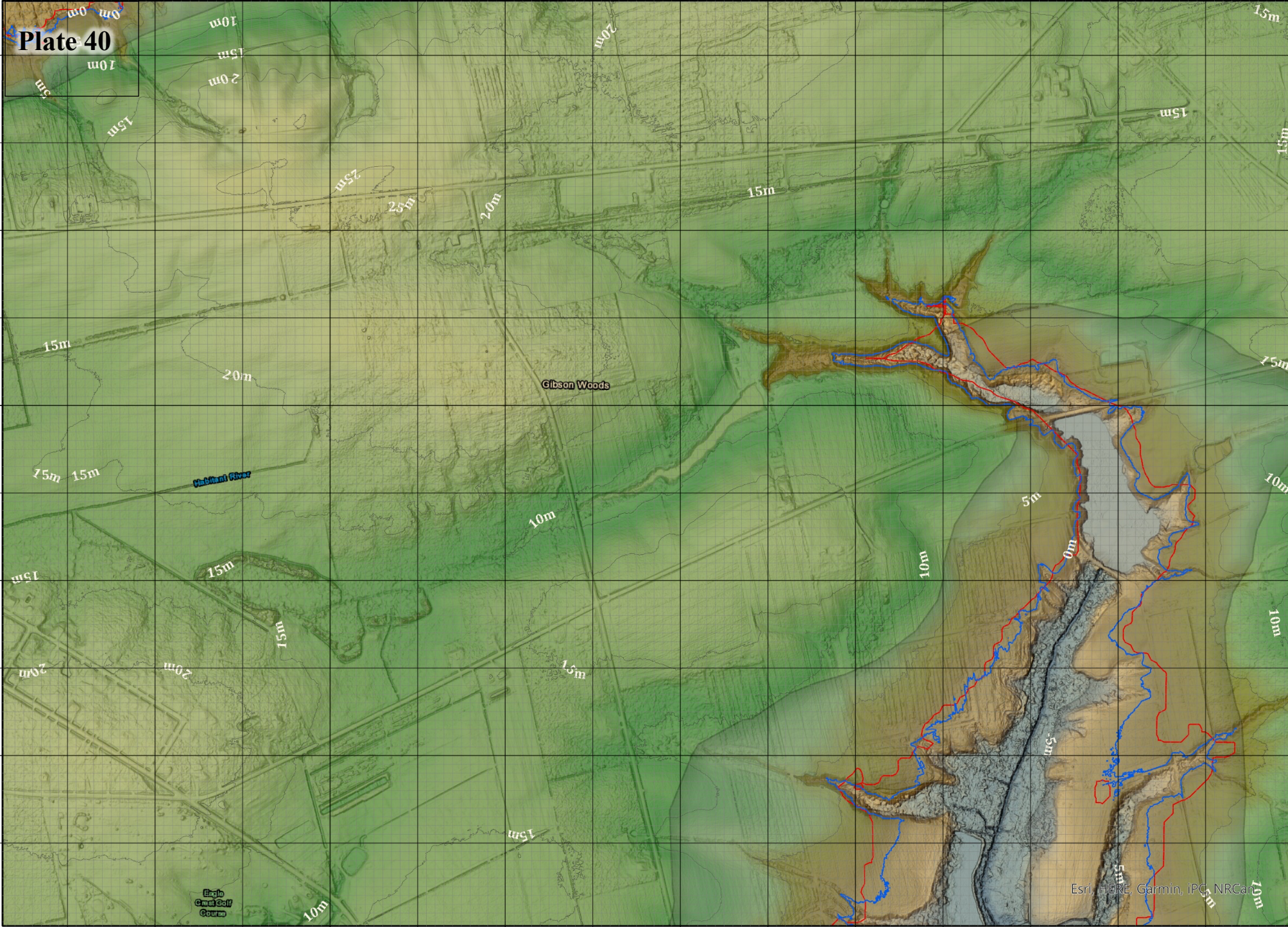


Plate 40

4999800
4999600
4999400
4999200
4999000
4998800
4998600
4998400
4998200
4998000

4999800
4999600
4999400
4999200
4999000
4998800
4998600
4998400
4998200
4998000

381000 381200 381400 381600 381800 382000 382200 382400 382600 382800 383000 383200 383400 383600

Reference Section	Mineral Occurrence	Artifacts from 2020	Lacustrine Limit (Paradis et al, 2006)	Nearshore Deposits (Paradis et al, 2006)	Ice Sheet Limit (Dalton et al, 2020)	<p>Metres</p>	<p>Cartography: Wesley Weatherbee. CRS: NAD1983 CSRS UTM Zone 20N. Black grid squares are 200m². Grey grid squares are 20m². Contains information licensed under the Open Government License - Nova Scotia.</p>
Delta	Dated Sample (Dalton et al, 2020)	Raised Beach Cusps (This Study)	Raised Beach Ridge (Paradis et al, 2006)	Raised Terrace (Paradis et al, 2006)	Ring Features (This Study)		



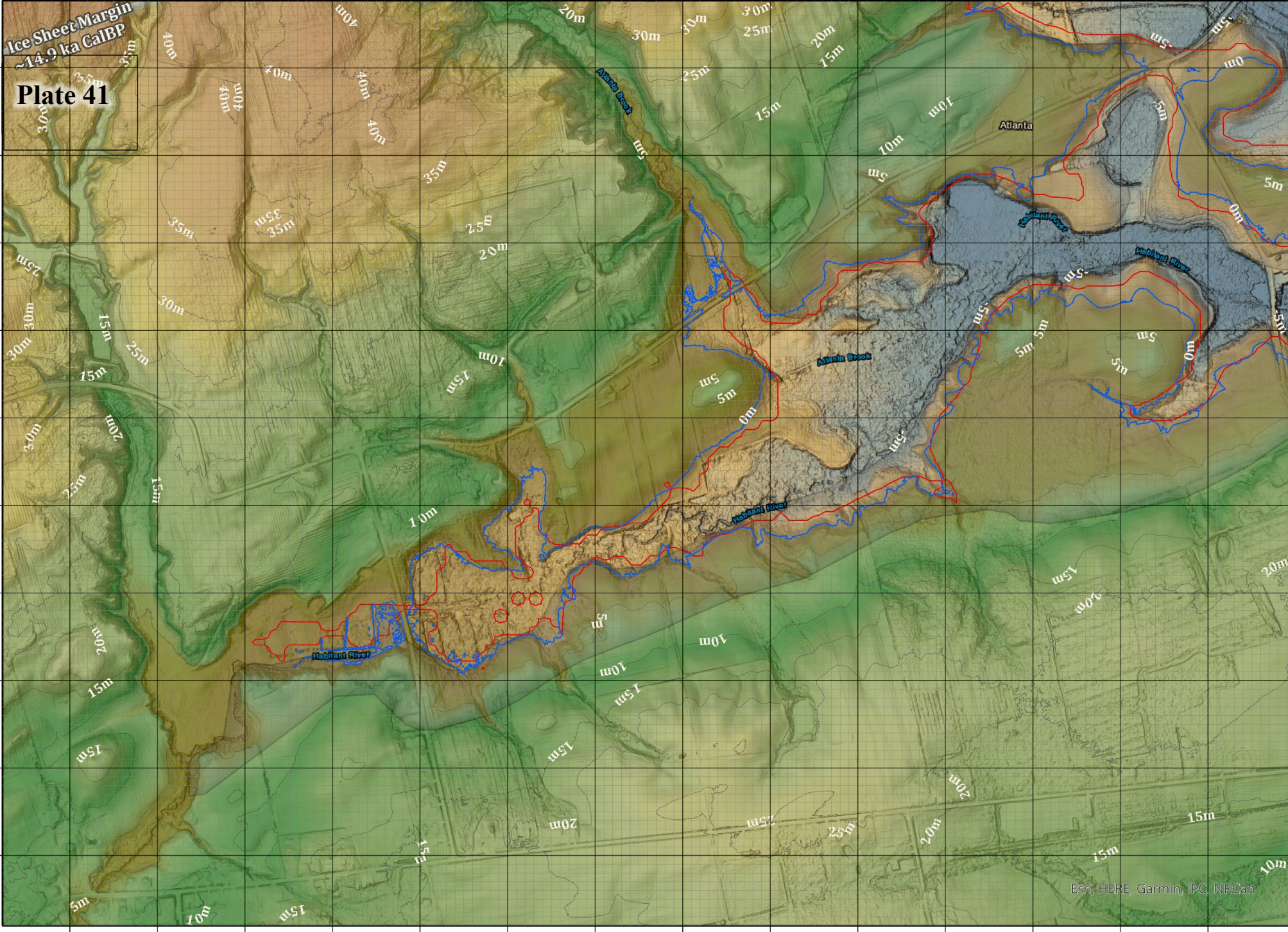


Plate 41

**Ice Sheet Margin
~14.9 ka CalBP**

Cartography: Wesley Weatherbee. CRS: NAD1983 CSRS UTM Zone 20N. Black grid squares are 200m². Grey grid squares are 20m². Contains information licensed under the Open Government License - Nova Scotia.

0 100 200 M

Contour (5m)

Metres
100
-10

- Reference Section
- Mineral Occurrence
- Dated Sample (Dalton et al, 2020)
- Artifacts from 2020
- Raised Beach Cusps (This Study)
- Modelled Marine Limit (1m)
- Modelled Marine Limit (20m)
- Delta
- Archaeological Site
- Lacustrine Limit (Paradis et al, 2006)
- Raised Beach Ridge (Paradis et al, 2006)
- Raised Terrace (Paradis et al, 2006)
- Ring Features (This Study)
- Nearshore Deposits (Paradis et al, 2006)
- Ice Sheet Limit (Dalton et al, 2020)

Esri, HERE, Garmin, IPC, NRCAN

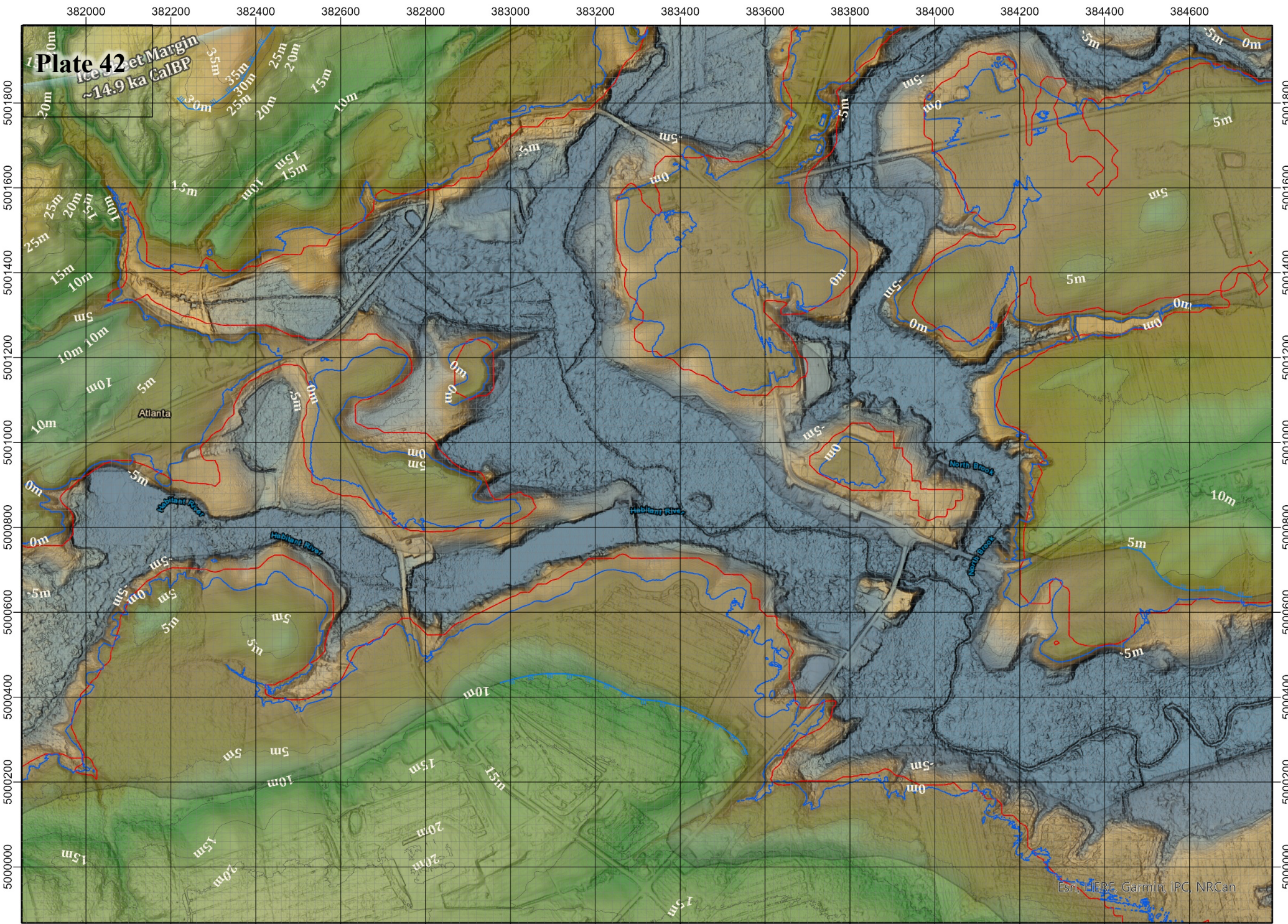


Plate 42
 Atlantic Margin
 ~14.9 ka CalBP

Reference Section	Mineral Occurrence	Artifacts from 2020	Lacustrine Limit (Paradis et al., 2006)	Nearshore Deposits (Paradis et al., 2006)	Ice Sheet Limit (Dalton et al., 2020)	Metres 100 -10
Dated Sample (Dalton et al., 2020)	Raised Beach Cusps (This Study)	Raised Beach Ridge (Paradis et al., 2006)	Raised Terrace (Paradis et al., 2006)	Ring Features (This Study)	Modelled Marine Limit (1m)	
Delta	Archaeological Site	Modelled Marine Limit (20m)				 0 100 200 M

Esri, HERE, Garmin, IPC, NRCan

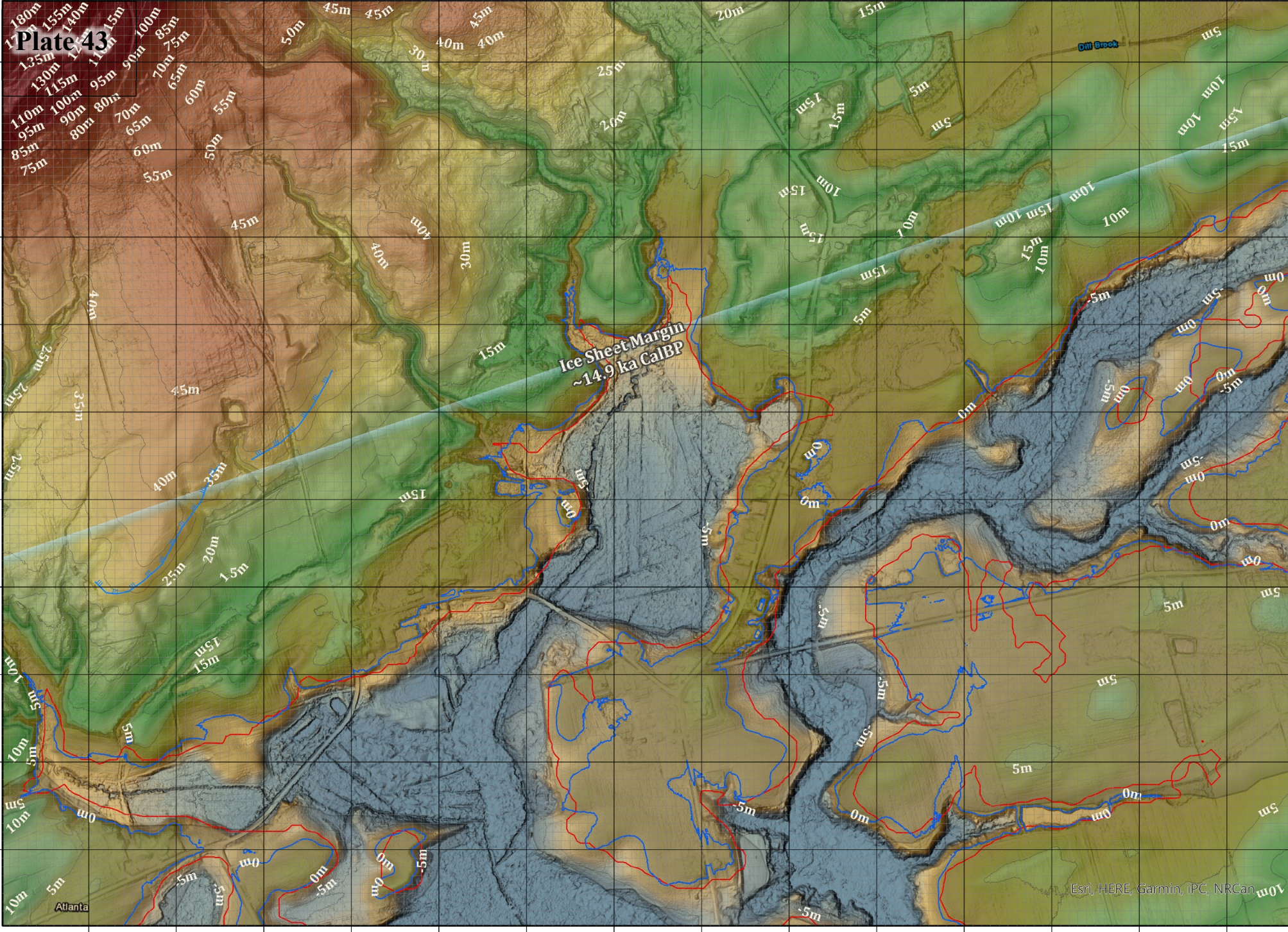


Plate 43

**Ice Sheet Margin
~14.9 ka CalBP**

Reference Section	Mineral Occurrence	Artifacts from 2020	Lacustrine Limit (Paradis et al, 2006)	Nearshore Deposits (Paradis et al, 2006)	Ice Sheet Limit (Dalton et al, 2020)	<p>Metres</p>	<p>Cartography: Wesley Weatherbee. CRS: NAD1983 CSRS UTM Zone 20N. Black grid squares are 200m². Grey grid squares are 20m². Contains information licensed under the Open Government License - Nova Scotia.</p>
Delta	Dated Sample (Dalton et al, 2020)	Raised Beach Cusps (This Study)	Raised Beach Ridge (Paradis et al, 2006)	Raised Terrace (Paradis et al, 2006)	Ring Features (This Study)		

Esri, HERE, Garmin, IPCan

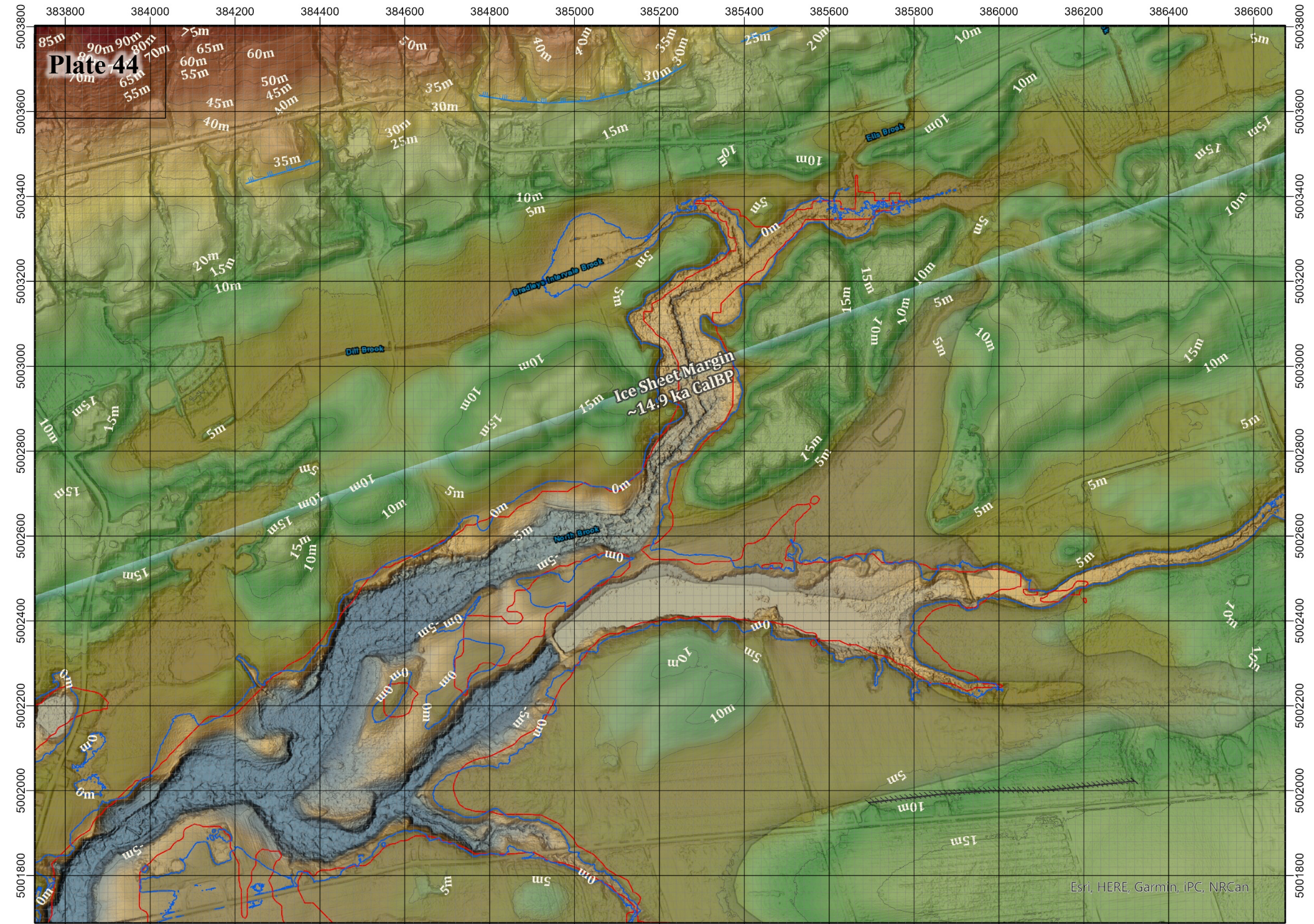


Plate 44

**Ice Sheet Margin
~14.9 ka CalBP**

Reference Section	Artifacts from 2020	Lacustrine Limit (Paradis et al, 2006)	Nearshore Deposits (Paradis et al, 2006)	Paleo-elevation
Dated Sample (Dalton et al, 2020)	Raised Beach Cusps (This Study)	Ice Sheet Limit (Dalton et al, 2020)	Raised Beach Ridge (Paradis et al, 2006)	Metres
Archaeological Site	Modelled Marine Limit (1m)	Raised Terrace (Paradis et al, 2006)	Ring Features (This Study)	0 100 200 M
Delta	Modelled Marine Limit (20m)			N

Cartography: Wesley Weatherbee. CRS: NAD1983 CSRS UTM Zone 20N. Black grid squares are 200m². Grey grid squares are 20m². Contains information licensed under the Open Government License - Nova Scotia.

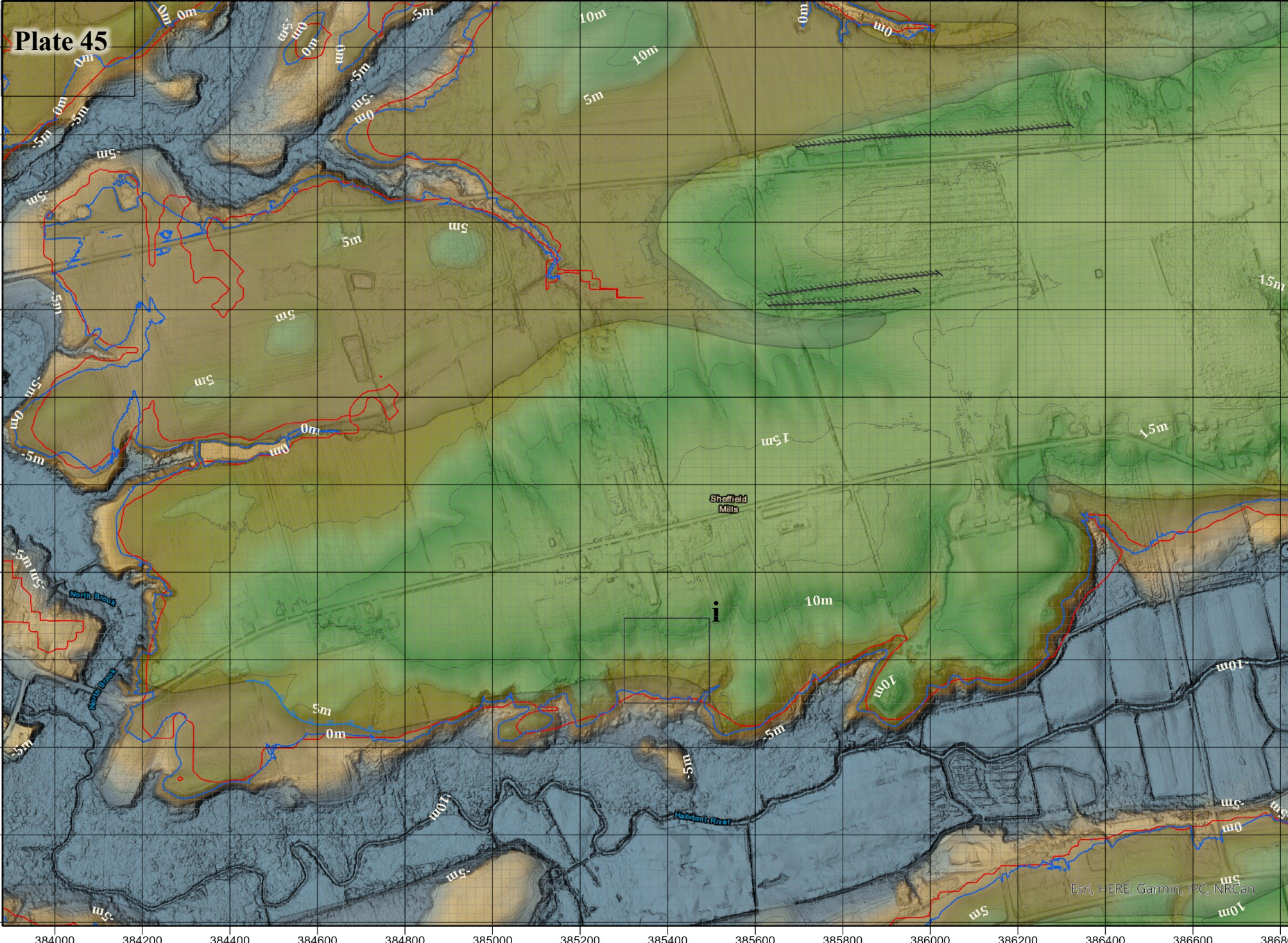


Plate 45

Reference Section	Mineral Occurrence	Artifacts from 2020	Lacustrine Limit (Paradis et. al, 2006)	Nearshore Deposits (Paradis et. al, 2006)	Paleo-elevation
Dated Sample (Dalton et. al, 2020)	Raised Beach Cusps (This Study)	Raised Beach Ridge (Paradis et. al, 2006)	Ice Sheet Limit (Dalton et. al, 2020)	Metres	<p>Cartography: Wesley Weatherbee. CRS: NAD1983 CSRS UTM Zone 20N. Black grid squares are 200m². Grey grid squares are 20m². Contains information licensed under the Open Government License - Nova Scotia.</p> <p>0 100 200 M</p>
Delta	Archaeological Site	Raised Terrace (Paradis et. al, 2006)	Modelled Marine Limit (1m)	Modelled Marine Limit (20m)	

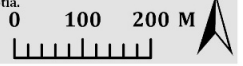
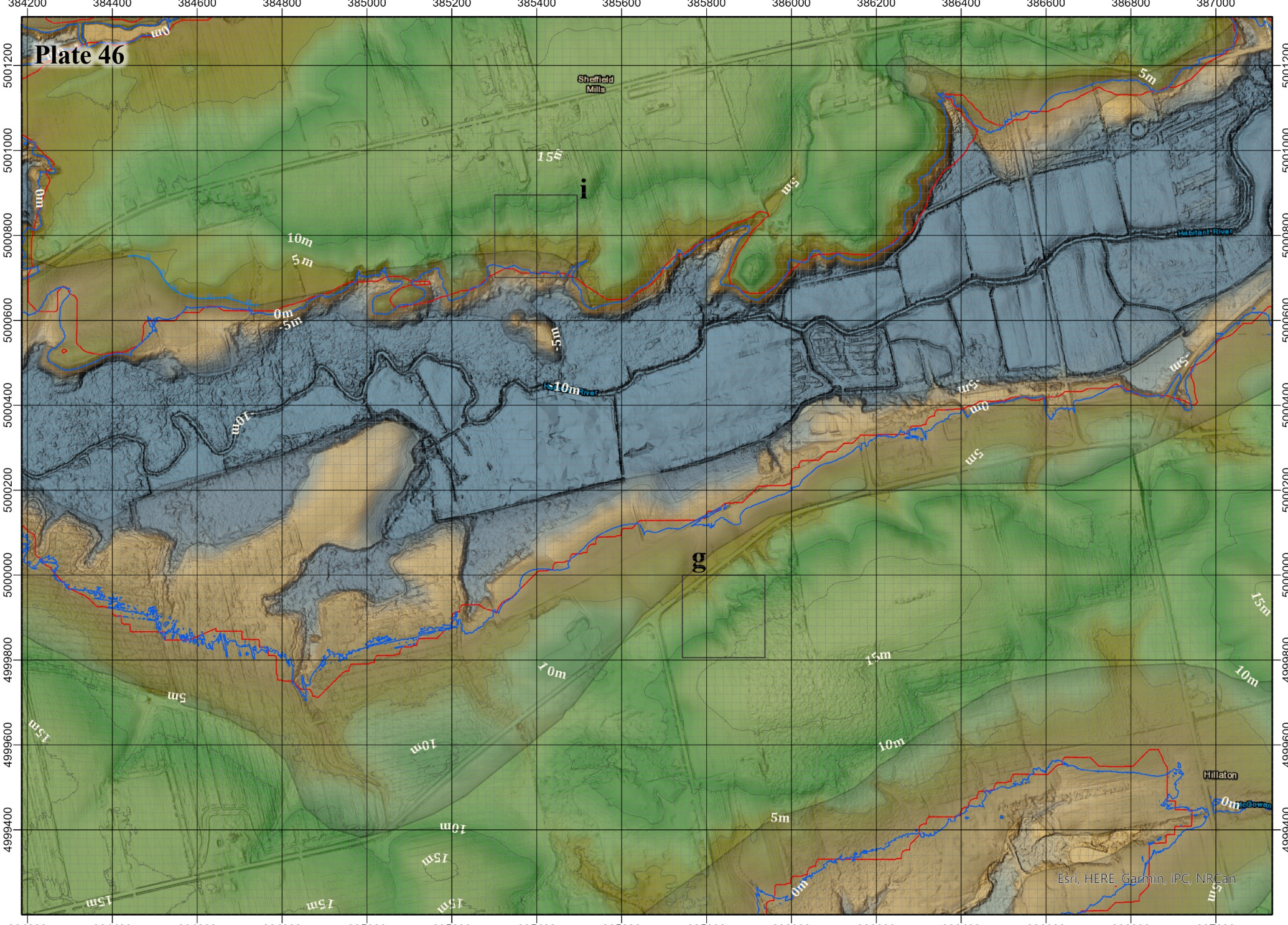


Plate 46

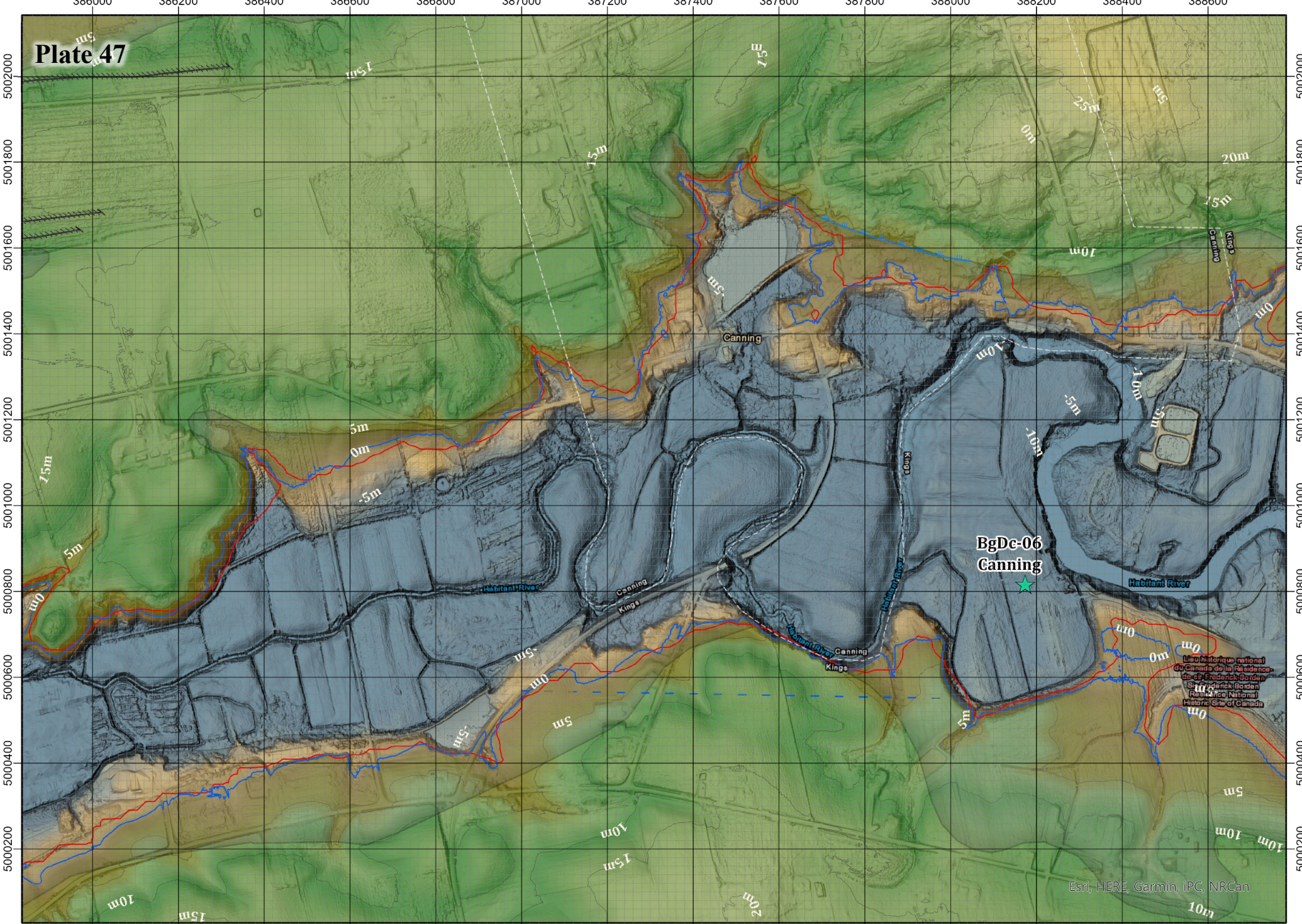


<ul style="list-style-type: none"> ✱ Mineral Occurrence ⊙ Dated Sample (Dalton et. al, 2020) ★ Archaeological Site 	<ul style="list-style-type: none"> ★ Artifacts from 2020 □ Raised Beach Cusps (This Study) — Modelled Marine Limit (1m) — Modelled Marine Limit (20m) 	<ul style="list-style-type: none"> — Lacustrine Limit (Paradis et. al, 2006) ▨ Raised Beach Ridge (Paradis et. al, 2006) — Raised Terrace (Paradis et. al, 2006) □ Ring Features (This Study) 	<ul style="list-style-type: none"> ▨ Nearshore Deposits (Paradis et. al, 2006) — Ice Sheet Limit (Dalton et. al, 2020) 	<p>Metres</p> <div style="display: flex; align-items: center;"> <div style="width: 20px; height: 20px; background-color: #c44e52; margin-right: 5px;"></div> 100 <div style="width: 20px; height: 20px; background-color: #90a46b; margin-left: 20px; margin-right: 5px;"></div> -10 </div>	<p>Cartography: Wesley Weatherbee, CRS: NAD1983 CSRS UTM Zone 20N. Black grid squares are 200m². Grey grid squares are 20m². Contains information licensed under the Open Government License - Nova Scotia.</p>
---	---	---	--	---	---

0 100 200 M

Contour (5m)

Plate 47



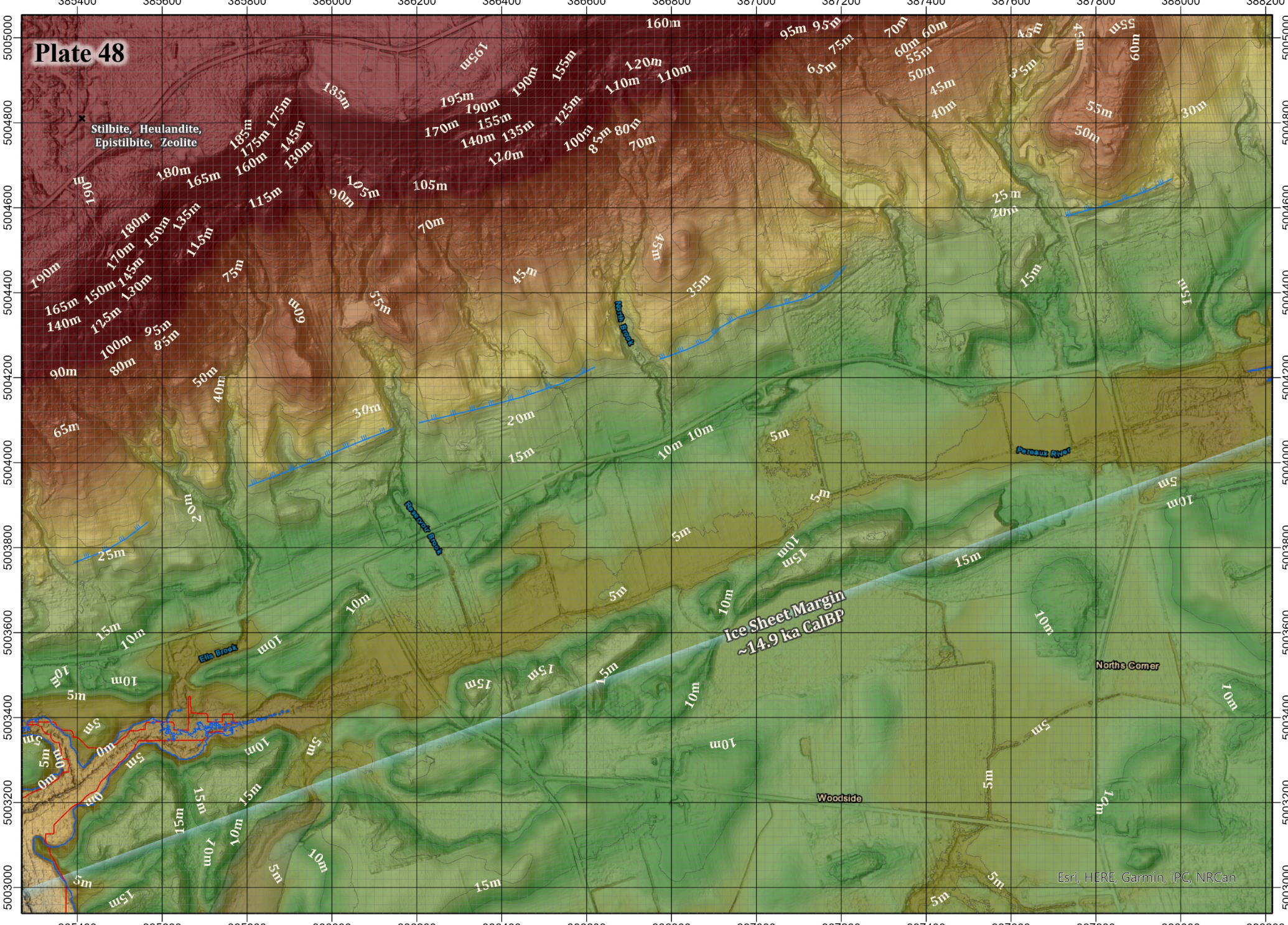
Reference Section	Artifacts from 2020	Lacustrine Limit (Paradis et al, 2006)	Nearshore Deposits (Paradis et al, 2006)	Paleo-elevation Metres 100 -10
Dated Sample (Dalton et al, 2020)	Raised Beach Cusps (This Study)	Modelled Marine Limit (1m)	Ice Sheet Limit (Dalton et al, 2020)	Contour (5m)
Delta	Archaeological Site	Modelled Marine Limit (20m)	Raised Terrace (Paradis et al, 2006)	Ring Features (This Study)

Cartography: Wesley Weatherbee. CRS: NAD1983 CSRS UTM Zone 20N. Black grid squares are 200m². Grey grid squares are 20m². Contains information licensed under the Open Government License - Nova Scotia.

Esri, HERE, Garmin, IPC, NRCAN

0 100 200 M

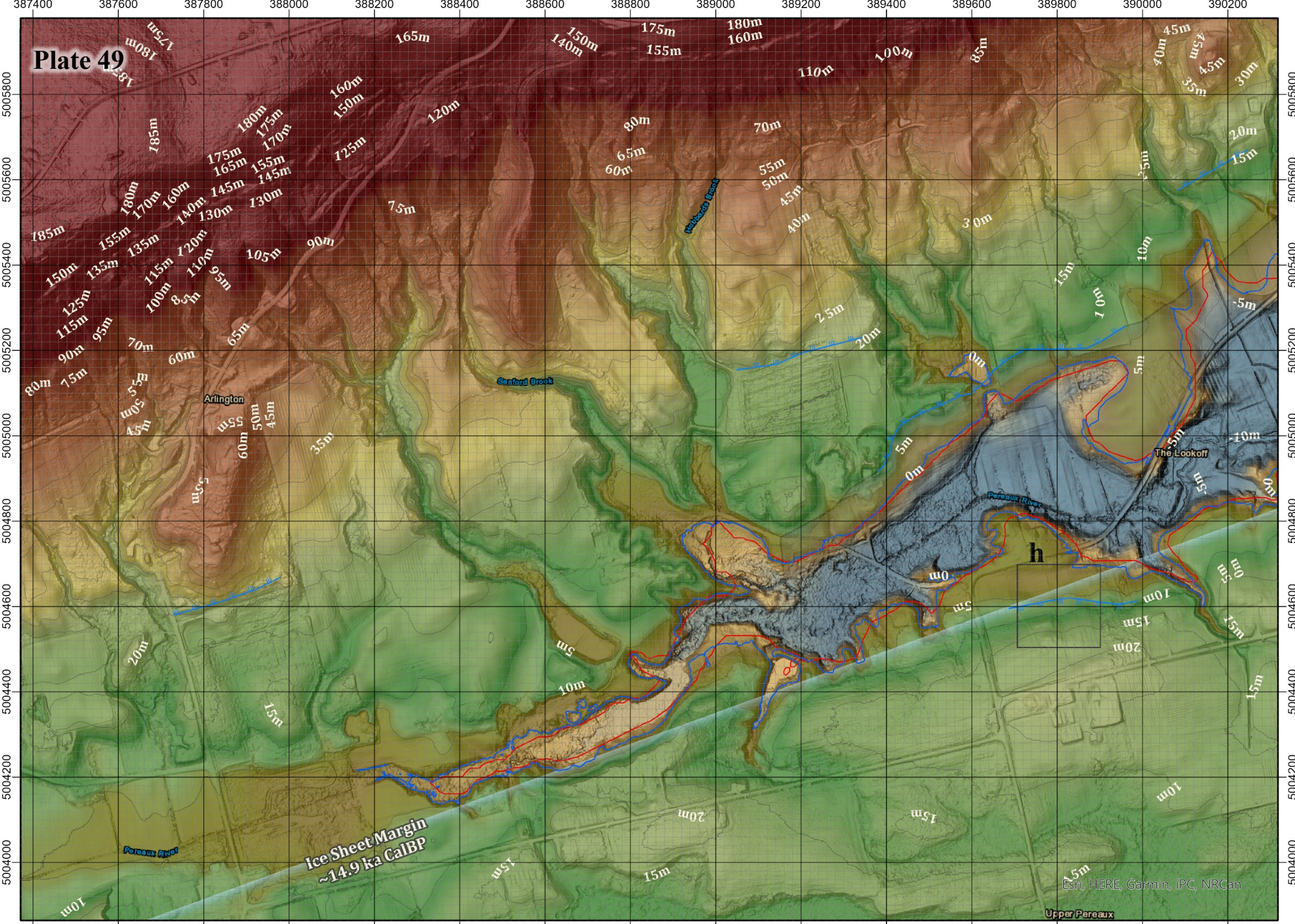
Plate 48



Reference Section	Mineral Occurrence	Artifacts from 2020	Lacustrine Limit (Paradis et al., 2006)	Nearshore Deposits (Paradis et al., 2006)	Paleo-elevation
Dated Sample (Dalton et al., 2020)	Raised Beach Cusps (This Study)	Raised Beach Ridge (Paradis et al., 2006)	Ice Sheet Limit (Dalton et al., 2020)	Metres	Cartography: Wesley Weatherbee. CRS: NAD1983 CSRS UTM Zone 20N. Black grid squares are 200m ² . Grey grid squares are 20m ² . Contains information licensed under the Open Government License - Nova Scotia.
Delta	Archaeological Site	Modelled Marine Limit (1m)	Raised Terrace (Paradis et al., 2006)	Contour (5m)	
	Modelled Marine Limit (20m)	Ring Features (This Study)			0 100 200 M

Esri, HERE, Garmin, IPC, NRCAN

Plate 49



Reference Section	Artifacts from 2020	Lacustrine Limit (Paradis et. al, 2006)	Nearshore Deposits (Paradis et. al, 2006)	Paleo-elevation
Dated Sample (Dalton et. al, 2020)	Raised Beach Cusps (This Study)	Raised Beach Ridge (Paradis et. al, 2006)	Ice Sheet Limit (Dalton et. al, 2020)	Metres
Archaeological Site	Modelled Marine Limit (1m)	Raised Terrace (Paradis et. al, 2006)	Ring Features (This Study)	N
Delta	Modelled Marine Limit (20m)			0 100 200 M

Cartography: Wesley Weatherbee. CRS: NAD1983 CSRS UTM Zone 20N. Black grid squares are 200m². Grey grid squares are 20m². Contains information licensed under the Open Government License - Nova Scotia.

Esri, HERE, Garmin, IPC, NRCAN